

Weather-based forecasting of energy generation, consumption and price for electrical microgrids management



Jonathan Dumas

Supervisor: Prof. Bertrand Cornélusse

Faculty of Applied Sciences
Department of Computer Science and Electrical Engineering
Liège University

This version of the manuscript is pending the approval of the jury.

This dissertation is submitted for the degree of
Doctor of Philosophy

Jury members

Prof. Quentin Louveaux (President) University of Liège, Belgium.

Prof. Bertrand Cornélusse (Supervisor) University of Liège, Belgium.

Prof. Gilles Louppe University of Liège, Belgium.

Prof. XX University of Y, COUNTRY.

Prof. XX University of Y, COUNTRY.

Prof. XX University of Y, COUNTRY.

“ Nothing is impossible, just do it and let’s see. ”

— **A true coconut-shaker**

“There are admirable potentialities in every human being. Believe in your strength and your youth. Learn to repeat endlessly to yourself: It all depends on me. ”

— **André Gide**

“In vino veritas. ”

— **Pliny the Elder, 23–79 A.D.**

Declaration

I hereby declare that except where specific reference is made to the work of others, the contents of this dissertation are original and have not been submitted in whole or in part for consideration for any other degree or qualification in this, or any other university. This dissertation is my own work and contains nothing which is the outcome of work done in collaboration with others, except as specified in the text and Acknowledgements.

Jonathan Dumas
November 2021

Acknowledgements

Family

I would like to acknowledge my family, and especially Perrine and Lily my daughter. Without their emotional and material support, I would have never achieved this thesis. Perrine spared me a lot of time managing our daughter to let me focus on this work, **she did, in fact, the most difficult part of the job**. It is easy to work especially in a research environment. It is much more difficult to raise a child. In addition, without her, I could have never been so much implied in the Shifters Belgium, a non-profit organization to help to make an energy transition to a carbon-free economy, and to be implied in activities organized by the working group on the sustainability of the ReD, an association aiming to gather the Ph.D. candidates from the University of Liège, the climate and digital collages, and the ClimActes 2021 summer school.

Supervisor

I would like to express my gratitude to my supervisor Prof. Bertrand Cornélusse. I would like to state that Bertrand Cornélusse is very implicated to design interesting lectures for the bachelor and master students. He is also implicated to supervise its Ph.D. students despite its busy agenda. Professors are supposed to be superman or superwoman: teach, teach and teach, then, being at the front end of the research, and of course, being deeply implicated in the University and Faculty challenges. But they have as everybody 24 hours per day :). He made it possible to work with the Sienna group and encouraged me all along the past three years. We have had nice discussions on technical topics such as optimization and machine learning but also friendly talks and numerous other topics. For instance, we had the opportunity to spend a very nice stay at the first microgrids summer school at Belfort in 2019. He also provided the funds for three summer schools: microgrids summer school at Belfort [2019], sustainable ICT summer school at Catholic University of Louvain [2020], and ClimActes at Liège University [2021]. He provided the funds for attending several conferences: 16th European Energy Market Conference (EEM 2019), XXI Power Systems Computation Conference (PSCC 2020), 16th International Conference on Probabilistic Methods

Applied to Power Systems (PMAFS 2020), 14th IEEE PowerTech (PowerTech 2021). Finally, my two stays at Sienna University in 2019 and 2020 (just before the lockdown of the covid-19 crisis).

Thesis committee and jury members

I am grateful to Prof. Simone Paoletti, Prof. Quentin Louveaux, and Xavier Fettweis, research associate FNRS, for being part of my thesis committee, their support, and discussions about optimization and weather forecasting, respectively. In addition, Xavier Fettweis taught me how to use the MAR regional climate model. I sincerely thank the members of the jury for devoting themselves to the reading of this manuscript and all the related administrative duties.

Liège University Applied Science Faculty colleagues

I would like to thank my colleagues and friends of the Applied Science Faculty for their support and for the interesting discussions we had together during the last three years: especially Selmane Dakir, Antonio Sutura, Antoine Wehenkel, Laurine Duchesne, Pascal Leroy, Adrien Bolland, Raphael Fonteneau, Sylvain Quoilin, Gauthier Gain, Ioannis Noulas, Miguel Manuel de Villena, and all the others that I did not mention. I thank also Gilles Louppe, associate professor at Liège University for the quality of his course "INFO8010 - Deep Learning". Gilles Louppe is very implicated to design interesting courses. I enjoyed following his lectures. I followed them in Spring 2021 at the very end of my thesis and I wish I had attended them at the beginning of my thesis to better understand the deep learning topic that I learned from scratch.

Coconut-shakers group and ReD

I thank my beloved friends of the *coconut-shakers group*: Antoine Dubois, François Rigo, Thibaut Theate, Gilles Corman, and Adrien Corman. We have worked together intensively to propose actions and ideas at the Applied Science Faculty to try to make tiny changes about the climate change issue. There is still a huge gap between rhetoric and actions. But we keep on believing that one-day things will change! I also thank the active members of the ReD: Kathleen Jacquerie, Chloe Stevenne, Coline Grégoire, and all the others that I did not mention.

Sienna University colleagues

I really appreciate working with Prof. Simone Paoletti, Prof. Antonello Giannitrapani, and Prof. Antonio Vicino from Sienna University. It was wonderful to work with them

at Sienna University and we have spent very nice friendly moments. They are devoted to their work, and they know how to make a good working relationship. They helped me to better understand stochastic programming and to develop interesting research directions.

Master students

I would like to thank all the master students that did incredible work on various topics such as forecasting, optimization, during their master thesis, and especially during the covid-19 crisis. It was my pleasure to work with them: Audrey Lempereur [2020-Applied Science Faculty], Clement Liu [2020-Ecole Polytechnique], Jean Cyrus de Gourcuff [2021-Ecole Polytechnique], Colin Cointe [2021-Mines ParisTech], Damien Lanaspeze [2021-Mines ParisTech], Benjamin Delvoye [2021-Applied Science Faculty], and Gabriel Guerra Martin [2021-Polytechnic University of Catalonia].

Liège University Applied Science Faculty staff

I sincerely thank the shadow workers of the Applied Science Faculty: the cleaning workers (thank you Patricia!), the administrative staff (Eric Vangenechten), and all the others that I did not mention. I thank also the academic staff of the Applied Science Faculty: Eric Delhez (for the discussions on sustainability even if I think can do better!), Angélique Leonard, Dominique Toye, and all the others that I did not mention.

Liège University human resource staff

I would like to thank all the human resource staff. We are so lucky at the University of Liège of having free and very high-quality training courses on various topics such as self-development, negotiation, teamwork, etc. In particular, I appreciate the training courses of Jean Yves Girin. He is incredible and he helped me to improve my human skills (but there is still a lot of work to do). I can only encourage all the academics (including professors), administrative staff, Ph.D. candidates, and researchers to attend these training courses. Most of the time I was the only man and the only one from the Applied Science Faculty. Does that mean that the 'men' do not need these training courses about human skills?

Liège University IFRES

I thank the IFRES for the pedagogical training that we attend as teaching assistants. We are lucky that the Liège University provides these training courses.

P. Pinson

I thank professor Prof. Pierre Pinson from the Technical University of Denmark. His work has been a great inspiration during this thesis. In addition, he is open to discussion and sharing all material from his courses. In particular, I used a lot of the materials of the course "Renewables in Electricity Markets" to design the forecasting lessons that I taught in the course "ELEN0445 Microgrids" at the University of Liège during the years 2018, 2019, 2020, and 2021.

Summer schools

Microgrids Belfort 2019 summer school. I thank all the members of the microgrids Belfort 2019 summer school, and especially Robin Roche. It was the first summer school on microgrids and we learned a lot in a very nice working environment. The Typhoon Hil team did a great job presenting its tools and organize the challenge.

Sustainable ICT 2020 summer school. I also thank the members of the Sustainable ICT 2020 summer school that took place at the Catholic University of Louvain (UCL). It was an incredible summer school with very skilled researchers and Ph.D. candidates. There is at UCL a group of Ph.D. candidates (Thibault Pirson, Gregoire Lebrun, and many others) and professors (Jean-Pierre Raskin, Hervé Jeanmart, David Bol) very motivated to address the sustainability challenges. It is a great source of inspiration.

ClimACTES 2021 summer school. I am grateful to all the members of the ClimACTES 2021 summer school that took place at Liège University. This event was outstanding where we have faced the challenges of climate change and the urgent need to drastically reduce the emission of greenhouse gases. The first week was dedicated to lessons from professors from several universities about these challenges. Then, we worked in the second week to develop projects to achieve ambitious targets to help to decarbonize the economy. I was part of the education team, and I learned from students and people from various backgrounds. It was one of the richest experiences in my life. Philippe Gilson that founded ClimACTES is a great source of inspiration. The work of all the ClimACTES volunteers was incredible. They dedicated two entire years to build this summer school. I can only say congratulations!

Reviewers

I would like to thank all the reviewers of the papers submitted to conferences and jour-

nals. They helped me to improve the work proposed, and to get out of my comfort zone.

Liège University

Finally, I thank the University of Liège. Indeed, they financed me as a teaching assistant during these two last years, and provide me a nice working environment.

Abstract

“*Do. Or do not. There is no try.*”

— Yoda

Climate Change

The Intergovernmental Panel on Climate Change proposes different mitigation strategies to achieve the net emissions reductions that would be required to follow a pathway that **limits global warming to 1.5°C** with no or limited overshoot. The decade 2009-2019 has been particularly intense in terms of rhetoric about efforts to tackle the climate crisis such as the 2015 United Nations Climate Change Conference, COP 21. However, the carbon dioxide emissions at the world scale have been constantly increasing from 29.7 (GtCO₂) in 2009 to 34.2 in 2019. *The current gap between rhetoric and reality on emissions is still huge.* However, there are still pathways to reach net-zero by 2050. Several reports have been published to propose detailed scenarios and strategies to achieve these targets. They remain narrow and extremely challenging, requiring all stakeholders, governments, businesses, investors, and citizens to take action this year and every year after so that the goal does not slip out of reach. In most of these trajectories, *electrification* and an increased share of *renewables* are some of the key pillars. The transition towards a carbon-free society goes through an inevitable increase of the share of renewable generation in the energy mix and a drastic decrease in terms of the total consumption of fossil fuels.

Thesis topic

Therefore, this thesis studies the *integration of renewables in power systems* by investigating forecasting and decision-making tools. Indeed, in contrast to conventional power plants, renewable energy is subject to uncertainty. Most of the generation technologies based on renewable sources are non-dispatchable, and their production is stochastic and hard to predict in advance. A high share of renewables is a great challenge for power systems that have been designed and sized for dispatchable units. In this context, *probabilistic* forecasts, which aim at modeling the distribution of all possible future

realizations, have become an important tool to equip decision-makers, hopefully leading to better decisions in energy applications.

Thesis content

This thesis focus on two main research questions: (1) How to produce reliable probabilistic forecasts of renewable generation, consumption, and electricity prices? (2) How to make decisions with uncertainty using probabilistic forecasts? The thesis perimeter is the energy management of "small" systems such as *microgrids* at a residential scale on a day-ahead basis. It is divided into two main parts to propose directions to address both research questions (1) a forecasting part; (2) a planning and control part.

Thesis first part

The forecasting part presents several techniques and strategies to produce probabilistic forecasts. First, we provide the forecasting basics by introducing the different types of forecasts to characterize the behavior of stochastic variables, such as renewable generation, and the tools to assess the different types of forecasts. The point forecasts, quantile forecasts, scenarios, and confidence intervals are studied in the next Chapters on several case studies. Second, common deep-learning models such as recurrent neural networks are used to compute PV and electrical consumption point forecasts. Third, deep-learning models such as the encoder-decoder architecture are implemented to produce PV quantile forecasts. Fourth, a confidence interval-based approach to compute probabilistic forecasting of imbalance prices is presented with a particular focus on the Belgian case. Finally, an investigation of the scenarios of renewable generation and electrical consumption is performed by comparing extensively a recent deep generative model, the normalizing flows, to common generative models such as variational autoencoders and generative adversarial networks.

Thesis second part

The planning and control part proposes approaches and methodologies, based on optimization for decision-making under uncertainty using probabilistic forecasts on several case studies. First, we introduce the basics of decision-making under uncertainty using optimization strategies: stochastic programming and robust optimization. Second, a value function-based approach as a way to propagate information from operational planning to real-time optimization is investigated in a deterministic framework. Third, three Chapters focus on the energy management of a grid-connected renewable generation plant coupled with a battery energy storage device in the capacity firming market,

designed to promote renewable power generation facilities in small non-interconnected grids. Both the stochastic and robust approaches are investigated to manage the day-ahead planning, and a sizing methodology of the system is proposed. Finally, the forecast value of deep learning generative models is investigated by considering the day-ahead market scheduling of an energy retailer.

Perspectives

The future directions of this thesis are: (1) new forecasting techniques that take advantage of the power system characteristics such as the graphical normalizing flows that are capable of learning the power network structure, and could be applied to hierarchical forecasting; (2) machine learning in power systems applications to design proxies. For instance, a deep learning model can be used for optimization by learning partially or totally the sizing space to provide a fast and efficient sizing tool, or simplifying optimization planning problems by learning a sub-optimal space. Indeed, neural network architecture can emulate the behavior of a physics solver that solves electricity differential equations to compute electricity flow in power grids. Such proxies could also be used to evaluate if a given operation planning decision would lead to acceptable trajectories where the reliability criterion is met in real-time.

Table of contents

List of figures	xxv
List of tables	xxxv
Foreword	1
1 General introduction	9
1.1 Context and motivations	9
1.2 Content and contributions	11
I Forecasting	19
Part I general nomenclature	23
2 Forecasting background	25
2.1 Point forecast	27
2.2 Probabilistic forecasts	28
2.2.1 Quantiles	28
2.2.2 Prediction intervals	29
2.2.3 Confidence intervals	30
2.2.4 Scenarios	31
2.2.5 Density forecasts	31
2.3 Model-based formulation	32
2.4 Model training	32
2.4.1 Regression with supervised learning	33
2.4.2 Empirical risk minimization	33
2.4.3 The "double descent" curve	35
2.4.4 Training methodology	36

2.4.5	Learning, validation, and testing sets	37
2.4.6	k-fold cross-validation	37
2.5	Conclusions	38
3	Forecast evaluation	41
3.1	Point forecasts metrics	43
3.2	Probabilistic forecasts metrics	44
3.2.1	Calibration	44
3.2.2	Univariate skill scores	45
3.2.3	Multivariate skill scores	47
3.3	Conclusions	49
4	Classification of load forecasting studies	51
5	Point forecasting	55
5.1	Formulation	57
5.2	Forecasting models	57
5.3	Results	58
5.4	Conclusions	60
6	Quantile forecasting	61
6.1	Formulation	64
6.2	Related work	65
6.3	Forecasting models	65
6.3.1	Gradient boosting regression (GBR)	65
6.3.2	Multi-layer perceptron (MLP)	66
6.3.3	Encoder-decoder (ED)	66
6.4	The ULiège case study	68
6.4.1	Case study description	68
6.4.2	Numerical settings	68
6.4.3	Day-ahead results	69
6.4.4	Intraday results	69
6.4.5	Conclusions	74
6.5	Comparison with generative models	75
6.6	Conclusions	77

7	Confidence interval forecasting	79
7.1	Related work	81
7.2	Formulation	82
7.2.1	Net regulation volume forecasting	82
7.2.2	Imbalance price forecasting	84
7.3	Case study	86
7.4	Results	86
7.5	Conclusions	91
7.6	Appendix: balancing mechanisms	93
7.6.1	Balancing mechanisms	93
7.6.2	Belgium balancing mechanisms	94
7.6.3	Additional results	94
8	Scenarios	99
8.1	Introduction	102
8.1.1	Related work	103
8.1.2	Research gaps and scientific contributions	105
8.1.3	Applicability of the generative models	109
8.1.4	Organization	109
8.2	Background	110
8.2.1	Multi-output forecasts using a generative model	110
8.2.2	Deep generative models	110
8.2.3	Theoretical comparison	118
8.3	Quality assessment	119
8.4	Case study	124
8.4.1	Implementation details	124
8.4.2	Hyper-parameters	127
8.5	Quality results	132
8.5.1	Wind track	132
8.5.2	All tracks	138
8.6	Conclusions and perspectives	145
8.7	Appendix: Table 8.1 justifications	146
8.8	Appendix: background	147
8.8.1	NFs	147
8.8.2	VAEs	148
8.8.3	GANs	150

9 Part I conclusions	153
II Planning and control	155
10 Decision-making background	159
10.1 Linear programming	161
10.2 Stochastic optimization	162
10.3 Robust optimization	164
10.3.1 Benders-dual cutting plane algorithm	165
10.3.2 Column and constraints generation algorithm	166
10.4 Conclusions	167
11 Coordination of the planner and controller	169
11.1 Notation	173
11.2 Problem statement	175
11.2.1 Assumptions	175
11.2.2 Formulation	175
11.3 Proposed method	176
11.3.1 Computing the cost-to-go function	177
11.3.2 OPP formulation	178
11.3.3 OP constraints	179
11.3.4 RTP formulation	180
11.3.5 RTO constraints	181
11.4 Test description	182
11.5 Numerical results	184
11.5.1 No symmetric reserve	184
11.5.2 Results with symmetric reserve	186
11.6 Conclusions	190
12 Capacity firming using a stochastic approach	191
12.1 Notation	194
12.1.1 Sets and indices	194
12.1.2 Parameters	195
12.1.3 Variables	196
12.2 The Capacity Firming Framework	196
12.2.1 Day-ahead engagement	197
12.2.2 Real-time control	197

12.3 Problem formulation	198
12.3.1 Evaluation methodology	201
12.4 MiRIS microgrid case study	202
12.4.1 Results for unbiased PV scenarios with fixed variance	203
12.4.2 BESS capacity sensitivity analysis	206
12.5 Conclusions and perspectives	210
12.6 Appendix: PV scenario generation	210
13 Capacity firming sizing	213
13.1 Problem statement	216
13.2 Forecasting methodology	218
13.2.1 Gaussian copula-based PV scenarios	219
13.2.2 PV point forecast parametric model	219
13.2.3 PV scenarios	220
13.3 Sizing study	222
13.3.1 Problem statement and assumptions	222
13.3.2 Levelized cost of energy (LCOE)	222
13.3.3 Case study description	224
13.3.4 Sizing parameters	225
13.3.5 Sizing results	225
13.4 Conclusions and perspectives	227
14 Capacity firming using a robust approach	229
14.1 Problem formulation	234
14.1.1 Deterministic planner formulation	235
14.1.2 Robust planner formulation	235
14.1.3 Second-stage planner transformation	237
14.1.4 Controller formulation	239
14.2 Solution methodology	239
14.2.1 Convergence warm start	240
14.2.2 Algorithm convergence	240
14.2.3 Benders-dual cutting plane algorithm	241
14.2.4 Column and constraints generation algorithm	243
14.3 Case Study	244
14.3.1 Numerical settings	245
14.3.2 Constant risk-averse parameters strategy	247
14.3.3 Dynamic risk-averse parameters strategy	247

14.3.4	BD convergence warm start improvement	248
14.3.5	BD and CCG comparison	252
14.4	Conclusion	253
15	Energy retailer	255
15.1	Notation	257
15.2	Problem formulation	258
15.3	Value results	261
15.3.1	Results summary	264
15.4	Conclusions	265
15.5	Appendix: Table 15.2 justifications	265
16	Part II conclusions	267
17	General conclusions and perspectives	269
17.1	Summary	269
17.2	Future directions	270
	References	273

List of figures

1	IPCC global net anthropogenic CO ₂ emission pathways and targets. Credits: [4, Figure SPM.3a].	2
2	Climate change fake news. Credits: Xavier Gorce.	5
3	Global GHG emissions under different scenarios and the emissions gap in 2030 (median and 10-th to 90-th percentile range; based on the pre-COVID-19 current policies scenario). Credits: [109, Figure ES.5].	6
4	World consumption of primary energy (left) and shares of global primary energy (left) from 1994 to 2020. Credits: BP's Statistical Review of World Energy 2020 [100].	7
1.1	Microgrid scheme. Credits: ELEN0445 Microgrids course https://github.com/bcornelusse/ELEN0445-microgrids , Liège University.	11
1.2	Thesis skeleton.	12
1.3	Part I skeleton.	22
2.1	Chapter 2 position in Part I.	26
2.2	The classical U-shaped risk curve arising from the bias-variance trade-off. Curves for training risk (dashed line) and test risk (solid line). Note, \mathcal{H} on the Figure is \mathcal{G} . Credits: [7].	35
2.3	The double descent risk curve, which incorporates the U-shaped risk curve (<i>i.e.</i> , the "classical" regime) together with the observed behavior from using high capacity function classes (<i>i.e.</i> , the "modern" interpolating regime), separated by the interpolation threshold. Credits: [7].	36
2.4	Proper evaluation protocols. Credits: Francois Fleuret, EE559 Deep Learning, EPFL https://fleuret.org/dlc/	37
2.5	k -fold cross-validation.	38
3.1	Chapter 3 position in Part I.	42
4.1	Chapter 4 position in Part I.	52

5.1	Chapter 5 position in Part I.	56
5.2	PV forecast scores, GBR (top) and LSTM (bottom).	59
5.3	Consumption forecast scores, GBR (top) and LSTM (bottom).	59
6.1	Chapter 6 position in Part I.	63
6.2	Encoder-decoder architecture.	67
6.3	NMAE, NRMSE, and CRPS of the day-ahead models per lead time k	70
6.4	CRPS of intraday models per lead time k	72
6.5	Quantiles <i>vs.</i> point forecasts of day-ahead models of gate 12:00 (left), and intraday models of gate 06:00 (right) on <i>August 2, 2020</i> , the observations are in red.	73
6.6	Quantile forecast quality evaluation of LSTM <i>v.s</i> NFs models.	76
7.1	Chapter 7 position in Part I.	80
7.2	TSPA imbalance price forecasting process.	82
7.3	NRV transition matrix from t to $t + 15$ min (left) and $t + 60$ min (right).	83
7.4	Rolling forecast strategy.	87
7.5	Scores.	88
7.6	ELIA NRV on <i>January 8, 2019</i> (blue) and <i>January 10, 2019</i> (orange).	89
7.7	MLP, GP and TSPA 15 minutes horizon forecasts on <i>January 8, 2019</i> (top) and <i>January 10, 2019</i> (bottom).	90
7.8	MLP, GP and TSPA 60 (top) and 360 (bottom) minutes horizon forecasts on <i>January 8, 2019</i>	95
7.9	MLP, GP and TSPA 60 (top) and 360 (bottom) minutes horizon forecasts on <i>January 10, 2019</i>	96
7.10	MLP, GP and TSPA forecasts on <i>January 8, 2019</i> (top) and <i>January 10, 2019</i> (bottom), 12h00 UTC, with an horizon of 360 minutes.	97
8.1	Chapter 8 position in Part I.	101

- 8.2 The framework of the study. The Chapter's main purpose is to present and demonstrate the potential of NFs in power systems. A fair comparison is conducted both in terms of quality and value with the state-of-the-art deep learning generative models, GANs and VAEs, using the open data of the Global Energy Forecasting Competition 2014 [75]. The PV, wind power, and load datasets are used to assess the models. The quality evaluation is conducted by using eight complementary metrics, and the value assessment by considering the day-ahead bidding of an energy retailer using stochastic optimization. Overall, NFs tend to be more accurate both in terms of quality and value and are competitive with GANs and VAEs. 108
- 8.3 High-level comparison of three categories of generative models considered in this Chapter: normalizing flows, generative adversarial networks, and variational autoencoders. All models are conditional as they use the weather forecasts \mathbf{c} to generate scenarios $\hat{\mathbf{x}}$ of the distribution of interest \mathbf{x} : PV generation, wind power, load. Normalizing flows allow exact likelihood calculation. In contrast to generative adversarial networks and variational autoencoders, they explicitly learn the data distribution and provide direct access to the exact likelihood of the model's parameters. The inverse of the flow is used to generate scenarios. The training of generative adversarial networks relies on a min-max problem where the generator and the discriminator parameters are jointly optimized. The generator is used to compute the scenarios. Variational autoencoders indirectly optimize the log-likelihood of the data by maximizing the variational lower bound. The decoder computes the scenarios. Note: Section 8.2.3 provides a theoretical comparison of these models. 111
- 8.4 The process of conditional normalizing flows is illustrated with a three-step NF for PV generation. The model f_θ is trained by maximizing the log-likelihood of the model's parameters θ given a dataset composed of PV observations and weather forecasts. Recall f_θ defines a bijection between the variable of interest \mathbf{x} , PV generation, and a Normal distribution \mathbf{z} . Then, the PV scenarios $\hat{\mathbf{x}}$ are generated by using the inverse of f_θ that takes as inputs samples from the Normal distribution \mathbf{z} and the weather forecasts \mathbf{c} 114

- 8.5 The process of conditional variational autoencoder is illustrated for PV generation. The VAE is trained by maximizing the variational lower bound given a dataset composed of PV observations and weather forecasts. The encoder q_ϕ maps the variable of interest \mathbf{x} to a latent space \mathbf{z} . The decoder p_θ generates the PV scenarios $\hat{\mathbf{x}}$ by taking as inputs samples \mathbf{z} from the latent space and the weather forecasts \mathbf{c} 115
- 8.6 The process of the conditional generative adversarial network is illustrated for PV generation. The GAN is trained by solving a min-max problem given a dataset composed of PV observations \mathbf{x} and weather forecasts. The generator g_θ computes PV scenarios $\hat{\mathbf{x}}$ by taking as inputs samples from the Normal distribution \mathbf{z} and the weather forecasts \mathbf{c} , and the decoder d_ϕ tries to distinguish true data from scenarios. . . . 117
- 8.7 Classifier-based metric methodology. Each generative model generates M scenarios per day of the learning and testing sets. They are used to build M pairs of learning and testing sets for a conditional classifier by including an equal proportion of observations and weather forecasts. M conditional classifiers, per model, are trained and make predictions. The M ROC and AUC are computed per model, and the results are compared. 122
- 8.8 Methodology to assess both the quality and value of the GAN, VAE, and NF models implemented in this study. The PV, wind power, and load datasets of the open-access Global Energy Forecasting Competition 2014 are divided into three parts: learning, validation, and testing sets. The learning set is used to train the models, the validation set to select the optimal hyper-parameters, and the testing set to conduct the numerical experiments. The quality and value of the models are assessed by using the scenarios generated on the testing set. The quality evaluation consists of eight complementary metrics, and the value assessment is performed by using the simple and easily reproducible case study of the day-ahead bidding of an energy retailer. The energy retailer portfolio is composed of PV, wind power generation, load, and a storage system device. The retailer bids on the day-ahead market by computing a planning based on stochastic optimization. The dispatch is computed by using the observations of the PV generation, wind power, and load. Then, the profits are evaluated and compared. 125

- 8.9 Variational autoencoder structure implemented for the wind dataset. Both the encoder and decoder are feed-forward neural networks composed of one hidden layer with 200 neurons. Increasing the number of layers did not improve the results for this dataset. The latent space dimension is 20. 129
- 8.10 Generative adversarial network structure implemented for the wind dataset. Both the discriminator and generator are feed-forward neural networks composed of two hidden layers with 256 neurons. The latent space dimension is 64. 130
- 8.11 Normalizing flow structure implemented for the wind dataset. A single-step monotonic normalizing flow is implemented with a feed-forward neural network composed of four hidden layers with 300 neurons. The latent space dimension is 40. Note: for the sake of clarity the integrand network is not included but is a feed-forward neural network composed of three hidden layers with 40 neurons. Increasing the number of steps of the normalizing flow did not improve the results. The monotonic transformation is complex enough to capture the stochasticity of the variable of interest. However, when considering affine autoregressive normalizing flows the number of steps should be generally more important. Numerical experiments indicated a five-step autoregressive flow was required to achieve similar results for this dataset. Note: the results are not reported in this study for the sake of clarity. 131
- 8.12 Quality common metrics comparison on the wind (markers), PV (plain), and load (dashed) tracks. Quantile score (a): the lower and the more symmetrical the better. Note: the quantile score has been averaged over the marginals (the 24 time periods of the day). Reliability diagram (b): the closer to the diagonal, the better. Continuous rank probability score per marginal (c): the lower, the better. NF outperforms the VAE and GAN for both the PV and load tracks and is slightly outperformed by the VAE on the wind track. Note: all models tend to have more difficulties in forecasting the wind power that seems to be less predictable than the PV generation or the load. 134

- 8.13 Wind track Diebold-Mariano tests of the CRPS, QS, ES, and VS metrics. The Diebold-Mariano tests of the continuous rank probability score, quantile score, energy score, and variogram score confirm the VAE outperforms the NF on the wind track for these metrics. The NF is only outperformed by the VAE, and the GAN by both the VAE and NF. The heat map indicates the range of the p -values, the closer they are to zero, dark green, the more significant the difference between the scores of two models for a given metric. The statistical threshold is set to 5 % but the scale color is capped at 10 % for a better exposition of the relevant results. 135
- 8.14 Wind track classifier-based metric. The VAE (orange) is the best to mislead the classifier followed by the NF (blue), and GAN (green). Note: there are 50 ROC curves depicted for each model, each one corresponding to a scenario generated that is used as input of the classifier. It allows taking into account the variability of the scenarios to avoid having results dependent on a particular scenario. 136
- 8.15 Wind power scenarios shape comparison and analysis. Left part (a) NF, (c) GAN, and (e) VAE: 50 wind power scenarios (grey) of a randomly selected day of the testing set along with the 10 % (blue), 50 % (black), and 90 % (green) quantiles, and the observations (red). Right part (b) NF, (d) GAN, and (f) VAE: the corresponding Pearson time correlation matrices of these scenarios with the time periods as rows and columns. The NF tends to exhibit no time correlation between scenarios. In contrast, the VAE and GAN tend to be partially time-correlated over a few time periods. 137
- 8.16 PV and load tracks Diebold-Mariano tests. The Diebold-Mariano tests of the CRPS, QS, ES, and VS demonstrate the NF outperforms both the VAE and GAN. Note: the GAN outperforms the VAE for both the ES and VS for the PV track. However, the VAE outperforms the GAN on this dataset for both the CRPS and QS. 140
- 8.17 Classifier-based metric for both the PV and load tracks. The NF (blue) is the best to fake the classifier, followed by the VAE (orange), and the GAN (green). 141

8.18	PV scenarios shape comparison and analysis. Left part (a) NF, (c) GAN, and (e) VAE: 50 PV scenarios (grey) of a randomly selected day of the testing set along with the 10 % (blue), 50 % (black), and 90 % (green) quantiles, and the observations (red). Right part (b) NF, (d) GAN, and (f) VAE: the corresponding Pearson time correlation matrices of these scenarios with the time periods as rows and columns. Similar to wind power and load scenarios, NF tends to exhibit no time correlation between scenarios. In contrast, the VAE and GAN tend to be partially time-correlated over a few time periods.	142
8.19	Load scenarios shape comparison and analysis. Left part (a) NF, (c) GAN, and (e) VAE: 50 load scenarios (grey) of a randomly selected day of the testing set along with the 10 % (blue), 50 % (black), and 90 % (green) quantiles, and the observations (red). Right part (b) NF, (d) GAN, and (f) VAE: the corresponding Pearson time correlation matrices of these scenarios with the time periods as rows and columns. Similar to PV and wind power scenarios, NF tends to exhibit no time correlation between scenarios. In contrast, the VAE and GAN tend to be highly time-correlated.	143
8.20	Average of the correlation matrices over the testing set for the three datasets. Left: wind power; center: PV; right:load. The trend in terms of time correlation is observed on each day of the testing set for all the datasets. The NF scenarios are not correlated. In contrast, the VAE and GAN scenarios tend to be time-correlated over a few periods. In particular, the VAE generates highly time-correlated scenarios for the load dataset.	144
8.21	VAE process. Credits: Francois Fleuret, EE559 Deep Learning, EPFL https://fleuret.org/dlc/	149
9.1	Part II skeleton.	158
10.1	Chapter 10 position in Part II.	160
11.1	Chapter 11 position in Part II.	171
11.2	Hierarchical control procedure illustration.	177
11.3	Top: PV & consumption simulation data. Bottom: zoom on <i>June</i> 12, 2019.	184
11.4	Case 3 PV forecast on <i>June</i> 12, 2019, 06h00 UTC.	184
11.5	Case 1 (top), 2 (middle), 3 (bottom) cumulative peak costs.	186
11.6	Case 3 SOC (top) and net export power (bottom) on <i>June</i> 12, 2019. . .	187

11.7 Case 3 SOC comparison for RTO-OP ^{RNN} with and without symmetric reserve.	187
11.8 Case 1 (top) and 2 (bottom) cumulative peak costs.	188
11.9 Case 1 (top) and 2 (bottom) SOC.	189
12.1 Chapter 12 position in Part II.	192
12.2 Day-ahead nomination process.	197
12.3 MiRIS February 2019 PV production.	202
12.4 Planner S ratio indicator with $\#\Omega = 5, 10, 50, 100$, $\sigma = 3.5, 7, 10.5, 14\%$	203
12.5 Planner S revenue indicators with $\#\Omega = 5, 10, 50, 100$, $\sigma = 3.5, 7, 10.5, 14\%$	207
12.6 Optimal BESS for a given CAPEX price.	208
12.7 Planner S revenue indicators BESS capacity sensitivity analysis with $\#\Omega = 100$, $\sigma = 3.5, 7, 10.5, 14\%$	209
13.1 Chapter 13 position in Part II.	215
13.2 5 PV scenarios (gray), PVUSA point forecasts (red), and PV measurements (black).	221
13.3 Sizing approach.	223
13.4 Sizing results: $\text{net}(\pi, r_{\overline{S}})$ (€/ MWh).	226
14.1 Chapter 14 position in Part II.	231
14.2 Forecast-driven robust optimization strategy.	233
14.3 Results illustration on <i>September</i> 14, 2019.	246
14.4 Results with constant risk-averse parameters. Normalized profit (%) of the BD and CCG RO planners ($[\Gamma, q]$), deterministic ($[/, q]$) planner, and the reference that is the deterministic planner with point-forecasts (Nominal). Left part: LSTM quantiles, right part: NF quantiles.	249
14.5 Results with dynamic risk-averse parameters. Normalized profit (%) of the BD and CCG RO planners ($[d_{\Gamma}, d_q]$), and deterministic ($[/, d_q]$) planner. Left part: LSTM quantiles, right part: NF quantiles.	250
14.6 Benders convergence without (left) and with (right) an initial set of cuts on <i>September</i> 14, 2019.	251
15.1 Chapter 15 position in Part II.	256

- 15.2 Energy retailer case study: illustration of the observations on a random day of the testing set. The energy retailer portfolio is composed of PV generation, wind power, load, and a storage device. The PV, wind power, and load scenarios from the testing set are used as inputs of the stochastic day-ahead planner to compute the optimal bids. The net is the power balance of the energy retailer portfolio. The day-ahead prices π_t are obtained from the Belgian day-ahead market on *February 6, 2020*.[262](#)

List of tables

6.1	Training computation time (s).	69
6.2	Day-ahead models results.	70
6.3	NMAE, NRMSE, CRPS of intraday models.	71
6.4	Interval scores of intraday models.	71
7.1	Average scores over all lead times k	87
7.2	Elia imbalance prices.	95
8.1	Comparison of the study's contributions to three state-of-the-art studies using deep generative models. ✓: criteria fully satisfied, ~: criteria partially satisfied, ×: criteria not satisfied, ?: no information, -: not applicable. GAN: a GAN model is implemented; VAE: a VAE model is implemented; NF: a NF model is implemented; PV: PV scenarios are generated; Wind power: wind power scenarios are generated; Load: load scenarios are generated; Weather-based: the model generates weather-based scenarios; Quality assessment: a quality evaluation is conducted: Quality metrics: number of quality metrics considered; Value assessment: a value evaluation is considered with a case study; Open dataset: the data used for the quality and value evaluations are in open-access; Value replicability: the case study considered for the value evaluation is easily reproducible; Open-access code: the code used to conduct the experiments is in open-access. Note: the justifications are provided in 8.7.107	

8.2	Dataset and implementation details. Each dataset is divided into three parts: learning, validation, and testing sets. The number of samples (#) is expressed in days and is set to 50 days for the validation and testing sets. T is the number of periods per day considered, n_z the number of zones of the dataset, n_f the number of weather variables used, and \mathbf{c}_d is the dimension of the conditional vector, for a given day, that includes the weather forecasts and the one hot-encoding variables when there are several zones. Note: the days of the learning, validation, and testing sets are selected randomly.	127
8.3	(a) NF, (b) VAE, and (c) GAN hyper-parameters. The hyper-parameters selection is performed on the validation set using the Python library Weights & Biases [18]. This library is an experiment tracking tool for machine learning making it easier to keep track of experiments. The GAN model was the most time-consuming during this process followed by the VAE, and NF. Indeed, the GAN is highly sensitive to hyper-parameter modifications making challenging to identify a relevant set of values. In contrast, the NF achieved satisfactory results, both in terms of scenarios shapes and quality, by testing only a few sets of hyper-parameter values.	128
8.4	Averaged quality scores per dataset. The best performing deep learning generative model for each track is written in bold. The CRPS, QS, MAE-r, and ES are expressed in %. Overall, for both the PV and load tracks, the NF outperforms the VAE and GAN and is slightly outperformed by the VAE on the wind track.	138
11.1	Case studies parameters and data statistics.	183
11.2	Results without symmetric reserve.	185
11.3	Results with symmetric reserve.	188
12.1	MiRIS February 2019 dataset statistics.	203
12.2	Comparison indicators.	204
12.3	Case study parameters.	205
12.4	BESS parameters.	205
12.5	Scenario generation parameters.	205
12.6	Averaged computation times.	206
12.7	Planner D^* ratio indicators.	206
12.8	Planner D^* revenue indicators.	206

12.9	BESS parameters.	207
12.10	Planner D [*] ratio and revenue indicators BESS capacity sensitivity analysis.	208
14.1	Computation times (min) statistics.	248
14.2	BD vs CCG statistics. \bar{t} (s) is the averaged computation time per day with the standard deviation in bracket. 1% (%) is the % of instances that did not terminate with optimality. \bar{t} and 1% are computed over all days of the testing set and for all pair of constant (dynamic) risk-averse parameters $[u_t^{min}, \Gamma]$ ($[d_\Gamma, d_q]$). J^{max} (%) is the best normalized profit achieved using the NF quantiles over all risk-averse parameters.	252
15.1	Total net profit (k€) and cumulative ranking (%). The stochastic planner using the NF PV, wind power, and load scenarios achieved the highest net profit with 107 k€, ranked first 39.0 %, second 30.6 %, and third 30.4 % over 1 500 days of simulation. In comparison, the second-best model, the VAE, achieved a net profit of 97 k€, ranked first 31.8 %, second 36,5 %, and third 31.7 %.	263
15.2	Comparison between the deep generative models. The rating for each criterion is determined using the following rules - 1 star: third rank, 2 stars: second rank, and 3 stars: first rank. Train speed: training computation time; Sample speed: scenario generation computation time; Quality: forecast quality based on the eight complementary metrics considered; Value: forecast value based on the day-ahead energy retailer case study; Hp search: assess the difficulty to identify relevant hyper-parameters; Hp sensibility: assess the sensitivity of the model to a given set of hyper-parameters (the more stars, the more robust to hyper-parameter modifications); Implementation: assess the difficulty to implement the model (the more stars, the more implementation-friendly). Note: the justifications are provided in Appendix 15.5.	264

Foreword

“The greatest glory in living lies not in never falling, but in rising every time we fall.”

— **Nelson Mandela**

“Adults keep saying we owe it to the young people, to give them hope, but I don’t want your hope. I don’t want you to be hopeful. I want you to panic. I want you to feel the fear I feel every day. I want you to act. I want you to act as you would in a crisis. I want you to act as if the house is on fire, because it is.”

— **Greta Thunberg**

Climate Change

The Intergovernmental Panel on Climate Change (IPCC) has set the global net anthropogenic CO₂ emission trajectories and targets, depicted in Figure 1, to limit climate change. This summary for policymakers (SPM) presents the key findings of the special report published in 2018¹, based on the assessment of the available scientific, technical and socio-economic literature relevant to Global Warming of 1.5°C and for the comparison between Global Warming of 1.5°C and 2°C above pre-industrial levels. The SPM presents the emission scenarios consistent with 1.5°C Global Warming:

‘In model pathways with no or limited overshoot of 1.5°C, global net anthropogenic CO₂ emissions decline by about 45% from 2010 levels by 2030

¹Since the first written version of this thesis, the IPCC has released in August 2021 the AR6 SPM [36]. It presents key findings of the Working Group I (WGI) contribution to the IPCC’s Sixth Assessment Report (AR6) on the physical science basis of climate change. It is a must to read for every decision-maker, professor, researcher, or person that wants to understand the challenges at stake.

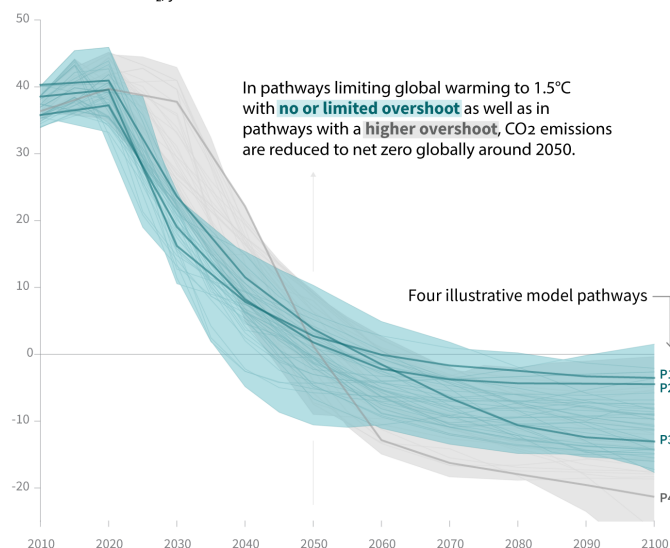
(40–60% interquartile range), reaching net-zero around 2050 (2045–2055 interquartile range).² [4][C.1]²

Global emissions pathway characteristics

General characteristics of the evolution of anthropogenic net emissions of CO₂, and total emissions of methane, black carbon, and nitrous oxide in model pathways that limit global warming to 1.5°C with no or limited overshoot. Net emissions are defined as anthropogenic emissions reduced by anthropogenic removals. Reductions in net emissions can be achieved through different portfolios of mitigation measures illustrated in Figure SPM.3b.

Global total net CO₂ emissions

Billion tonnes of CO₂/yr



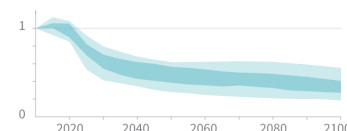
Timing of net zero CO₂
Line widths depict the 5-95th percentile and the 25-75th percentile of scenarios

Pathways limiting global warming to 1.5°C with no or limited overshoot
Pathways with higher overshoot
Pathways limiting global warming below 2°C (Not shown above)

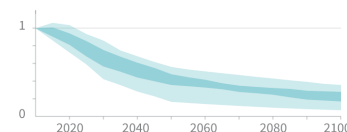
Non-CO₂ emissions relative to 2010

Emissions of non-CO₂ forcers are also reduced or limited in pathways limiting global warming to 1.5°C with no or limited overshoot, but they do not reach zero globally.

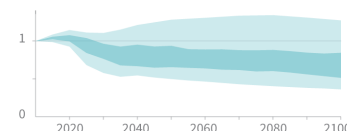
Methane emissions



Black carbon emissions



Nitrous oxide emissions



Source: IPCC Special Report on Global Warming of 1.5°C

Fig. 1 IPCC global net anthropogenic CO₂ emission pathways and targets. Credits: [4, Figure SPM.3a].

The IPCC proposes different mitigation strategies to achieve the net emissions reductions that would be required to follow a pathway that limits Global Warming to 1.5°C with no or limited overshoot. These strategies require a tremendous amount of effort from all countries.

²<https://www.ipcc.ch/sr15/chapter/spm/>

'Pathways limiting Global Warming to 1.5°C with no or limited overshoot would require rapid and far-reaching transitions in energy, land, urban and infrastructure (including transport and buildings), and industrial systems (high confidence). These systems transitions are unprecedented in terms of scale, but not necessarily in terms of speed, and imply deep emissions reductions in all sectors, a wide portfolio of mitigation options and a significant upscaling of investments in those options (medium confidence).'

[4][C.2]²

Trajectories to achieve IPCC targets

Several reports have been published to propose detailed pathways and strategies to achieve these targets. For instance, the International Energy Agency (IEA³) special report 'Net-zero by 2050: A roadmap for the global energy system' [2] provides a comprehensive study of how to transition to a net-zero energy system by 2050 that is consistent with limiting the global temperature rise to 1.5 °C without a temperature overshoot (with a 50 % probability). The Net-Zero Emissions by 2050 Scenario (NZE) shows what is needed for the global energy sector to achieve net-zero CO₂ emissions by 2050:

'In the NZE, global energy-related and industrial process CO₂ emissions fall by nearly 40% between 2020 and 2030 and to net-zero in 2050. Universal access to sustainable energy is achieved by 2030. There is a 75% reduction in methane emissions from fossil fuel use by 2030. These changes take place while the global economy more than doubles through to 2050 and the global population increases by 2 billion.' [2, Chapter 2: Summary]

In this report, the key pillars of decarbonization of the global energy system are (1) energy efficiency, (2) behavioral changes, (3) **electrification**, (4) **renewables**, (5) hydrogen and hydrogen-based fuels, (6) bioenergy, and (7) carbon capture, utilization and storage.

First, concerning electrification, the direct use of low-emissions electricity in place of fossil fuels is one of the most important drivers of emissions reductions in the NZE, accounting for around 20% of the total reduction achieved by 2050. The share of the electricity in the total final consumption increases from 20% in 2020 to 49% in 2050. It concerns the sectors of the industry, transport, and buildings. Second, concerning renewables:

³<https://www.iea.org/>

'At a global level, renewable energy technologies are the key to reducing emissions from electricity supply. Hydropower has been a leading low-emission source for many decades, but it is mainly the expansion of wind and solar that triples renewables generation by 2030 and increases it more than eightfold by 2050 in the NZE. The share of renewables in total electricity generation globally increases from 29% in 2020 to over 60% in 2030 and to nearly 90% in 2050. To achieve this, annual capacity additions of wind and solar between 2020 and 2050 are five-times higher than the average over the last three years. Dispatchable renewables are critical to maintain electricity security, together with other low-carbon generation, energy storage and robust electricity networks. In the NZE, the main dispatchable renewables globally in 2050 are hydropower (12% of generation), bioenergy (5%), concentrating solar power (2%) and geothermal (1%).' [2, Section 2.4.5]

The IEA report is not the ground truth but has the merit to propose guidelines and directions. There are many other reports and organizations that present strategies and scenarios to achieve the IPCC targets. For instance, The Shift Project (TSP) is a European think tank⁴ advocating the shift to a post-carbon economy. It proposes guidelines and information on energy transition in Europe. The key message is that **there are still pathways to reach net-zero by 2050**. They remain narrow and extremely challenging, requiring all stakeholders, governments, businesses, investors, and citizens to take action this year and every year after so that the goal does not slip out of reach.

Gap between rhetoric and reality

However, the **current gap between rhetoric and reality on emissions is still huge**:

'We are approaching a decisive moment for international efforts to tackle the climate crisis – a great challenge of our times. The number of countries that have pledged to reach net-zero emissions by mid-century or soon after continues to grow, but so do global greenhouse gas emissions. This gap between rhetoric and action needs to close if we are to have a fighting chance of reaching net-zero by 2050 and limiting the rise in global temperatures to 1.5 °C.' [2, Foreword]

This gap is humorously illustrated by Figure 2. For over a decade, the UNEP Emissions

⁴<https://theshiftproject.org/en/home/>



Fig. 2 Climate change fake news. Credits: Xavier Gorce.

Gap Report has provided a yearly review of the difference between where greenhouse emissions are predicted to be in 2030 and where they should be to avoid the worst impacts of climate change. Figure 3 depicts the global GHG emissions under different scenarios and the emissions gap in 2030. Indeed, the decade 2009-2019 has been particularly intense in terms of rhetoric about efforts to tackle the climate crisis such as the 2015 United Nations Climate Change Conference, COP 21. However, the carbon dioxide emissions at the world scale have been constantly increasing from 29.7 (GtCO₂) in 2009 to 34.2 in 2019 [100]⁵. In the meantime, the primary energy consumption has been increasing from 134 000 TWh to 162 000. In 2019, the primary energy consumption by fuel is composed of oil 53 600 (33.1%), coal 39 300 (24.2%), natural gas 43 900 (27.0%), nuclear energy 6 900 (4.3%), hydro-electricity 10 500 (6%), and renewables 8 100 (5%), as depicted in Figure 4. The share of renewables in the energy mix has increased and reached 5% in 2019 (a record). However, fossil fuels such as oil coal, and natural gas have increased in terms of total consumption during this period. Oil continues to hold the largest share of the energy mix, coal is the second-largest fuel, and the share of natural gas rose to a record high of 24.2%.

The Covid-19 pandemic delivered a major shock to the world economy, resulting in an unprecedented 5.8% decline in CO₂ emissions in 2020. The IPCC targets for 2050 require a decline of 5% each year from 2020 to 2050. However, the IEA data

⁵<https://www.bp.com/content/dam/bp/business-sites/en/global/corporate/pdfs/energy-economics/statistical-review/bp-stats-review-2020-full-report.pdf>

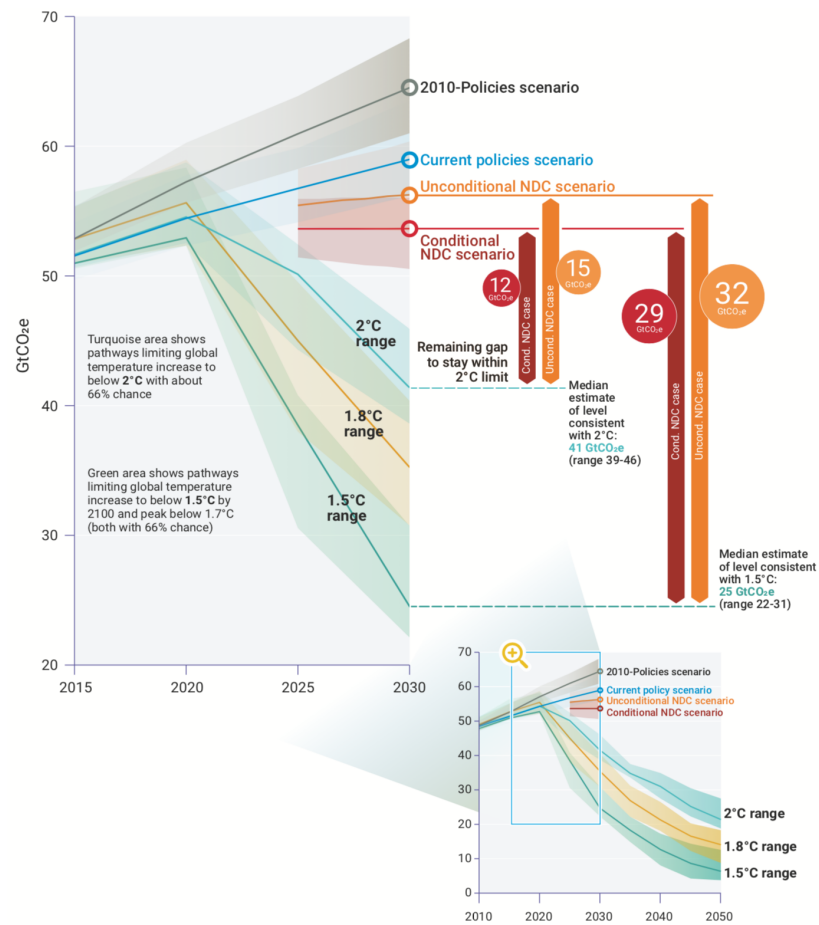


Fig. 3 Global GHG emissions under different scenarios and the emissions gap in 2030 (median and 10-th to 90-th percentile range; based on the pre-COVID-19 current policies scenario). Credits: [109, Figure ES.5].

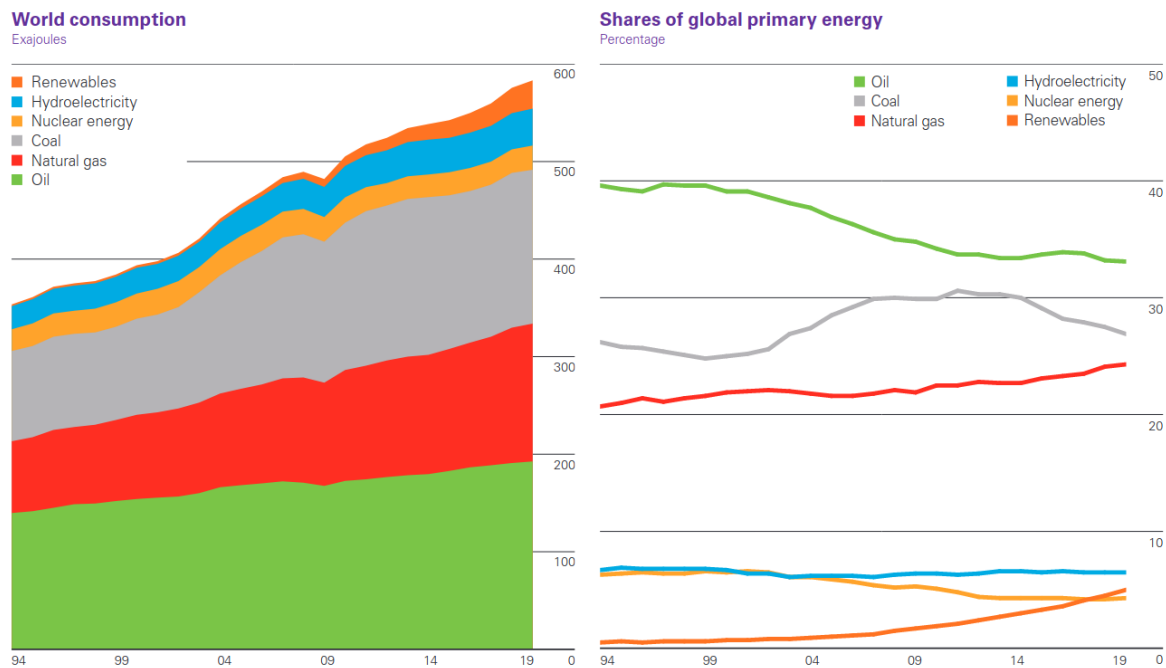


Fig. 4 World consumption of primary energy (left) and shares of global primary energy (left) from 1994 to 2020. Credits: BP's Statistical Review of World Energy 2020 [100].

shows that global energy-related CO₂ emissions started to climb again in December 2020. But, there is still hope, and every action to decrease the CO₂ emissions to gain a reduction of 0.1°C is a victory!

Chapter 1

General introduction

Overview

First, this chapter introduces the context and motivations of this thesis. Second, it provides the content and contributions. This manuscript is divided into two main parts: (1) forecasting; (2) planning and control. Finally, it lists the publications.

“*Life has no meaning a priori. . . It is up to you to give it a meaning, and value is nothing but the meaning that you choose.*”

— Jean-Paul Sartre

1.1 Context and motivations

Assumption 1. *Let suppose a utopian world where the current gap between rhetoric and reality on emissions is drastically decreasing to limit climate change and achieve the ambitious targets prescribed by the Intergovernmental Panel on Climate Change.*

Therefore, the transition towards a carbon-free society goes through an inevitable increase of the share of renewable generation in the energy mix and a drastic decrease of the share in terms of the total consumption of fossil fuels.

Assumption 2. *This thesis does not debate or study whether and where renewables should be implemented.*

Renewables are not carbon-free, and we assume, the preliminary studies are conducted to evaluate the relevance of a particular type of renewable energy in the energy transition pathways. We take as inputs the scenarios proposed by the IPCC, IEA, etc.

Assumption 3. *This thesis studies the integration of renewables in power systems by investigating forecasting and decision-making tools.*

Indeed, in contrast to conventional power plants, renewable energy is subject to uncertainty. Generation technologies based on renewable sources, with the notable exception of hydro and biomass, are *non-dispatchable*, *i.e.*, their output cannot or can only partly be controlled at the will of the producer, and their production is *stochastic* [105] and therefore, hard to forecast. A high share of renewables is a great challenge for power systems that have been designed and sized for dispatchable units. Therefore, it is necessary to redefine the flexible power system features [78]. In this context, *probabilistic* forecasts [58], which aim at modeling the distribution of all possible future realizations, have become an important tool to equip decision-makers, hopefully leading to better decisions in energy applications [105, 74, 76]. Therefore, the two main research questions are:

1. How to produce reliable probabilistic forecasts of renewable generation, consumption, and electricity prices?
2. How to make decisions with uncertainty using probabilistic forecasts?

Assumption 4. *This thesis considers the energy management of "small" systems such as microgrids at a residential scale on a day-ahead basis.*

Indeed, an effective way to integrate renewable energy sources and exploit the available flexibility in a decentralized manner is through the development of microgrids. They are small electrical networks composed of decentralized energy resources and loads that are controlled locally. They can be operated either interconnected or in islanded mode. Figure 1.1 depicts a microgrid composed of PV generation, diesel generator (Genset), storage systems, load, and an energy management system (EMS). Energy storage is a key component for the stable and safe operation of a microgrid. Storage devices can compensate for the variability of the renewable energy sources and the load in order to balance the system. A comparative and critical analysis on decision making strategies and their solution methods for microgrid energy management systems is proposed by Zia et al. [166].

Assumption 5. *This thesis considers the energy management of grid-connected microgrids on a day-ahead basis.*

Therefore, we are interested to produce reliable day-ahead probabilistic forecasts of renewable generation, consumption, and electricity prices¹ for a microgrid composed of

¹In this thesis, only the imbalance prices are considered in the Belgian case study.

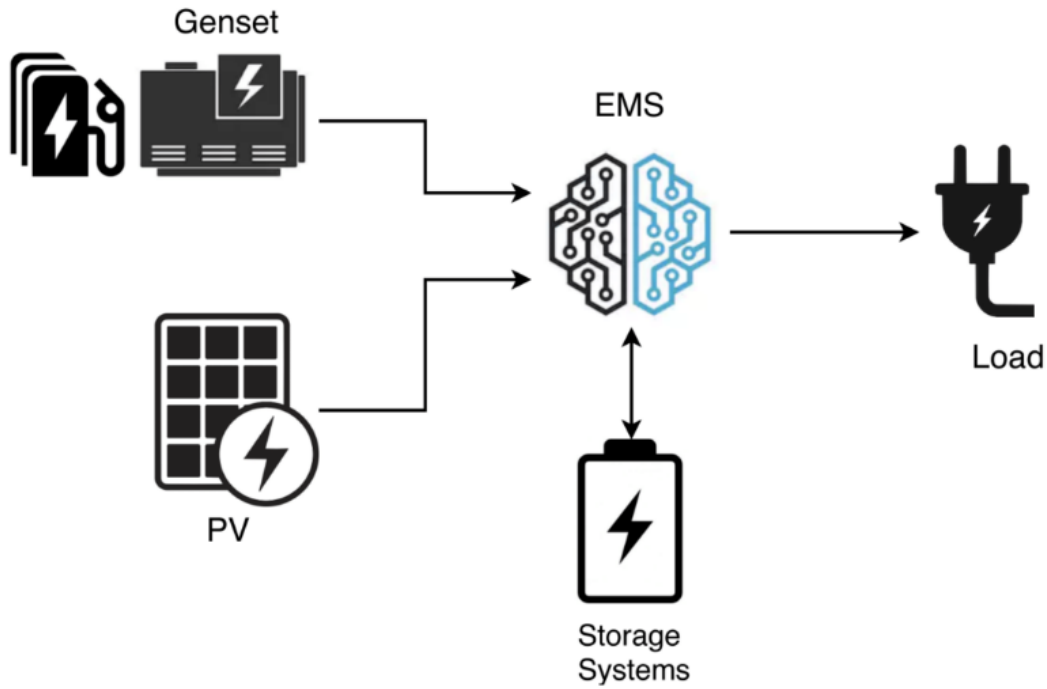


Fig. 1.1 Microgrid scheme. Credits: ELEN0445 Microgrids course <https://github.com/bcornelusse/ELEN0445-microgrids>, Liège University.

PV or wind generation, and electrical consumption. However, in some specific cases, this perimeter is not strictly respected. For instance, the sizing of a grid-connected PV plant with a battery energy storage system is studied in the specific framework of capacity firming. Or the day-ahead planning of an energy retailer.

1.2 Content and contributions

The thesis is divided into two main parts to propose directions to address both research questions: Part I forecasting; Part II planning and control. The thesis skeleton is depicted in Figure 1.2. Part I provides the forecasting tools and metrics required to produce and evaluate reliable point and probabilistic forecasts to be used as input of decision-making models in the second part of this thesis. Part II proposes approaches and methodologies, based on optimization for decision-making under uncertainty using probabilistic forecasts on several case studies.

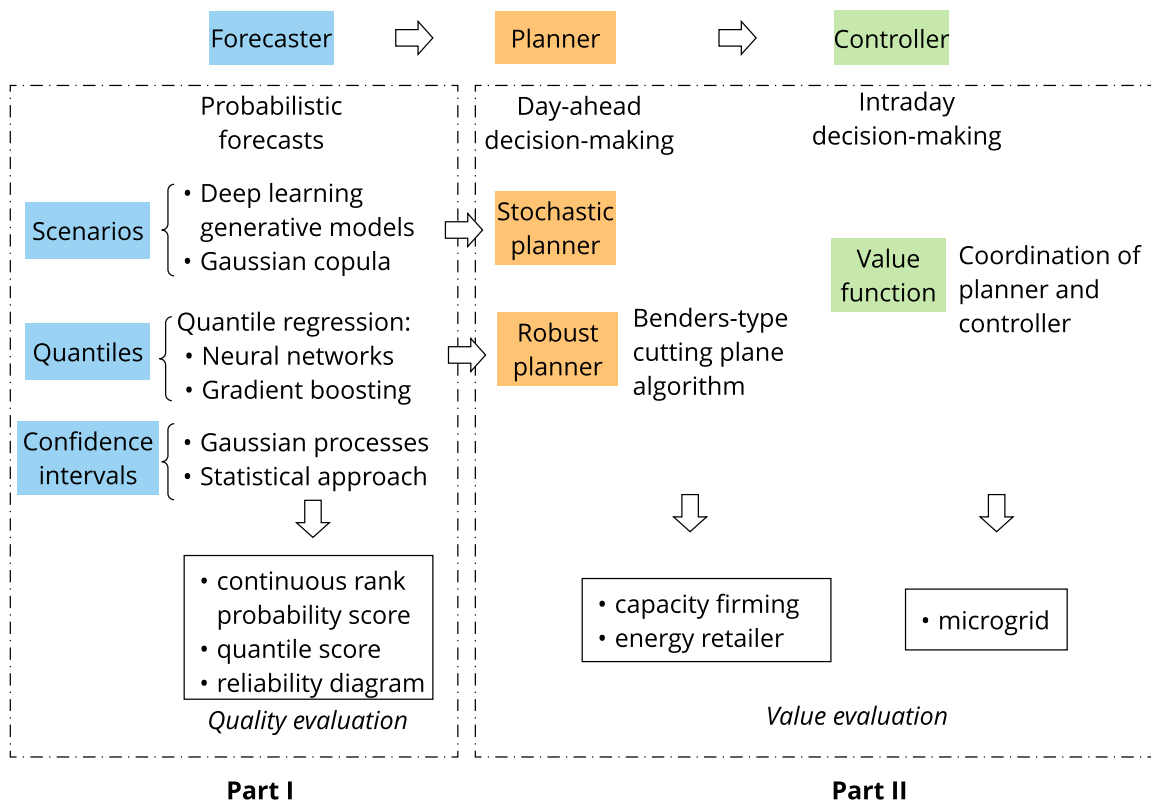


Fig. 1.2 Thesis skeleton.

Part I content and contributions

The main contributions and structure of the forecasting part are:

- Chapter 2 introduces different types of forecasts to characterize the behavior of stochastic variables, such as renewable generation, electrical consumption, and electricity prices.
- Chapter 3 provides the tools to assess the different types of forecasts. For predictions in any form, one must differentiate between their quality and their value. This Chapter focus on forecast quality, and the forecast value is considered in Part II.
- Chapter 4 differs from the next Chapters and proposes a classification in two dimensions of load forecasting studies to decide which forecasting tools to use in which case. For the sake of clarity, this study is not detailed in this thesis, and only a summary of the main ideas is proposed.

References: This chapter is an adapted version of Jonathan Dumas and Bertrand Cornélusse. Classification of load forecasting studies by forecasting problem to select load forecasting techniques and methodologies. *arXiv preprint arXiv:1901.05052*, 2018. URL <https://arxiv.org/abs/1901.05052>.

- Chapter 5 presents the PV and electrical consumption point forecasts considered as input of day-ahead planning using common deep-learning models such as recurrent neural networks. The point forecasts are assessed using quality metrics.

References: This chapter is an extract of Jonathan Dumas, Selmane Dakir, Clément Liu, and Bertrand Cornélusse. Coordination of operational planning and real-time optimization in microgrids. *Electric Power Systems Research*, 190: 106634, 2021. URL <https://arxiv.org/abs/2106.02374>.

- Chapter 6 investigates PV quantiles forecasts using deep-learning models such as the encoder-decoder architecture. The PV intraday point and quantiles forecasts are used as inputs of a robust optimization planner in 14.

References: This chapter is an adapted version of Jonathan Dumas, Colin Cointe, Xavier Fettweis, and Bertrand Cornélusse. Deep learning-based multi-output quantile forecasting of pv generation. In *2021 IEEE Madrid PowerTech*, pages 1–6, 2021. doi: 10.1109/PowerTech46648.2021.9494976. URL <https://arxiv.org/abs/2106.01271>.

- Chapter 7 proposes probabilistic forecasting of imbalance prices with a particular focus on the Belgian case. It uses a confidence interval-based approach in two steps. It consists of computing the net regulation volume state transition probabilities used to infer the imbalance prices.

References: This chapter is an adapted version of Jonathan Dumas, Ioannis Boukas, Miguel Manuel de Villena, Sébastien Mathieu, and Bertrand Cornélusse. Probabilistic forecasting of imbalance prices in the belgian context. In *2019 16th International Conference on the European Energy Market (EEM)*, pages 1–7. IEEE, 2019. URL <https://arxiv.org/abs/2106.07361>.

- Chapter 8 studies the generation of scenarios for renewable production and electrical consumption by implementing deep generative models. It provides a fair comparison both in terms of quality and value of a recent deep learning technique, the normalizing flows, with the state-of-the-art deep learning generative models, Variational AutoEncoders and Generative Adversarial Networks. The forecast value is evaluated in Chapter 15.

References: This chapter is an adapted version of Jonathan Dumas, Antoine Wehenkel, Damien Lanaspeze, Bertrand Cornélusse, and Antonio Sutera. Deep generative modeling for probabilistic forecasting in power systems. Manuscript submitted for publication to *Applied Energy*, 2021. URL <https://arxiv.org/abs/2106.09370>.

- Chapter 9 draws the general conclusions and perspectives of Part I.

Part II content and contributions

The main contributions and structure of the planning and control part are:

- Chapter 10 introduces different types of decision-making under uncertainty using optimization strategies.
- Chapter 11 presents a value function-based approach as a way to propagate information from operational planning to real-time optimization.

References: This chapter is an adapted version of Jonathan Dumas, Selmane Dakir, Clément Liu, and Bertrand Cornélusse. Coordination of operational planning and real-time optimization in microgrids. *Electric Power Systems Research*, 190:106634, 2021. URL <https://arxiv.org/abs/2106.02374>.

- Chapter 12 addresses the energy management, using a stochastic approach, of a grid-connected renewable generation plant coupled with a battery energy storage device in the capacity firming market, designed to promote renewable power generation facilities in small non-interconnected grids.

References: This chapter is an adapted version of Jonathan Dumas, Bertrand Cornélusse, Antonello Giannitrapani, Simone Paoletti, and Antonio Vicino. Stochastic and deterministic formulations for capacity firming nominations. In *2020 International Conference on Probabilistic Methods Applied to Power Systems (PMAPS)*, pages 1–7. IEEE, 2020. URL <https://arxiv.org/abs/2106.02425>.

- Chapter 13 extends Chapter 12 and propose a methodology size the system.

References: This chapter is an adapted version of Jonathan Dumas, Bertrand Cornélusse, Xavier Fettweis, Antonello Giannitrapani, Simone Paoletti, and Antonio Vicino. Probabilistic forecasting for sizing in the capacity firming framework. In *2021 IEEE Madrid PowerTech*, pages 1–6, 2021. doi: 10.1109/PowerTech46648.2021.9494947. URL <https://arxiv.org/abs/2106.02323>.

- Chapter 14 extends Chapter 12 and investigates the day-ahead planning using robust optimization.

References: This chapter is an adapted version of Jonathan Dumas, Colin Cointe, Antoine Wehenkel, Antonio Sutera, Xavier Fettweis, and Bertrand Cornélusse. A probabilistic forecast-driven strategy for a risk-aware participation in the capacity firming market. Manuscript submitted for publication to IEEE Transactions on Sustainable Energy, 2021. URL <https://arxiv.org/abs/2105.13801>.

- Chapter 15, is the extension of Chapter 8, and presents the forecast value evaluation of the deep learning generative models by considering the day-ahead market scheduling of electricity aggregators, such as energy retailers or generation companies.

References: This chapter is an adapted version of Jonathan Dumas, Antoine Wehenkel, Damien Lanaspeze, Bertrand Cornélusse, and Antonio Sutera. Deep generative modeling for probabilistic forecasting in power systems. Manuscript submitted for publication to Applied Energy, 2021. URL <https://arxiv.org/abs/2106.09370>.

- Chapter 16 draws the general conclusions and perspectives of Part II.

Publications

The thesis is mainly based on the following studies, all available on open-access with arXiv, listed in chronological order:

- Jonathan Dumas and Bertrand Cornélusse. Classification of load forecasting studies by forecasting problem to select load forecasting techniques and methodologies. *arXiv preprint arXiv:1901.05052*, 2018. URL <https://arxiv.org/abs/1901.05052>
- Jonathan Dumas, Ioannis Boukas, Miguel Manuel de Villena, Sébastien Mathieu, and Bertrand Cornélusse. Probabilistic forecasting of imbalance prices in the belgian context. In *2019 16th International Conference on the European Energy Market (EEM)*, pages 1–7. IEEE, 2019. URL <https://arxiv.org/abs/2106.07361>
- Jonathan Dumas, Selmane Dakir, Clément Liu, and Bertrand Cornélusse. Coordination of operational planning and real-time optimization in microgrids. *Electric Power Systems Research*, 190:106634, 2021. URL <https://arxiv.org/abs/2106.02374>
- Jonathan Dumas, Bertrand Cornélusse, Antonello Giannitrapani, Simone Paoletti, and Antonio Vicino. Stochastic and deterministic formulations for capacity firming nominations. In *2020 International Conference on Probabilistic Methods Applied to Power Systems (PMAPS)*, pages 1–7. IEEE, 2020. URL <https://arxiv.org/abs/2106.02425>
- Jonathan Dumas, Colin Cointe, Xavier Fettweis, and Bertrand Cornélusse. Deep learning-based multi-output quantile forecasting of pv generation. In *2021 IEEE Madrid PowerTech*, pages 1–6, 2021. doi: 10.1109/PowerTech46648.2021.9494976. URL <https://arxiv.org/abs/2106.01271>
- Jonathan Dumas, Bertrand Cornélusse, Xavier Fettweis, Antonello Giannitrapani, Simone Paoletti, and Antonio Vicino. Probabilistic forecasting for sizing in the capacity firming framework. In *2021 IEEE Madrid PowerTech*, pages 1–6, 2021. doi: 10.1109/PowerTech46648.2021.9494947. URL <https://arxiv.org/abs/2106.02323>
- Jonathan Dumas, Colin Cointe, Antoine Wehenkel, Antonio Sutera, Xavier Fettweis, and Bertrand Cornélusse. A probabilistic forecast-driven strategy for a risk-aware participation in the capacity firming market. Manuscript submitted for publication to *IEEE Transactions on Sustainable Energy*, 2021. URL <https://arxiv.org/abs/2105.13801>

- Jonathan Dumas, Antoine Wehenkel, Damien Lanaspeze, Bertrand Cornélusse, and Antonio Sutera. Deep generative modeling for probabilistic forecasting in power systems. Manuscript submitted for publication to Applied Energy, 2021. URL <https://arxiv.org/abs/2106.09370>.

Part I

Forecasting

Overview

Part I presents the forecasting techniques and metrics required to produce and evaluate reliable point and probabilistic forecasts to be used as input of decision-making models in Part II. Then, it investigates several cases studied the various type of forecasts: point forecasts, quantile forecasts, prediction intervals, confidence intervals, and scenarios.

“ I never think of the future — it comes soon enough.”

— **Albert Einstein**

“ We have two classes of forecasters: Those who don't know — and those who don't know they don't know.”

— **John Kenneth Galbraith**

Figure 1.3 illustrates the organization of Part I, which can be read in two passes depending on the forecasting knowledge. First, a forecasting practitioner may be interested in identifying the forecasting type of interest and selecting the corresponding Chapter. For instance, Chapter 8 studies the scenarios of renewable generation and electrical consumption. Second, a forecasting beginner should be interested in reading Chapters 2 and 3 to acquire the forecasting basics. Then, the following Chapters are the application on case studies for each type of forecast.

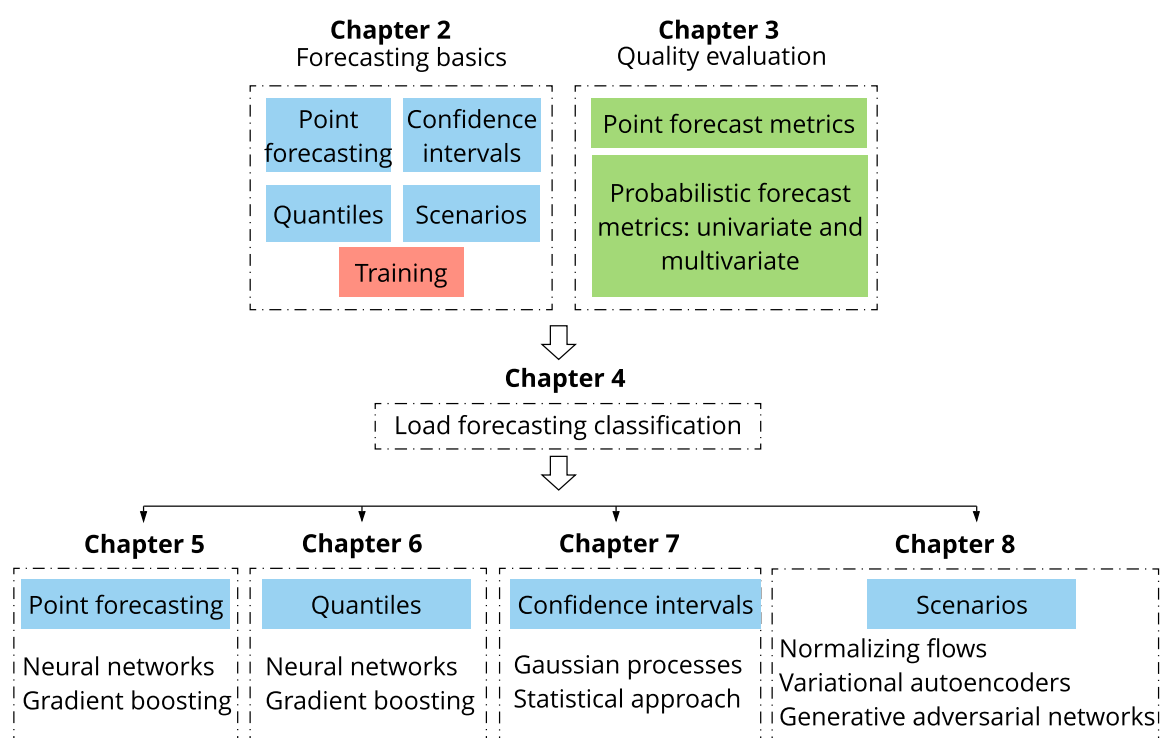


Fig. 1.3 Part I skeleton.

Part I general nomenclature

Acronyms

Name	Description
PDF	Probability Density Function.
CDF	Cumulative Distribution Function.
MAE	Mean absolute error.
NMAE	Normalized mean absolute error.
RMSE	Root mean square error.
NRMSE	Normalized root mean square error.
CRPS	Continuous rank probability score.
IS	Interval score.
DM	Diebold-Mariano.
RNN	Recurrent Neural Network.
LSTM	Long Short-Term Memory.
BLSTM	Bidirectional LSTM.
GBR	Gradient boosting regression.
MLP	Multi-layer perceptron.
ED	Encoder-decoder.
NFs	Normalizing Flows.
GANs	Generative adversarial Networks.
VAEs	Variational AutoEncoders.

Variables and parameters

Name	Range	Description
X		Continuous random variable.
\mathbf{X}		Continuous multivariate random variable.
x	$\in \mathbb{R}$	Realization of the random variable X .

\mathbf{x}	$\in \mathbb{R}^T$	Realization of the multivariate random variable \mathbf{X} .
\hat{x}	$\in \mathbb{R}$	Point forecast of x .
$\hat{\mathbf{x}}$	$\in \mathbb{R}^T$	Multi-output point forecast of \mathbf{x} .
$\hat{x}^{(q)}$	$\in \mathbb{R}$	Quantile forecast of x .
$\hat{\mathbf{x}}^{(q)}$	$\in \mathbb{R}^T$	Multi-output quantile forecast of \mathbf{x} .
$\hat{I}^{(\alpha)}$	$\in \mathbb{R}^2$	Prediction interval with a coverage rate of $(1 - \alpha)$.
$\hat{\mathbf{I}}^{(\alpha)}$	$\in \mathbb{R}^{2T}$	Multi-output prediction interval with a coverage rate of $(1 - \alpha)$.
\hat{x}^i	$\in \mathbb{R}$	Scenario i of x .
$\hat{\mathbf{x}}^i$	$\in \mathbb{R}^T$	Scenario i of \mathbf{x} .
ϵ	$\in \mathbb{R}$	Point forecast error.
ξ	$\in \{0, 1\}$	Indicator variable.
$\tilde{\xi}$	$\in \mathbb{R}^+$	Empirical level.

Symbols

Name	Description
g_θ	Forecasting model with parameters θ .
\mathbb{E}	Expectation.
f	Probability Density Function.
F	Cumulative Distribution Function.
\hat{f}	Density forecast of the pdf.
\hat{F}	Density forecast of the cdf.
ρ	Pinball loss function.

Sets and indices

Name	Description
t	Time index.
k	Forecasting lead time index.
T	Forecasting horizon.
q	Quantile index.
ω	Scenario index.
$\#\Omega$	Number of scenarios.
\mathcal{T}	Set of time periods, $\mathcal{T} = \{1, 2, \dots, T\}$.
Ω	Set of scenarios, $\Omega = \{1, 2, \dots, \#\Omega\}$.
\mathcal{D}	Information set.

Chapter 2

Forecasting background

Overview

This chapter introduces the main concepts in forecasting, as a background for the work developed in the following chapters of this manuscript. It presents the various types of forecasts: point forecasts, quantile forecasts, prediction intervals, confidence intervals, and scenarios. In addition, it provides some knowledge on how to train a forecasting model.

The interested reader is referred to more general textbooks for further information [105, 72, 159, 63]. The lectures of the course "Renewables in Electricity Markets"^a given by Pierre Pinson, professor at the Technical University of Denmark. It covers some basics of electricity markets, impact of renewables on markets, participation of renewable energy producers in electricity markets, as well as renewable energy analytics (mainly, forecasting). The lectures of the course "INFO8010 - Deep Learning"^b, ULiège, Spring 2021, given by Gilles Louppe, associate professor at Liège University. It covers the foundations and the landscape of deep learning.

^a<http://pierrepinson.com/index.php/teaching/>

^b<https://github.com/glouppe/info8010-deep-learning>

“*If life were predictable it would cease to be life, and be without flavor.*”

— Eleanor Roosevelt

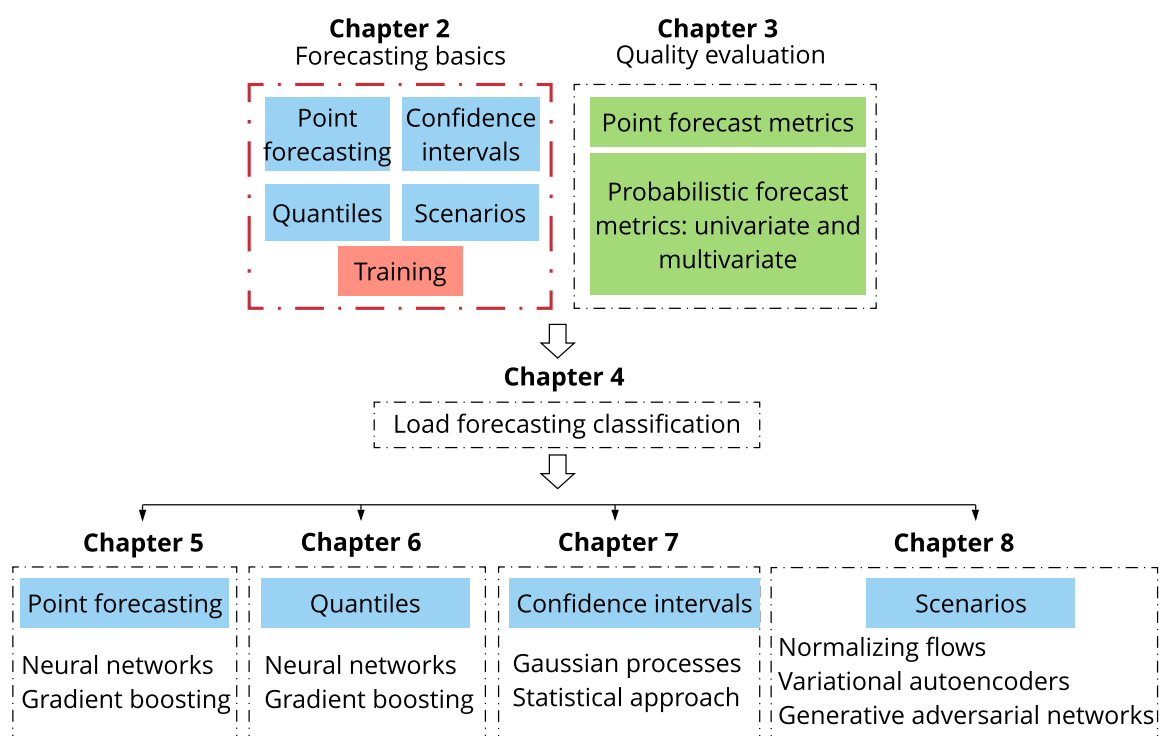


Fig. 2.1 Chapter 2 position in Part I.

Following Morales et al. [105] power generation from renewable energy sources, such as wind and solar, will be referred to as *stochastic power generation* in this thesis. The same assumption is adopted for electrical consumption and electricity prices. Predictions of renewable energy generation, consumption, and electricity prices can be obtained and presented in a number of different manners. The choice for the type of forecasts and their presentation somewhat depends upon the process characteristics of interest to the decision-maker, and also upon the type of operational problem. The various types of forecasts and their presentation are introduced in the following, starting from the most common *point forecasts* and building up towards the more advanced products that are *probabilistic forecasts* and scenarios.

This Chapter is organized as follows. Section 2.1 introduces the point forecasts. Section 2.2 presents the various types of probabilistic forecasts. Section 2.3 proposes an abstract formulation of a model-based forecaster. Section 2.4 provides some knowledge on how to train a forecasting model. Finally, conclusions are drawn in Section 2.5.

2.1 Point forecast

Let $x_t \in \mathbb{R}$ be the variable of interest, *e.g.*, renewable energy generation, consumption, or electricity prices, measured at time t , which corresponds to a realization of the random variable X_t .

Definition 2.1.1 (A model-based forecast). [105, Chapter 2] A (model-based) forecast $\hat{x}_{t+k|t} \in \mathbb{R}$ is an estimate of some of the characteristics of the stochastic process X_{t+k} issued at time t for time $t+k$ given a model g_θ , with parameters θ and the information set \mathcal{D} gathering all data and knowledge about the processes of interest up to time t , such as weather forecasts, historical observations, calendars variables, *etc.*

In the above definition, k is the *lead time*, though sometimes also referred to as *forecast horizon*. The 'hat' symbol expresses that $\hat{x}_{t+k|t}$ is an estimate only. It models the presence of uncertainty both in our knowledge of the process and inherent to the process itself. The forecast for time $t+k$ is conditional on our knowledge on the stochastic process up to time t , including the data used as input to the forecasting process, as well as the models identified and parameters estimated. Therefore, a forecaster somewhat makes the crucial assumption that the future will be like the past.

Forecasts are issued as series of consecutive values $\hat{x}_{t+k|t}$, $k = k_1, \dots, k_T$, that is, for regularly spaced lead times up to the *forecast length* T . That regular spacing Δt is called the *temporal resolution* of the forecasts. For instance, when one talks of

day-ahead forecasts with an hourly resolution, this means that forecasts consist of forecast series gathering predicted power values for each of the following 24 h of the next day.

Definition 2.1.2 (Point forecast). [105, Chapter 2] A *point forecast* $\hat{x}_{t+k|t} \in \mathbb{R}$ is a single-valued issued at time t for $t+k$, and corresponds to the conditional expectation of X_{t+k}

$$\hat{x}_{t+k|t} := \mathbb{E}[X_{t+k|t} | g_\theta, \mathcal{D}], \quad (2.1)$$

given g_θ , and the information set \mathcal{D} .

A forecast in the form of a conditional expectation translates to acknowledging the presence of uncertainty, even though it is not quantified and communicated.

Definition 2.1.3 (Multi-output point forecast). A *multi-output point forecast* computed at t for $t+k_1$ to $t+k_T$ is the vector

$$\hat{\mathbf{x}}_t := [\hat{x}_{t+k_1|t}, \dots, \hat{x}_{t+k_T|t}]^\top \in \mathbb{R}^T. \quad (2.2)$$

It can be computed directly as a vector or as an aggregate of single output forecasts depending on the problem formulation.

2.2 Probabilistic forecasts

In contrast to point predictions, probabilistic forecasts aim at providing decision-makers with the full information about potential future outcomes. Let f_t and F_t be the *probability density function* (PDF) and related *cumulative distribution function* (CDF) of X_t , respectively.

Definition 2.2.1 (Probabilistic forecast). [105, Chapter 2] A probabilistic forecast issued at time t for time $t+k$ consists of a prediction of the PDF (or equivalently, the CDF) of X_{t+k} , or of some summary features.

Various types of probabilistic forecasts have been developed: *quantile*, *prediction intervals*, *scenarios*, and *density* forecasts.

2.2.1 Quantiles

Definition 2.2.2 (Quantile forecast). [105, Chapter 2] A *quantile forecast* $\hat{x}_{t+k|t}^{(q)} \in \mathbb{R}$ with nominal level q is an estimate, issued at time t for time $t+k$ of the quantile $x_{t+k|t}^{(q)}$

for the random variable $X_{t+k|t}$

$$P[X_{t+k|t} \leq \hat{x}_{t+k|t}^{(q)} | g_\theta, \mathcal{D}] = q, \quad (2.3)$$

given g_θ , and the information set \mathcal{D} . Or equivalently $\hat{x}_{t+k|t}^{(q)} = \hat{F}_{t+k|t}^{-1}(q)$, with \hat{F} the estimated cumulative distribution function of the continuous random variable X .

By issuing a quantile forecast $\hat{x}_{t+k|t}^{(q)}$, the forecaster tells at time t that there is a probability q that x_{t+k} will be less than $\hat{x}_{t+k|t}^{(q)}$ at time $t+k$. Quantile forecasts are of interest for several operational problems, such as the design of optimal offering strategies by wind power producers, where optimal bids are quantile forecasts whose nominal level is a simple function of day-ahead and balancing market prices [20]. Furthermore, quantile forecasts also define prediction intervals that can be used for robust optimization.

Definition 2.2.3 (Multi-output quantile forecast). A *multi-output quantile forecast* of length T with nominal level q computed at t for $t+k_1$ to $t+k_T$ is the vector

$$\hat{\mathbf{x}}_t^{(q)} := [\hat{x}_{t+k_1|t}^{(q)}, \dots, \hat{x}_{t+k_T|t}^{(q)}]^\top \in \mathbb{R}^T. \quad (2.4)$$

2.2.2 Prediction intervals

Quantile forecasts give probabilistic information in the form of a threshold level associated with a probability. Even though they may be of direct use for several operational problems, they cannot provide forecast users with a feeling about the level of forecast uncertainty for the coming period. For that purpose, prediction intervals define the range of values within which the observation is expected to be with a certain probability, *i.e.*, its nominal coverage rate [123].

Definition 2.2.4 (Prediction interval). [105, Chapter 2] A *prediction interval* $\hat{I}_{t+k|t}^{(\alpha)} \in \mathbb{R}^2$ issued at t for $t+k$, defines a range of potential values for X_{t+k} , for a certain level of probability $(1-\alpha)$, $\alpha \in [0, 1]$. Its nominal coverage rate is

$$P[X_{t+k} \in \hat{I}_{t+k|t}^{(\alpha)} | g_\theta, \mathcal{D}] = 1 - \alpha. \quad (2.5)$$

Definition 2.2.5 (Central prediction interval). [105, Chapter 2] A *central prediction interval* consists of centering the prediction interval on the median where there is the same probability of risk below and above the median. A central prediction interval

with a coverage rate of $(1 - \alpha)$ is estimated by using the quantiles $q = (\alpha/2)$ and $q = (1 - \alpha/2)$. Its nominal coverage rate is

$$\hat{I}_{t+k|t}^{(\alpha)} = [\hat{x}_{t+k|t}^{(q=\alpha/2)}, \hat{x}_{t+k|t}^{(q=1-\alpha/2)}]. \quad (2.6)$$

For instance, central prediction interval with a nominal coverage rate of 90%, *i.e.*, $(1 - \alpha) = 0.9$, are defined by quantile forecasts with nominal levels of 5 and 95%.

Definition 2.2.6 (Multi-output central prediction interval). A *multi-output central prediction interval* with a coverage rate of $(1 - \alpha)$ computed at t for $t + k_1$ to $t + k_T$ is the vector

$$\hat{\mathbf{I}}_{t+k|t}^{(\alpha)} = [\hat{I}_{t+k_1|t}^{(\alpha)}, \dots, \hat{I}_{t+k_T|t}^{(\alpha)}]^\top \in \mathbb{R}^{2T}. \quad (2.7)$$

2.2.3 Confidence intervals

Another type of probabilistic forecast consists of forecasting the variable of interest with a confidence interval. It is a type of estimate computed from the statistics of the observed data that provides a range of values for an unknown parameter such as the mean of the variable of interest. The interval has an associated confidence level that gives the probability with which an estimated interval will contain the true value of the parameter. For an estimation using a given dataset, using a higher confidence level generates a wider, *i.e.*, less accurate, confidence interval.

Definition 2.2.7 (Confidence interval). Let α be the statistical parameter to estimate, such as the mean of the random variable X , and $C \in [0, 1]$. A *confidence interval* for the parameter α , with confidence level or confidence coefficient C , is an interval with random endpoints $(u(X), v(X))$, determined by the pair of random variables $u(X)$ and $v(X)$ such as

$$P[u(X) < \alpha < v(X)] = C \quad \forall \alpha. \quad (2.8)$$

For instance, if we assume the samples are drawn from a *Normal* distribution, confidence intervals can be calculated using the z -tables

$$[\bar{x} - z \frac{\sigma}{\sqrt{N}}, \bar{x} + z \frac{\sigma}{\sqrt{N}}], \quad (2.9)$$

with \bar{x} the estimated mean from a dataset composed of N samples, and σ the standard deviation assumed to be known. The confidence level C corresponds to the percentage of the area of the Normal density curve. For instance, a 95% confidence interval covers 95% of the Normal curve. The value z representing the point on the standard Normal

density curve such that the probability of observing a value greater than z is equal to p is known as the upper p critical value of the standard Normal distribution. For a confidence interval with level C , the value p is equal to $(1 - C)/2$. A 95% confidence interval for the standard Normal distribution is the interval $[-1.96, 1.96]$, since 95% of the area under the curve falls within this interval. Note, the interval (2.9) is only exact when the population distribution is Normal. For large samples from other population distributions, the interval is approximately correct by the *Central Limit Theorem*.

2.2.4 Scenarios

Let us introduce the *multivariate* random variable

$$\mathbf{X}_t := \{X_{t+k}\}, \quad k = k_1, \dots, k_T, \quad (2.10)$$

which gathers the random variables characterizing the stochastic power generation process for the T following lead times, hence covering their marginal densities as well as their interdependence structure.

Definition 2.2.8 (Scenarios). *Scenarios* issued at time t and for a set of T successive lead times, *i.e.*, with $k = k_1, \dots, k_T$ consist of a set of M time trajectories

$$\hat{\mathbf{x}}_t^i := [\hat{x}_{t+k_1|t}^i, \dots, \hat{x}_{t+k_T|t}^i]^\top \in \mathbb{R}^T \quad i = 1, \dots, M. \quad (2.11)$$

The resulting time trajectories comprise scenarios like those commonly used as input to operational problems in a stochastic programming framework.

2.2.5 Density forecasts

All the various types of predictions presented in the above, *i.e.*, point, quantile, and interval forecasts, are only partly describing the whole information about future of X at every lead time. This whole information would be given by density forecasts for each point of time in the future.

Definition 2.2.9 (Density forecast). [105, Chapter 2] A *density forecasts* $\hat{f}_{t+k|t}$ ($\hat{F}_{t+k|t}$) issued at time t for $t+k$, is a complete description of the pdf (or cdf) of X_{t+k} conditional on a given model g_θ , and the information set \mathcal{D} .

2.3 Model-based formulation

Let assume the information set $\mathcal{D} := \{\mathbf{x}_t, \mathbf{c}_t\}_{t=1}^N$ is composed of N independent and identically distributed samples from the joint distribution $p(\mathbf{x}, \mathbf{c})$ of two continuous variables X and C . X is the variable of interest, *e.g.*, renewable energy generation, consumption, or electricity prices, and C is the context, *e.g.*, the weather forecasts, calendar variables, or exogenous variables. Generically, any prediction of a random variable X issued at time t , being point or probabilistic forecast is a linear or nonlinear function of \mathcal{D} . The goal of Part I is to generate multi-output context-based forecasts $\hat{\mathbf{x}}$ that are distributed under $p(\mathbf{x}|\mathbf{c})$.

Definition 2.3.1 (Multi-output model-based forecasts). A *multi-output model-based forecasts* of length T computed by g_θ at t for $t + k_1$ to $t + k_T$ is the vector

$$\hat{\mathbf{x}}_t \sim g_\theta(\mathbf{x}_{<t}, \mathbf{c}_t) \in \mathbb{R}^T, \quad (2.12)$$

given the context \mathbf{c}_t , and observations $\mathbf{x}_{<t} = [x_1, \dots, x_{t-1}]^\top$ up to time t .

Its purpose is to generate synthetic but realistic data $\hat{\mathbf{x}}_t$ whose distribution is as close as possible to the unknown data distribution $p(\mathbf{x}|\mathbf{c})$. When considering point forecasts, quantile forecasts, and scenarios, $\hat{\mathbf{x}}_t$ is defined by (2.2), (2.4), and (2.11), respectively. This abstract formulation is used in the Chapters (5), (6), and (8) where the forecasting models and the related inputs including the context are specified.

2.4 Model training

This Section provides the basics of supervised learning that is used in Part I to train the forecasting models g_θ . It relies mainly on Lecture 1 of INFO8010 - Deep Learning¹, ULiège, Spring 2021, from Gilles Louppe [101], associate professor at Liège University. We refer the interested reader to Duchesne [40, Chapter 3] and Sutera [140, Chapter 2] that introduce the different types of machine learning problems, then focuses on supervised learning, describes its characteristics, the procedure to apply supervised learning, how to assess the accuracy of a model, presents the main supervised learning algorithms, and finally discusses feature selection and feature engineering.

¹<https://github.com/glouppe/info8010-deep-learning>

2.4.1 Regression with supervised learning

Consider the unknown joint probability distribution $p(\mathbf{x}, \mathbf{c})$ of two continuous variables X , *e.g.*, renewable energy generation, and C , *e.g.*, the weather forecasts, introduced in the previous Section. Let assume some training data $\mathcal{D} = \{\mathbf{x}_t, \mathbf{c}_t\}_{t=1}^N$ composed of N independent and identically distributed samples.

Supervised learning is usually concerned with the two following *inference* problems: *classification* and *regression*. Classification consists of identifying a decision boundary between objects of distinct classes. Regression aims at estimating relationships among (usually continuous) variables. In this thesis, we focus on regression.

Definition 2.4.1 (Regression). Given $\mathbf{x}_t, \mathbf{c}_t \in \mathcal{D}$, for $t = 1, \dots, N$ we would like to estimate for any new \mathbf{c}

$$\mathbb{E}[X = \mathbf{x} | C = \mathbf{c}]. \quad (2.13)$$

For instance, let assume g_θ is parameterized with a neural network which last layer does not contain any final activation. If we make the assumption that $p(\mathbf{x}, \mathbf{c}) \sim \mathcal{N}(\mathbf{x}; \mu = g_\theta(\mathbf{x}|\mathbf{c}); \sigma^2 = 1)$, we can perform maximum likelihood estimation to estimate the model's parameters θ that is equivalent to minimize the negative log likelihood

$$\arg \max_{\theta} p(\mathcal{D}|\theta) \sim \arg \min_{\theta} - \log \prod_{\mathbf{x}_t, \mathbf{c}_t \in \mathcal{D}} p(\mathbf{x} = \mathbf{x}_t | \mathbf{c}_t, \theta) \quad (2.14a)$$

$$= \arg \min_{\theta} - \sum_{\mathbf{x}_t, \mathbf{c}_t \in \mathcal{D}} \log p(\mathbf{x} = \mathbf{x}_t | \mathbf{c}_t, \theta) \quad (2.14b)$$

$$= \arg \min_{\theta} - \sum_{\mathbf{x}_t, \mathbf{c}_t \in \mathcal{D}} \log \left(\frac{1}{\sqrt{2\pi}} \exp \left(-\frac{1}{2} \|\mathbf{x}_t - g_\theta(\mathbf{x}_t | \mathbf{c}_t)\|^2 \right) \right) \quad (2.14c)$$

$$\sim \arg \min_{\theta} \sum_{\mathbf{x}_t, \mathbf{c}_t \in \mathcal{D}} \|\mathbf{x}_t - g_\theta(\mathbf{x}_t | \mathbf{c}_t)\|^2, \quad (2.14d)$$

which recovers the common squared error loss $L(\mathbf{x}, \hat{\mathbf{x}} \sim g_\theta(\mathbf{x}|\mathbf{c})) = \|\mathbf{x} - \hat{\mathbf{x}}\|^2$ that will be used in Chapter 5 for point forecasting.

2.4.2 Empirical risk minimization

Consider a function g_θ produced a some learning algorithm. The predictions of this function can be evaluated through a loss $L : \mathbb{R}^T \times \mathbb{R}^T \rightarrow \mathbb{R}$, such that $L(\mathbf{x}, \hat{\mathbf{x}} \sim g_\theta(\mathbf{x}|\mathbf{c})) \geq 0$ measures how close the prediction $\hat{\mathbf{x}}$ from \mathbf{x} is. For instance, in point forecasting L is the mean squared error or the pinball loss for quantile forecasting.

The key idea of the model training relies on the *empirical risk minimization*. Let \mathcal{G} denote the hypothesis space, *i.e.* the set of all functions g_θ than can be produced by the chosen learning algorithm.

Definition 2.4.2 (Empirical risk minimization). [145] We are looking for a function g_θ with a small expected risk

$$R(g_\theta) = \mathbb{E}_{\mathbf{x}, \mathbf{c} \sim p(\mathbf{x}, \mathbf{c})} [L(\mathbf{x}, \hat{\mathbf{x}} \sim g_\theta(\mathbf{x}|\mathbf{c}))], \quad (2.15)$$

also called the generalization error.

Therefore, for a given data generating distribution $p(\mathbf{x}, \mathbf{c})$ and for a given hypothesis space \mathcal{G} , the optimal model is

$$g_\theta^* = \arg \min_{g_\theta \in \mathcal{G}} R(g_\theta). \quad (2.16)$$

However, since $p(\mathbf{x}, \mathbf{c})$ is unknown, the expected risk cannot be evaluated and the optimal model cannot be determined. Nevertheless, if we have some training data $\mathcal{D} = \{\mathbf{x}_t, \mathbf{c}_t\}_{t=1}^N$ composed of N independent and identically distributed samples, we can compute an estimate [145], the empirical risk (or training error)

$$\hat{R}(g_\theta, \mathcal{D}) = \frac{1}{N} \sum_{\mathbf{x}_t, \mathbf{c}_t \in \mathcal{D}} L(\mathbf{x}_t, \hat{\mathbf{x}}_t \sim g_\theta(\mathbf{x}_t|\mathbf{c}_t)). \quad (2.17)$$

This estimator is unbiased and can be used for finding a good enough approximation of g_θ^* , resulting in the empirical risk minimization principle

$$g_{\theta, \mathcal{D}}^* = \arg \min_{g_\theta \in \mathcal{G}} \hat{R}(g_\theta, \mathcal{D}). \quad (2.18)$$

Note, most machine learning algorithms, including neural networks, implement empirical risk minimization. Under regularity assumptions, empirical risk minimizers converge: $\lim_{N \rightarrow \infty} g_{\theta, \mathcal{D}}^* \rightarrow g_\theta^*$.

The capacity of a hypothesis space induced by a learning algorithm intuitively represents the ability to find a good model $g_\theta \in \mathcal{G}$ for any function, regardless of its complexity. In practice, capacity can be controlled through hyper-parameters θ of the learning algorithm. Then, the goal is to adjust the capacity of the hypothesis space \mathcal{G} such that the expected risk of the empirical risk minimizer gets as low as possible. This is where the famous bias-variance trade-off [54] occurs: (1) reducing the capacity makes $g_{\theta, \mathcal{D}}^*$ fit the data less on average, which increases the bias term (under-fitting);

(2) increasing the capacity makes $g_{\theta, \mathcal{D}}^*$ vary a lot with the training data, which increases the variance term (over-fitting). Therefore, the bias-variance trade-off implies that a model should balance under-fitting and over-fitting: rich enough to express underlying structure in data, simple enough to avoid fitting spurious patterns. This is summarized in the classical U-shaped risk curve [7], shown in Figure 2.2 that has been widely used to guide model selection.

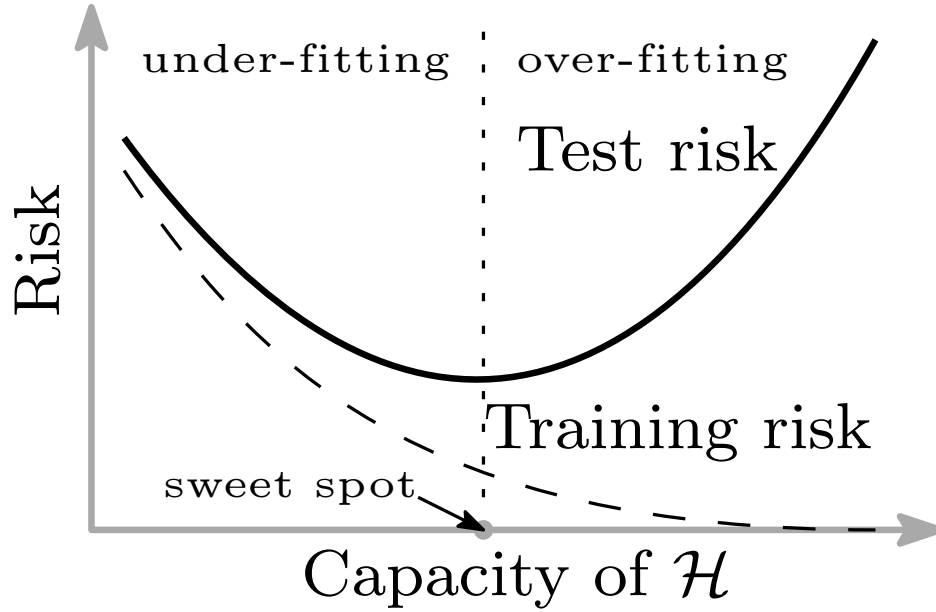


Fig. 2.2 The classical U-shaped risk curve arising from the bias-variance trade-off. Curves for training risk (dashed line) and test risk (solid line). Note, \mathcal{H} on the Figure is \mathcal{G} . Credits: [7].

2.4.3 The "double descent" curve

'However, in the modern practice, very rich models such as neural networks are trained to exactly fit (i.e., interpolate) the data. Classically, such models would be considered over-fit, and yet they often obtain high accuracy on test data. This apparent contradiction has raised questions about the mathematical foundations of machine learning and their relevance to practitioners.' [7]

This is illustrated by Figure 2.3 from Belkin et al. [7] that discuss empirical evidence for the double descent curve.

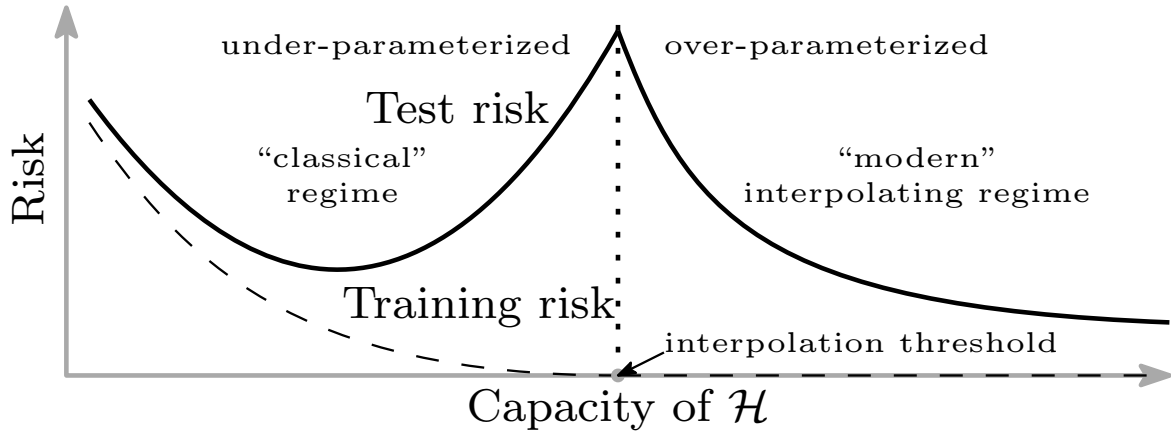


Fig. 2.3 The double descent risk curve, which incorporates the U-shaped risk curve (*i.e.*, the "classical" regime) together with the observed behavior from using high capacity function classes (*i.e.*, the "modern" interpolating regime), separated by the interpolation threshold. Credits: [7].

' ... the capacity of the function class does not necessarily reflect how well the predictor matches the *inductive bias* appropriate for the problem at hand. For the learning problems we consider (a range of real-world datasets as well as synthetic data), the inductive bias that seems appropriate is the regularity or smoothness of a function as measured by a certain function space norm. ... By considering larger function classes, which contain more candidate predictors compatible with the data, we are able to find interpolating functions that have smaller norm and are thus "simpler". Thus increasing function class capacity improves performance of classifiers.' [7]

This connection investigated by Belkin et al. [7] between the performance and the structure of machine learning models delineates the limits of classical analyses, and has implications for both the theory and practice of machine learning.

2.4.4 Training methodology

In practice, one has a finite dataset of input-output pairs \mathcal{D} and no further information about the joint probability distribution $p(\mathbf{x}, \mathbf{c})$. Then, the model is selected by minimizing the empirical risk (2.17) over the dataset. Therefore, it is typically strongly biased in an optimistic way and is a bad estimate of the generalization error also called the testing error. A "good" model should be able to predict well data independent from the dataset used for training but drawn from the same distribution.

2.4.5 Learning, validation, and testing sets

A *good practice* in machine learning is to use a dedicated part of the dataset as an independent testing set, that is not used to train the models but only to estimate the generalization error. Ideally, the dataset \mathcal{D} is divided randomly into three parts, as depicted in Figure 2.4.

1. The learning set is used to learn the models.
2. The validation set is may be used to evaluate the generalization error of the trained models to select among several learning algorithms the one more suited to the studied problem, or to optimize some algorithm's hyper-parameters θ and to avoid over-fitting.
3. Finally, the testing set is kept until the end of the process and is used to assess the performance of the selected model on independent data.

A common rule is to build the training set as large as possible to obtain good predictors while keeping enough samples in the validation and testing sets to correctly conduct the hyper-parameters selection and estimate properly the generalization error. This procedure is adopted in 8.

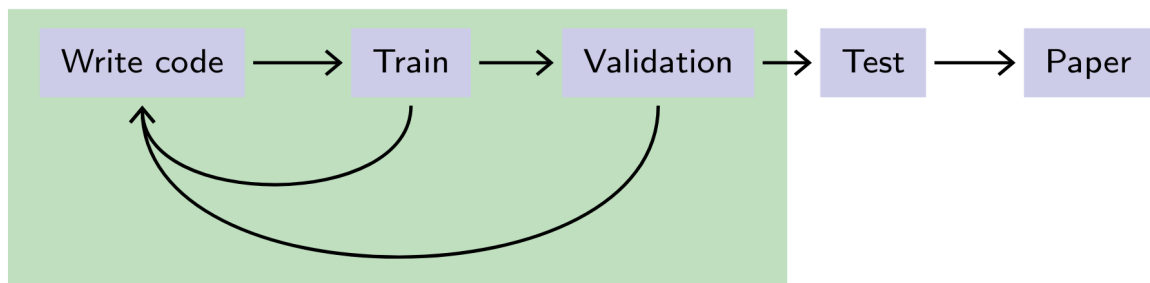


Fig. 2.4 Proper evaluation protocols. Credits: Francois Fleuret, EE559 Deep Learning, EPFL <https://fleuret.org/dlc/>.

2.4.6 k-fold cross-validation

When the dataset is composed of only a few months of data, dividing it into three parts can lead to a learning set too "small" to learn good predictors regarding both the empirical risk and the generalization error. In this case, the k -fold cross-validation methodology can be used to still evaluate correctly the generalization error of the algorithm [72].

This process consists of dividing the dataset into k -folds where each model is trained, each time with a different fold left out that is used to evaluate the testing error. In total, the model is trained k times with k pairs of learning and testing sets. The generalization error is estimated by averaging the k errors computed on k testing sets. This procedure is adopted in Chapters 6 and 7 where the dataset is composed of only a few months. Figure 2.5 depicts a 5-folds cross validation.

However, it is said that k -fold cross-validation may suffer from high variability, which can be responsible for bad choices in model selection and erratic behavior in the estimated expected prediction error. A study conducted by Bengio and Grandvalet [11] demonstrated there is no unbiased estimator of the variance of k -fold cross-validation. Therefore, the assessment of the significance of observed differences in cross-validation scores should be treated with caution.

Iteration 1	Test	Train	Train	Train	Train
Iteration 2	Train	Test	Train	Train	Train
Iteration 3	Train	Train	Test	Train	Train
Iteration 4	Train	Train	Train	Test	Train
Iteration 5	Train	Train	Train	Train	Test

Fig. 2.5 k -fold cross-validation.

2.5 Conclusions

This Chapter introduces the forecasting basics with the various types of forecasts, starting from the most common point forecasts and building up towards the more advanced products that are probabilistic forecasts: quantiles, prediction intervals, confidence intervals, scenarios, and density forecasts. It also provides some basics on

how to train and evaluate properly a forecasting model. The next Chapter presents the methodologies to evaluate the quality of these various types of forecasts.

Chapter 3

Forecast evaluation

Overview

This chapter introduces the main concepts in forecasting evaluation, as a background for the work developed in the following chapters of this manuscript. It presents the basics necessary to appraise the quality of predictions.

The interested reader is referred to more general textbooks for further information [105] and the lectures of the course "Renewables in Electricity Markets"^a given by Pierre Pinson, professor at the Technical University of Denmark.

^a<http://pierrepinson.com/index.php/teaching/>

“Everything that can be counted does not necessarily count; everything that counts cannot necessarily be counted.”

— **Albert Einstein**

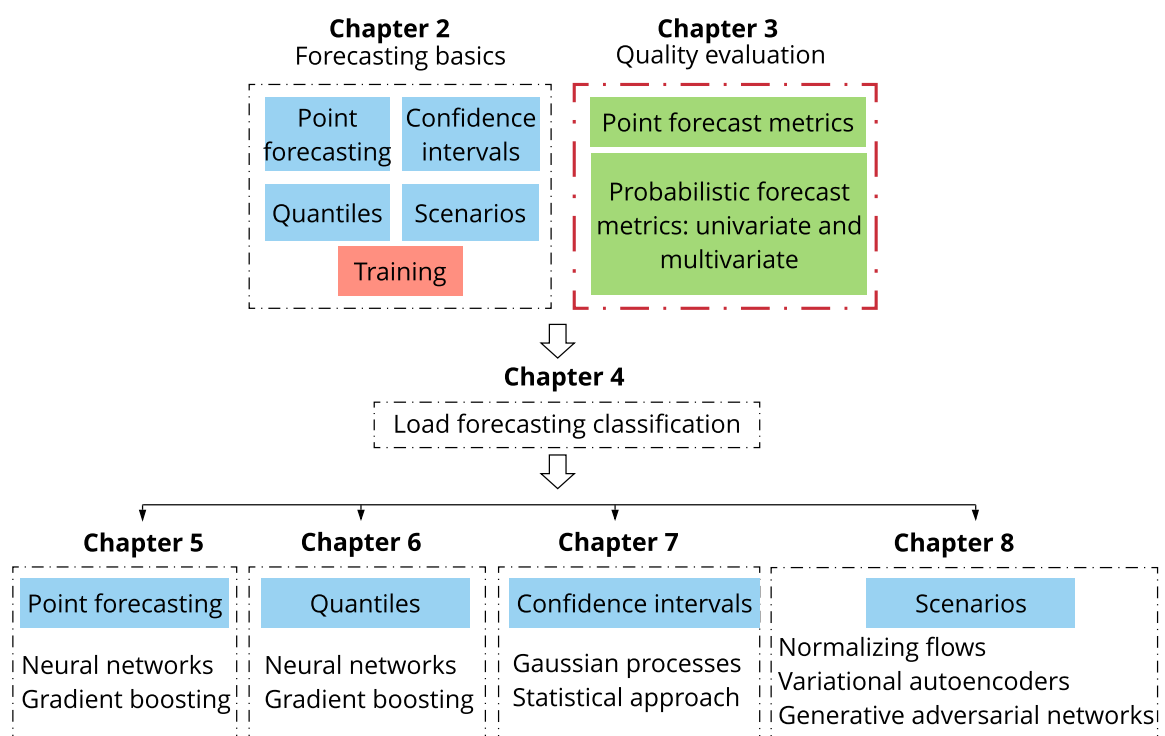


Fig. 3.1 Chapter 3 position in Part I.

Predictions ought to be evaluated before to be used as input to operational problems. For predictions in any form, one must differentiate between their *quality* and their *value* [105]. The forecast quality corresponds to the ability of the forecasts to genuinely inform of future events by mimicking the characteristics of the processes involved. The forecast value relates to the benefits from using forecasts in a decision-making process such as participation in the electricity market. Consequently, forecast quality is independent of the operational problem at hand, while this is not the case of forecast value.

In Part II, we will mainly seek to exploit the value of forecasts, insofar as these forecasts will be considered as input to operational problems. In contrast, here, the aim is to provide the reader with the basics necessary to appraise the quality of predictions. The general framework provided is mainly derived from Morales et al. [105]. This Chapter is organized as follows. Section 3.1 provides the point forecasting metrics. Section 3.2 presents the forecasting the probabilistic forecasting metrics. Finally, conclusions are drawn in Section 3.3.

3.1 Point forecasts metrics

The base quantity for evaluating point forecasts of a continuous random variable is the forecast error.

Definition 3.1.1 (Forecast error). [105, Chapter 2] The *forecast error* $\epsilon_{t+k|t}$ is the difference between observed and predicted values

$$\epsilon_{t+k|t} := x_{t+k|t} - \hat{x}_{t+k|t}. \quad (3.1)$$

Note that the forecast error may be normalized so that verification results may be comparable for different time-series. If so, normalization is most commonly performed by the nominal capacity of the site of interest. The first error criterion that may be computed is the bias of the forecasts, which corresponds to the systematic part of the forecast error. It may be corrected in a straightforward manner using simple statistical models.

Definition 3.1.2 (Bias). [105, Chapter 2] The *bias* is the mean of all errors over the evaluation period of length N , considered indifferently. For lead time k , it is

$$\text{bias}(k) := \frac{1}{N} \sum_{t=1}^N \epsilon_{t+k|t}. \quad (3.2)$$

However, this summary measure does not tell much about the quality of point forecasts, but only about a systematic error that should be corrected. Therefore, for a better appraisal of the forecasts, it is advised to use scores such as the mean absolute error and the root mean square error.

Definition 3.1.3 (Mean absolute error). [105, Chapter 2] The *mean absolute error* (MAE) is defined as the average of the absolute forecast errors over an evaluation set of length N

$$\text{MAE}(k) := \frac{1}{N} \sum_{t=1}^N |\epsilon_{t+k|t}|. \quad (3.3)$$

Definition 3.1.4 (Root mean square error). [105, Chapter 2] The *root mean square error* (RMSE) is defined as the square root of the sum of squared errors over an evaluation of length N

$$\text{RMSE}(k) := \sqrt{\frac{1}{N} \sum_{t=1}^N (\epsilon_{t+k|t})^2}. \quad (3.4)$$

All the above error criteria are independent of the length of the evaluation set. They are normalized by its length. They may also be normalized by the nominal capacity of the renewable energy site of interest, and then referred to as Nbias, NRMSE, and NMAE.

3.2 Probabilistic forecasts metrics

3.2.1 Calibration

The first requirement of probabilistic forecasts is to consistently inform about the probability of events, leading to the concept of *probabilistic calibration*, also referred to as *reliability*. As for the case of the bias for point forecasts, the assessment of probabilistic calibration only informs about a form of bias of probabilistic forecasts. A frequentist approach, based on an evaluation set of sufficient length, can be performed by assessing the reliability of each of the defining quantile forecasts using the indicator variable.

Definition 3.2.1 (Indicator variable). [105, Chapter 2] The *indicator variable* $\xi_{t,k}^q$, for a given quantile forecast $\hat{x}_{t+k|t}^{(q)}$ and corresponding realization x_{t+k} is

$$\xi_{t,k}^q := 1_{\{x_{t+k} < \hat{x}_{t+k|t}^{(q)}\}} = \begin{cases} 1 & x_{t+k} < \hat{x}_{t+k|t}^{(q)} \\ 0 & x_{t+k} \geq \hat{x}_{t+k|t}^{(q)} \end{cases}. \quad (3.5)$$

$\xi_{t,k}^q$ is a binary variable indicating if the quantile forecasts cover, or not, the measurements. Using this indicator variable, the empirical level of quantile forecasts can be defined, estimated, and eventually compared with their nominal one.

Definition 3.2.2 (Empirical level). [105, Chapter 2] The *empirical level* $\tilde{\xi}_{t,k}^q$, for a nominal level q and lead time k , is obtained by calculating the mean of the $\{\xi_{t,k}^q\}_{t=1}^N$ time-series over an evaluation set of length N

$$\tilde{\xi}_{t,k}^q := \frac{1}{N} \sum_{t=1}^N \xi_{t,k}^q. \quad (3.6)$$

The difference between nominal and empirical levels of quantile forecasts is to be seen as a probabilistic bias. Then, probabilistic calibration may be appraised visually by using *reliability diagrams* plotting empirical *vs.* nominal levels of the quantiles defining density forecasts.

3.2.2 Univariate skill scores

Perfectly calibrated probabilistic forecasts do not guarantee that the forecasts are "good". For instance, they may not be able to discriminate among situations with various uncertainty levels, while these aspects are of crucial importance in decision-making. The overall quality of probabilistic forecasts may be assessed based on skill scores. First, we consider the *univariate* skill score that can only assess the quality of the forecasts with respect to their marginals (time period). Second, we focus on the *multivariate* skill score that can directly assess multivariate scenarios.

Continuous ranked probability score

The continuous rank probability score (CRPS) [59] is a univariate scoring rule that penalizes the lack of resolution of the predictive distributions as well as biased forecasts. It is negatively oriented, *i.e.*, the lower, the better, and for deterministic forecasts, it turns out to be the mean absolute error (MAE). Thus, it can be directly compared to the MAE criterion used for point forecasts since the CRPS is its generalization in a probabilistic forecasting framework. The CRPS is used to compare the skill of predictive marginals for each component of the random variable of interest. In our case for the twenty-four time periods of the day. It allows to quantitatively assess the performance of the generative methods similar to the MAE when considering point forecasts.

Definition 3.2.3 (CRPS-integral). [59] The *CRPS* for predictive densities $\hat{F}_{t+k|t}$ and corresponding measurement $x_{t+k|t}$, is calculated as over an evaluation set of length N

$$\text{CRPS}(k) := \frac{1}{N} \sum_{t=1}^N \int_{x'} [\hat{F}_{t+k|t}(x') - 1_{\{x' > x_{t+k|t}\}}]^2 dx'. \quad (3.7)$$

However, it is difficult to estimate the integral form of the CRPS defined by (3.7).

Definition 3.2.4 (CRPS-energy). [59] Gneiting and Raftery [59] propose a formulation called the *energy form* of the CRPS since it is just the one-dimensional case of the energy score, defined in negative orientation as follows

$$\text{CRPS}(P, x_{t+k|t}) = \mathbb{E}_P[|X - x_{t+k|t}|] - \frac{1}{2} \mathbb{E}_P[|X - X'|], \quad (3.8)$$

where X and X' are independent random variables with distribution P and finite first moment, and \mathbb{E}_P is the expectation according to the probabilistic distribution P .

The CRPS can be computed for quantile forecasts and scenarios. Let $\{\hat{x}_{t+k|t}^i\}_{i=1}^M$ be the set of M scenarios generated at time t for lead time k . The estimator of (3.8) proposed by Zamo and Naveau [156], over an evaluation set of length N for lead time k , is

$$\text{CRPS}(k) = \frac{1}{N} \left[\sum_{t=1}^N \frac{1}{M} \sum_{i=1}^M |\hat{x}_{t+k|t}^i - x_{t+k|t}| - \frac{1}{2M^2} \sum_{i,j=1}^M |\hat{x}_{t+k|t}^i - \hat{x}_{t+k|t}^j| \right]. \quad (3.9)$$

Let $\{\hat{x}_{t+k|t}^{(q)}\}_{q=1}^Q$ be the set of Q quantiles generated at time t for lead time k . (3.8) is over an evaluation set of length N for lead time k

$$\text{CRPS}(k) = \frac{1}{N} \left[\sum_{t=1}^N \frac{1}{Q} \sum_{q=1}^Q |\hat{x}_{t+k|t}^{(q)} - x_{t+k|t}| - \frac{1}{2Q^2} \sum_{q,q'=1}^Q |\hat{x}_{t+k|t}^{(q)} - \hat{x}_{t+k|t}^{(q')}| \right]. \quad (3.10)$$

Quantile score

The quantile score (QS), also known as the *pinball loss*, is complementary to the CRPS as it permits obtaining detailed information about the forecast quality at specific probability levels, *i.e.*, over-forecasting or under-forecasting, and particularly those related to the tails of the predictive distribution [96]. It is negatively oriented and assigns asymmetric weights to negative and positive errors for each quantile.

Definition 3.2.5 (Pinball loss). The pinball loss function for a given quantile q is

$$\rho_q(\hat{x}, x) := \max \left\{ (1 - q)(\hat{x} - x), q(x - \hat{x}) \right\}. \quad (3.11)$$

Definition 3.2.6 (Quantile score). The *quantile score*, over an evaluation set of length N for lead time k , is

$$\text{QS}(k) := \frac{1}{N} \sum_{t=1}^N \frac{1}{Q} \sum_{q=1}^Q \rho_q(\hat{x}_{t+k|t}^{(q)}, x_{t+k}). \quad (3.12)$$

The quantile score, over an evaluation set of length N for a given quantile q over all lead times k , is

$$\text{QS}(q) := \frac{1}{N} \sum_{t=1}^N \frac{1}{T} \sum_{k=k_1}^{k_T} \rho_q(\hat{x}_{t+k|t}^{(q)}, x_{t+k}). \quad (3.13)$$

Interval score

The interval score (IS) is proposed by Gneiting and Raftery [59] to specifically assess the quality of central prediction interval forecasts. It rewards narrow prediction intervals but penalizes, with the penalty term that depends on α , the forecasts for which the observation is outside the interval.

Definition 3.2.7 (IS). The *interval score*, for a central prediction interval with a coverage rate of $(1 - \alpha)$, over an evaluation set of length N and for lead time k is

$$\begin{aligned} \text{IS}(k) = & \frac{1}{N} \sum_{t=1}^N (\hat{x}_{t+k|t}^{(1-\alpha/2)} - \hat{x}_{t+k|t}^{(\alpha/2)}) + \frac{2}{\alpha} (\hat{x}_{t+k|t}^{(\alpha/2)} - x_{t+k}) 1_{\{x_{t+k} \leq \hat{x}_{t+k|t}^{(\alpha/2)}\}} \\ & + \frac{2}{\alpha} (x_{t+k} - \hat{x}_{t+k|t}^{(1-\alpha/2)}) 1_{\{x_{t+k} \geq \hat{x}_{t+k|t}^{(1-\alpha/2)}\}}. \end{aligned} \quad (3.14)$$

Note, the skill scores can be normalized by a normalizing factor, such as the total installed capacity for a renewable generation plant.

3.2.3 Multivariate skill scores

Energy score

The most commonly used scoring rule when distributions are represented by a finite number of trajectories is known as energy score (ES). It is a multivariate generalization of the CRPS and has been formulated and introduced by Gneiting and Raftery [59]. The ES is proper and negatively oriented, *i.e.*, a lower score represents a better forecast.

The ES is used as a multivariate scoring rule by Golestaneh et al. [61] to investigate and analyze the spatio-temporal dependency of PV generations. They emphasize the ES pros and cons. It is capable of evaluating forecasts relying on marginals with correct variances but biased means. Unfortunately, its ability to detect incorrectly specified correlations between the components of the multivariate quantity is somewhat limited.

Definition 3.2.8 (Energy score). Gneiting and Raftery [59] introduced a generalization of the continuous rank probability score defined in negative orientation as follows

$$\text{ES}(P, \mathbf{x}) = \mathbb{E}_P \|X - \mathbf{x}\| - \frac{1}{2} \mathbb{E}_P \|X - X'\|, \quad (3.15)$$

where X and X' are independent random variables with distribution P and finite first moment, \mathbb{E}_P is the expectation according to the probabilistic distribution P , and $\|\cdot\|$ the Euclidean norm.

The ES is computed following Gneiting et al. [60] over an evaluation set of length N as follows

$$\text{ES} = \frac{1}{N} \sum_{t=1}^M \left[\frac{1}{M} \sum_{i=1}^M \|\hat{\mathbf{x}}_t^i - \mathbf{x}_t\| - \frac{1}{2M^2} \sum_{i,j=1}^M \|\hat{\mathbf{x}}_t^i - \hat{\mathbf{x}}_t^j\| \right]. \quad (3.16)$$

Note: when we consider the marginals of \mathbf{x} , it is easy to recognize that (3.16) is the CRPS.

Variogram score

An alternative class of proper scoring rules based on the geostatistical concept of variograms is proposed by Scheuerer and Hamill [135]. The sensitivity of these variogram-based scoring rules to incorrectly predicted means, variances, and correlations is studied. The results indicate these scores are shown to be distinctly more discriminative with respect to the correlation structure. Thus, in contrast to the Energy score, the Variogram score captures correlations between multivariate components.

Definition 3.2.9 (Variogram score). For a given day t of the testing set and a T -variate observation $\mathbf{x}_t \in \mathbb{R}^T$, the Variogram score metric of order γ is formally defined as

$$\text{VS}_t = \sum_{k,k'}^T w_{kk'} \left(|x_{t,k} - x_{t,k'}|^\gamma - \mathbb{E}_P |\hat{x}_{t,k} - \hat{x}_{t,k'}|^\gamma \right)^2, \quad (3.17)$$

where $\hat{x}_{t,k}$ and $\hat{x}_{t,k'}$ are the k -th and k' -th components of the random vector $\hat{\mathbf{x}}_t$ distributed according to P for which the γ -th absolute moment exists, and $w_{kk'}$ are non-negative weights. Given a set of M scenarios $\{\hat{\mathbf{x}}_t^i\}_{i=1}^M$ for this given day t , the forecast variogram $\mathbb{E}_P|\hat{x}_{t,k} - \hat{x}_{t,k'}|^\gamma$ can be approximated $\forall k, k' = 1, \dots, T$ by

$$\mathbb{E}_P|\hat{x}_{t,k} - \hat{x}_{t,k'}|^\gamma \approx \frac{1}{M} \sum_{i=1}^M |\hat{x}_{t,k}^i - \hat{x}_{t,k'}^i|^\gamma. \quad (3.18)$$

Then, the VS is averaged over the testing set of length N

$$\text{VS} = \frac{1}{N} \sum_{t=1}^N \text{VS}_t. \quad (3.19)$$

In this thesis, we evaluate the Variogram score with equal weights across all hours of the day $w_{kk'} = 1$ and using a γ of 0.5 which for most cases provides a good discriminating ability as reported in Scheuerer and Hamill [135].

3.3 Conclusions

This Chapter provides the basics of forecast verification, for the reader to acquire background knowledge on forecast quality, that is independent of the operational problem at hand. In contrast, the forecast value relates to the benefits from using forecasts in a decision-making process such as participation in the electricity market, and will be investigated in Part II. However, it is intuitively expected that higher-quality forecasts will yield better policies and decisions. Therefore, quality evaluation is complementary to value evaluation and provides an insight of the forecasting model skills. In the following Chapters, the quality metrics will be used to evaluate the various of probabilistic forecasts on several case studies.

Chapter 4

Classification of load forecasting studies

Overview

This Chapter differs from the previous ones and proposes a *classification* into *two dimensions* of load forecasting studies to decide which forecasting tools to use in which case. This classification aims to provide a synthetic view of the relevant forecasting techniques and methodologies by forecasting problem. This methodology is illustrated by reviewing several papers where the key principles of the main techniques and methodologies used are summarized.

References: This chapter is an adapted version of the following publication:

Jonathan Dumas and Bertrand Cornélusse. Classification of load forecasting studies by forecasting problem to select load forecasting techniques and methodologies. *arXiv preprint arXiv:1901.05052*, 2018. URL <https://arxiv.org/abs/1901.05052>.

For the sake of clarity, this study is not detailed in this manuscript.

“*A classification is a definition comprising a system of definitions.*”

— **Karl Wilhelm Friedrich Schlegel**

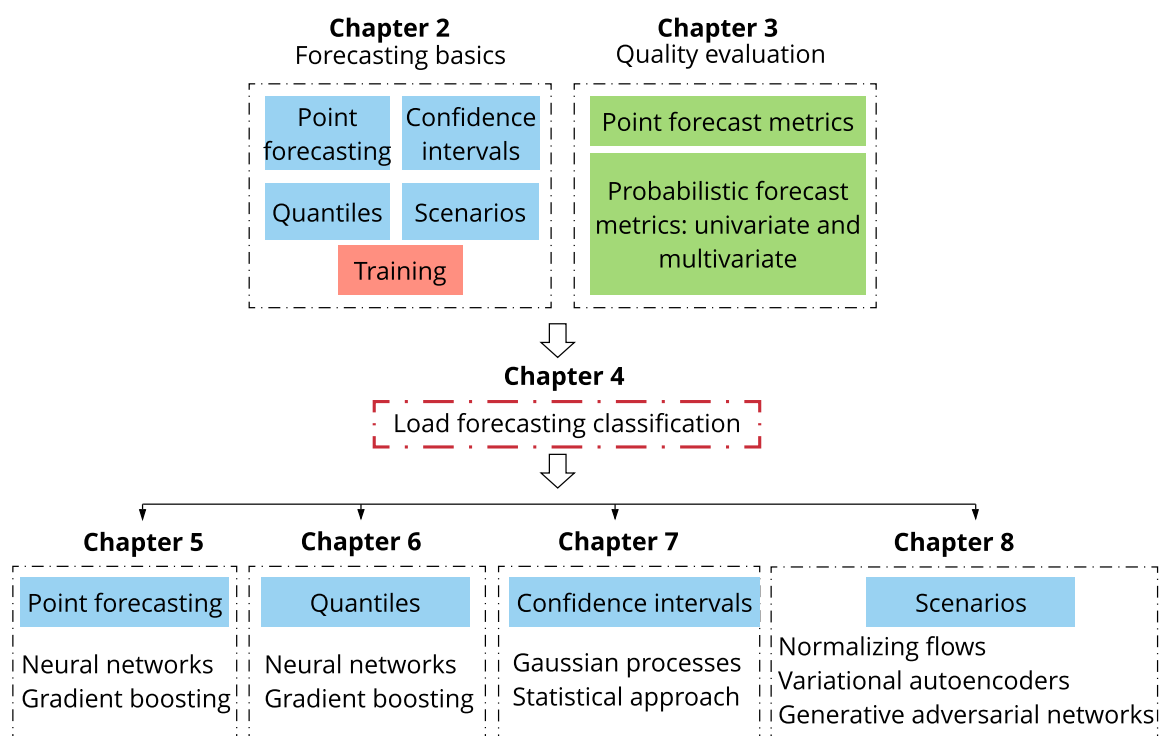


Fig. 4.1 Chapter 4 position in Part I.

The classification process relies on two couples of parameters that define a forecasting problem. Each article is classified with key information about the dataset used and the forecasting tools implemented: the forecasting techniques (probabilistic or deterministic) and methodologies, the data cleansing techniques, and the error metrics.

The process to select the articles reviewed was conducted into two steps. First, a set of load forecasting studies was built based on relevant load forecasting reviews and forecasting competitions. The second step consisted of selecting the most relevant studies of this set based on the following criteria: the quality of the description of the forecasting techniques and methodologies implemented, the description of the results, and the contributions. The study can be read in two passes.

1. The first one by identifying the forecasting problem of interest to select the corresponding class into one of the four classification tables. Each one references all the articles classified across a forecasting horizon. They provide a synthetic view of the forecasting tools used by articles addressing similar forecasting problems. Then, a second level composed of four Tables summarizes key information about the forecasting tools and the results of these studies.
2. The second pass consists of reading the key principles of the main techniques and methodologies of interest and the reviews of the articles.

Chapter 5

Point forecasting

Overview

This Chapter contributions are two-fold.

1. It proposes an introduction to multi-output weather-based point forecasting by defining the problem formulation, and an implementation on a real-case study to compute PV and electrical consumption forecasts used by a deterministic planner in Dumas et al. [47], presented in Chapter 11.
2. A second approach considers an intraday PV point forecast model using an encoder-decoder architecture, developed in Dumas et al. [44]. However, for the sake of clarity and the consistency of this thesis, this methodology and the results are detailed in Chapter 6.

References: This chapter is an adapted version of the following publication:

Jonathan Dumas, Selmane Dakir, Clément Liu, and Bertrand Cornélusse. Coordination of operational planning and real-time optimization in microgrids. *Electric Power Systems Research*, 190:106634, 2021. URL <https://arxiv.org/abs/2106.02374>.

Terminology and notations have been slightly adjusted for the sake of consistency with the rest of this manuscript. The text has also been processed to minimize overlap with respect to the next chapters.

“The most reliable way to predict the future
is to create it.”

— Abraham Lincoln

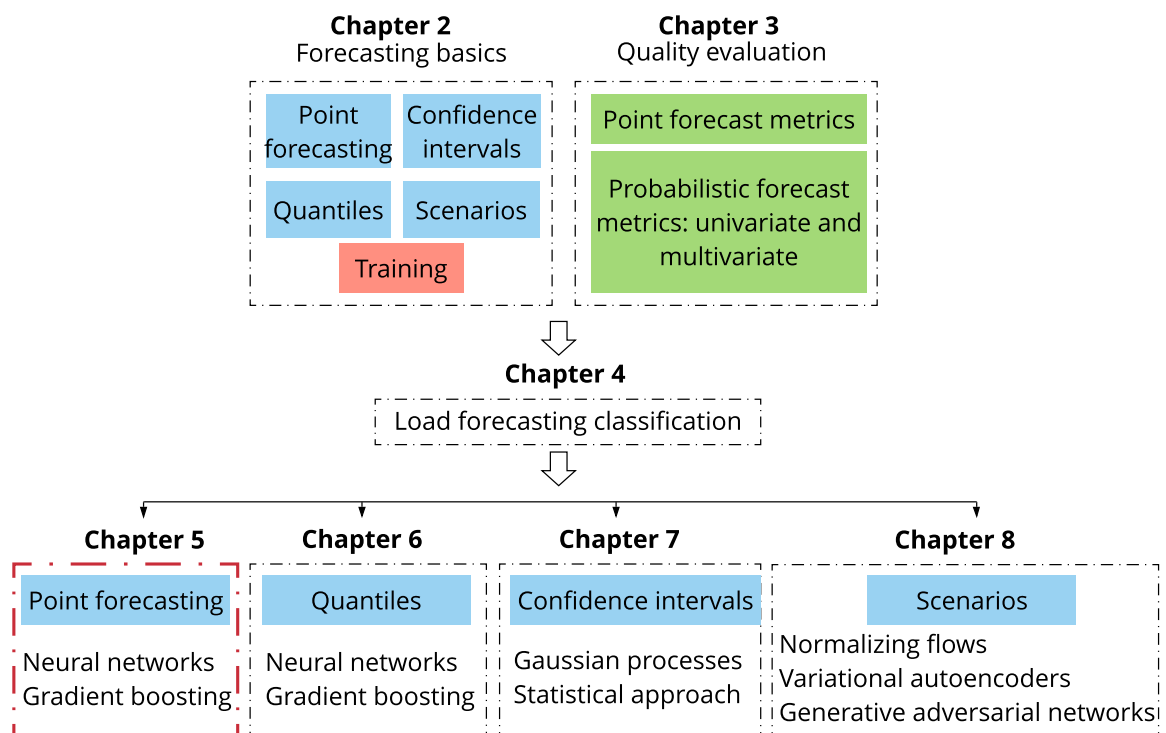


Fig. 5.1 Chapter 5 position in Part I.

This Chapter is organized as follows. Section 5.1 proposes a formulation of a multi-output point forecasting model. Section 5.2 presents the forecasting techniques. Section 5.3 reports the results. Finally, conclusions are drawn in Section 5.4.

5.1 Formulation

Point forecasting corresponds to the conditional expectation of the stochastic process for every lead time (2.1). This definition is linked to the so-called *loss function* $L(\hat{x}, x)$. Loss functions assign a penalty to forecast errors, as a proxy of the cost of these errors for those making decisions based on such forecasts. There exist various types of loss functions such as the mean squared error or the pinball loss. A special relevant case of a loss function to compute point forecasts is the mean squared error

$$L_2(\hat{x}, x) = (\hat{x} - x)^2. \quad (5.1)$$

At time t a point forecast $\hat{x}_{t+k|t}$ for time $t + k$ is the value of the process such that it minimizes the expected loss for the forecast user for all potential realizations of the process, given our state of knowledge at that time. Therefore, when considering multi-output point forecasts of length T the estimation of the model parameters is performed by solving

$$\theta^* = \arg \min_{\theta} \frac{1}{N} \sum_{t=1}^N \|\hat{\mathbf{x}}_t - \mathbf{x}_t\|_2^2, \quad (5.2a)$$

$$\hat{\mathbf{x}}_t \sim g_{\theta}(\mathbf{x}_{<t}, \mathbf{c}_t), \quad (5.2b)$$

given the information set \mathcal{D} of length N , and $\|\cdot\|_2$ the Euclidean norm.

5.2 Forecasting models

Two common forecasting techniques are implemented to forecast the PV production and the consumption, with a dedicated model per variable of interest. The first model uses a Recurrent Neural Network (RNN) of the Keras Python library [30]. The RNN is a Long Short Term Memory (LSTM) with one hidden layer composed of $2 \times n + 1$ neurons with n the number of input features. The second model is a Gradient Boosting Regressor (GBR) of the Scikit-learn Python library [119]. They both use past values of the PV production and consumption, and the weather forecasts provided by the Laboratory of Climatology of the Liège University, based on the MAR regional climate

model [50]. It is an atmosphere model designed for meteorological and climatic research, used for a wide range of applications, from km-scale process studies to continental-scale multi-decade simulations. The study Dumas et al. [47] focuses on the real-time control of microgrids based on planning that requires a forecast horizon of a few hours up to a few days. Both models are trained by solving (5.2a) that becomes

$$\hat{\mathbf{x}}_t \sim g_\theta(\mathbf{x}_{<t}, \mathbf{c}_t), \quad (5.3a)$$

$$\mathbf{x}_{<t} = [x_t, \dots, x_{t-k_4}], \quad (5.3b)$$

$$\mathbf{c}_t = [\hat{c}_{t+k_1|t}^i, \dots, \hat{c}_{t+k_T|t}^i], \quad (5.3c)$$

with $\hat{\mathbf{x}}_t$ the variable to forecast, *i.e.*, PV, consumption, and \hat{c}_i the forecast of the i^{th} weather variable, *e.g.*, direct solar irradiance, wind speed, air temperature. In the case study considered, the point forecasts are computed each quarter for the next $T = 96$ periods with a resolution $\Delta t = 15$ minutes. The forecasting process is implemented by using a rolling forecast methodology where the learning set is updated every six hours, with a fixed size limited to the week preceding the forecasts, to maintain a reasonable computation time.

5.3 Results

The point forecasts are evaluated each quarter over the entire forecasting horizon, the next 96 periods, using the Normalized Mean Absolute Error (NMAE), the Normalized Root Mean Squared Error (NRMSE), and the Normalized Energy Measurement Error (NEME). The normalizing coefficients for both the NMAE and NRMSE are the mean of the absolute values of the PV and consumption over all the simulation data set. The NEME is the NMAE of the energy summed over the entire forecasting horizon. Figures 5.2 and 5.3 provide the scores for both GBR and LSTM models for each quarter, plain lines, and the average over the entire simulation dataset, dashed lines. On average, the LSTM model yields slightly smaller average NMAE, NRMSE, and NEME values. However, the differences are not significant, and the forecast value (see Chapter 11) needs to be evaluated to decide which model is the best.

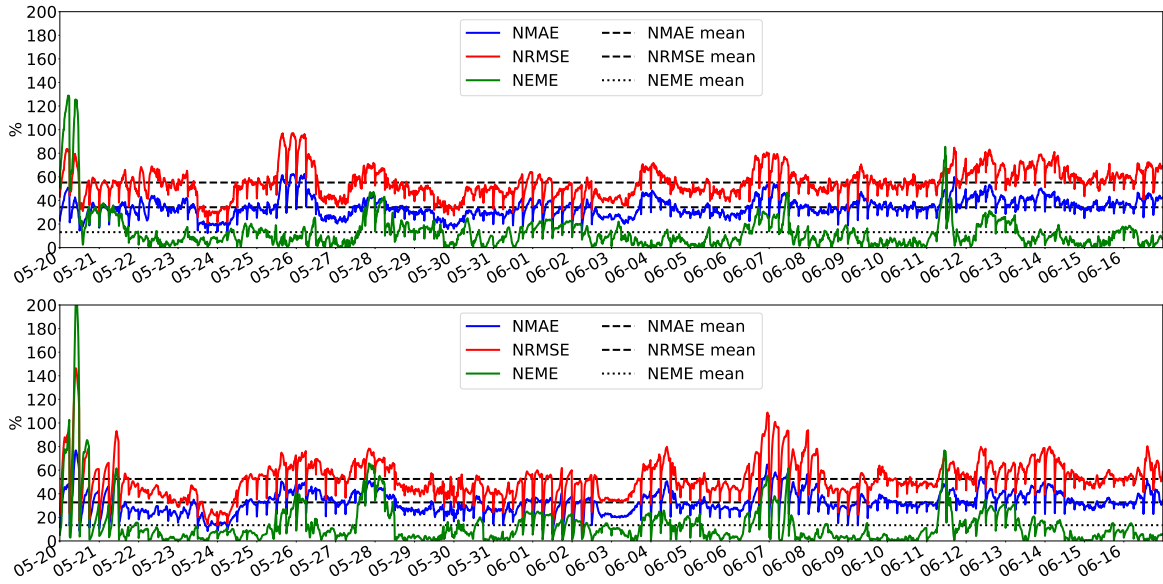


Fig. 5.2 PV forecast scores, GBR (top) and LSTM (bottom).

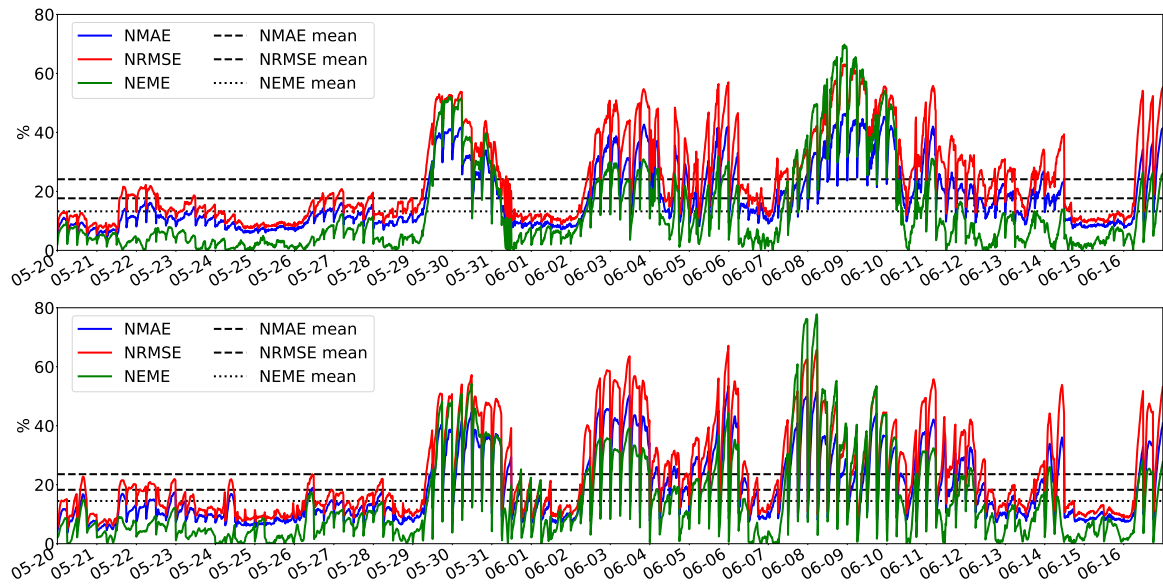


Fig. 5.3 Consumption forecast scores, GBR (top) and LSTM (bottom).

5.4 Conclusions

This Chapter proposes a formulation of a multi-output point forecasting model and an implementation on a real-case study by using two common techniques. The weather-based forecasting models are trained to compute day-ahead PV and electrical consumption point forecasts on a quarterly basis. This Chapter illustrates the forecasting process on a simple case study. This framework will be extended in the next Chapters for probabilistic forecasting.

Chapter 6

Quantile forecasting

Overview

Overall, the Chapter contributions can be summarized as follows.

1. A deep learning-based multi-output quantile architecture computes prediction intervals of PV generation on a day-ahead and intraday basis. The goal is to implement an improved probabilistic intraday forecaster, the encoder-decoder, to benefit from the last PV generation observations. This architecture is compared to a feed-forward neural network.
2. The weather forecasts are used to directly take into account the impact of the weather forecast updates generated every six hours.
3. A proper assessment of the quantile forecasts is conducted by using a k -fold cross-validation methodology and probabilistic metrics. It allows computing average scores over several testing sets and mitigating the dependency of the results to specific days of the dataset.
4. Finally, a comparison of deep learning quantile regression models is conducted with quantiles derived from deep learning generative models.

References: This chapter is an adapted version of the following publications:

Jonathan Dumas, Colin Cointe, Xavier Fettweis, and Bertrand Cornélusse. Deep learning-based multi-output quantile forecasting of pv generation. In *2021 IEEE Madrid PowerTech*, pages 1–6, 2021. doi: 10.1109/PowerTech46648.2021.9494976. URL <https://arxiv.org/abs/2106.01271>.

Jonathan Dumas, Antoine Wehenkel, Damien Lanaspeze, Bertrand Cornélusse, and Antonio Sutera. Deep generative modeling for probabilistic forecasting in power systems. Manuscript submitted for publication to *Applied Energy*, 2021. URL <https://arxiv.org/abs/2106.09370>.

Terminology and notations have been slightly adjusted for the sake of consistency with the rest of this manuscript. The text has also been processed to minimize overlap with respect to the other chapters.

“Prediction is very difficult, especially if it’s
about the future.”

— Niels Bohr

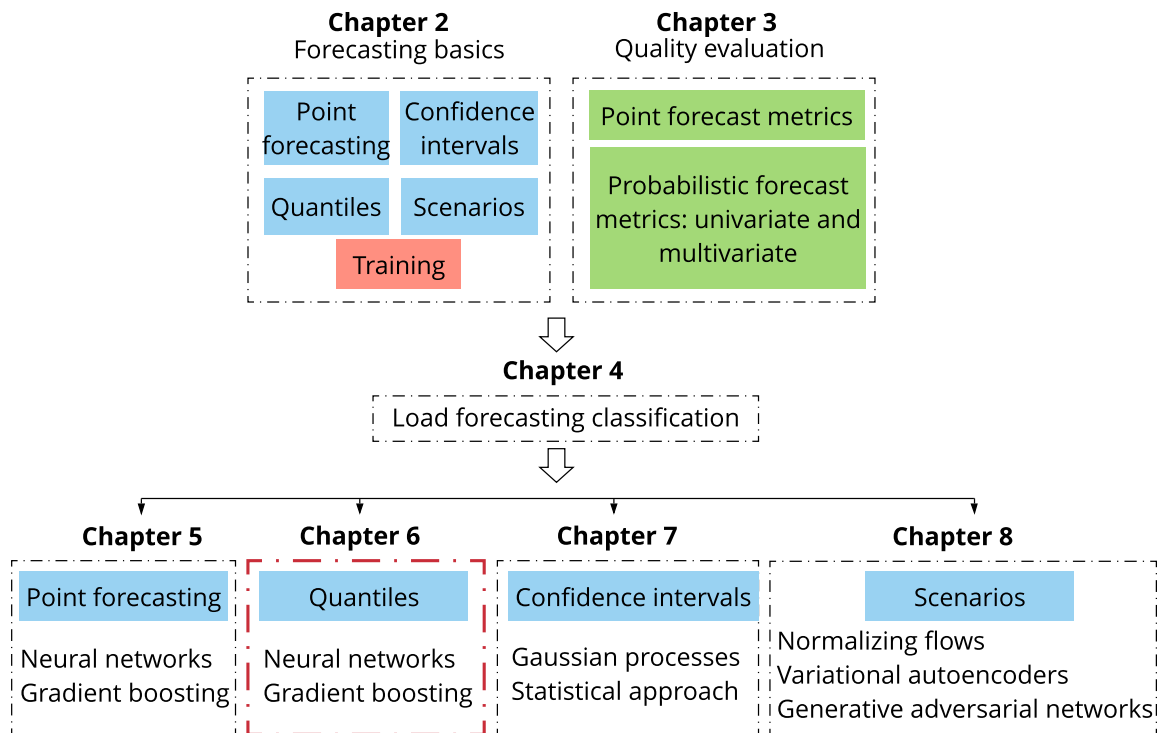


Fig. 6.1 Chapter 6 position in Part I.

This Chapter focuses on *quantile* forecasts that provide probabilistic information about future renewable power generation, in the form of a threshold level associated with a probability. This approach is investigated in Dumas et al. [44] with probabilistic PV forecasters that exploit recent breakthroughs in the field of data science by using advanced deep learning structures, such as the *encoder-decoder* architecture [24]. It is implemented to compute day-ahead and intraday multi-output PV quantiles forecasts, to efficiently capture the correlation between time periods, and to be used as input of a robust optimization model. For instance, to address the energy management system of a grid-connected renewable generation plant coupled with a battery energy storage device detailed in Dumas et al. [45] and Chapter 14. The case study is composed of PV production monitored on-site at the University of Liège (ULiège), Belgium. The weather forecasts from the MAR climate regional model [50] provided by the Laboratory of Climatology are used as inputs of the deep learning models.

The remainder of this Chapter is organized as follows. Section 6.1 presents the non-parametric quantile forecasting framework. Section 6.2 provides the related work. Section 6.3 details the forecasting techniques. Section 6.4 describes the case study and presents the results. Section 6.5 proposes a comparison of the quantile regression models with quantiles derived from deep learning generative models. Finally, Section 6.6 summarizes the main findings and highlights ideas for further work.

6.1 Formulation

Quantile regression [92] is one of the most famous non-parametric approach. It does not assume the shape of the predictive distributions and can be implemented with various types of forecasting techniques, *e.g.*, neural networks, linear regression, gradient boosting, or any other regression techniques. The estimation of the model parameters θ to compute multi-output quantile forecasts of length T is performed by minimizing the pinball loss (3.11) over all lead times

$$\theta^* = \arg \min_{\theta} \frac{1}{N} \sum_{t=1}^N \frac{1}{Q} \sum_{q=1}^Q \sum_{k=k_1}^{k_T} \rho_q(\hat{x}_{t+k}^{(q)}, x_{t+k}), \quad (6.1)$$

$$\hat{\mathbf{x}}_t^{(q)} \sim g_{\theta}(\mathbf{x}_{<t}, \mathbf{c}_t), \quad (6.2)$$

given the information set \mathcal{D} of length N , and a set of Q quantiles.

6.2 Related work

The literature on quantile forecasting is vast. The following papers have gained our attention in quantile PV probabilistic forecasting. At the Global Energy Forecasting Competition 2014 [74] solar forecasts were to be expressed in the form of 99 quantiles with various nominal proportions between zero and one. The models were evaluated by using the pinball loss function. This paper summarizes the recent research progress on probabilistic energy forecasting at that time, and this competition made it possible to develop interesting and innovative techniques. A systematic framework for generating PV probabilistic forecasts is developed by Golestaneh et al. [62]. A non-parametric density forecasting method based on Extreme Learning Machine is adopted to avoid restrictive assumptions on the shape of the forecast densities. A combination of bidirectional Recurrent Neural Networks (RNNs) with Long Short-Term Memory (LSTM) resulting in Bidirectional LSTM (BLSTM) is proposed by Toubreau et al. [143]. It has the benefits of both long-range memory and bidirectional processing. The BLSTM is trained by minimizing the quantile loss to compute quantile forecasts of aggregated load, wind and PV generation, and electricity prices on a day-ahead basis. Finally, an innovative architecture, referred to as encoder-decoder (ED), is developed by Bottieau et al. [24] to generate reliable predictions of the future system imbalance used for robust optimization.

6.3 Forecasting models

This Section presents the forecasting techniques implemented to compute multi-output point and quantile forecasts of PV generation.

6.3.1 Gradient boosting regression (GBR)

Gradient boosting builds an additive model in a forward stage-wise fashion [72]. It allows for the optimization of arbitrary differentiable loss functions. In each stage, a regression tree is fit on the negative gradient of the given loss function. The gradient boosting regressor (GBR) from the Scikit-learn [119] Python library is trained by minimizing the quantile loss. The learning rate is set to 10^{-2} , the max depth to 5, and the number of estimators to 500. There is a GBR model trained per quantile as this library does not handle a single model for several quantiles.

6.3.2 Multi-layer perceptron (MLP)

A description of the most widely used "vanilla" neural network, the *multi-layer perceptron* (MLP), is provided by [72]. A MLP with a single hidden layer is considered for the day-ahead forecasts and as the benchmark for the intraday forecasts. Note, MLPs with two and three hidden layers did not provide any significant improvement on the case study considered. The activation function is the Rectified Linear Unit (ReLU). The number of neurons of the hidden layer is $n_{\text{input}} + (n_{\text{output}} - n_{\text{input}})/2$, with n_{input} and n_{output} the number of neurons of the input and output layers, respectively. The learning rate is set to 10^{-2} and the number of epoch to 500 with a batch size of 8. It is implemented using the PyTorch Python library [118].

6.3.3 Encoder-decoder (ED)

Several technical information about recent advances in neural networks is provided by Toubeau et al. [143], Bottieau et al. [24]. In particular, recurrent neural networks, have shown a high potential in processing and predicting complex time series with multi-scale dynamics. However, RNNs are known to struggle in accessing time dependencies more than a few time steps long due to the vanishing gradient problem. Indeed, back-propagated errors during the training stage either fades or blows up over time. Long Short-Term Memory and Gated Recurrent Units networks tackle this problem by using internal memory cells [24]. A neural network composed of a LSTM and feed-forward layers, referred to as LSTM in the rest of the Chapter, is implemented for the day-ahead and intraday forecasts. The number of LSTM units is $n_{\text{input}} + (n_{\text{output}} - n_{\text{input}})/3$, and the number of neurons of the feed-forward layer $n_{\text{input}} + 2 \times (n_{\text{output}} - n_{\text{input}})/3$.

An innovative architecture, referred to as encoder-decoder [24], is composed of two different networks and has recently shown promising results for translation tasks and speech recognition applications and imbalance price forecasting. The encoder-decoder, depicted in Figure 6.2, processes features from the past, such as past PV observations, to extract the relevant historical information that is contained into a reduced vector of fixed dimensions, based on the last hidden state. Then, the decoder processes this representation along with the known future information such as weather forecasts. A version of the encoder-decoder architecture (ED-1) is implemented with a LSTM as the encoder and a MLP as the decoder. In a second version (ED-2) the decoder is a LSTM followed by an additional feed-forward layer. Both versions of the encoder-decoder are used as intraday forecasters. In ED-1, the encoder has $2 \times n_{\text{input}}$ units with n_{input} the number of neurons of the encoder input layer, features from the past. Then, the

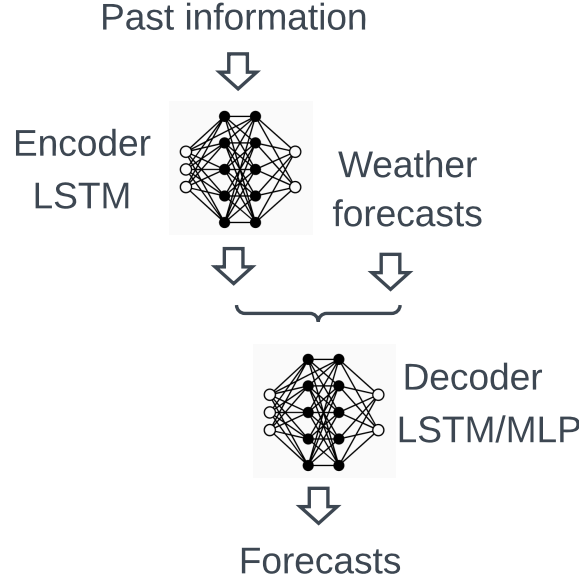


Fig. 6.2 Encoder-decoder architecture.

encoder output is merged with the weather forecasts becoming the decoder input layer that has $n_{\text{output}}/2$ neurons. In ED-2, the decoder has the same number of cells as the encoder, and the feed-forward layer is composed of $n_{\text{output}}/2$ neurons. The LSTM, ED-1, and ED-2 models are implemented using the TensorFlow Python library [1]. The activation functions are the ReLU, the learning rate is set to 10^{-3} , the number of epoch to 500 with a batch size of 64 for the three models.

A sensitivity analysis has been conducted to select the hyperparameters: number of hidden layers, neurons, epochs, and learning rate. Overall, increasing the number of hidden layers and neurons increases the model complexity. It can enhance the accuracy, but only up to a limited number of layers and neurons due to overfitting issues. In addition, the hyperparameter solution is closely related to the size of the historical database [143]. A deep learning model with a larger amount of hidden layers and neurons requires a large amount of data to accurately estimate the parameters. In the case study considered, there are only 157 days of data with a 15 minutes resolution. Thus, we decided to restrict the number of layers and neurons to select a smaller model that performs better with the available information.

6.4 The ULiège case study

6.4.1 Case study description

The ULiège case study is composed of a PV generation plant with an installed capacity of 466.4 kW. The PV generation has been monitored on a minute basis for 157 days in total, and the data is resampled to 15 minutes. The set of quantiles is $\{q = 10\%, \dots, 90\%\}$ for both the day-ahead and intraday forecasts. Numerical experiments are performed on an Intel Core i7-8700 3.20 GHz based computer with 12 physical CPU cores and 32 GB of RAM running on Ubuntu 18.04 LTS.

6.4.2 Numerical settings

The MAR regional climate model [50] provided by the Laboratory of Climatology of the Liège University is forced by GFS (Global Forecast System) to compute weather forecasts on a six hours basis, four-time gates per day at 00:00, 06:00, 12:00, and 18:00 with a 10-day horizon and a 15 minutes resolution. The solar irradiance and air temperature at 2 meters are normalized by a standard scaler and used as inputs to the forecasting models.

A k -fold cross-validation strategy is used to compute average scores over several testing sets to mitigate the dependency of the results to specific days of the dataset. The dataset is divided into k parts of equal length, and there are k possible testing sets $1 \leq i \leq k$. For a given testing set i , the models are trained over the $k - 1$ parts of the dataset. Eleven pairs of fixed lengths of 142 and 15 days are built. One pair is used to conduct the hyperparameters sensitivity analysis, and the ten others for testing where the scores are averaged. The Mean Absolute Error and Root Mean Squared Error are introduced to evaluate the point forecasts. The MAE, RMSE, CRPS, and IS are normalized by the PV total installed capacity with NMAE and NRMSE the normalized MAE and RMSE.

The day-ahead models, MLP, LSTM, and GBR compute forecasts at 12:00 for the next day. Four intraday time gates are considered at 00:00, 06:00, 12:00, and 18:00. The intraday forecasts of time gate 00:00 are computed by the day-ahead models using only the weather forecasts. Then, the next three intraday forecasts are computed by intraday models where the MLP, ED-1, and ED-2, models use the weather forecasts and the last three hours of PV generation.

The day-ahead and the first intraday predictions are delivered for the 96 quarters of the next day from 00:00 to 23:45 indexed by time steps $0 \leq k \leq 95$. The prediction

horizons span from 12 to 36 hours, for the day-ahead gate 12:00, and 0 to 24 hours, for the intraday gate 00:00. The prediction horizon is cropped to $11 \leq k \leq 80$ because the PV generation is always 0 for time steps $0 \leq k \leq 10$ and $81 \leq k \leq 95$ on the ULiège case study. The next three intraday predictions are performed for the 72, 48, and 24 next quarters of the day corresponding to the gates 06:00, 12:00, and 18:00. Therefore, the prediction horizons span from 0 to 18 hours, 0 to 12 hours, and 0 to 6 hours. The intraday forecasting time periods are $24 \leq k \leq 80$, $48 \leq k \leq 80$, and $72 \leq k \leq 80$. Table 6.1 compares the mean and the standard deviation of the computation times, over the ten learning sets, to train the point and quantile forecast models¹.

day-ahead	MLP	LSTM	GBR
point	5.3 (0.1)	23.7 (0.3)	3.4 (0.1)
quantile	7.6 (0.2)	69.0 (0.6)	44.6 (0.4)
intraday	MLP	ED-1	ED-2
point	5.0 (0.1)	5.2 (0.1)	17.2 (0.2)
quantile	17.9 (0.2)	6.4 (0.2)	18.0 (0.3)

Table 6.1 Training computation time (s).

6.4.3 Day-ahead results

Figure 6.3a compares the NMAE (plain lines), NRMSE (dashed lines), and Figure 6.3b the CRPS per lead time k of the day-ahead models of gate 12:00. Table 6.2 provides the mean and standard deviation of the NMAE, NRMSE, and CRPS. The LSTM achieved the best results for both point and quantile forecasts. Figures 6.5a, 6.5c, and 6.5e compare the MLP, LSTM, and GBR day-ahead quantile and point forecasts (black line named dad 12) of gate 12:00 on *August 2, 2020* with the observation in red. One can see that the predicted intervals of the LSTM model better encompass the actual realizations of uncertainties than the MLP and GBR.

6.4.4 Intraday results

Table 6.3 provides the averaged NMAE, NRMSE, and CRPS per gate of intraday models. The LSTM achieved the best NMAE and NRMSE for the 06:00 gate and the

¹The day-ahead and intraday LSTM training times are identicals for both point and quantile forecasts as they only take the weather forecasts as inputs.

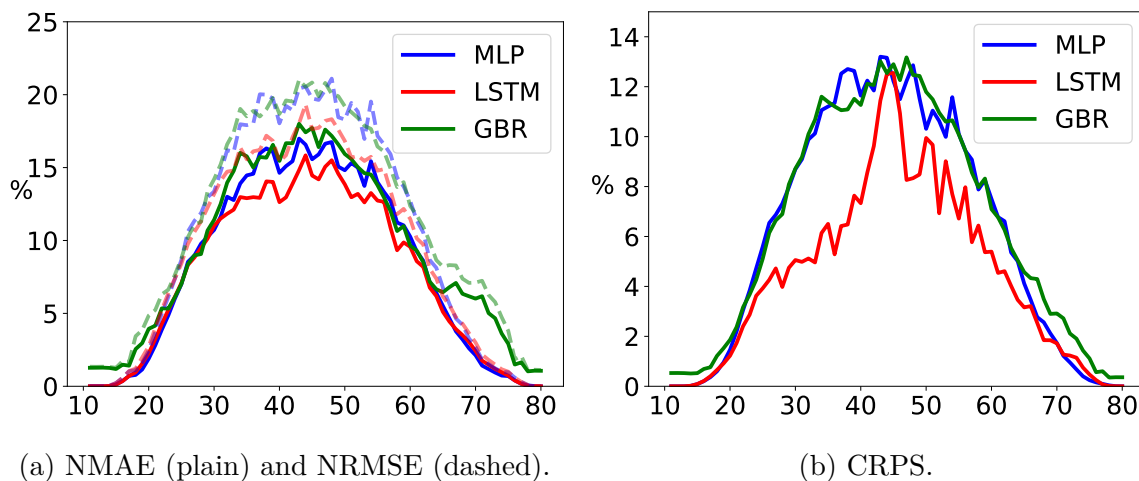


Fig. 6.3 NMAE, NRMSE, and CRPS of the day-ahead models per lead time k .

Score	Gate	MLP	LSTM	GBR
NMAE	12	8.2 (1.2)	7.6 (1.5)	9.2 (0.9)
	24	7.9 (1.2)	7.7 (1.6)	9.0 (0.8)
NRMSE	12	10.2 (1.4)	9.2 (1.6)	11.2 (0.9)
	24	9.7 (1.2)	9.4 (1.8)	10.9 (0.8)
CRPS	12	6.2 (1.1)	4.4 (0.2)	6.4 (0.7)
	24	6.2 (1.0)	4.4 (0.2)	6.3 (0.6)

Table 6.2 Day-ahead models results.

ED-1 achieved the best NMAE and NRMSE for the 12:00 gate and the best CRPS for both gates. Figure 6.4 compares the CRPS per lead time k of the intraday models. The ED-1 benefits from the last PV generation observations. Indeed, some CRPS values for both 06:00 and 12:00 gates are below the ones of 00:00 gate. Table 6.4 provides the interval score of intraday models for 80%, 60%, 40%, and 20% width of central intervals. The ED-1 model achieved the best results for both 06:00 and 12:00 gates and all prediction intervals except for the 06:00 gate and the prediction interval width of 80% where it is ED-2. The LSTM achieved close results to the ED-1. Figures 6.5b, 6.5d, and 6.5f compare the ED-1, LSTM, and ED-2 intraday quantile and point forecasts (black line named intra 6) of 06:00 gate on *August 2*, 2020 with the observation in red. Generally, one can see that the predicted intervals of ED-1 and LSTM models better encompass the actual realizations of uncertainties than ED-2.

Score	Gate	MLP	ED-1	ED-2	LSTM
NMAE	6	8.9 (1.0)	8.5 (1.4)	9.4 (1.0)	7.6 (1.5)
	12	6.7 (1.4)	6.4 (1.3)	7.1 (1.1)	7.2 (1.1)
NRMSE	6	10.9 (0.9)	10.3 (1.3)	11.3 (1.1)	7.7 (1.6)
	12	8.7 (1.3)	7.8 (1.2)	8.5 (1.2)	9.4 (1.8)
CRPS	6	8.1 (0.7)	5.9 (0.9)	6.6 (0.7)	6.2 (0.7)
	12	5.8 (1.2)	4.5 (0.7)	5.6 (1.8)	4.7 (0.5)

Table 6.3 NMAE, NRMSE, CRPS of intraday models.

Width	Gate	MLP	ED-1	ED-2	LSTM
80%	6	24.4 (2.9)	14.9 (4.0)	13.9 (4.9)	19.3 (4.2)
	12	17.4 (3.5)	10.6 (1.8)	11.6 (10.1)	9.6 (2.0)
60%	6	37.6 (3.2)	29.9 (5.0)	32.2 (4.2)	30.7 (4.6)
	12	27.2 (4.3)	22.4 (4.2)	27.5 (10.8)	22.6 (3.1)
40%	6	58.0 (4.5)	50.1 (6.5)	57.2 (6.0)	51.6 (5.8)
	12	42.4 (6.9)	37.7 (5.9)	48.1 (16.8)	39.2 (4.9)
20%	6	111.8 (8.4)	97.1 (11.7)	112.1 (10.3)	99.5 (10.4)
	12	81.5 (13.8)	72.7 (10.0)	94.8 (32.1)	76.5 (8.0)

Table 6.4 Interval scores of intraday models.

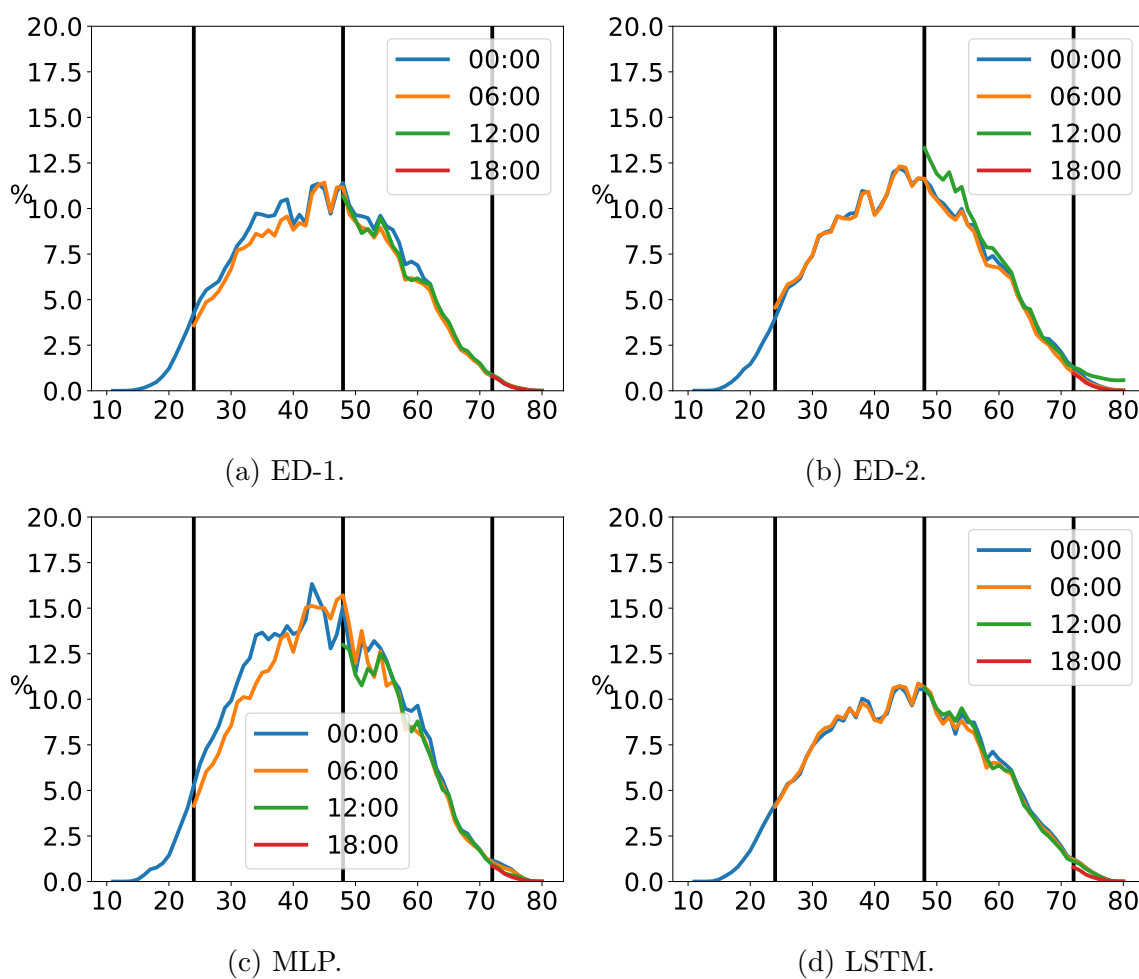


Fig. 6.4 CRPS of intraday models per lead time k .

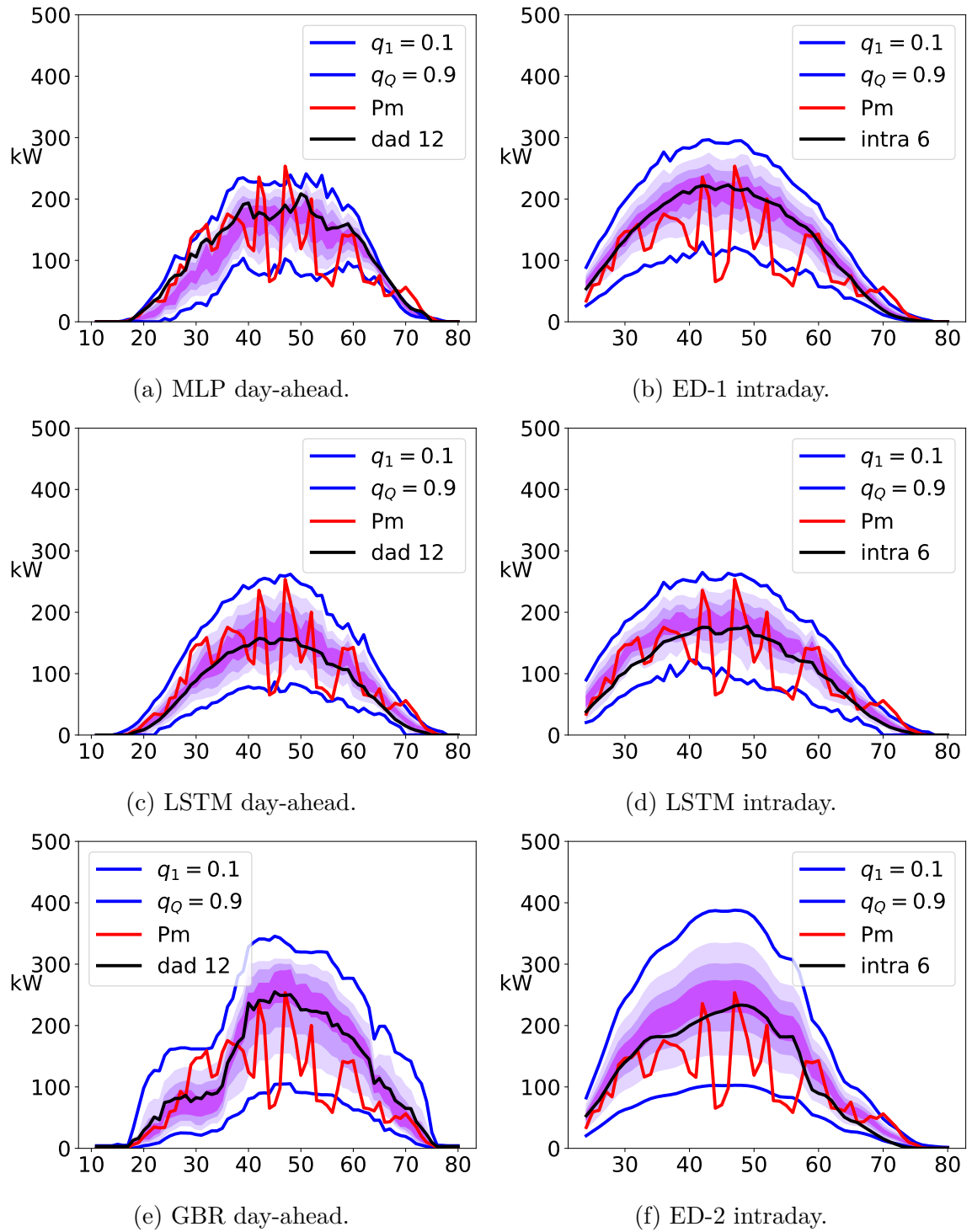


Fig. 6.5 Quantiles *vs.* point forecasts of day-ahead models of gate 12:00 (left), and intraday models of gate 06:00 (right) on August 2, 2020, the observations are in red.

6.4.5 Conclusions

An encoder-decoder architecture is implemented on the intraday scale to produce accurate forecasts. It efficiently captures the contextual information composed of past PV observations and future weather forecasts, while capturing the temporal dependency between forecasting time periods over the entire forecasting horizon. The models are compared by using a k -fold cross-validation methodology and quality metrics on a real case study composed of the PV generation of the parking rooftops of the Liège University. The best day-ahead model for both point and quantile forecasts is a neural network composed of a LSTM cell and an additional feed-forward layer. Then, the encoder-architecture composed of a LSTM-MLP yields accurate and calibrated forecast distributions learned from the historical dataset in comparison with the MLP and LSTM-LSTM models for the intraday point and quantile forecasts. However, the LSTM produced similar results.

Several extensions are under investigation.

1. First, considering a larger dataset of at least one full year to take into account the entire PV seasonality.
2. Second, developing a PV scenario approach based on the encoder-decoder architecture.

6.5 Comparison with generative models

This Section proposes a quality evaluation of the normalizing flows (NFs) and LSTM PV quantiles, used in Chapter 14 for robust optimization, using the quantile score, the reliability diagram, and the continuous rank probability score. Indeed, the two-phase engagement control of the capacity firming framework requires day-ahead and intraday *top-quality* forecasts. The more accurate the forecasts, the better the planning and the control. To this end, the Normalizing Flows technique is used to compute quantile day-ahead forecasts that are compared to a common alternative technique using a Long Short-Term Memory neural network. The controller requires intraday point forecasts that are computed by an encoder-decoder architecture. NFs are investigated in Section 8.2 of Chapter 8. Both NFs and LSTM models use as input the weather forecasts of the MAR climate regional model provided by the Laboratory of Climatology of the Liège University [50]. The NFs model generates day-ahead scenarios, and the quantiles are derived. The LSTM model computes directly the quantiles as it is trained by minimizing the quantile loss. The set of PV quantiles considered for the assessment is $\{q = 10\%, \dots, 90\%\}$.

In this study, the class of Affine Autoregressive flows is implemented². A five-step Affine Autoregressive flow is trained by maximum likelihood estimation with 500 epochs, and a learning rate set to 10^{-4} . The LSTM learning rate is set to 10^{-3} , the number of epoch to 500 with a batch size of 64. Figure 6.6 provides the results for these quality metrics computed over the entire dataset normalized by the total installed capacity. The NFs model outperforms the LSTM model with average values of 1.49% and 2.80% *vs.* 1.69% and 3.15% for the QS and CRPS, respectively. The NFs quantiles are also more reliable as indicated by the reliability diagram. These results motivate the use of the NFs as they outperform common deep learning approaches such as LSTM models.

²<https://github.com/AWehenkel/Normalizing-Flows> [151]

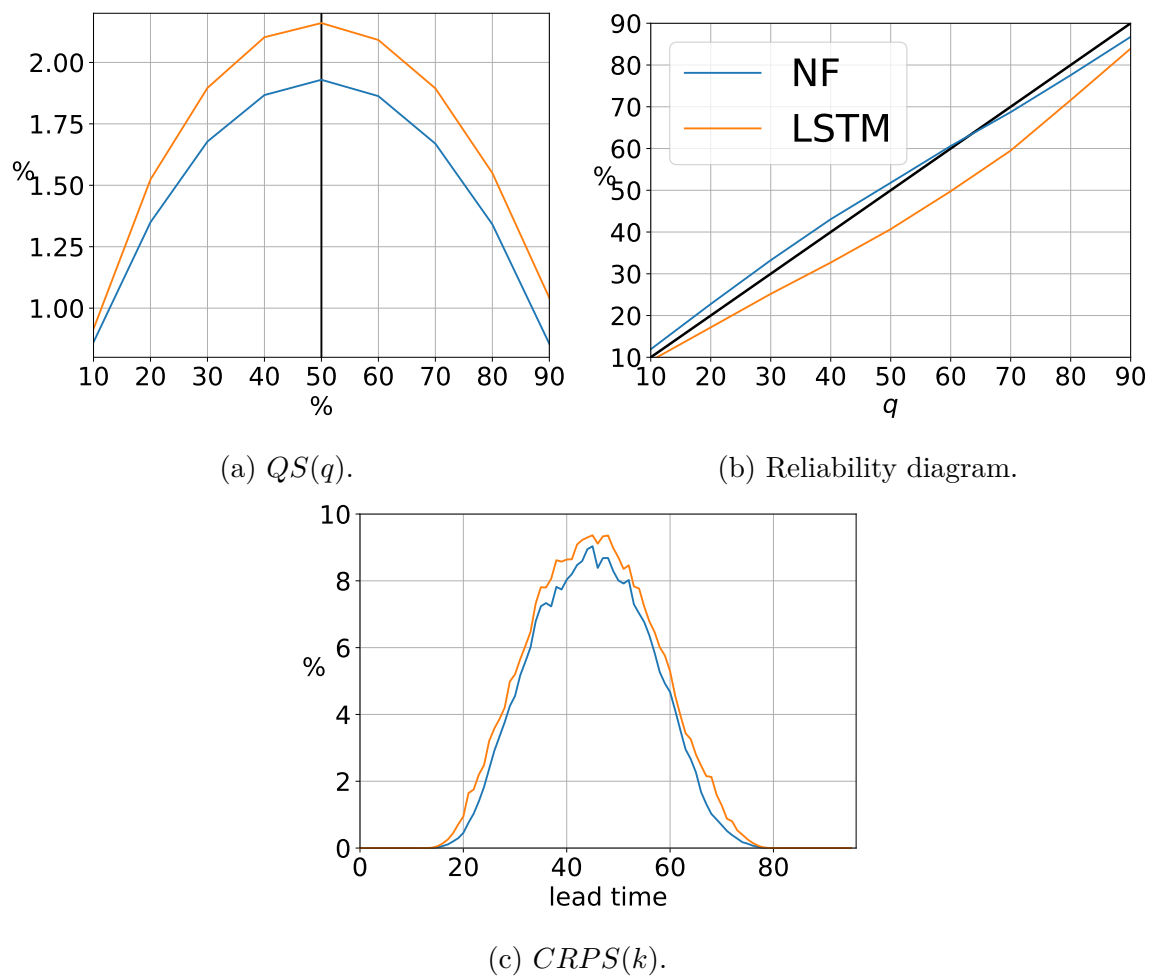


Fig. 6.6 Quantile forecast quality evaluation of LSTM *v.s* NFs models.

6.6 Conclusions

This Chapter proposes a formulation of the quantile forecasts problem using deep learning models trained by quantile regression to compute multi-output PV quantiles. The forecast quality is evaluated on a real case study composed of the PV generation of the parking rooftops of the Liège University. In addition, these quantile regression models are compared to PV quantiles derived from deep learning generative models, which will be investigated in detail in Chapter 8. In terms of forecast quality, the generative models outperform on this case study the quantile regression models. However, it does not mean they are better in terms of forecast value which will be assessed in Chapter 14 where a robust planner uses the PV quantiles in the form of prediction intervals.

Chapter 7

Confidence interval forecasting

Overview

The contributions of this Chapter are two-fold.

1. A novel two-step probabilistic approach (TSPA) is proposed for forecasting the Belgium imbalance prices. The TSPA uses a direct forecasting strategy [141]. It consists of forecasting an imbalance price for each quarter of the horizon independently from the others, requiring a model per quarter.
2. It sets a reference for other studies as this subject is rarely addressed.

References: This chapter is an adapted version of the following publication:

Jonathan Dumas, Ioannis Boukas, Miguel Manuel de Villena, Sébastien Mathieu, and Bertrand Cornélusse. Probabilistic forecasting of imbalance prices in the belgian context. In *2019 16th International Conference on the European Energy Market (EEM)*, pages 1–7. IEEE, 2019. URL <https://arxiv.org/abs/2106.07361>.

Terminology and notations have been slightly adjusted for the sake of consistency with the rest of this manuscript. The text has also been processed to minimize overlap with respect to the other chapters.

“*If you don't know where you're going any road will do.*”

— Lewis Carroll

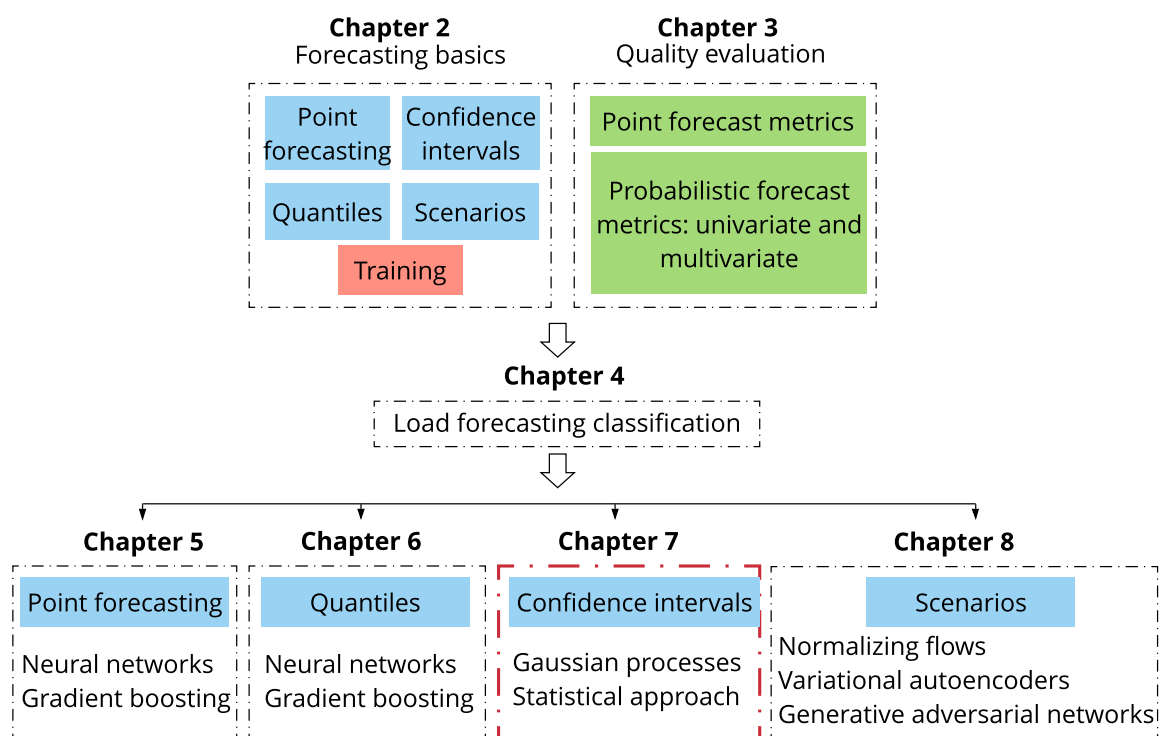


Fig. 7.1 Chapter 7 position in Part I.

This Chapter proposes a probabilistic forecasting of imbalance prices, developed in Dumas et al. [42]. A novel *two-step probabilistic approach* is proposed, with a particular focus on the Belgian case. The first step consists of computing the net regulation volume (NRV) *state transition probabilities*. It is modeled as a matrix estimated using historical data. This matrix is then used to infer the imbalance prices. Indeed, the NRV can be related to the level of reserves activated, and the corresponding marginal prices for each activation level are published by the Belgian Transmission System Operator (TSO) one day before electricity delivery. This approach is compared to a deterministic model, implemented with a multi-layer perceptron, and a widely adopted probabilistic technique, Gaussian Processes (GP).

This Chapter is organized as follows. Section 7.1 details the related work. Section 7.2 introduces the novel two-step probabilistic approach formulation and the assumptions made. Section 7.3 describes the numerical tests on the Belgian case. Section 7.4 reports the results. Conclusions are drawn in Section 7.5. Appendix 7.5 lists the acronyms, parameters, and forecasted or computed variables. Finally, Annex 7.6 provides a short reminder of the imbalance market and the Belgian balancing mechanisms.

7.1 Related work

The progressive large-scale integration of renewable energy sources has altered electricity market behavior and increased the electricity price volatility over the last few years [35, 66, 85]. In this context, imbalance price forecasting is an essential tool the strategic participation in short-term energy markets. Several studies take into account the imbalance prices as penalties, for deviation from the bids, to compute the optimal bidding strategy [57, 122, 20, 22]. However, these penalties are known only *a posteriori*. A forecast indicating the imbalance prices and the system position, short or long, with a confidence interval is a powerful tool for decision making. Probabilistic forecasting usually outperforms deterministic models when used with the appropriate bidding strategies [122]. Whereas the literature on day-ahead electricity forecast models is large, studies about balancing market prices forecast have received less attention. A combination of classical and data mining techniques to forecast the system imbalance volume is given in Garcia and Kirschen [52]. A statistical description of imbalance prices for shortage and surplus is made by Saint-Drenan [132]. A review and benchmark of time series-based methods for balancing market price forecasting are brought by Klæboe et al. [90]. Both one-hour and one-day-ahead forecasts are considered for state

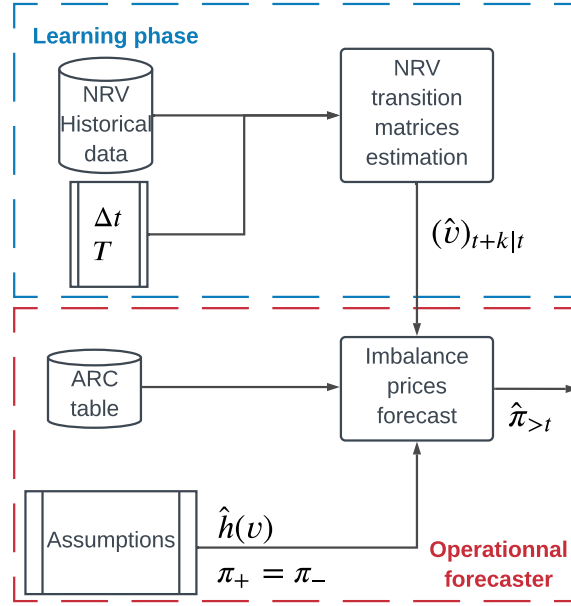


Fig. 7.2 TSPA imbalance price forecasting process.

determination, balancing volume, and prices forecasting on the Nord Pool price zone NO2 in Norway.

7.2 Formulation

This study focuses on the intraday market time scale that requires a forecasting horizon from a few minutes to a few hours with a resolution Δt . The day-ahead time scale requires forecasts of the imbalance prices from 12 to 36 hours, which is not realistic at this stage. The input data are the imbalance price history, the NRV, and the marginal prices for activation published by the TSO. The probabilistic approach consists of forecasting the imbalance prices in two steps: computing the NRV state transition probabilities, then forecasting the imbalance prices, as depicted in Figure 7.2. It is motivated by the ELIA imbalance price mechanisms detailed in Appendix 7.6.

7.2.1 Net regulation volume forecasting

Let consider the T forecasting horizons $k_1 = \Delta t, \dots, k_T = T\Delta t$ with Δt the market period, 15 minutes for Belgium. The NRV historical data is discretized into N bins, v_i , centered around $v_{i,1/2}$. Note, this discretization has been determined after a statistical study of the NRV distribution. The T NRV transition matrices $(v)_{t+k|t}$, of dimensions $N \times N$, from a known state at time t to a future state at time $t + k$ are estimated by

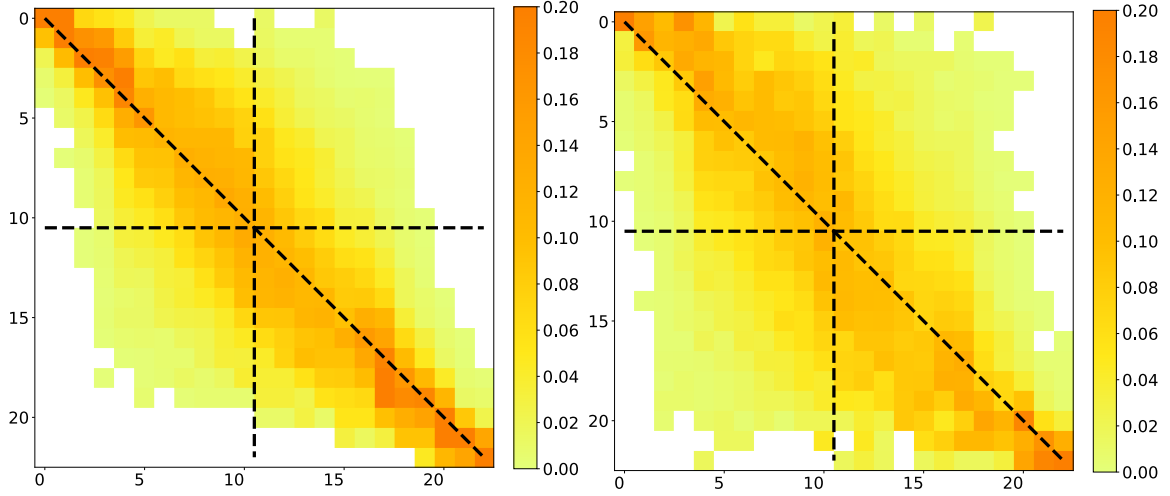


Fig. 7.3 NRV transition matrix from t to $t + 15$ min (left) and $t + 60$ min (right).

using the NRV historical data, and referred to as $(\hat{v})_{t+k|t}$. They are composed of the following conditional probabilities $\forall k = k_1, \dots, k_T$

$$p_{t+k|t}^{ij} = \Pr[v(t+k) \in v_j \mid v(t) \in v_i], \quad i, j \in \llbracket 1; N \rrbracket^2, \quad (7.1)$$

with $v(t)$ the measured NRV at time t , and $\sum_{j=1}^N p_{t+k|t}^{ij} = 1 \forall i \in \llbracket 1; N \rrbracket$. The conditional probabilities (7.1) are estimated statistically over the learning set (LS) $\forall k = k_1, \dots, k_T$

$$\hat{p}_{t+k|t}^{ij} = \frac{\sum_{t \in LS} 1_{\{v(t) \in v_i\}}}{\sum_{t \in LS} 1_{\{v(t+k) \in v_j \mid v(t) \in v_i\}}}, \quad i, j \in \llbracket 1; N \rrbracket^2. \quad (7.2)$$

Figure 7.3 illustrates the matrices $(\hat{v})_{t+k_1|t}$ and $(\hat{v})_{t+k_4|t}$ with 2017 as learning set. The estimated mean $\hat{v}_{t+k|t}^m$ and standard deviation $\hat{v}_{t+k|t}^{std}$ of the NRV at time t for $t+k$ are calculated as follows

$$\begin{aligned} \hat{v}_{t+k|t}^m &= \sum_{j=1}^N \hat{p}_{t+k|t}^{ij} v_{j,1/2} \\ \hat{v}_{t+k|t}^{std} &= \sqrt{\sum_{j=1}^N \hat{p}_{t+k|t}^{ij} (v_{j,1/2} - \hat{v}_{t+k|t}^m)^2}, \end{aligned} \quad (7.3)$$

with i such as $v(t) \in v_i$.

7.2.2 Imbalance price forecasting

The NRV can be related to the level of reserves activated, and the corresponding marginal prices for each activation level, published by the TSO one day before electricity delivery. We thus first forecast the NRV and its spread among the Gross Upward regulation Volume (GUV) and Gross Downward regulation Volume (GDV). Then, we forecast the reserve products activated (contracted or not) to select the most probable MIP and MDP into the ARC table. Finally, the mean and the standard deviation of the imbalance price forecast are derived.

However, the ARC table contains only the contracted reserve products. Most of the time, the first activated reserve products come from the non contracted International Grid Control Cooperation platform (IGCC-/ +), the contracted secondary reserve (R2-/ +) and the non contracted regulation reserves (Bids-/ +)¹. For instance, consider a quarter of an hour with an NRV of 150 MW, spread into 170 MW of GUV and 20 MW of GDV. Suppose ELIA activated 80 MW of IGCC+ and 90 MW of R2+. Then, the MIP is given in the marginal activation price of R2+ in the ARC table at the range $[0, 100]$ MW. Suppose now that ELIA has activated 20 MW of IGCC+, 20 MW of R2 +, and 130 MW of Bids+. Then, the MIP is given in the marginal activation price of Bids+. However, this is not a contracted reserve and its price is not in the ARC table. Then, it is more complicated to predict the MIP and consequently the imbalance prices. Therefore, we introduce several simplifying assumptions, justified by a statistical study on the 2017 ELIA imbalance data.

Assumption 6. *The NRV is entirely spread into either the GUV, if the NRV is positive, or GDV, if the NRV is negative.*

The mean and standard deviation of the GUV and GDV are 109 ± 82 MW *vs.* 17 ± 27 MW when the NRV is positive, while it is 13 ± 20 MW *vs.* 110 ± 73 MW when the NRV is negative. This assumption enables to select directly in the ARC table the marginal price for activation corresponding to the range of activation equal to the NRV, minus IGCC.

Assumption 7. *The Bids reserve product is not taken into account, thus we suppose that the NRV is spread over the IGCC and reserve products of the ARC table.*

The percentage of Bids reserve product, positive or negative, activated over each quarter of the 2017 is 11.5%.

¹More information about the reserve products is available at <http://www.elia.be>.

Assumption 8. *The level of activated IGCC reserve product is modeled by a function \hat{h} of the NRV.*

\hat{h} assigns for a given value of NRV a range of activation p into the ARC table. c_t^p is the ARC marginal price at t and for the activation range p , with $p \in \llbracket 1; P \rrbracket$. If $\hat{h}(v)$ falls into the activation range p , then $c_t^p(\hat{h}(v))$ is equal to c_t^p . Due to the 2017 statistical distribution of the IGCC versus the NRV, \hat{h} is defined as follows

$$\hat{h}(x) = \begin{cases} x & \text{if } |x| \leq 100, \\ x - 100 & \text{if } x > 100, \\ x + 100 & \text{if } x < -100. \end{cases} \quad (7.4)$$

The mean and standard deviation (MW) of the IGCC+ and IGCC- are

$$\begin{cases} 17 \pm 25 \text{ \& } 23 \pm 24 & \text{if } |NRV| \leq 100, \\ 50 \pm 48 \text{ \& } 5 \pm 15 & \text{if } NRV > 100, \\ 2 \pm 10 \text{ \& } 67 \pm 47 & \text{if } NRV < -100. \end{cases}$$

Generally, ELIA first tries to activate the IGCC product to balance the system. However, when the system imbalance is too high other reserve products are required.

Assumption 9. *The positive imbalance price is equal to the negative one.*

The mean of the positive and negative imbalance prices are 42.23 and 43.04 €/MWh. They are different 30.38% of the time, but the NMAE and NRMSE are 0.02 and 0.06%. Indeed, the positive and negative prices differ only by a small correction parameter if the system imbalance is greater than 140 MW, cf. Appendix 7.6.2.

Under these assumptions, the estimated mean $\hat{\pi}_{t+k|t}^m$ and standard deviation $\hat{\pi}_{t+k|t}^{std}$ of the imbalance prices at time t for $t+k$ are calculated as follows

$$\begin{aligned} \hat{\pi}_{t+k|t}^m &= \sum_{j=1}^N \hat{p}_{t+k|t}^{ij} c_j^{t+k}(\hat{h}(v_{j,1/2})) \\ \hat{\pi}_{t+k|t}^{std} &= \sqrt{\sum_{j=1}^N \hat{p}_{t+k|t}^{ij} (c_j^{t+k}(\hat{h}(v_{j,1/2})) - \hat{\pi}_{t+k|t}^m)^2}, \end{aligned} \quad (7.5)$$

with i such as $v(t) \in v_i$. Finally, on a quarterly basis a forecast is issued at time t and composed of a set of T couples $\hat{\pi}_{>t} := \left\{ (\hat{\pi}_{t+k|t}^m, \hat{\pi}_{t+k|t}^{std}) \right\}_{k=k_1}^{k_T}$.

7.3 Case study

This approach is compared to a widely used probabilistic technique, the Gaussian Processes, and a "classic" deterministic technique, a Multi-Layer Perceptron (MLP). Both techniques are implemented using the Scikit-learn Python library [119]. The GP uses Matérn, constant and white noise kernels. The MLP has one hidden layer composed of $2 \times n + 1$ neurons with n the number of input features. The dataset is composed of the 2017 and 2018 historical Belgium imbalance price and NRV, available on Elia's website. Both the MLP and GP models forecast the imbalance prices based on the previous twenty-four hours of NRV and imbalance prices, representing in total 2×96 input features. The MLP is implemented with a Multi-Input Multi-Output (MIMO) strategy and the GP with a Direct strategy [141]². The Direct strategy consists of training a model \hat{g}_k per market period

$$\hat{\pi}_{t+k|t} = \hat{g}_k(\pi_t, \dots, \pi_{t-k_T}, v_t, \dots, v_{t-k_T}), \quad \forall k = k_1, \dots, k_T, \quad (7.6)$$

and the forecast is composed of the T predicted values computed by the T models \hat{g}_k . In contrast, the MIMO strategy consists of training only one model \hat{g} to directly compute the T values of the variable of interest

$$[\hat{\pi}_{t+k_1|t}, \dots, \hat{\pi}_{t+k_T|t}]^T = \hat{g}(\pi_t, \dots, \pi_{t-k_T}, v_t, \dots, v_{t-k_T}). \quad (7.7)$$

For both MIMO and Direct strategies, the forecast is computed quarterly and composed of T values. The forecasting process is implemented by using a *rolling forecast strategy* where the training set is updated every month, depicted in Figure 7.4. The validation set is 2018 where and each month is forecasted by a model trained on a different learning set. For both the MLP and TSPA techniques, the LS size increases by one month each new forecasted month of 2018 with the first LS set to 2017. For the GP technique, the LS is limited to the month preceding the forecast, to maintain a reasonable computation time.

7.4 Results

The probabilistic forecasts are evaluated using the Pinball Loss Function (PLF) and the Continuous Rank Probability Score, and compared to the deterministic ones with the Normalized Mean Absolute Error (NMAE) and the Normalized Root Mean Squared

²GP regression with multiple outputs is non-trivial and still a field of active research [147, 99].

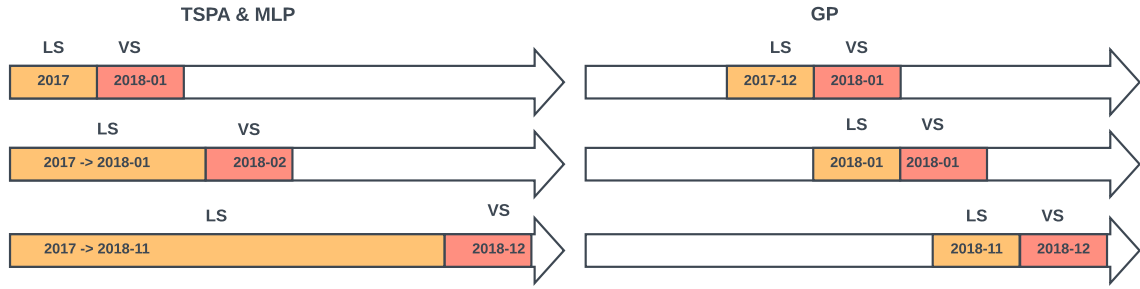


Fig. 7.4 Rolling forecast strategy.

k	Technique	NMAE	NRMSE	PLF	CRPS
15 min	MLP	52.74	84.37	-	-
	GP	61.33	98.59	16.48	32.64
	TSPA	61.91	101.24	16.07	31.84
60 min	MLP	61.85	97.26	-	-
	GP	62.13	101.14	16.09	31.87
	TSPA	66.47	105.43	15.22	30.15
360 min	MLP	72.64	112.90	-	-
	GP	72.61	114.56	14.79	29.29
	TSPA	73.35	114.2	14.2	28.12

Table 7.1 Average scores over all lead times k .

Error (NRMSE) of the mean predicted imbalance prices. The scores $NMAE(k)$, $NRMSE(k)$, $PLF(k)$, and $CRPS(k)$ for a lead time k are computed over the entire validation set. The normalizing coefficient for both the NMAE and NRMSE is 55.02 €/MWh, the mean of the absolute value of the imbalance prices over 2018.

The forecaster computes the mean and standard deviation of the imbalance prices per market period. Then, from a Gaussian distribution, samples are generated and the percentiles $1, \dots, 99$ are derived. These percentiles are used to compute the PLF. The CRPS is computed using the *crps_gaussian* function of the Python *proprscoring*³ library. Table 7.1 presents the average scores over all lead times k for the horizons of 15, 60 and 360 minutes. Figure 7.5a provides the average scores over all lead times k for each forecasting horizon, and Figure 7.5b depicts the score per lead time k for the forecasting horizon of 360 minutes.

³<https://pypi.org/project/proprscoring/>

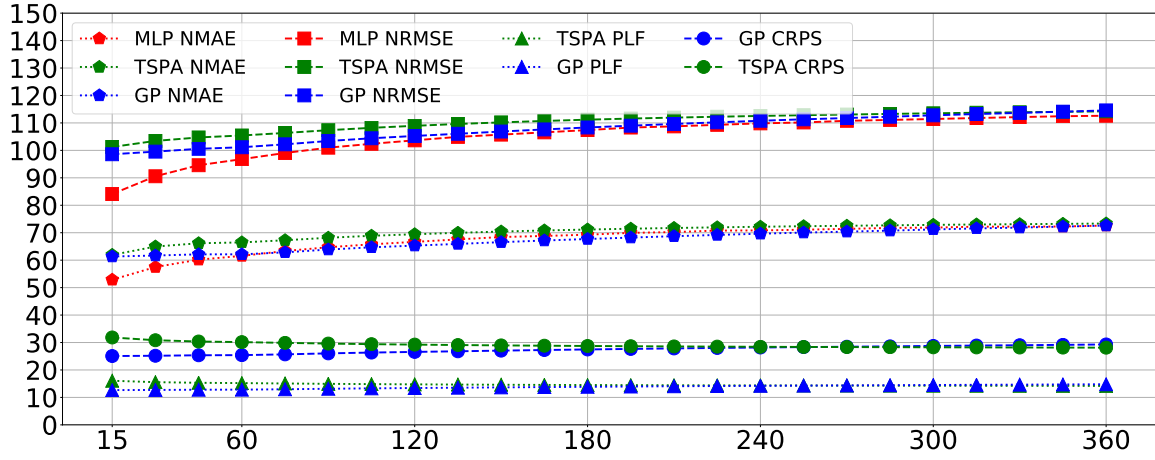
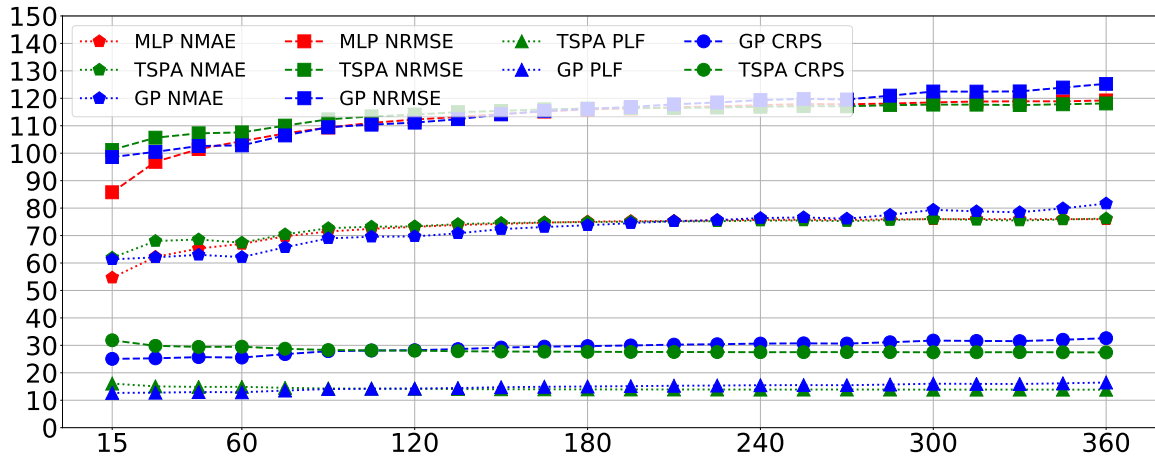
(a) Average scores over all lead times k for each forecasting horizon.(b) Score per lead time k for the forecasting horizon of 360 minutes.

Fig. 7.5 Scores.

Two days, depicted in Figure 7.6, from the validation set are selected to illustrate the results. On *January 8, 2019*, the ELIA system was short on average, leading to a high NRV and imbalance prices. On *January 10, 2019*, the ELIA system was alternatively short and long leading to fluctuating NRV and imbalance prices. The 15 minutes horizon forecasts are depicted in Figure 7.7, where only the last forecasted value for each quarter is shown. The 60 and 360 minutes horizon forecasts are depicted in Figures 7.8 and 7.9 in Appendix 7.6.3. On *January 8, 2019* the GP provides better results on average as it follows more accurately the actual prices. On *January 10, 2019*, there is no clear winner. Other figures are reported in Appendix 7.6.3 for other forecasting horizons. The MLP provides the best NMAE and NRMSE, except for the horizon of 360 minutes, and the TSPA the best CRPS and PLF scores for the three

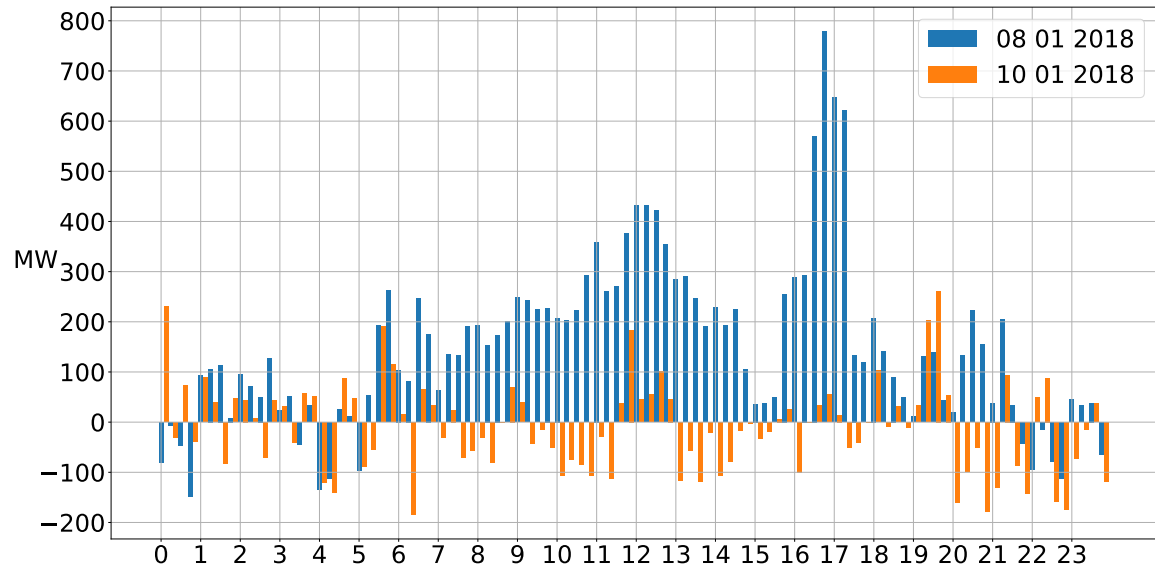


Fig. 7.6 ELIA NRV on *January 8, 2019* (blue) and *January 10, 2019* (orange).

forecasting horizons considered. However, to select the best forecasting model it would be necessary to measure the accuracy of the global bidding chain composed of the forecasting and decision-making modules.

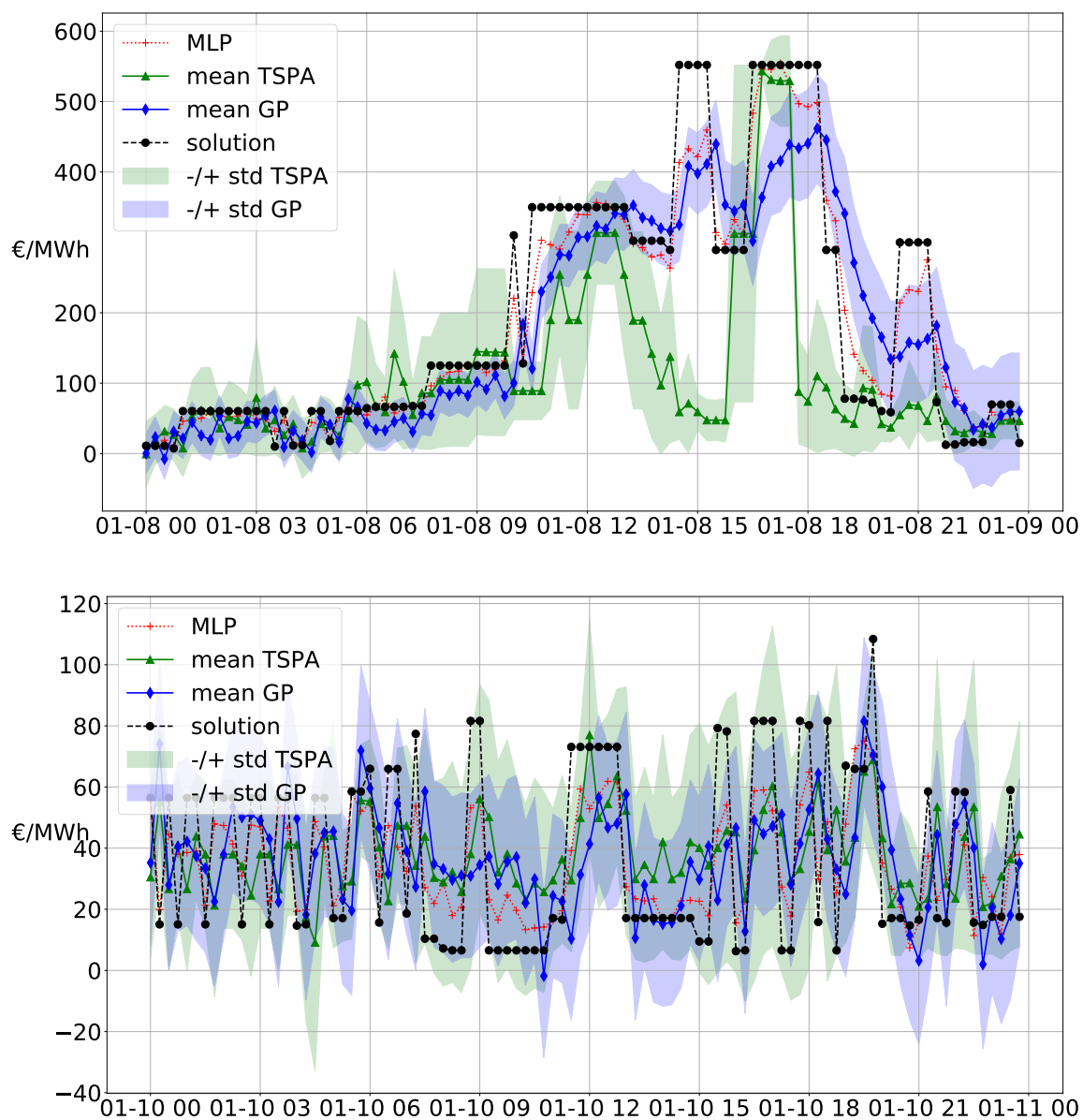


Fig. 7.7 MLP, GP and TSPA 15 minutes horizon forecasts on *January 8, 2019* (top) and *January 10, 2019* (bottom).

7.5 Conclusions

This study addressed the problem of forecasting the imbalance prices in a probabilistic framework. The novel two-step probabilistic approach consists of the first step to compute the net regulation volume state transition probabilities. It is used in the second step to infer the imbalance price from the ELIA ARC table and computes a probabilistic forecast. A numerical comparison of this approach to MLP and GP forecasting techniques is performed on the Belgium case. This approach outperforms other approaches on probabilistic error measures but is less accurate at predicting the precise imbalance prices.

This novel probabilistic approach could be improved by learning models to avoid making our simplifying assumptions, by adding input features to better describe the market situation, and by extending the approach to implement the whole bidding strategy chain, which would allow determining which approach is the best.

Appendix: notation

Acronyms

ARC	Available Regulation Capacity
BRP	Balancing Responsible Party
GP	Gaussian Processes
GDV	Gross Downward regulation Volume
GUV	Gross Upward regulation Volume
IGCC	International Grid Control Cooperation
MDP	Marginal price for Downward Regulation
metric	NMAE, NRMSE, PLF, CRPS
MIMO	Multi-Input Multi-Output
MIP	Marginal price for Upward Regulation
NRV	Net Regulation Volume
R2	Secondary reserve, upwards or downwards
TSO	Transmission System Operator
TSPA	Two-Step Probabilistic Approach

Parameters

Symbol	Description	Unit
π_+, π_-	Positive/Negative imbalance price	€/MWh
α_1, α_2	ELIA parameters for π_+ and π_-	€/MWh
c_t^p	ARC marginal price at t and for activation range p	€/MWh
$v(t)$	NRV measured at time t	MW
v_i	NRV bin i	MW
$v_{i,1/2}$	Center of NRV bin i	MW
$(v)_{t+k t}$	NRV transition matrix from t to $t+k$	-
$p_{t+k t}^{ij}$	NRV conditional probabilities at t for $t+k$	-

Forecasted or computed variables

Symbol	Description	Unit
$\hat{\pi}_{t+k t}^m$	Predicted mean imbalance price at t for $t+k$	€/MWh
$\hat{\pi}_{t+k t}^{std}$	Standard deviation of $\hat{\pi}_{t+k t}^m$ at t for $t+k$	€/MWh
$\hat{\pi}_{>t}$	Set $\left\{ (\hat{\pi}_{t+k t}^m, \hat{\pi}_{t+k t}^{std}) \right\}_{k=k_1}^{k_T}$	€/MWh

$\hat{v}_{t+k t}^m$	Predicted mean NRV at t for $t + k$	MW
$\hat{v}_{t+k t}^{std}$	Standard deviation of $\hat{v}_{t+k t}^m$ at t for $t + k$	MW
$(\hat{v})_{t+k t}$	Estimated NRV transition matrix from t to $t + k$	-
$(\hat{v})_{>t}$	Set $\left\{ (\hat{v})_{t+k t} \right\}_{k=k_1}^{k_T}$	-
$\hat{p}_{t+k t}^{ij}$	Estimated NRV conditional probability at t for $t + k$	-

7.6 Appendix: balancing mechanisms

7.6.1 Balancing mechanisms

A balancing mechanism is designed to maintain the balance over a given geographical area and to control sudden imbalances between injection and off-take. Generally, this mechanism relies on exchanges with neighboring TSOs, the balance responsible parties, and the usage of reserve capacities. Each party that desires to inject or off-take to the grid must be managed by a Balancing Responsible Party (BRP). The BRP is responsible for balancing all off-takes and injections within its customer's portfolio. The TSO applies an imbalance tariff when it identifies an imbalance between total physical injections, imports, and purchases on the one hand and total off-takes, exports, and sales on the other. When the BRPs are unable to balance their customer's portfolios, the TSO activates reserves to balance the control area. These reserves are mainly from conventional power plants, which can be quickly activated upward or downward to cover real-time system imbalances. The main types of reserve are the Frequency Containment Reserve (FCR), the Automatic Frequency Restoration Reserve (aFRR), the Manual Frequency Restoration Reserve (mFRR), and the Replacement Reserve (RR)⁴. The activation of these reserves results from a merit order representing the activation cost of reserve capacity. If the system faces a power shortage, the TSO activates upward reserves that result in a positive marginal price on the reserve market. Then, the TSO pays the Balancing Service Provider. The cost of this activation is transferred to the BRPs. BRPs facing short positions are reinforcing the system imbalance. They must pay the marginal price to the TSO. BRPs facing long positions are restoring the system imbalance. They receive the marginal price from the TSO. This mechanism incentives market players to maintain their portfolios in balance, as well as to reduce the net system imbalance.

⁴<https://www.entsoe.eu/>

7.6.2 Belgium balancing mechanisms

This section describes the ELIA imbalance price mechanisms and the data publication that is part of the TSPA inputs. On a 15 minutes basis, the NRV is defined as the sum of the GUV and GDV. The Gross Upward Volume (GUV) is the sum of the volumes of all upward regulations. The Gross Downward Volume (GDV) the sum of the volumes of all downward regulations. If the NRV is positive, the highest price of all upward activated products, the Marginal price for Upward Regulation (MIP), is applied for the imbalance price calculation. If the NRV is negative, the lowest price of all downward activated products, the Marginal price for Downward Regulation (MDP), is applied. The definitions of the positive π_+ and negative π_- imbalance prices are provided in Table 7.2. The correction parameters α_1 and α_2 are zero when the system imbalance is lower than 140 MW and proportional to it when greater than 140 MW.

The MIP and MDP prices are most of the time in the third Available Regulation Capacity (ARC) table. The ARC publication takes into account the applicable merit order, i.e. the order in which Elia must activate the reserve products. Then, within a given priority level, the volumes are ranked by activation price (cheapest first). The marginal price is the highest price for every extra MW upward volume and the lowest price for every extra MW downward volume. The ARC table, showing the activation price of the contracted reserves per activation range of 100 MW, displays the estimated activation price considering a certain NRV. For a given quarter-hour t there are P marginal prices for activation c_t^p , $p \in \llbracket 1; P \rrbracket$, each one of them related to the activation range p . P is equal to 22 with 11 negatives ranges and 11 positives ranges. The first activation range, $p = 1$, corresponds to the interval $[-\infty, -1000]$ MW, the second one to $[-1000, -900]$, ..., $[-100, 0]$, $[0, 100]$ up to $[1000, +\infty]$. The data of day D are published on $D - 1$ at 6 pm based on the nomination of day-ahead and intraday programs and bids submitted by the concerned parties. The values, of each quarter-hour of the day, are refreshed quarterly. Therefore, the published values are an estimation. However, they are likely to include the MIP and MDP prices at the condition to determine the NRV and its spread between the GUV and GDV. The TSPA takes as input the third ARC table to determine the most probable MIP and MDP prices.

7.6.3 Additional results

BRP perimeter	$NRV < 0$	$NRV > 0$
> 0	$\pi_+ = MDP - \alpha_1$	$\pi_+ = MIP$
< 0	$\pi_- = MDP$	$\pi_- = MIP + \alpha_2$

Table 7.2 Elia imbalance prices.

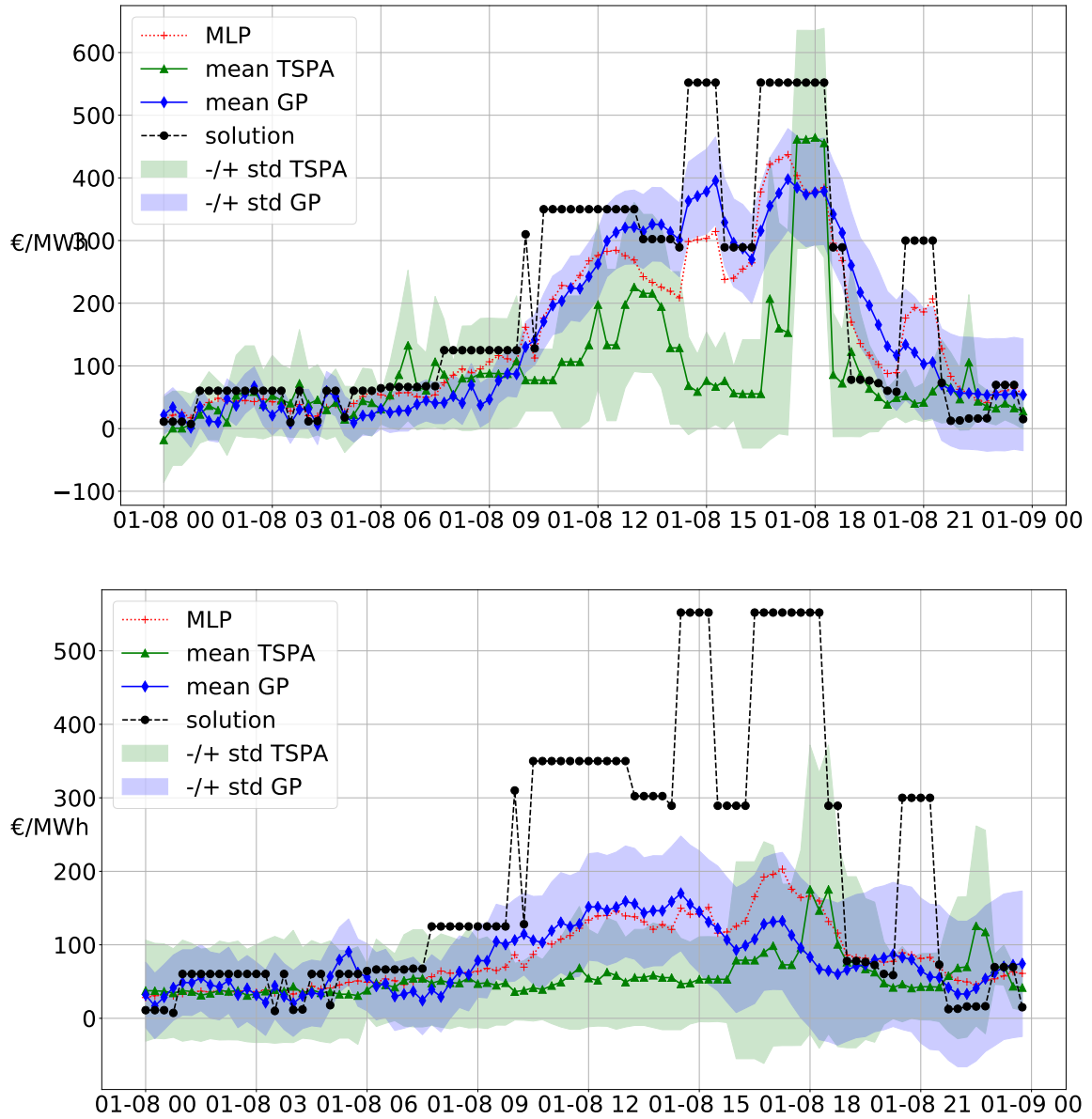


Fig. 7.8 MLP, GP and TSPA 60 (top) and 360 (bottom) minutes horizon forecasts on January 8, 2019.

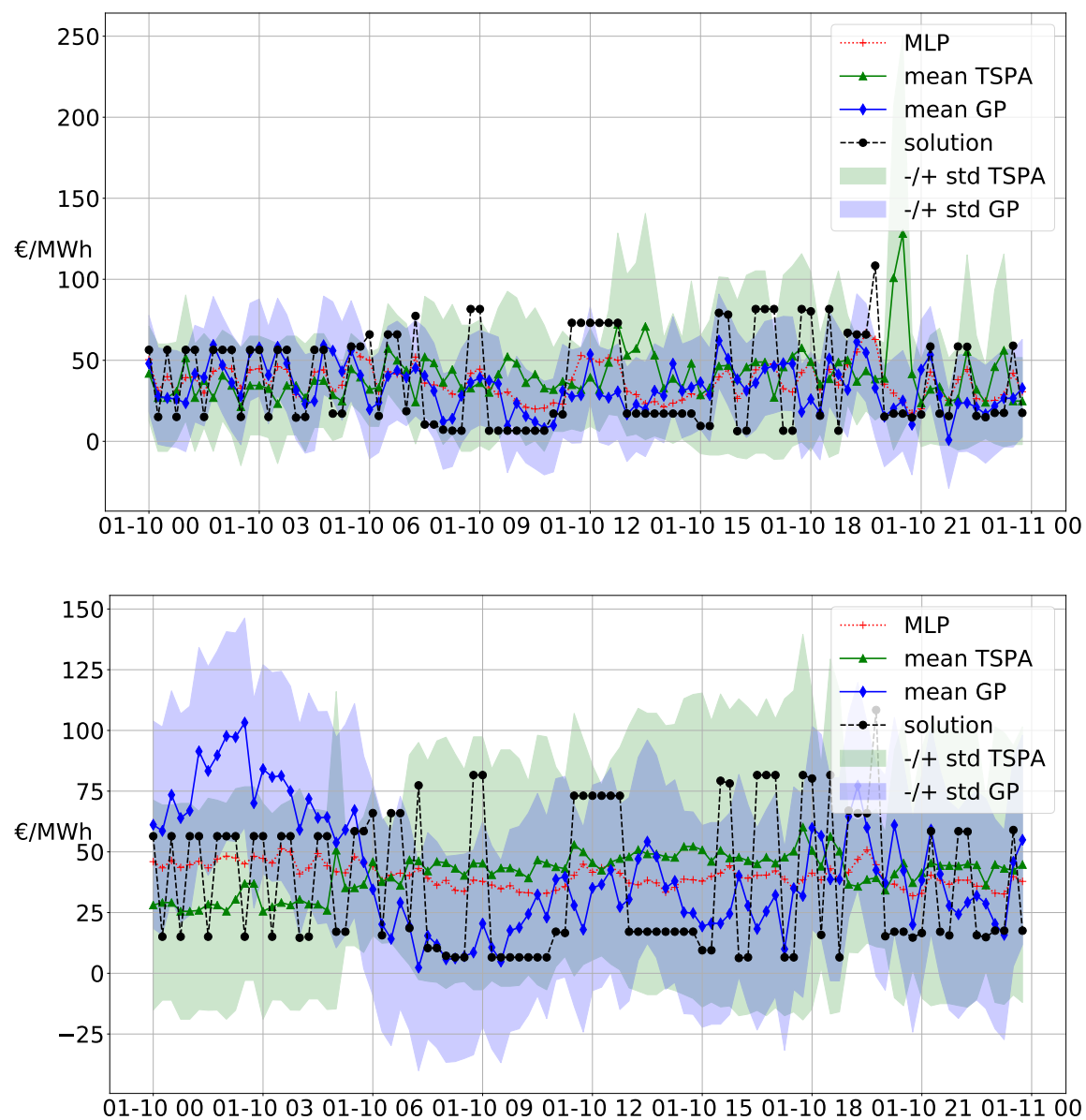


Fig. 7.9 MLP, GP and TSPA 60 (top) and 360 (bottom) minutes horizon forecasts on *January 10, 2019*.

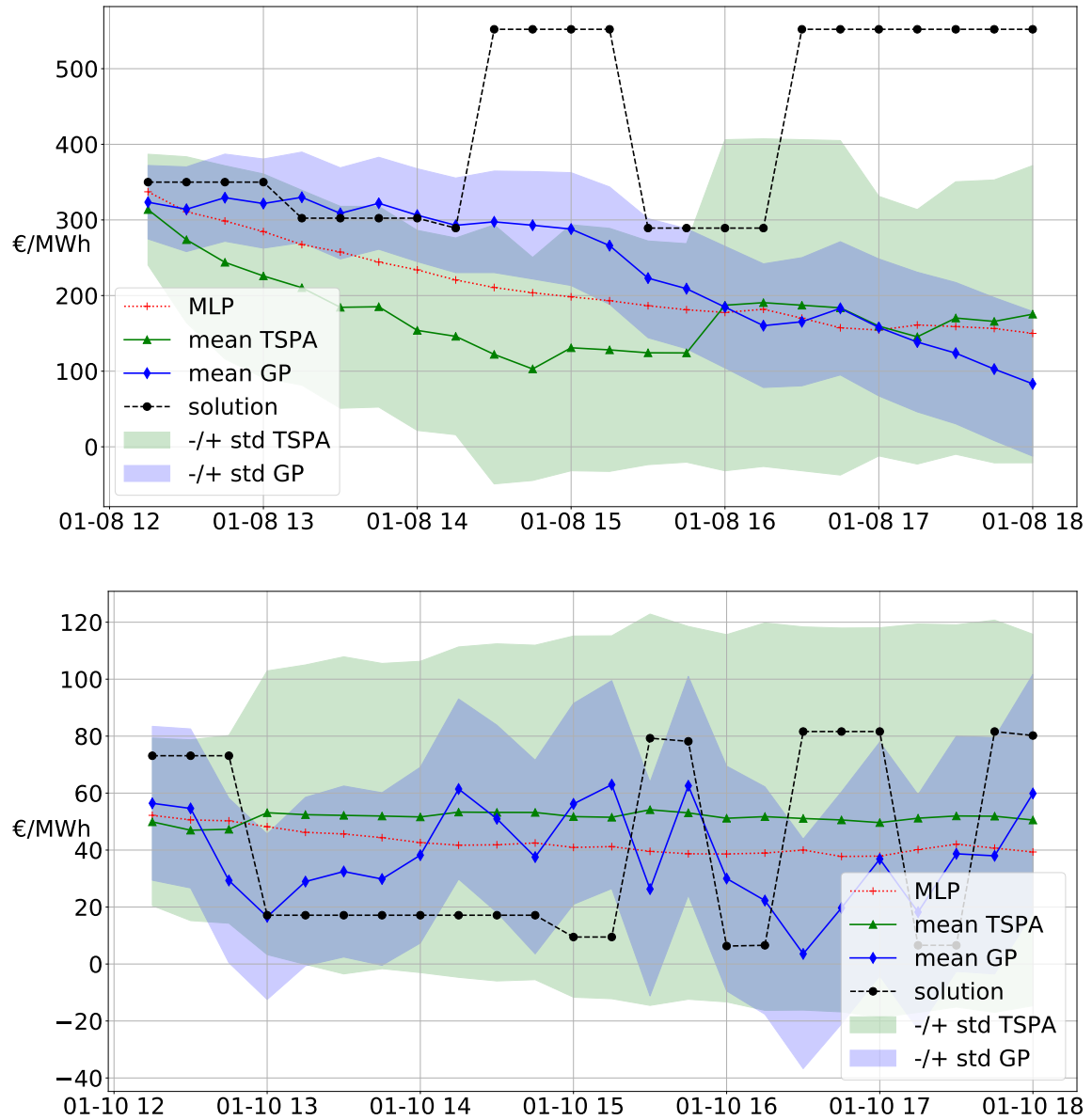


Fig. 7.10 MLP, GP and TSPA forecasts on *January 8, 2019* (top) and *January 10, 2019* (bottom), 12h00 UTC, with an horizon of 360 minutes.

Chapter 8

Scenarios

Overview

The main contributions of this Chapter are three-fold:

1. We provide a fair comparison both in terms of quality and value with the state-of-the-art deep learning generative models, Generative Adversarial Networks (GANs) and Variational AutoEncoders (VAEs), using the open data of the Global Energy Forecasting Competition 2014 (GEFcom 2014) [75]. To the best of our knowledge it is the first study that extensively compares the Normalizing Flows (NFs), GANs, and VAEs on several datasets, PV generation, wind generation, and load with a proper assessment of the quality and value based on complementary metrics, and an easily reproducible case study;
2. We implement conditional generative models to compute improved weather-based PV, wind power, and load scenarios. In contrast to most of the previous studies that focused mainly on past observations;
3. Overall, we demonstrate that NFs are more accurate both in terms of quality and value, providing further evidence for deep learning practitioners to implement this approach in more advanced power system applications.

This study provides [open-access to the Python code^a](#).

References: This chapter is an adapted version of the following publication:

Jonathan Dumas, Antoine Wehenkel, Damien Lanaspeze, Bertrand Cornélusse, and Antonio Sutera. Deep generative modeling for probabilistic forecasting in power systems. Manuscript submitted for publication to Applied Energy, 2021. URL <https://arxiv.org/abs/2106.09370>.

Terminology and notations have been slightly adjusted for the sake of consistency with the rest of this manuscript. The text has also been processed to minimize overlap with respect to the other chapters.

^a**TODO**

“I won’t say ‘See you tomorrow’ because that would be like predicting the future, and I’m pretty sure I can’t do that.”

— Ludwig Wittgenstein

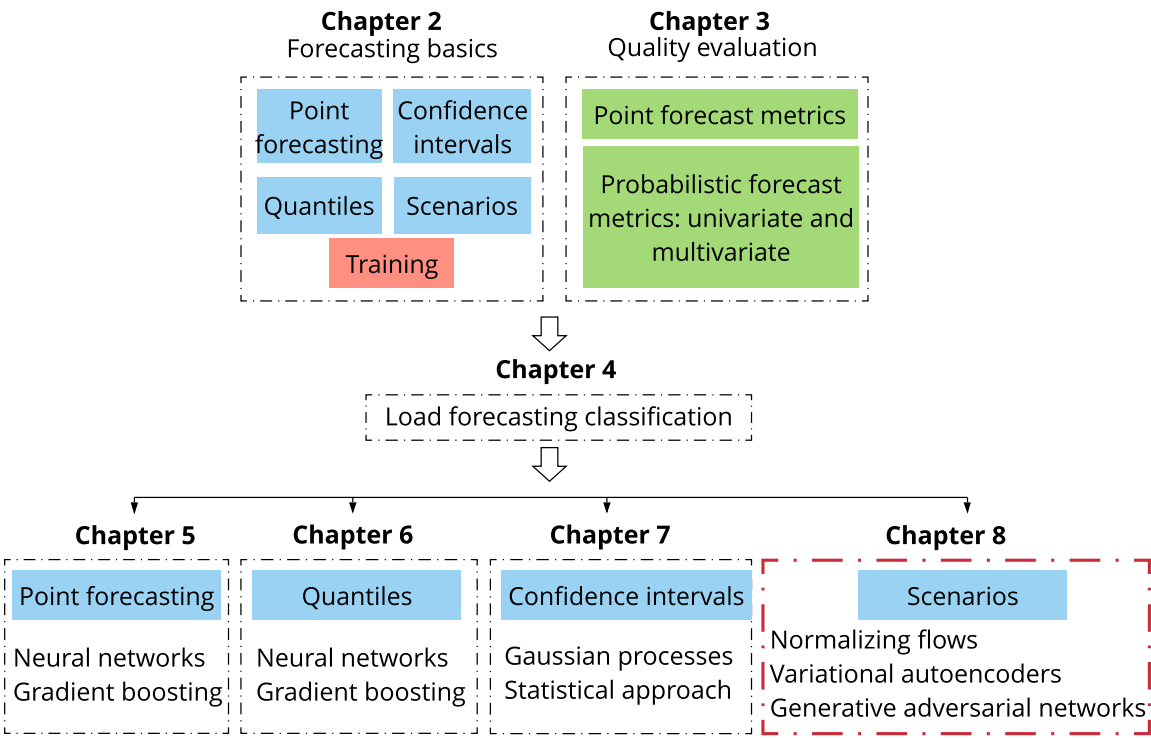


Fig. 8.1 Chapter 8 position in Part I.

8.1 Introduction

This Chapter focuses on *scenario generation*, a popular probabilistic forecasting method to capture the uncertainty of load, photovoltaic (PV) generation, and wind generation. It consists of producing sequences of possible load or power generation realizations for one or more locations.

Forecasting methodologies can typically be classified into two groups: *statistical* and *machine learning* models. On the one hand, statistical approaches are said to be more interpretable than machine learning techniques sometimes referred to as black-box models. On the other hand, they are generally more robust, user-friendly, and successful in addressing the non-linearity in the data than statistical techniques. We provide in the following a few examples of statistical approaches. More references can be found in Khoshrou and Pauwels [86] and Mashlakov et al. [102].

Multiple linear regression models [148] and autoregressive integrated moving average [34] are among the most fundamental and widely-used models. For instance, an autoregressive moving average model is used by Morales et al. [104] to generate spatiotemporal scenarios with given power generation profiles at each renewables generation site. These models mostly learn a relationship between several explanatory variables and a dependent target variable. Therefore, the performance of such models is only satisfactory if the dependent variables are well formulated based on explanatory variables. However, they require some expert knowledge to formulate the relevant interaction between different variables. Another class of statistical approaches consists of using simple parametric distributions, *e.g.*, the Weibull distribution for wind speed [83], or the beta distribution for solar irradiance [84] to model the density associated with the generative process. In this line, the (Gaussian) copula method has been widely used to model the spatial and temporal characteristics of wind [124] and PV generation [160]. For instance, the problem of generating probabilistic forecasts for the aggregated power of a set of renewable power plants harvesting different energy sources is addressed by Camal et al. [26].

Overall, these approaches usually make statistical assumptions increasing the difficulty to model the underlying stochastic process. The generated scenarios approximate the future uncertainty but cannot correctly describe all the salient features in the power output from renewable energy sources. *Deep learning* is one of the newest trends in artificial intelligence and machine learning to tackle the limitations of statistical methods with promising results across various application domains.

8.1.1 Related work

Recurrent neural networks (RNNs) are one of the most famous deep learning techniques adopted in energy forecasting applications. A novel pooling-based deep recurrent neural network is proposed by Shi et al. [136] in the field of short-term household load forecasting. It outperforms statistical approaches such as autoregressive integrated moving average and classical RNN. A tailored forecasting tool, named encoder-decoder, is implemented in Dumas et al. [44] to compute intraday multi-output PV quantiles forecasts. Guidelines and best practices are developed by Hewamalage et al. [73] for forecasting practitioners on an extensive empirical study with an open-source software framework of existing RNN architectures. In the continuity, Toubreau et al. [143] implemented a bidirectional long short-term memory (BLSTM) architecture. It is trained using quantile regression and combined with a copula-based approach to generate scenarios. This methodology is compared with other models in terms of forecast quality and value using a scenario-based stochastic optimization case study. Finally, Salinas et al. [133] trained an autoregressive recurrent neural network on several real-world datasets producing accurate probabilistic forecasts with little or no hyper-parameter tuning.

Deep generative modeling is a class of techniques that trains deep neural networks to model the distribution of the observations. In recent years, there has been a growing interest in this field made possible by the appearance of large open-access datasets and breakthroughs in both general deep learning architectures and generative models. Several approaches exist such as energy-based models, variational autoencoders, generative adversarial networks, autoregressive models, normalizing flows, and numerous hybrid strategies. They all make trade-offs in terms of computation time, diversity, and architectural restrictions. We recommend two papers to get a broader knowledge of this field. (1) The comprehensive overview of generative modeling trends conducted by Bond-Taylor et al. [21]. It presents generative models to forecasting practitioners under a single cohesive statistical framework. (2) The thorough comparison of normalizing flows, variational autoencoders, and generative adversarial networks provided by Ruthotto and Haber [130]. It describes the advantages and disadvantages of each approach using numerical experiments in the field of computer vision. In the following, we focus on the applications of generative models in power systems.

In contrast to statistical approaches, deep generative models such as *Variational AutoEncoders* (VAEs) [88] and *Generative Adversarial Networks* (GANs) [65] directly learn a generative process of the data. They have demonstrated their effectiveness in many applications to compute accurate probabilistic forecasts including power system

applications. They both make probabilistic forecasts in the form of Monte Carlo samples that can be used to compute consistent quantile estimates for all sub-ranges in the prediction horizon. Thus, they cannot suffer from the issue raised by Ordiano et al. [112] on the non-differentiable quantile loss function. Note that generative models such as GANs and VAEs allow to directly generate scenarios of the variable of interest. In contrast with methods that first compute weather scenarios to generate probabilistic forecasts such as implemented by Sun et al. [139] and Khoshrou and Pauwels [86]. A VAE composed of a succession of convolutional and feed-forward layers is proposed by Zhanga et al. [162] to capture the spatial-temporal complementary and fluctuant characteristics of wind and PV power with high model accuracy and low computational complexity. Both single and multi-output PV forecasts using a VAE are compared by Dairi et al. [32] to several deep learning methods such as LSTM, BLSTM, convolutional LSTM networks and stacked autoencoders, where the VAE consistently outperformed the other methods. A GAN is used by Chen et al. [28] to produce a set of wind power scenarios that represent possible future behaviors based only on historical observations and point forecasts. This method has a better performance compared to Gaussian Copula. A Bayesian GAN is introduced by Chen et al. [27] to generate wind and solar scenarios, and a progressive growing of GANs is designed by Yuan et al. [155] to propose a novel scenario forecasting method. In a different application, a GAN is implemented for building occupancy modeling without any prior assumptions [29]. Finally, a conditional version of the GAN using several labels representing some characteristics of the demand is introduced by Lan et al. [94] to output power load data considering demand response programs.

Improved versions of GANs and VAEs have also been studied in the context of energy forecasting. The Wasserstein GAN consists of enforcing the Lipschitz continuity through a gradient penalty term (WGAN-GP), as the original GANs are challenging to train and suffer from mode collapse and over-fitting. Several studies applied this improved version in power systems: (1) a method using unsupervised labeling and conditional WGAN-GP models the uncertainties and variation in wind power [161]; (2) a WGAN-GP models both the uncertainties and the variations of the load [150]; (3) Jiang et al. [79] implemented scenario generation tasks both for a single site and for correlated multiple sites without any changes to the model structure. Concerning VAEs, they suffer from inherent shortcomings such as the difficulties to tune the hyper-parameters or to generalize a specific generative model structure to other databases. An improved VAE is proposed by Qi et al. [126] with the implementation of a β

hyper-parameter into the VAE objective function to balance the two parts of the loss. This improved VAE is used to generate PV and power scenarios from historical values.

However, most of these studies did not benefit from conditional information such as weather forecasts to generate improved PV power, wind power, and load scenarios. In addition, to the best of our knowledge, only Ge et al. [53] compared NFs to these techniques for the generation of daily load profiles. Nevertheless, the comparison only considers quality metrics, and the models do not incorporate weather forecasts.

8.1.2 Research gaps and scientific contributions

This study investigates the implementation of *Normalizing Flows* [128, NFs] in power system applications. NFs define a new class of probabilistic generative models that has gained increasing interest from the deep learning community in recent years. A NF learns a sequence of transformations, a *flow*, from a density known analytically, *e.g.*, a *Normal* distribution, to a complex target distribution. In contrast to other deep generative models, NFs can directly be trained by maximum likelihood estimation. They have proven to be an effective way to model complex data distributions with neural networks in many domains such as speech synthesis [111], fundamental physics to increase the speed of gravitational wave inference by several orders of magnitude [67] or for sampling Boltzmann distributions of lattice field theories [3], and have been applied in the capacity firming framework by Dumas et al. [45].

This present work goes several steps further than Ge et al. [53] that demonstrated the competitiveness of NFs regarding GANs and VAEs for generating daily load profiles. First, we study the conditional version of these models to demonstrate they can handle additional contextual information such as weather forecasts or geographical locations. Second, we extensively compare the model's performances both in terms of forecast value and quality. The forecast quality corresponds to the ability of the forecasts to genuinely inform of future events by mimicking the characteristics of the processes involved. The forecast value relates to the benefits from using forecasts in a decision-making process such as participation in the electricity market. Third, we consider PV and wind generations in addition to load profiles. Finally, in contrast to the affine NFs used in their work, we rely on monotonic transformations which are universal density approximators [77].

Given the statement that Normalizing Flows are rarely used in the power systems community despite their potential, our main aim is to present this recent deep learning technique and to demonstrate its interest and competitiveness with state-of-the-art

generative models such as GANs and VAEs on a simple and easily reproducible case study. The research gaps motivating this study are three-fold:

1. To the best of our knowledge, only Ge et al. [53] compared NFs to GANs and VAEs for the generation of daily load profiles. Nevertheless, the comparison is only based on quality metrics, and the models do not take into account weather forecasts;
2. Most of the studies that propose or compare forecasting techniques only consider the forecast quality such as Ge et al. [53], Sun et al. [139], and Mashlakov et al. [102];
3. The conditional versions of the models are not always addressed such as in Ge et al. [53]. However, weather forecasts are essential for computing accurate probabilistic forecasts.

With these research gaps in mind, the main contributions of this Chapter are three-fold:

1. We provide a fair comparison both in terms of quality and value with the state-of-the-art deep learning generative models, GANs and VAEs, using the open data of the Global Energy Forecasting Competition 2014 (GEFcom 2014) [75]. To the best of our knowledge it is the first study that extensively compares the NFs, GANs, and VAEs on several datasets, PV generation, wind generation, and load with a proper assessment of the quality and value based on complementary metrics, and an easily reproducible case study;
2. We implement conditional generative models to compute improved weather-based PV, wind power, and load scenarios. In contrast to most of the previous studies that focused mainly on past observations;
3. Overall, we demonstrate that NFs are more accurate both in terms of quality and value, providing further evidence for deep learning practitioners to implement this approach in more advanced power system applications.

In addition to these contributions, this study also provides open-access to the Python code¹ to help the community to reproduce the experiments. Figure 8.2 provides the framework of the proposed method and Table 8.1 presents a comparison of the present study to three state-of-the-art papers using deep learning generative models to generate scenarios.

¹[TODO](#)

Criteria	[150]	[126]	[53]	study
GAN	✓	×	✓	✓
VAE	×	✓	✓	✓
NF	×	×	✓	✓
Number of models	4	1	3	3
PV	×	✓	×	✓
Wind power	×	✓	×	✓
Load	✓	~	✓	✓
Weather-based	✓	×	×	✓
Quality assessment	✓	✓	✓	✓
Quality metrics	5	3	5	8
Value assessment	×	✓	×	✓
Open dataset	~	×	✓	✓
Value replicability	-	~	-	✓
Open-access code	×	×	×	✓

Table 8.1 Comparison of the study’s contributions to three state-of-the-art studies using deep generative models.

✓: criteria fully satisfied, ~: criteria partially satisfied, ×: criteria not satisfied, ?: no information, -: not applicable. GAN: a GAN model is implemented; VAE: a VAE model is implemented; NF: a NF model is implemented; PV: PV scenarios are generated; Wind power: wind power scenarios are generated; Load: load scenarios are generated; Weather-based: the model generates weather-based scenarios; Quality assessment: a quality evaluation is conducted; Quality metrics: number of quality metrics considered; Value assessment: a value evaluation is considered with a case study; Open dataset: the data used for the quality and value evaluations are in open-access; Value replicability: the case study considered for the value evaluation is easily reproducible; Open-access code: the code used to conduct the experiments is in open-access. Note: the justifications are provided in 8.7.

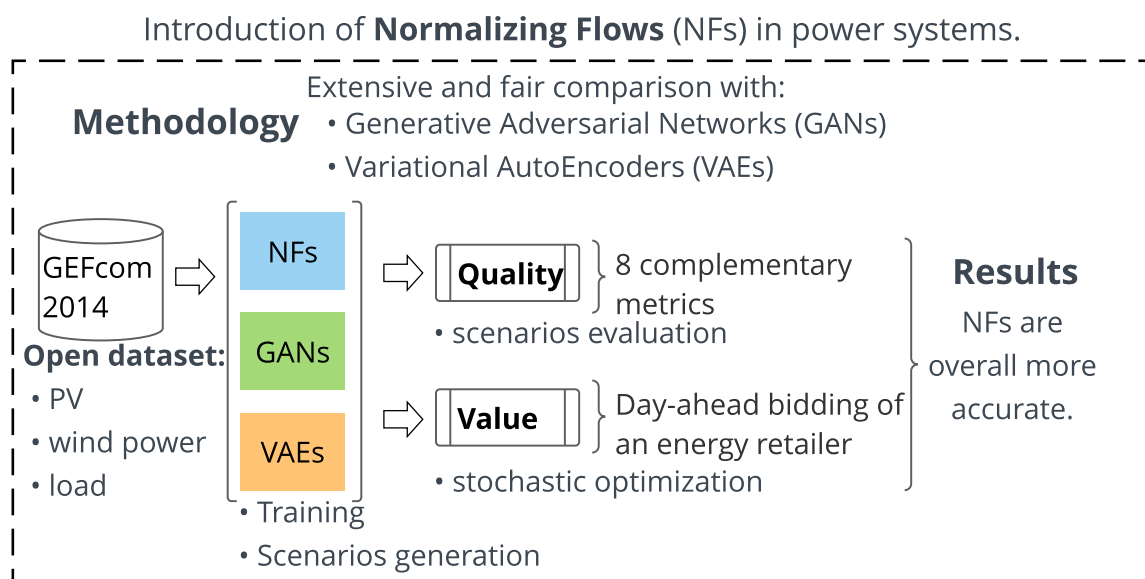


Fig. 8.2 The framework of the study.

The Chapter's main purpose is to present and demonstrate the potential of NFs in power systems. A fair comparison is conducted both in terms of quality and value with the state-of-the-art deep learning generative models, GANs and VAEs, using the open data of the Global Energy Forecasting Competition 2014 [75]. The PV, wind power, and load datasets are used to assess the models. The quality evaluation is conducted by using eight complementary metrics, and the value assessment by considering the day-ahead bidding of an energy retailer using stochastic optimization. Overall, NFs tend to be more accurate both in terms of quality and value and are competitive with GANs and VAEs.

8.1.3 Applicability of the generative models

Probabilistic forecasting of PV, wind generation, electrical consumption, and electricity prices plays an important role in renewable integration and power system operations. The deep learning generative models presented in this Chapter can be integrated into practical engineering applications. We present a non-exhaustive list of five applications in the following. (1) The forecasting module of an energy management system (EMS) [137]. Indeed, EMSs are used by several energy market players to operate various power systems such as a single renewable plant, a grid-connected or off-grid microgrid composed of several generation, consumption, and storage devices. An EMS is composed of several key modules: monitoring, forecasting, planning, control, *etc.* The forecasting module aims to provide the most accurate forecast of the variable of interest to be used as inputs of the planning and control modules. (2) Stochastic unit commitment models that employ scenarios to model the uncertainty of weather-dependent renewables. For instance, the optimal day-ahead scheduling and dispatch of a system composed of renewable plants, generators, and electrical demand are addressed by Camal et al. [26]. (3) Ancillary services market participation. A virtual power plant aggregating wind, PV, and small hydropower plants is studied by Camal et al. [26] to optimally bid on a day-ahead basis the energy and automatic frequency restoration reserve. (4) More generally, generative models can be used to compute scenarios for any variable of interest, *e.g.*, energy prices, renewable generation, loads, water inflow of hydro reservoirs, as long as data are available. (5) Finally, quantiles can be derived from scenarios and used in robust optimization models such as in the capacity firming framework [45].

8.1.4 Organization

The remainder of this Chapter is organized as follows. Section 8.2 presents the generative models implemented: NFs, GANs, and VAEs. Section 8.3 provides the quality and assessment methodology. Section 8.5 details empirical results on the GEFcom 2014 dataset, and Section 8.6 summarizes the main findings and highlights ideas for further work. Chapter 15 in Part II provides the forecast value assessment. Appendix 8.7 presents the justifications of Table 8.1, and Appendix 8.8 provides additional information on the generative models.

8.2 Background

This section formally introduces the conditional version of NFs, GANs, and VAEs implemented in this study. We assume the reader is familiar with the neural network's basics. However, for further information Goodfellow et al. [64], Zhang et al. [158] provide a comprehensive introduction to modern deep learning approaches.

8.2.1 Multi-output forecasts using a generative model

Let us consider some dataset $\mathcal{D} = \{\mathbf{x}^i, \mathbf{c}^i\}_{i=1}^N$ of N independent and identically distributed samples from the joint distribution $p(\mathbf{x}, \mathbf{c})$ of two continuous variables X and C . X being the wind generation, PV generation, or load, and C the weather forecasts. They are both composed of T periods per day, with $\mathbf{x}^i := [x_1^i, \dots, x_T^i]^\top \in \mathbb{R}^T$ and $\mathbf{c}^i := [c_1^i, \dots, c_T^i]^\top \in \mathbb{R}^T$. The goal of this work is to generate multi-output weather-based scenarios $\hat{\mathbf{x}} \in \mathbb{R}^T$ that are distributed under $p(\mathbf{x}|\mathbf{c})$.

A generative model is a probabilistic model $p_\theta(\cdot)$, with parameters θ , that can be used as a generator of the data. Its purpose is to generate synthetic but realistic data $\hat{\mathbf{x}} \sim p_\theta(\mathbf{x}|\mathbf{c})$ whose distribution is as close as possible to the unknown data distribution $p(\mathbf{x}|\mathbf{c})$. In our application, it computes on a day-ahead basis a set of M scenarios at day $d - 1$ for day d

$$\hat{\mathbf{x}}_d^i := [\hat{x}_{d,1}^i, \dots, \hat{x}_{d,T}^i]^\top \in \mathbb{R}^T \quad i = 1, \dots, M. \quad (8.1)$$

For the sake of clarity, we omit the indexes d and i when referring to a scenario $\hat{\mathbf{x}}$ in the following.

8.2.2 Deep generative models

Figure 8.3 provides a high-level comparison of three categories of generative models considered in this Chapter: Normalizing Flows, Generative Adversarial Networks, and Variational AutoEncoders.

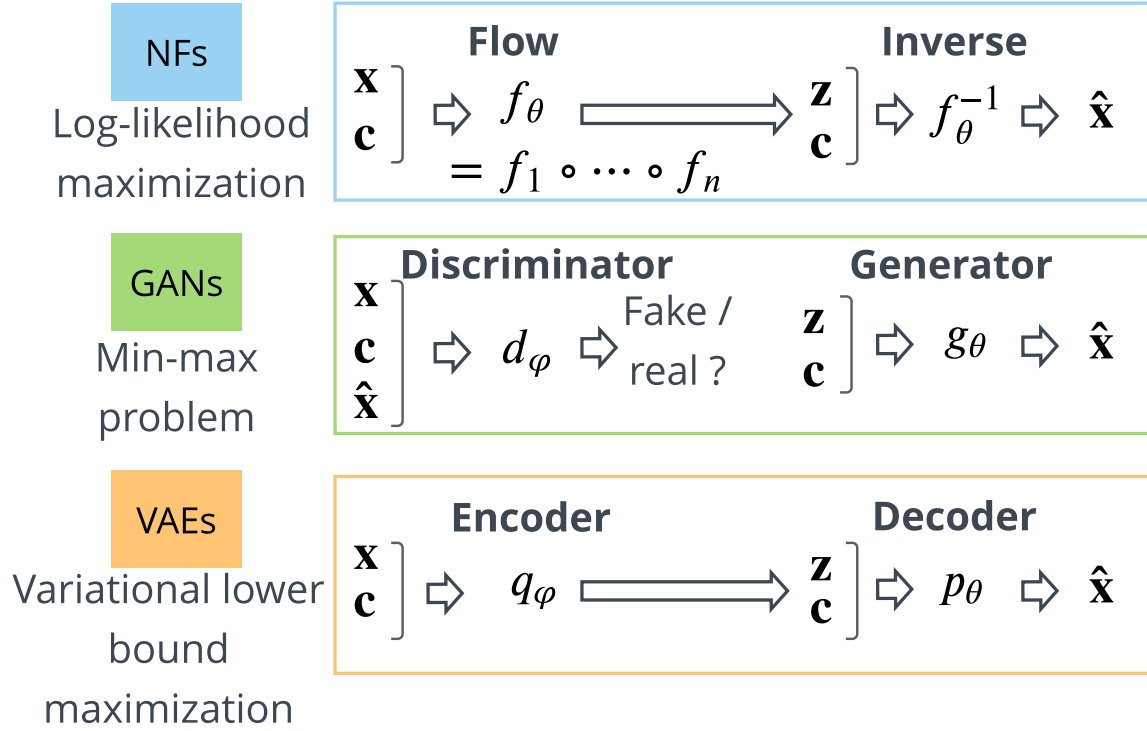


Fig. 8.3 High-level comparison of three categories of generative models considered in this Chapter: normalizing flows, generative adversarial networks, and variational autoencoders.

All models are conditional as they use the weather forecasts \mathbf{c} to generate scenarios $\hat{\mathbf{x}}$ of the distribution of interest \mathbf{x} : PV generation, wind power, load. Normalizing flows allow exact likelihood calculation. In contrast to generative adversarial networks and variational autoencoders, they explicitly learn the data distribution and provide direct access to the exact likelihood of the model's parameters. The inverse of the flow is used to generate scenarios. The training of generative adversarial networks relies on a min-max problem where the generator and the discriminator parameters are jointly optimized. The generator is used to compute the scenarios. Variational autoencoders indirectly optimize the log-likelihood of the data by maximizing the variational lower bound. The decoder computes the scenarios. Note: Section 8.2.3 provides a theoretical comparison of these models.

Normalizing flows

A normalizing flow is defined as a sequence of invertible transformations $f_k : \mathbb{R}^T \rightarrow \mathbb{R}^T$, $k = 1, \dots, K$, composed together to create an expressive invertible mapping $f_\theta := f_1 \circ \dots \circ f_K : \mathbb{R}^T \rightarrow \mathbb{R}^T$. This composed function can be used to perform density estimation, using f_θ to map a sample $\mathbf{x} \in \mathbb{R}^T$ onto a latent vector $\mathbf{z} \in \mathbb{R}^T$ equipped with a known and tractable probability density function p_z , *e.g.*, a Normal distribution. The transformation f_θ implicitly defines a density $p_\theta(\mathbf{x})$ that is given by the change of variables

$$p_\theta(\mathbf{x}) = p_z(f_\theta(\mathbf{x})) |\det J_{f_\theta}(\mathbf{x})|, \quad (8.2)$$

where J_{f_θ} is the Jacobian of f_θ regarding \mathbf{x} . The model is trained by maximizing the log-likelihood $\sum_{i=1}^N \log p_\theta(\mathbf{x}^i, \mathbf{c}^i)$ of the model's parameters θ given the dataset \mathcal{D} . For simplicity let us assume a single-step flow f_θ to drop the index k for the rest of the discussion.

In general, f_θ can take any form as long as it defines a bijection. However, a common solution to make the Jacobian computation tractable in (8.2) consists of implementing an *autoregressive* transformation [89], *i.e.*, such that f_θ can be rewritten as a vector of scalar bijections f^i

$$f_\theta(\mathbf{x}) := [f^1(x_1; h^1), \dots, f^T(x_T; h^T)]^\top, \quad (8.3a)$$

$$h^i := h^i(\mathbf{x}_{<i}; \varphi^i) \quad 2 \leq i \leq T, \quad (8.3b)$$

$$\mathbf{x}_{<i} := [x_1, \dots, x_{i-1}]^\top \quad 2 \leq i \leq T, \quad (8.3c)$$

$$h^1 \in \mathbb{R}, \quad (8.3d)$$

where $f^i(\cdot; h^i) : \mathbb{R} \rightarrow \mathbb{R}$ is partially parameterized by an autoregressive conditioner $h^i(\cdot; \varphi^i) : \mathbb{R}^{i-1} \rightarrow \mathbb{R}^{|h^i|}$ with parameters φ^i , and θ the union of all parameters φ^i .

There is a large choice of transformers f^i : affine, non-affine, integration-based, etc. In this work, an integration-based transformer is implemented by using the class of Unconstrained Monotonic Neural Networks (UMNN) proposed by Wehenkel and Louppe [151], which have been demonstrated to be a universal density approximator of continuous random variables when combined with autoregressive functions. The UMNN consists of a neural network architecture that enables learning arbitrary monotonic functions. It is achieved by parameterizing the bijection f^i as follows

$$f^i(x_i; h^i) = \int_0^{x_i} \tau^i(x_i, h^i) dt + \beta^i(h^i), \quad (8.4)$$

where $\tau^i(\cdot; h^i) : \mathbb{R}^{|h^i|+1} \rightarrow \mathbb{R}^+$ is the integrand neural network with a strictly positive scalar output, $h^i \in \mathbb{R}^{|h^i|}$ an embedding made by the conditioner, and $\beta^i(\cdot) : \mathbb{R}^{|h^i|} \rightarrow \mathbb{R}$ a neural network with a scalar output. The forward evaluation of f^i requires solving the integral (8.4) and is efficiently approximated numerically by using the Clenshaw-Curtis quadrature. The pseudo-code of the forward and backward passes is provided by Wehenkel and Louppe [151].

Papamakarios et al. [115]’s Masked Autoregressive Network (MAF) is implemented to simultaneously parameterize the T autoregressive embeddings h^i of the flow (8.3). Then, the change of variables formula applied to the UMMN-MAF transformation results in the following log-density when considering weather forecasts

$$\log p_\theta(\mathbf{x}, \mathbf{c}) = \log p_z(f_\theta(\mathbf{x}, \mathbf{c})) |\det J_{f_\theta}(\mathbf{x}, \mathbf{c})|, \quad (8.5a)$$

$$= \log p_z(f_\theta(\mathbf{x}, \mathbf{c})) + \sum_{i=1}^T \log \tau^i(x_i, h^i(\mathbf{x}_{<i}), \mathbf{c}), \quad (8.5b)$$

that can be computed exactly and efficiently with a single forward pass. The UMMN-MAF approach implemented is referred to as NF in the rest of the Chapter. Figure 8.4 depicts the process of conditional normalizing flows with a three-step NF for PV generation. Note: 8.8.1 provides additional information on NFs.

Variational autoencoders

A VAE is a deep latent variable model composed of an *encoder* and a *decoder* which are jointly trained to maximize a lower bound on the likelihood. The encoder $q_\varphi(\cdot) : \mathbb{R}^T \times \mathbb{R}^{|\mathbf{c}|} \rightarrow \mathbb{R}^d$ approximates the intractable posterior $p(\mathbf{z}|\mathbf{x}, \mathbf{c})$, and the decoder $p_\theta(\cdot) : \mathbb{R}^d \times \mathbb{R}^{|\mathbf{c}|} \rightarrow \mathbb{R}^T$ the likelihood $p(\mathbf{x}|\mathbf{z}, \mathbf{c})$ with $\mathbf{z} \in \mathbb{R}^d$. Maximum likelihood is intractable as it would require marginalizing with respect to all possible realizations of the latent variables \mathbf{z} . Kingma and Welling [88] addressed this issue by maximizing the *variational lower bound* $\mathcal{L}_{\theta, \varphi}(\mathbf{x}, \mathbf{c})$ as follows

$$\log p_\theta(\mathbf{x}|\mathbf{c}) = KL[q_\varphi(\mathbf{z}|\mathbf{x}, \mathbf{c}) || p(\mathbf{z}|\mathbf{x}, \mathbf{c})] + \mathcal{L}_{\theta, \varphi}(\mathbf{x}, \mathbf{c}), \quad (8.6a)$$

$$\geq \mathcal{L}_{\theta, \varphi}(\mathbf{x}, \mathbf{c}), \quad (8.6b)$$

$$\mathcal{L}_{\theta, \varphi}(\mathbf{x}, \mathbf{c}) := \mathbb{E}_{q_\varphi(\mathbf{z}|\mathbf{x}, \mathbf{c})} \left[\log \frac{p(\mathbf{z}) p_\theta(\mathbf{x}|\mathbf{z}, \mathbf{c})}{q_\varphi(\mathbf{z}|\mathbf{x}, \mathbf{c})} \right], \quad (8.6c)$$

as the Kullback-Leibler (KL) divergence [120] is non-negative. 8.8.2 details how to compute the gradients of $\mathcal{L}_{\theta, \varphi}(\mathbf{x}, \mathbf{c})$, and its exact expression for the implemented VAE composed of fully connected neural networks for both the encoder and decoder.

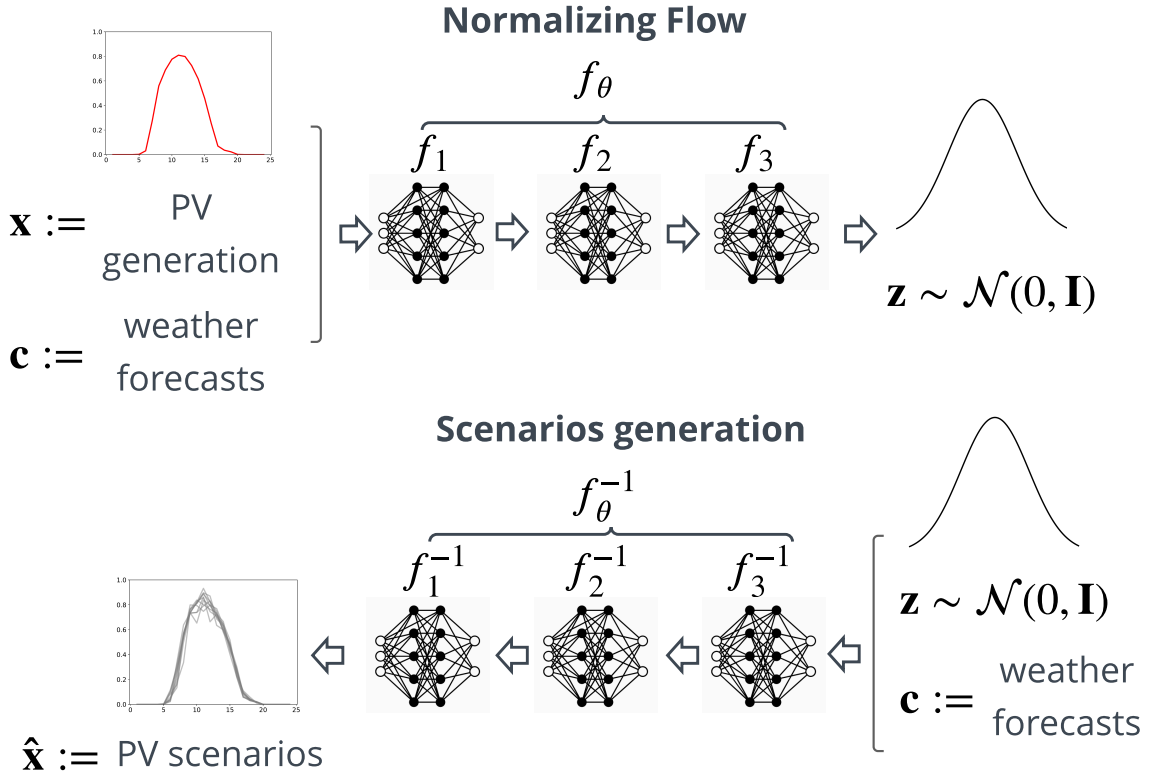


Fig. 8.4 The process of conditional normalizing flows is illustrated with a three-step NF for PV generation.

The model f_θ is trained by maximizing the log-likelihood of the model's parameters θ given a dataset composed of PV observations and weather forecasts. Recall f_θ defines a bijection between the variable of interest \mathbf{x} , PV generation, and a Normal distribution \mathbf{z} . Then, the PV scenarios $\hat{\mathbf{x}}$ are generated by using the inverse of f_θ that takes as inputs samples from the Normal distribution \mathbf{z} and the weather forecasts \mathbf{c} .

Figure 8.5 depicts the process of a conditional variational autoencoder for PV generation.

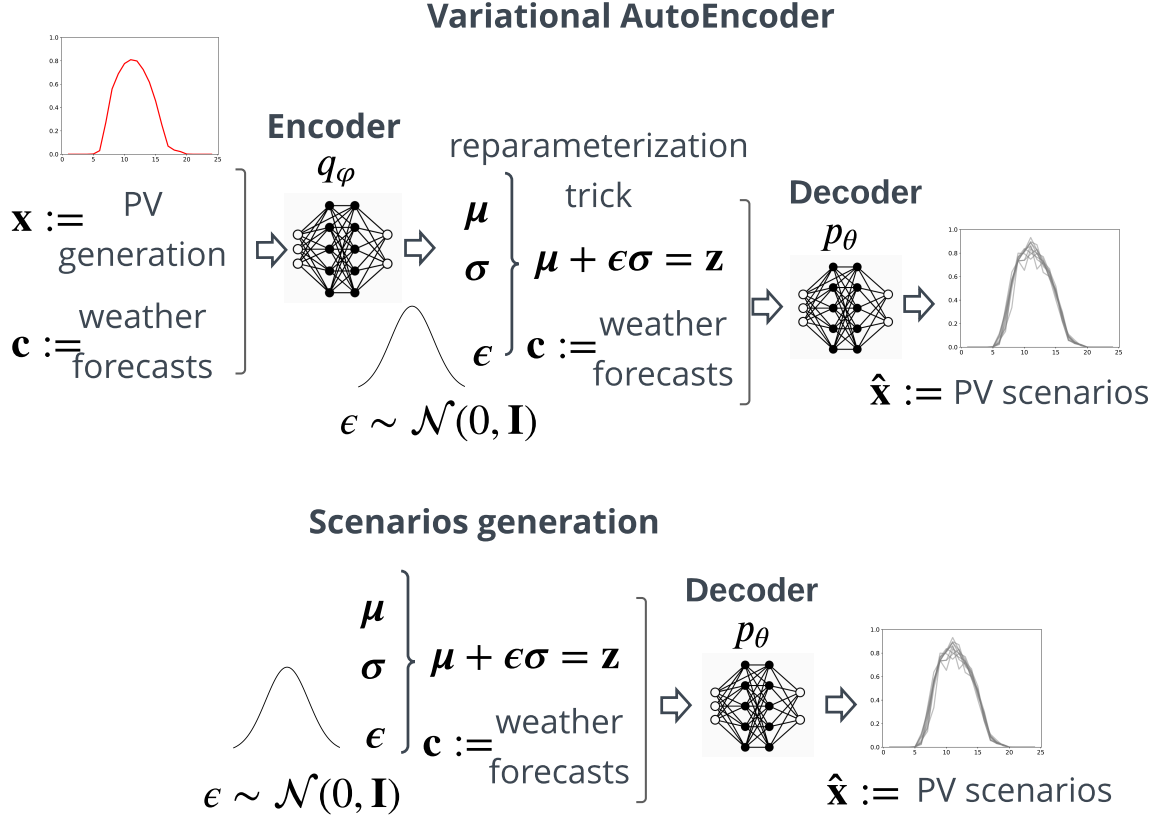


Fig. 8.5 The process of conditional variational autoencoder is illustrated for PV generation.

The VAE is trained by maximizing the variational lower bound given a dataset composed of PV observations and weather forecasts. The encoder q_ϕ maps the variable of interest \mathbf{x} to a latent space \mathbf{z} . The decoder p_θ generates the PV scenarios $\hat{\mathbf{x}}$ by taking as inputs samples \mathbf{z} from the latent space and the weather forecasts \mathbf{c} .

Generative adversarial networks

GANs are a class of deep generative models proposed by Goodfellow et al. [65] where the key idea is the adversarial training of two neural networks, the *generator* and the *discriminator*, during which the generator learns iteratively to produce realistic scenarios until they cannot be distinguished anymore by the discriminator from real data. The generator $g_\theta(\cdot) : \mathbb{R}^d \times \mathbb{R}^{|\mathbf{c}|} \rightarrow \mathbb{R}^T$ maps a latent vector $\mathbf{z} \in \mathbb{R}^d$ equipped with a known and tractable prior probability density function $p(\mathbf{z})$, *e.g.*, a Normal distribution, onto a sample $\mathbf{x} \in \mathbb{R}^T$, and is trained to fool the discriminator. The

discriminator $d_\phi(\cdot) : \mathbb{R}^T \times \mathbb{R}^{|\mathbf{c}|} \rightarrow [0, 1]$ is a classifier trained to distinguish between true samples \mathbf{x} and generated samples $\hat{\mathbf{x}}$. Goodfellow et al. [65] demonstrated that solving the following min-max problem

$$\theta^* = \arg \min_{\theta} \max_{\phi} V(\phi, \theta), \quad (8.7)$$

where $V(\phi, \theta)$ is the value function, recovers the data generating distribution if $g_\theta(\cdot)$ and $d_\phi(\cdot)$ are given enough capacity. The state-of-the-art conditional Wasserstein GAN with gradient penalty (WGAN-GP) proposed by Gulrajani et al. [68] is implemented with $V(\phi, \theta)$ defined as

$$V(\phi, \theta) = - \left(\mathbb{E}_{\tilde{\mathbf{x}}} [d_\phi(\tilde{\mathbf{x}}|\mathbf{c})] - \mathbb{E}_{\mathbf{x}} [d_\phi(\mathbf{x}|\mathbf{c})] + \lambda \text{GP} \right), \quad (8.8a)$$

$$\text{GP} = \mathbb{E}_{\tilde{\mathbf{x}}} \left[\left(\|\nabla_{\tilde{\mathbf{x}}} d_\phi(\tilde{\mathbf{x}}|\mathbf{c})\|_2 - 1 \right)^2 \right], \quad (8.8b)$$

where $\tilde{\mathbf{x}}$ is implicitly defined by sampling convex combinations between the data and the generator distributions $\tilde{\mathbf{x}} = \rho \hat{\mathbf{x}} + (1 - \rho) \mathbf{x}$ with $\rho \sim \mathbb{U}(0, 1)$. The WGAN-GP constraints the gradient norm of the discriminator's output with respect to its input, to enforce the 1-Lipschitz conditions, in contrast to the weight clipping of WGAN that sometimes generates only poor samples or fails to converge. 8.8.3 details the successive improvements from the original GAN to the WGAN, and the final WGAN-GP implemented, referred to as GAN in the rest of the Chapter. Figure 8.6 depicts the process of a conditional generative adversarial network for PV generation.

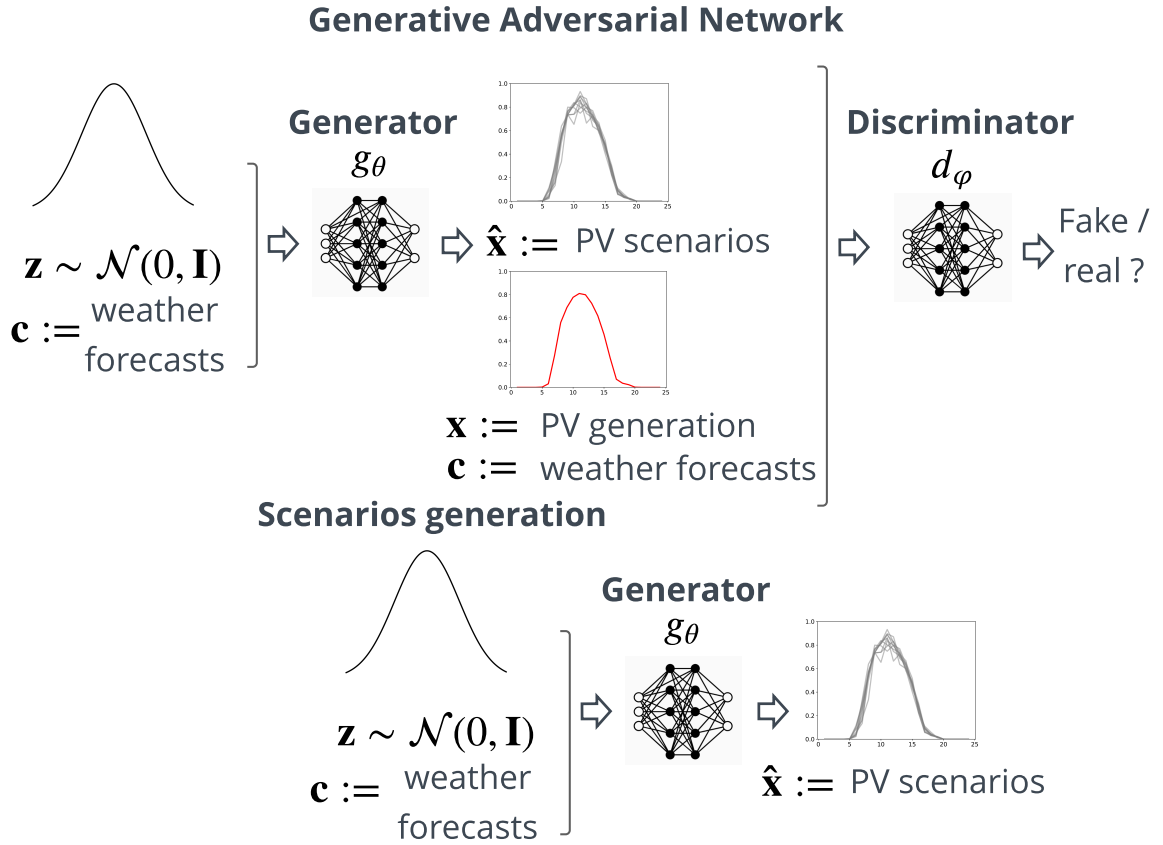


Fig. 8.6 The process of the conditional generative adversarial network is illustrated for PV generation.

The GAN is trained by solving a min-max problem given a dataset composed of PV observations \mathbf{x} and weather forecasts. The generator g_θ computes PV scenarios $\hat{\mathbf{x}}$ by taking as inputs samples from the Normal distribution \mathbf{z} and the weather forecasts \mathbf{c} , and the decoder d_ϕ tries to distinguish true data from scenarios.

8.2.3 Theoretical comparison

Normalizing flows are a generative model that allows exact likelihood calculation, the loss function to optimize is simply the log-likelihood, while being efficiently parallelizable and offering a useful latent space for downstream tasks. In contrast to GANs and VAEs, NFs explicitly learn the data distribution and provide direct access to the exact likelihood of the model's parameters, hence offering a sound and direct way to optimize the network parameters [152]. However, NFs suffer from some drawbacks [21]: (1) one disadvantage of requiring transformations to be invertible is that the input dimension must be equal to the output dimension which may make the model difficult to train or inefficient; (2) each transformation must be sufficiently expressive while being easily invertible to efficiently compute the Jacobian determinant. The first issue is also raised by Ruthotto and Haber [130] where it is said ensuring sufficient similarity of the distribution of interest and the latent distribution is of high importance to obtain meaningful and relevant samples. However, in our numerical simulations, we did not encounter this problem. Concerning the second issue, the UMNN-MAF transformation provides an expressive and effective way of computing the Jacobian.

VAEs indirectly optimize the log-likelihood of the data by maximizing the variational lower bound. The advantage of VAEs over NFs is their ability to handle non-invertible generators and the arbitrary dimension of the latent space. However, it has been observed when applied to complex datasets such as natural images, VAEs samples tend to be unrealistic. There is evidence that the limited approximation of the true posterior, with a common choice being a normally distributed prior with diagonal covariance, is the root cause [165]. This statement comes from the field of computer vision. However, it may explain the shape of the scenarios observed in our numerical experiments in Section 8.5.

The training of GANs relies on a min-max problem where the generator and the discriminator are jointly optimized. Therefore, it does not rely on estimates of the likelihood or latent variable. The adversarial nature of GANs makes them notoriously difficult to train due to the saddle point problem [5]. Another drawback is the mode collapsing, where one network stays in bad local minima and only a small subset of the data distribution is learned. Several improvements have been designed to address these issues such as the Wasserstein GAN with gradient penalty. Thus, GANs models are widely used in computer vision and power systems. However, most GAN approaches require cumbersome hyperparameter tuning to achieve similar results to VAEs or NFs. In our numerical simulations, the GAN is highly sensitive to hyperparameter variations, which is consistent with [130].

Each method has its advantages and drawbacks and makes trade-offs in terms of computing time, hyper-parameter tuning, architecture complexity, *etc.* Therefore, the choice of a particular method is dependent on the user criteria and the dataset considered. In addition, the challenges of power systems are different from computer vision. Therefore, the limitations established in the computer vision literature such as Bond-Taylor et al. [21] and Ruthotto and Haber [130] must be addressed with caution. Therefore, we encourage the energy forecasting practitioners to test and compare these methods in power systems applications.

8.3 Quality assessment

For predictions in any form, one must differentiate between their quality and their value [105]. Forecast quality corresponds to the ability of the forecasts to genuinely inform of future events by mimicking the characteristics of the processes involved. Forecast value relates, instead, to the benefits from using forecasts in a decision-making process such as participation in the electricity market. The forecast value is assessed in Part II Chapter 15, by considering the day-ahead market scheduling of electricity aggregators, such as energy retailers or generation companies.

Evaluating and comparing generative models remains a challenging task. Several measures have been introduced with the emergence of new models, in particular, in the field of computer vision. However, there is no consensus or guidelines as to which metric best captures the strengths and limitations of models. Generative models need to be evaluated directly with respect to the application they are intended for [142]. Indeed, good performance with respect to one criterion does not imply good performance with respect to the other criteria. Several studies propose metrics and make attempts to determine the pros and cons. We selected two that provide helpful information: (1) 24 quantitative and 5 qualitative measures for evaluating generative models are reviewed and compared by Borji [23] with a particular emphasis on GAN-derived models; (2) several representative sample-based evaluation metrics for GANs are investigated by Xu et al. [154] where the kernel Maximum Mean Discrepancy (MMD) and the 1-Nearest-Neighbour (1-NN) two-sample test seem to satisfy most of the desirable properties. The key message is to combine several complementary metrics to assess the generative models. Some of the metrics proposed are related to image generation and cannot directly be transposed to energy forecasting.

Therefore, we decided to use eight complementary quality metrics to conduct a relevant quality analysis inspired by the energy forecasting and computer vision

fields. They can be divided in four groups: (1) the *univariate* metrics composed of the continuous rank probability score, the quantile score, and the reliability diagram. They can only assess the quality of the scenarios with respect to their marginals; (2) the *multivariate* metrics composed of the energy and the variogram scores. They can directly assess multivariate scenarios; (3) the *specific* metrics composed of a classifier-based metric, and the correlation matrix between scenarios for a given context; (4) the Diebold and Mariano statistical test. The univariate and multivariate metrics are already defined in Chapter 3. Therefore, only the specific metrics and statistical test are introduced in this Section.

Classifier-based metric

Modern binary classifiers can be easily turned into powerful two-sample tests where the goal is to assess whether two samples are drawn from the same distribution [97]. In other words, it aims at assessing whether a generated scenario can be distinguished from an observation. To this end, the generator is evaluated on a held-out testing set that is split into a testing-train and testing-test subsets. The testing-train set is used to train a classifier, which tries to distinguish generated scenarios from the real distribution. Then, the final score is computed as the performance of this classifier on the testing-test set.

In principle, any binary classifier can be adopted for computing classifier two-sample tests (C2ST). A variation of this evaluation methodology is proposed by Xu et al. [154] and is known as the 1-Nearest Neighbor (NN) classifier. The advantage of using 1-NN over other classifiers is that it requires no special training and little hyper-parameter tuning. This process is conducted as follows. Given two sets of observations S_r and generated S_g samples with the same size, *i.e.*, $|S_r| = |S_g|$, it is possible to compute the leave-one-out (LOO) accuracy of a 1-NN classifier trained on S_r and S_g with positive labels for S_r and negative labels for S_g . The LOO accuracy can vary from 0 % to 100 %. The 1-NN classifier should yield a 50 % LOO accuracy when $|S_r| = |S_g|$ is large. This is achieved when the two distributions match. Indeed, the level 50 % happens when a label is randomly assigned to a generated scenario. It means the classifier is not capable of discriminating generated scenarios from observations. If the generative model over-fits S_g to S_r , *i.e.*, $S_g = S_r$, and the accuracy would be 0 %. On the contrary, if it generates samples that are widely different than observations the performance should be 100 %. Therefore, the closer the LOO accuracy is to 1, the higher the degree of under-fitting of the model, while the closer the LOO accuracy is to 0, the higher

the degree of over-fitting of the model. The C2ST approach using LOO with 1-NN is adopted by Qi et al. [126] to assess the PV and wind power scenarios of a β VAE.

However, this approach has several limitations. First, it uses the testing set to train the classifier during the LOO. Second, the 1-NN is very sensitive to outliers as it simply chose the closest neighbor based on distance criteria. This behavior is amplified when combined with the LOO where the testing-test set is composed of only one sample. Third, the euclidian distance cannot deal with a context such as weather forecasts. Therefore, we cannot use a conditional version of the 1-NN using weather forecasts to classify weather-based renewable generation and the observations. Fourth, C2ST with LOO cannot provide ROC curve but only accuracy scores. An important point about ROC graphs is that they measure the ability of a classifier to produce good relative instance scores. In our case we are interested in discriminating the generated scenarios from the observations and the ROC provide more information than the accuracy metric to achieve this goal. A common method to reduce ROC performance to a single scalar value representing expected performance is to calculate the area under the ROC curve, abbreviated AUC. The AUC has an important statistical property: it is equivalent to the probability that the classifier will rank a randomly chosen positive instance higher than a randomly chosen negative instance [49].

To deal with these issues, we decided to implement a modification of this classifier-based evaluation by conducting the C2ST as follows: (1) the scenarios generated on the learning set are used to train the classifier using the C2ST. Therefore, the classifier uses the entire testing set and can be used to compute ROC; (2) the classifier is an Extra-Trees classifier that can deal with context such as weather forecasts.

More formally, for a given generative model g the following steps are conducted:

1. Initialization step: the generative model g has been trained on the LS and has generated M weather-based scenarios per day of both the LS and TS: $\{\hat{\mathbf{x}}_{\text{LS}}^i\}_{i=1}^M := \cup_{d \in \text{LS}} \{\hat{\mathbf{x}}_d^i\}_{i=1}^M$ and $\{\hat{\mathbf{x}}_{\text{TS}}^i\}_{i=1}^M := \cup_{d \in \text{TS}} \{\hat{\mathbf{x}}_d^i\}_{i=1}^M$. For the sake of clarity the index g is omitted, but both of these sets are dependent on model g .
2. M pairs of learning and testing sets are built with an equal proportion of generated scenarios and observations: $\mathcal{D}_{\text{LS}}^i := \left\{ \{\hat{\mathbf{x}}_{\text{LS}}^i, 0\} \cup \{\{\mathbf{x}_{\text{LS}}^i, 1\}\} \right\}$ and $\mathcal{D}_{\text{TS}}^i = \left\{ \{\hat{\mathbf{x}}_{\text{TS}}^i, 0\} \cup \{\{\mathbf{x}_{\text{TS}}^i, 1\}\} \right\}$. Note: $|\mathcal{D}_{\text{LS}}^i| = 2|\text{LS}|$ and $|\mathcal{D}_{\text{TS}}^i| = 2|\text{TS}|$.
3. For each pair of learning and testing sets $\{\mathcal{D}_{\text{LS}}^i, \mathcal{D}_{\text{TS}}^i\}_{i=1}^M$ a classifier d_g^i is trained and makes predictions.

4. The ROC_g^i curves and corresponding AUC_g^i are computed for $i = 1, \dots, M$.

This classifier-based methodology is conducted for all models g , and the results are compared. Figure 8.7 depicts the overall approach. The classifiers d_g^i are all Extra-Trees classifier made of 1000 unconstrained trees with the hyper-parameters "max_depth" set to "None", and "n_estimators" to 1 000.

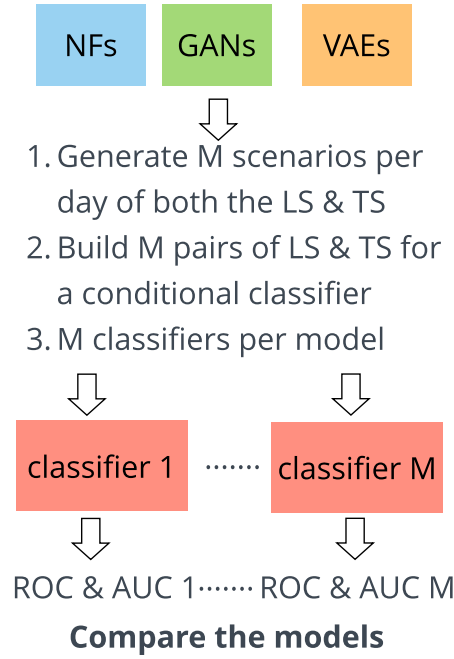


Fig. 8.7 Classifier-based metric methodology.

Each generative model generates M scenarios per day of the learning and testing sets. They are used to build M pairs of learning and testing sets for a conditional classifier by including an equal proportion of observations and weather forecasts. M conditional classifiers, per model, are trained and make predictions. The M ROC and AUC are computed per model, and the results are compared.

Correlation matrix between scenarios

The second specific metric consists of computing the correlation matrix between the scenarios generated for given weather forecasts. Formally, let $\{\hat{\mathbf{x}}^i\}_{i=1}^M$ be the set of M scenarios generated for a given day of the testing set. It is a matrix $(M \times 24)$ where each row is a scenario. Then, the Pearson's correlation coefficients are computed into a correlation matrix (24×24) . This metric indicates the variety of scenario shapes.

Diebold-Mariano test

Using relevant metrics to assess the forecast quality is important. However, it is also necessary to analyze whether any difference in accuracy is statistically significant. Indeed, when different models have almost identical values in the selected error measures, it is difficult to draw statistically significant conclusions on the outperformance of the forecasts of one model by those of another. The Diebold-Mariano (DM) test [37] is probably the most commonly used statistical testing tool to evaluate the significance of differences in forecasting accuracy. It is model-free, *i.e.*, it compares the forecasts of models, and not models themselves. The DM test is used in this study to assess the CRPS, QS, ES, and VS metrics. The CRPS and QS are univariate scores, and a value of CRPS and QS is computed per marginal (time period of the day). Therefore, the multivariate variant of the DM test is implemented following Ziel and Weron [167], where only one statistic for each pair of models is computed based on the 24-dimensional vector of errors for each day.

For a given day d of the testing set, let $\epsilon_d \in \mathbb{R}$ be the error computed by an arbitrary forecast loss function of the observation and scenarios. The test consists of computing the difference between the errors of the pair of models g and h over the testing set

$$\Delta(g, h)_d = \epsilon_d^g - \epsilon_d^h, \quad \forall d \in \text{TS}, \quad (8.9)$$

and to perform an asymptotic z -test for the null hypothesis that the expected forecast error is equal and the mean of differential loss series is zero $\mathbb{E}[\Delta(g, h)_d] = 0$. It means there is no statistically significant difference in the accuracy of the two competing forecasts. The statistic of the test is deduced from the asymptotically standard normal distribution as follows

$$\text{DM}(g, h) = \sqrt{\# \text{TS}} \frac{\hat{\mu}}{\hat{\sigma}}, \quad (8.10)$$

with $\# \text{TS}$ the number of days of the testing set, $\hat{\mu}$ and $\hat{\sigma}$ the sample mean and the standard deviation of $\Delta(g, h)$. Under the assumption of covariance stationarity of the loss differential series $\Delta(g, h)_d$, the DM statistic is asymptotically standard normal. The lower the p -value, *i.e.*, the closer it is to zero, the more the observed data is inconsistent with the null hypothesis: $\mathbb{E}[\Delta(g, h)_d] < 0$ the forecasts of the model h are more accurate than those of model g . If the p -value is less than the commonly accepted level of 5 %, the null hypothesis is typically rejected. It means that the forecasts of model g are significantly more accurate than those of model h .

When considering the ES or VS scores, there is a value per day of the testing set ES_d or VS_d . In this case, $\epsilon_d = \text{ES}_d$ or $\epsilon_d = \text{VS}_d$. However, when considering the

CRPS or QS, there is a value per marginal and per day of the testing set $\text{CRPS}_{d,k}$ or $\text{QS}_{d,k}$. A solution consists of computing 24 independent tests, one for each hour of the day. Then, to compare the models based on the number of hours for which the predictions of one model are significantly better than those of another. Another way consists of a multivariate variant of the DM-test with the test performed jointly for all hours using the multivariate loss differential series. In this case, for a given day d , $\epsilon_d^g = [\epsilon_{d,1}^g, \dots, \epsilon_{d,24}^g]^\top$, $\epsilon_d^h = [\epsilon_{d,1}^h, \dots, \epsilon_{d,24}^h]^\top$ are the vectors of errors for a given metric of models g and h , respectively. Then the multivariate loss differential series

$$\Delta(g, h)_d = \|\epsilon_d^g\|_1 - \|\epsilon_d^h\|_1, \quad (8.11)$$

defines the differences of errors using the $\|\cdot\|_1$ norm. Then, for each model pair, the p -value of two-sided DM tests is computed as described above. The univariate version of the test has the advantage of providing a deeper analysis as it indicates which forecast is significantly better for which hour of the day. The multivariate version enables a better representation of the results as it summarizes the comparison in a single p -value, which can be conveniently visualized using heat maps arranged as chessboards. In this study, we decided to adopt the multivariate DM-test for the CRPS and QS.

8.4 Case study

The quality and value evaluations of the models are conducted on the load, wind, and PV tracks of the open-access GEFCom 2014 dataset [75], composed of one, ten, and three zones, respectively. See Chapter 15 for the value evaluation and the energy retailer problem statement. Figure 8.8 depicts the methodology to assess both the quality and value of the GAN, VAE, and NF models implemented in this study.

8.4.1 Implementation details

By appropriate normalization, we standardize the weather forecasts to have a zero mean and unit variance. Table 8.2 provides a summary of the implementation details described in what follows. For the sake of proper model training and evaluation, the dataset is divided into three parts per track considered: learning, validation, and testing sets. The learning set (LS) is used to fit the models, the validation set (VS) to select the optimal hyper-parameters, and the testing set (TS) to assess the forecast quality and value. The number of samples ($\#$), expressed in days, of the VS and TS is $50 \cdot n_z$, with n_z the number of zones of the track considered. The 50 days are selected

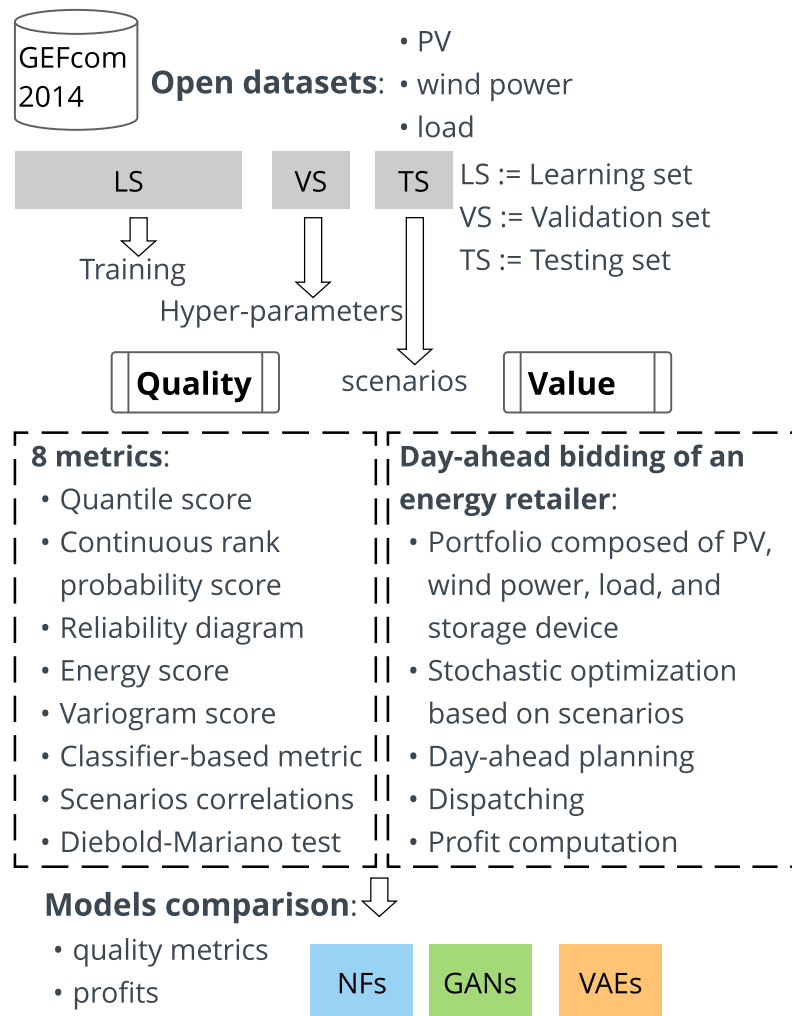


Fig. 8.8 Methodology to assess both the quality and value of the GAN, VAE, and NF models implemented in this study.

The PV, wind power, and load datasets of the open-access Global Energy Forecasting Competition 2014 are divided into three parts: learning, validation, and testing sets. The learning set is used to train the models, the validation set to select the optimal hyper-parameters, and the testing set to conduct the numerical experiments. The quality and value of the models are assessed by using the scenarios generated on the testing set. The quality evaluation consists of eight complementary metrics, and the value assessment is performed by using the simple and easily reproducible case study of the day-ahead bidding of an energy retailer. The energy retailer portfolio is composed of PV, wind power generation, load, and a storage system device. The retailer bids on the day-ahead market by computing a planning based on stochastic optimization. The dispatch is computed by using the observations of the PV generation, wind power, and load. Then, the profits are evaluated and compared.

randomly from the dataset, and the learning set is composed of the remaining part with $D \cdot n_z$ samples, where D is provided for each track in Table 8.2. The NF, VAE, and GAN use the weather forecasts as inputs to generate on a day-ahead basis M scenarios $\hat{\mathbf{x}} \in \mathbb{R}^T$.

Wind track

The zonal \mathbf{u}^{10} , \mathbf{u}^{100} and meridional \mathbf{v}^{10} , \mathbf{v}^{100} wind components at 10 and 100 meters are selected, and six features are derived following the formulas provided by Landry et al. [95] to compute the wind speed \mathbf{ws}^{10} , \mathbf{ws}^{100} , energy \mathbf{we}^{10} , \mathbf{we}^{100} and direction \mathbf{wd}^{10} , \mathbf{wd}^{100} at 10 and 100 meters

$$\mathbf{ws} = \sqrt{\mathbf{u} + \mathbf{v}}, \quad (8.12a)$$

$$\mathbf{we} = \frac{1}{2} \mathbf{ws}^3, \quad (8.12b)$$

$$\mathbf{wd} = \frac{180}{\pi} \arctan(\mathbf{u}, \mathbf{v}). \quad (8.12c)$$

For each generative model, the wind zone is taken into account with one hot-encoding variable Z_1, \dots, Z_{10} , and the wind feature input vector for a given day d is

$$\mathbf{c}_d^{\text{wind}} = [\mathbf{u}_d^{10}, \mathbf{u}_d^{100}, \mathbf{v}_d^{10}, \mathbf{v}_d^{100}, \mathbf{ws}_d^{10}, \mathbf{ws}_d^{100}, \mathbf{we}_d^{10}, \mathbf{we}_d^{100}, \mathbf{wd}_d^{10}, \mathbf{wd}_d^{100}, Z_1, \dots, Z_{10}], \quad (8.13)$$

of dimension $n_f \cdot T + n_z = 10 \cdot 24 + 10$.

PV track

The solar irradiation \mathbf{I} , the air temperature \mathbf{T} , and the relative humidity \mathbf{rh} are selected, and two features are derived by computing \mathbf{I}^2 and \mathbf{IT} . For each generative model, the PV zone is taken into account with one hot-encoding variable Z_1, Z_2, Z_3 , and the PV feature input vector for a given day d is

$$\mathbf{c}_d^{\text{PV}} = [\mathbf{I}_d, \mathbf{T}_d, \mathbf{rh}_d, \mathbf{I}_d^2, \mathbf{IT}_d, Z_1, Z_2, Z_3], \quad (8.14)$$

of dimension $n_f \cdot T + n_z$. For practical reasons, the periods where the PV generation is always 0, across all zones and days, are removed, and the final dimension of the input feature vector is $n_f \cdot T + n_z = 5 \cdot 16 + 3$.

Load track

The 25 weather station temperature $\mathbf{w}_1, \dots, \mathbf{w}_{25}$ forecasts are used. There is only one zone, and the load feature input vector for a given day d is

$$\mathbf{c}_d^{\text{load}} = [\mathbf{w}_1, \dots, \mathbf{w}_{25}], \quad (8.15)$$

of dimension $n_f \cdot T = 25 \cdot 24$.

	Wind	PV	Load
T periods	24	16	24
n_z zones	10	3	—
n_f features	10	5	25
\mathbf{c}_d dimension	$n_f \cdot T + n_z$	$n_f \cdot T + n_z$	$n_f \cdot T$
# LS (days)	$631 \cdot n_z$	$720 \cdot n_z$	1999
# VS/TS (days)	$50 \cdot n_z$	$50 \cdot n_z$	50

Table 8.2 Dataset and implementation details.

Each dataset is divided into three parts: learning, validation, and testing sets. The number of samples (#) is expressed in days and is set to 50 days for the validation and testing sets. T is the number of periods per day considered, n_z the number of zones of the dataset, n_f the number of weather variables used, and \mathbf{c}_d is the dimension of the conditional vector, for a given day, that includes the weather forecasts and the one hot-encoding variables when there are several zones. Note: the days of the learning, validation, and testing sets are selected randomly.

8.4.2 Hyper-parameters

Table 8.3 provides the hyper-parameters of the NF, VAE, and GAN implemented. The Adam optimizer [87] is used to train the generative models with a batch size of 10% of the learning set. The NF implemented is a one-step monotonic normalizer using the UMNN-MAF². The embedding size $|h^i|$ is set to 40, and the embedding neural network is composed of l layers of n neurons ($l \times n$). The same integrand neural network $\tau^i(\cdot) \forall i = 1, \dots, T$ is used and composed of 3 layers of $|h^i|$ neurons (3×40). Both the encoder and decoder of the VAE are feed-forward neural networks ($l \times n$), ReLU activation functions for the hidden layers, and no activation function for

²<https://github.com/AWehenkel/Normalizing-Flows>

	Wind	PV	Load
Embedding Net	4×300	4×300	4×300
Embedding size	40	40	40
(a)Integrand Net	3×40	3×40	3×40
Weight decay	5.10^{-4}	5.10^{-4}	5.10^{-4}
Learning rate	10^{-4}	5.10^{-4}	10^{-4}
Latent dimension	20	40	5
(b)E/D Net	1×200	2×200	1×500
Weight decay	$10^{-3.4}$	$10^{-3.5}$	10^{-4}
Learning rate	$10^{-3.4}$	$10^{-3.3}$	$10^{-3.9}$
Latent dimension	64	64	256
(c)G/D Net	2×256	3×256	2×1024
Weight decay	10^{-4}	10^{-4}	10^{-4}
Learning rate	2.10^{-4}	2.10^{-4}	2.10^{-4}

Table 8.3 (a) NF, (b) VAE, and (c) GAN hyper-parameters.

The hyper-parameters selection is performed on the validation set using the Python library Weights & Biases [18]. This library is an experiment tracking tool for machine learning making it easier to keep track of experiments. The GAN model was the most time-consuming during this process followed by the VAE, and NF. Indeed, the GAN is highly sensitive to hyper-parameter modifications making challenging to identify a relevant set of values. In contrast, the NF achieved satisfactory results, both in terms of scenarios shapes and quality, by testing only a few sets of hyper-parameter values.

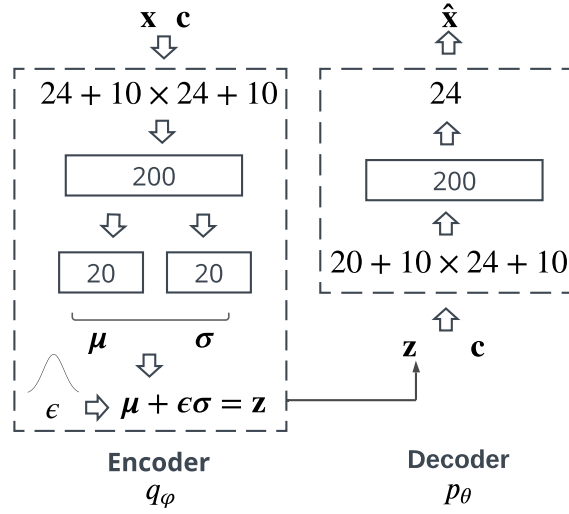


Fig. 8.9 Variational autoencoder structure implemented for the wind dataset. Both the encoder and decoder are feed-forward neural networks composed of one hidden layer with 200 neurons. Increasing the number of layers did not improve the results for this dataset. The latent space dimension is 20.

the output layer. Both the generator and discriminator of the GAN are feed-forward neural networks ($l \times n$). The activation functions of the hidden layers of the generator (discriminator) are ReLU (Leaky ReLU). The activation function of the discriminator output layer is ReLU, and there is no activation function for the generator output layer. The generator is trained once after the discriminator is trained five times to stabilize the training process, and the gradient penalty coefficient λ in (8.7) is set to 10 as suggested by Gulrajani et al. [68].

Figures 8.9, 8.10, and 8.11 illustrate the VAE, GAN, and NF structures implemented for the wind dataset where the number of weather variables selected and the number of zones is 10, and 10, respectively. Recall, $\mathbf{c} :=$ weather forecasts, $\hat{\mathbf{x}} :=$ scenarios $\mathbf{x} :=$ wind power observations, $\mathbf{z} :=$ latent space variable, $\epsilon :=$ Normal variable (only for the VAE).

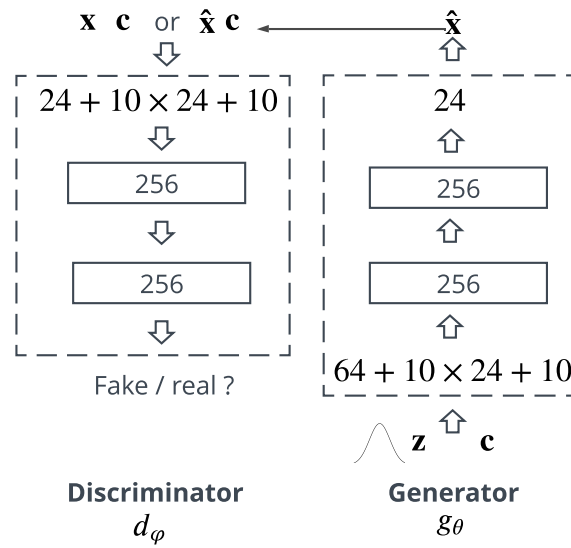


Fig. 8.10 Generative adversarial network structure implemented for the wind dataset. Both the discriminator and generator are feed-forward neural networks composed of two hidden layers with 256 neurons. The latent space dimension is 64.

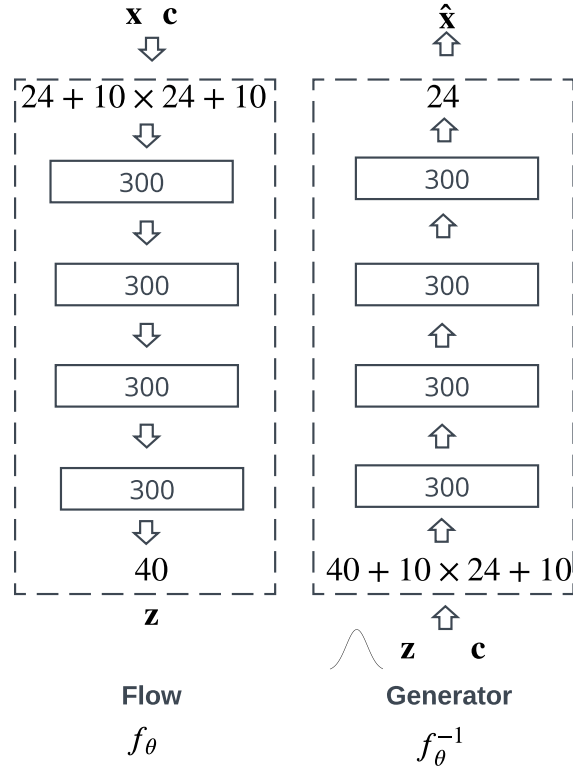


Fig. 8.11 Normalizing flow structure implemented for the wind dataset.

A single-step monotonic normalizing flow is implemented with a feed-forward neural network composed of four hidden layers with 300 neurons. The latent space dimension is 40. Note: for the sake of clarity the integrand network is not included but is a feed-forward neural network composed of three hidden layers with 40 neurons. Increasing the number of steps of the normalizing flow did not improve the results. The monotonic transformation is complex enough to capture the stochasticity of the variable of interest. However, when considering affine autoregressive normalizing flows the number of steps should be generally more important. Numerical experiments indicated a five-step autoregressive flow was required to achieve similar results for this dataset. Note: the results are not reported in this study for the sake of clarity.

8.5 Quality results

First, a thorough comparison of the models is conducted on the wind track. Second, all tracks are considered for the sake of clarity. Note that the model ranking slightly differs depending on the track.

8.5.1 Wind track

In addition to the generative models, a naive approach is designed (RAND), where the scenarios of the learning, validation, and testing sets are sampled randomly from the learning, validation, and testing sets, respectively. Intuitively, it boils down to assume that past observations are repeated. These scenarios are realistic but may not be compatible with the context. Each model generates a set of 100 scenarios for each day of the testing set. Figure 8.12 compares the QS, reliability diagram, and CRPS of the wind (markers), PV (plain), and load (dashed) tracks. Overall, for the wind track in terms of CRPS, QS, and reliability diagrams the VAE achieves slightly better scores, then followed by the NF, and the GAN. The ES and VS multivariate scores confirm this trend with 54.82 and 18.87 for the VAE *vs* 56.71 and 18.54 for the NF, respectively.

Figure 8.13 provides the results of the DM tests for these metrics. The heat map indicates the range of the p -values, the closer they are to zero, dark green, the more significant the difference between the scores of two models for a given metric. The statistical threshold is set to 5 % but the scale color is capped at 10 % for a better exposition of the relevant results. For instance, when considering the DM test for the RAND CRPS, all the columns of the RAND row are in dark green indicating that the RAND scenarios are always significantly outperformed by the other models. These DM tests confirm the VAE outperforms the NF for the wind track considering these metrics. Then, the NF is only outperformed by the VAE, and the GAN by both the VAE and NF. These results are consistent with the classifier-based metric depicted in Figure 8.14, where the VAE is the best to mislead the classifier followed by the NF, and GAN.

The left part of Figure 8.15 provides 50 scenarios, (a) NF, (c) GAN, and (e) VAE, generated for a given day selected randomly from the testing set. Notice how the shape of the NF's scenarios differs significantly from the GAN and VAE as they tend to be more variable with no identifiable trend. In contrast, the VAE and GAN scenarios seem to differ mainly in terms of nominal power but have similar shapes. This behavior is even more pronounced for the GAN where the scenarios rarely crossed over the

time periods. For instance, there is a gap in terms of generation around time periods 17 and 18 where all the GAN's scenarios follow this trend. These observations are confirmed by computing the corresponding time correlation matrices, depicted by the right part of Figure 8.15 demonstrating there is no correlation between NF's scenarios. On the contrary, the VAE and GAN correlation matrices tend to be similar with a time correlation of the scenarios over a few time periods, with more correlated periods when considering the GAN. This difference in terms of the scenario's shape is striking and not necessarily captured by metrics such as the CRPS, QS, or even the classifier-based metric, and is also observed on the PV and load tracks as explained in the next paragraph.

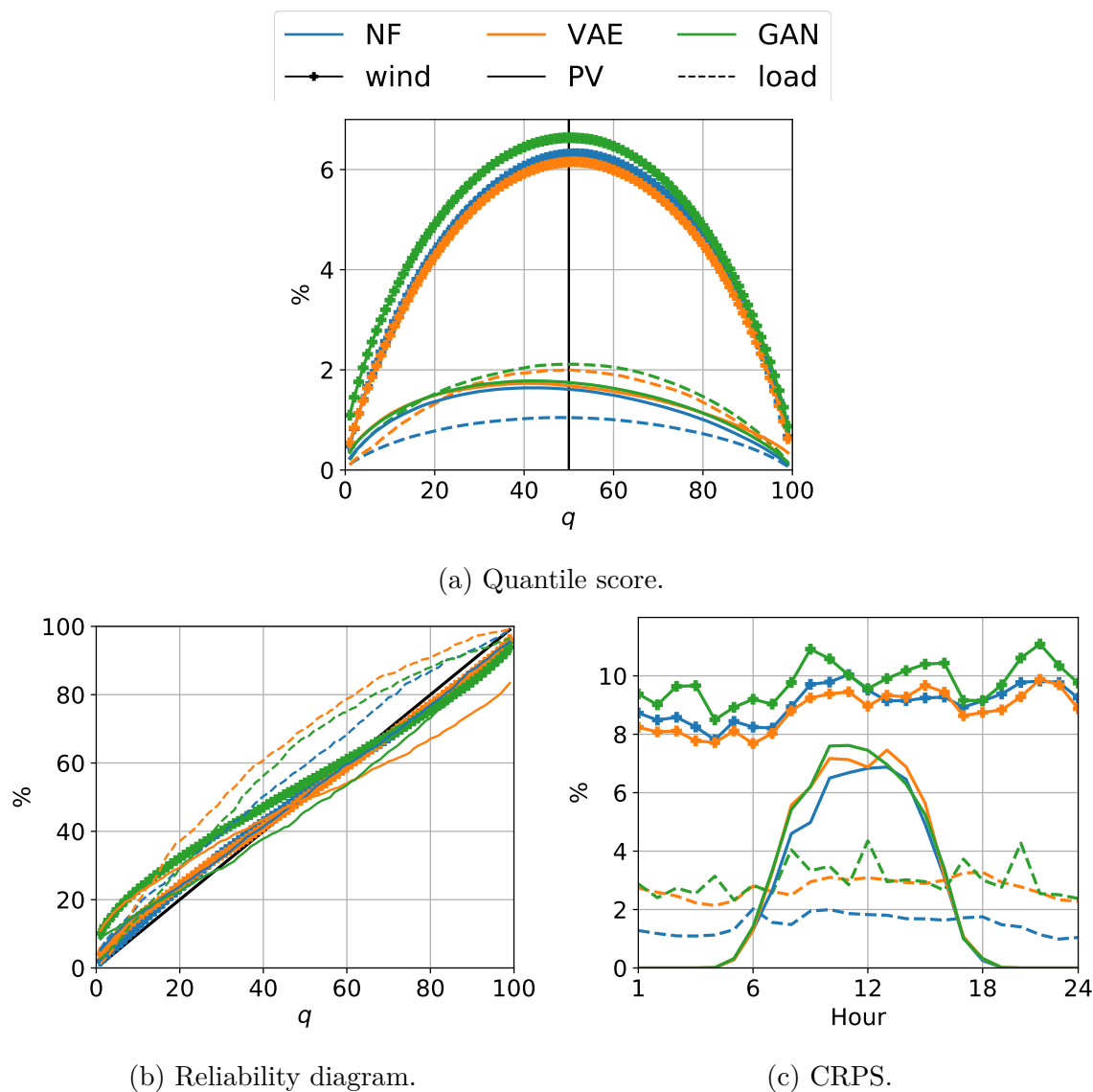


Fig. 8.12 Quality common metrics comparison on the wind (markers), PV (plain), and load (dashed) tracks.

Quantile score (a): the lower and the more symmetrical the better. Note: the quantile score has been averaged over the marginals (the 24 time periods of the day). Reliability diagram (b): the closer to the diagonal, the better. Continuous rank probability score per marginal (c): the lower, the better. NF outperforms the VAE and GAN for both the PV and load tracks and is slightly outperformed by the VAE on the wind track. Note: all models tend to have more difficulties in forecasting the wind power that seems to be less predictable than the PV generation or the load.

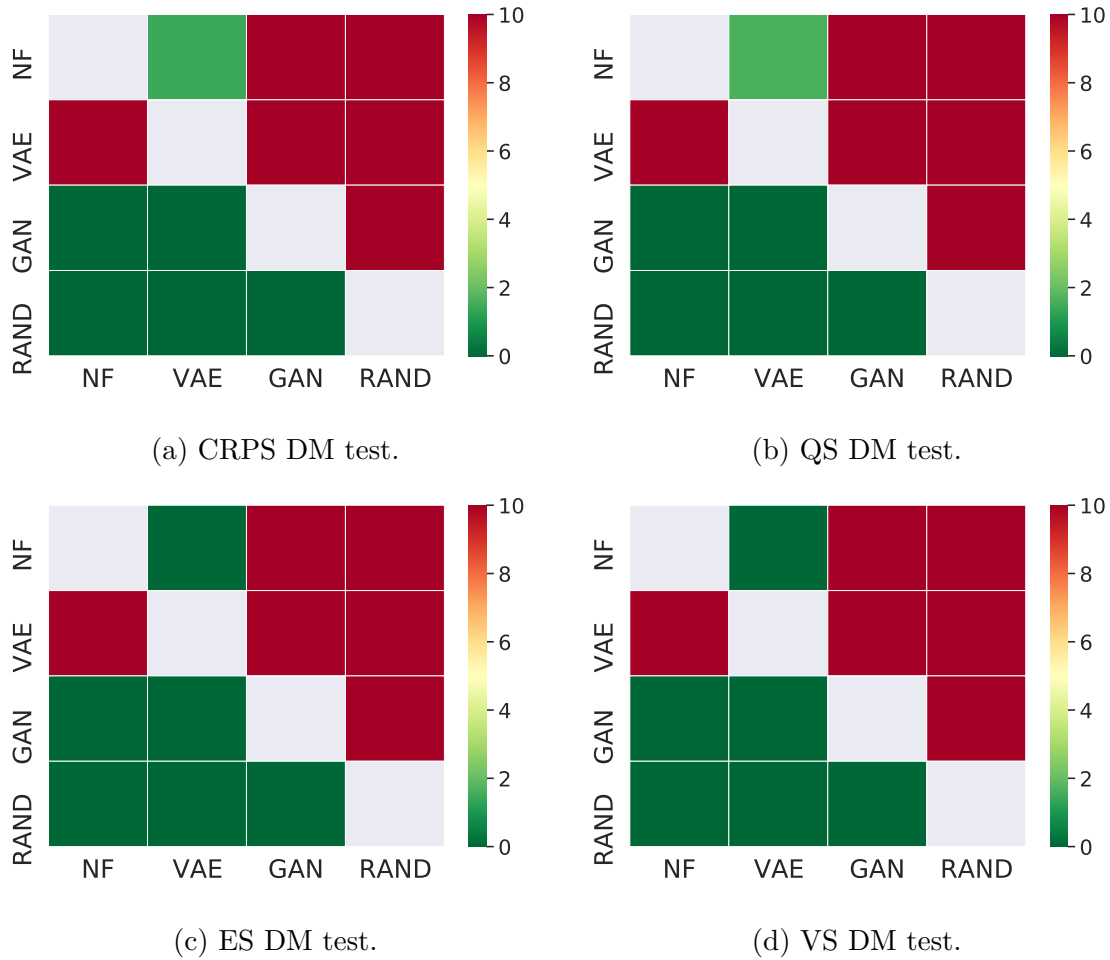


Fig. 8.13 Wind track Diebold-Mariano tests of the CRPS, QS, ES, and VS metrics. The Diebold-Mariano tests of the continuous rank probability score, quantile score, energy score, and variogram score confirm the VAE outperforms the NF on the wind track for these metrics. The NF is only outperformed by the VAE, and the GAN by both the VAE and NF. The heat map indicates the range of the p -values, the closer they are to zero, dark green, the more significant the difference between the scores of two models for a given metric. The statistical threshold is set to 5 % but the scale color is capped at 10 % for a better exposition of the relevant results.

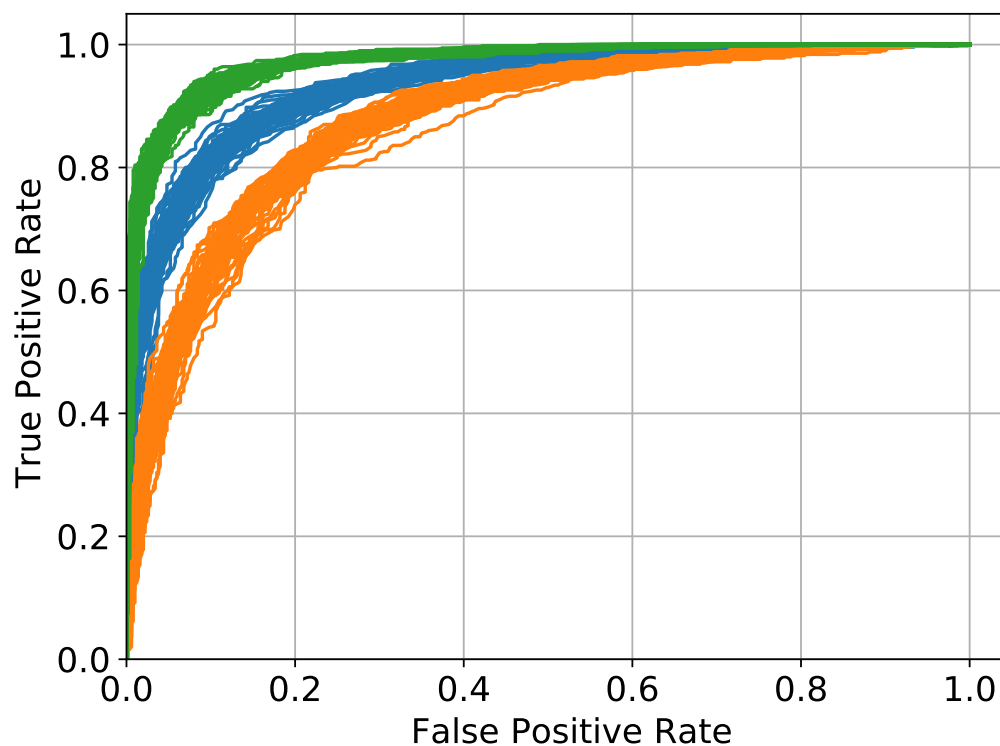


Fig. 8.14 Wind track classifier-based metric.

The VAE (orange) is the best to mislead the classifier followed by the NF (blue), and GAN (green). Note: there are 50 ROC curves depicted for each model, each one corresponding to a scenario generated that is used as input of the classifier. It allows taking into account the variability of the scenarios to avoid having results dependent on a particular scenario.

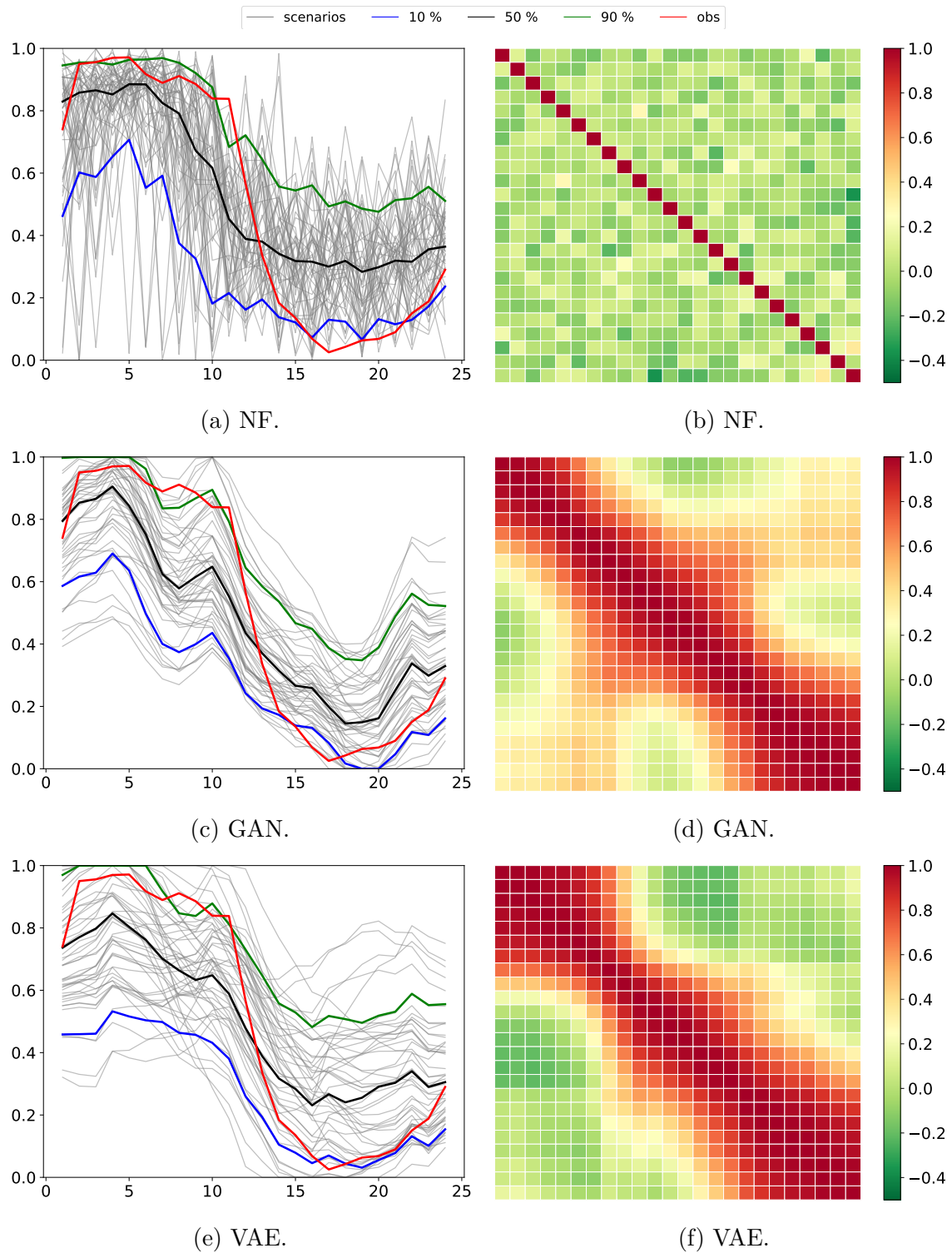


Fig. 8.15 Wind power scenarios shape comparison and analysis.

Left part (a) NF, (c) GAN, and (e) VAE: 50 wind power scenarios (grey) of a randomly selected day of the testing set along with the 10 % (blue), 50 % (black), and 90 % (green) quantiles, and the observations (red). Right part (b) NF, (d) GAN, and (f) VAE: the corresponding Pearson time correlation matrices of these scenarios with the time periods as rows and columns. The NF tends to exhibit no time correlation between scenarios. In contrast, the VAE and GAN tend to be partially time-correlated over a few time periods.

8.5.2 All tracks

Table 8.4 provides the averaged quality scores where the CRPS is averaged over the 24 time periods $\overline{\text{CRPS}}$, the QS over the 99 percentiles $\overline{\text{QS}}$, MAE-r is the mean absolute error between the reliability curve and the diagonal, and $\overline{\text{AUC}}$ is the mean of the 50 AUC. Overall, for both the PV and load tracks in terms of CRPS, QS, reliability

		NF	VAE	GAN	RAND
Wind	$\overline{\text{CRPS}}$	9.07	8.80	9.79	16.92
	$\overline{\text{QS}}$	4.58	4.45	4.95	8.55
	MAE-r	2.83	2.67	6.82	1.01
	$\overline{\text{AUC}}$	0.935	0.877	0.972	0.918
	ES	56.71	54.82	50.62	96.15
	VS	18.54	17.87	19.87	23.21
PV	$\overline{\text{CRPS}}$	2.35	2.60	2.61	4.92
	$\overline{\text{QS}}$	1.19	1.31	1.32	2.48
	MAE-r	2.66	9.04	4.94	3.94
	$\overline{\text{AUC}}$	0.950	0.969	0.997	0.947
	ES	23.08	24.65	24.15	41.53
	VS	4.68	5.02	4.88	13.40
Load	$\overline{\text{CRPS}}$	1.51	2.74	3.01	6.74
	$\overline{\text{QS}}$	0.76	1.39	1.52	3.40
	MAE-r	7.70	13.97	9.99	0.88
	$\overline{\text{AUC}}$	0.823	0.847	0.999	0.944
	ES	9.17	15.11	17.96	38.08
	VS	1.63	1.66	3.81	7.28

Table 8.4 Averaged quality scores per dataset.

The best performing deep learning generative model for each track is written in bold. The CRPS, QS, MAE-r, and ES are expressed in %. Overall, for both the PV and load tracks, the NF outperforms the VAE and GAN and is slightly outperformed by the VAE on the wind track.

diagrams, AUC, ES, and VS the NF outperforms the VAE and GAN and is slightly outperformed by the VAE on the wind track. On the load track, the VAE outperforms the GAN. However, on the PV track, the VAE and GAN achieved similar results, and the GAN performed better in terms of ES and VS. These results are confirmed by the

DM tests depicted in Figure 8.16. The classifier-based metric results for both the load and PV tracks, provided by Figure 8.17, confirm this trend where the NF is the best to trick the classifier followed by the VAE, and GAN.

Similar to the wind track, the shape of the scenarios differs significantly between the NF and the other models for both the load and PV tracks as indicated by the left part of Figures 8.18 and 8.19, and the corresponding correlation matrices provided by the right part of Figures 8.18 and 8.19. Note: the load track scenarios are highly correlated for both the VAE and GAN. Finally, Figure 8.20 provides the average of the correlation matrices over all days of the testing set for each dataset. The trend depicted above is confirmed. This difference between the NF and the other generative model may be explicated by the design of the methods. The NF learns explicitly the probability density function (PDF) of the multi-dimensional random variable considered. Thus, the NF scenarios are generated according to the learned PDF producing multiple shapes of scenarios. In contrast, the generator of the GAN is trained to fool the discriminator, and it may find a shape particularly efficient leading to a set of similar scenarios. Concerning the VAE, it is less obvious, but by design, the decoder is trained to generate scenarios from the latent space assumed to follow a Gaussian distribution that may lead to less variability.

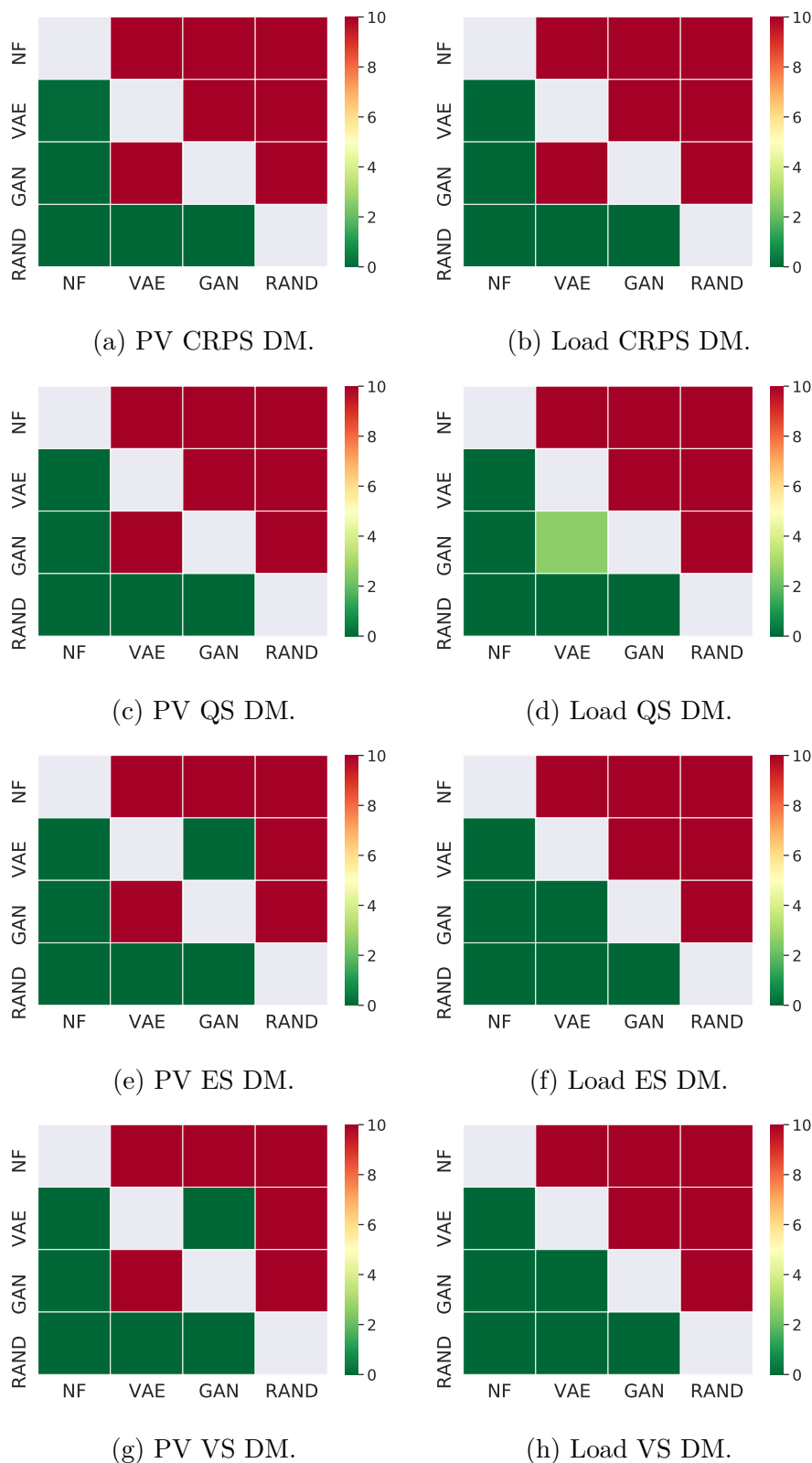


Fig. 8.16 PV and load tracks Diebold-Mariano tests.

The Diebold-Mariano tests of the CRPS, QS, ES, and VS demonstrate the NF outperforms both the VAE and GAN. Note: the GAN outperforms the VAE for both the ES and VS for the PV track. However, the VAE outperforms the GAN on this dataset for both the CRPS and QS.

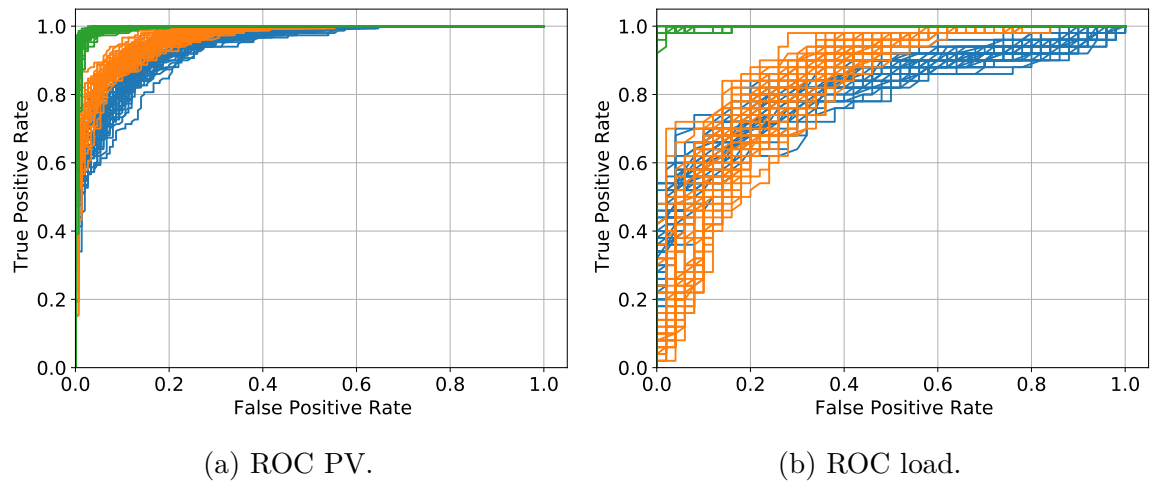


Fig. 8.17 Classifier-based metric for both the PV and load tracks. The NF (blue) is the best to fake the classifier, followed by the VAE (orange), and the GAN (green).

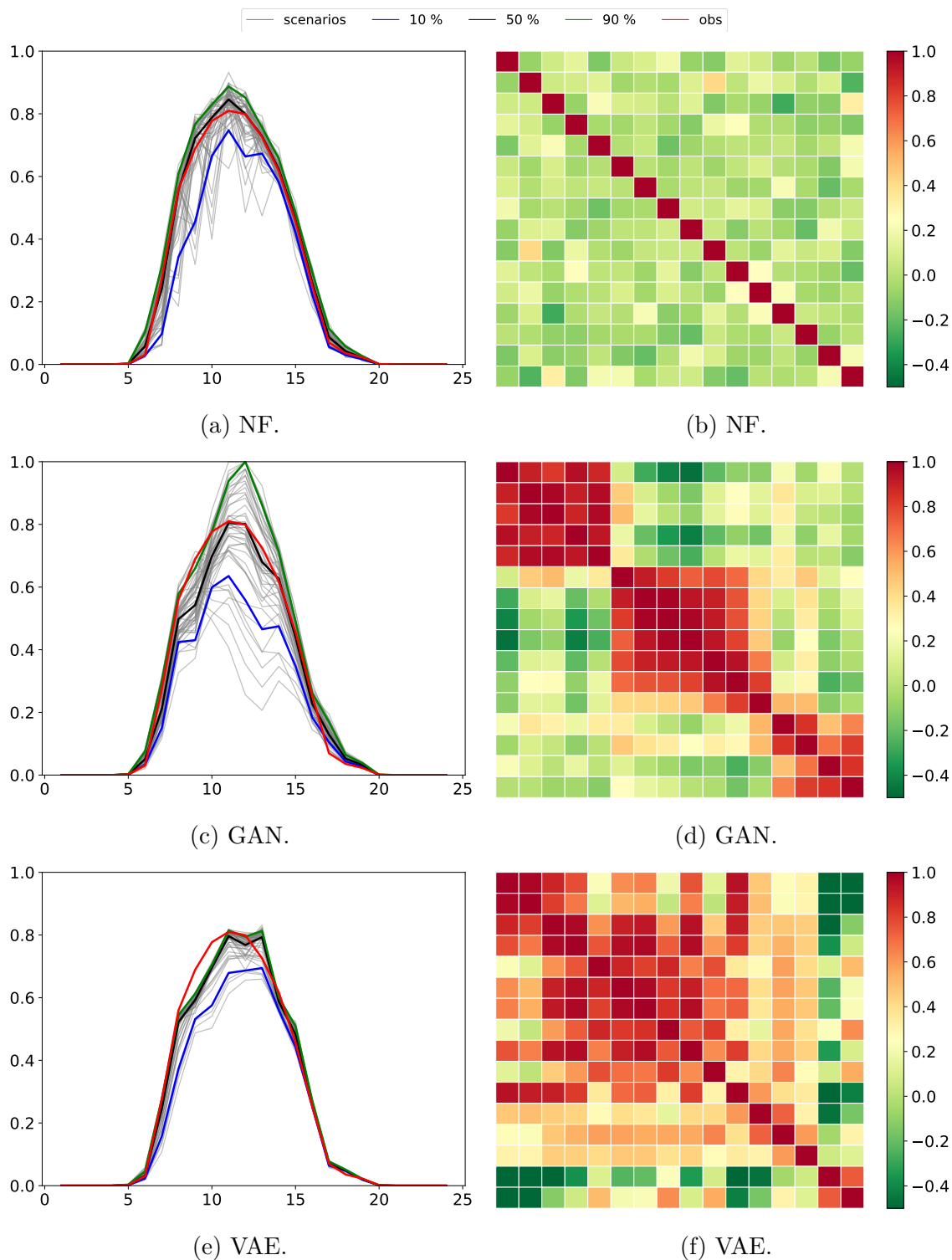


Fig. 8.18 PV scenarios shape comparison and analysis.

Left part (a) NF, (c) GAN, and (e) VAE: 50 PV scenarios (grey) of a randomly selected day of the testing set along with the 10 % (blue), 50 % (black), and 90 % (green) quantiles, and the observations (red). Right part (b) NF, (d) GAN, and (f) VAE: the corresponding Pearson time correlation matrices of these scenarios with the time periods as rows and columns. Similar to wind power and load scenarios, NF tends to exhibit no time correlation between scenarios. In contrast, the VAE and GAN tend to be partially time-correlated over a few time periods.

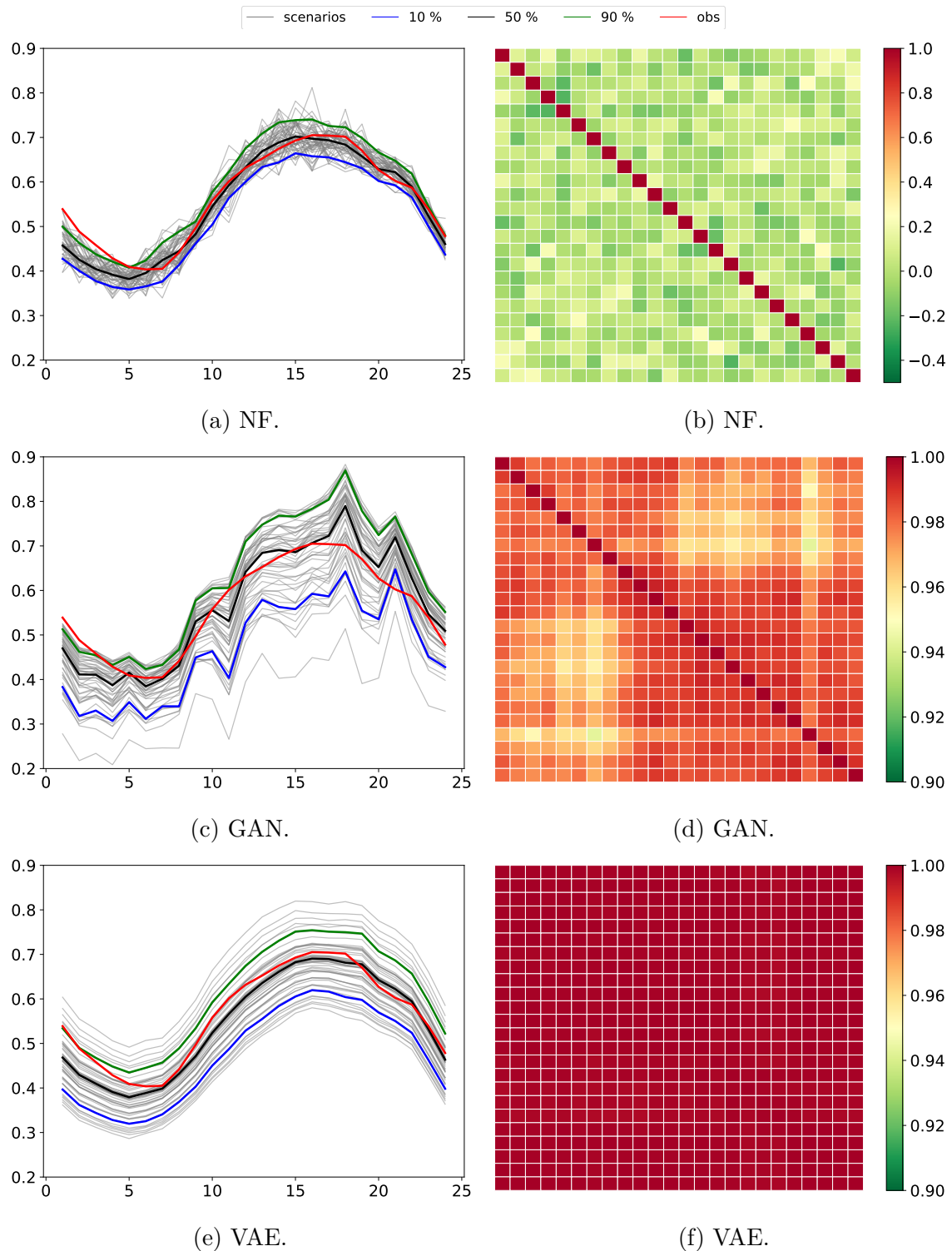


Fig. 8.19 Load scenarios shape comparison and analysis.

Left part (a) NF, (c) GAN, and (e) VAE: 50 load scenarios (grey) of a randomly selected day of the testing set along with the 10 % (blue), 50 % (black), and 90 % (green) quantiles, and the observations (red). Right part (b) NF, (d) GAN, and (f) VAE: the corresponding Pearson time correlation matrices of these scenarios with the time periods as rows and columns. Similar to PV and wind power scenarios, NF tends to exhibit no time correlation between scenarios. In contrast, the VAE and GAN tend to be highly time-correlated.

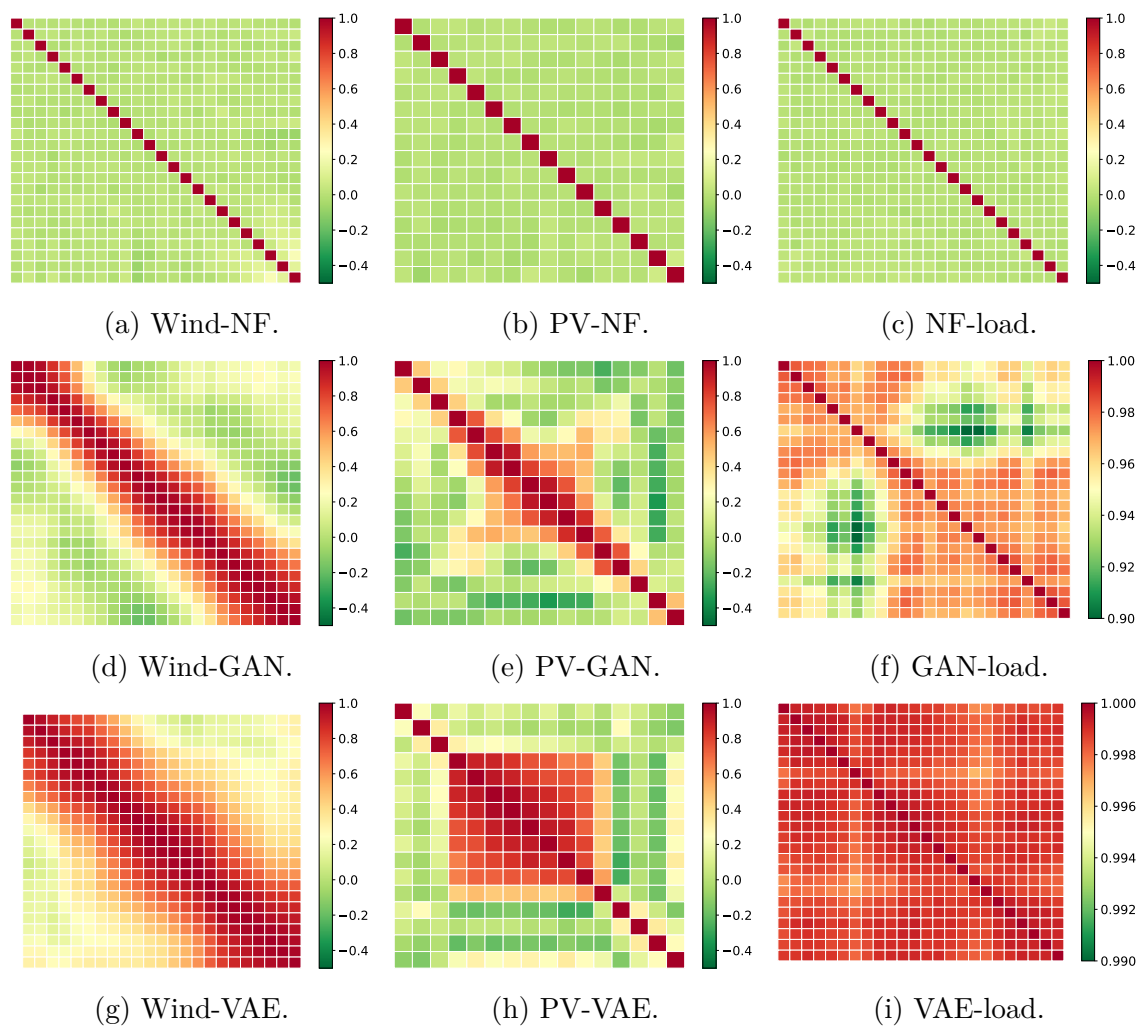


Fig. 8.20 Average of the correlation matrices over the testing set for the three datasets. Left: wind power; center: PV; right: load. The trend in terms of time correlation is observed on each day of the testing set for all the datasets. The NF scenarios are not correlated. In contrast, the VAE and GAN scenarios tend to be time-correlated over a few periods. In particular, the VAE generates highly time-correlated scenarios for the load dataset.

8.6 Conclusions and perspectives

This Chapter proposed a fair and thorough comparison of NFs with the state-of-the-art deep learning generative models, GANs and VAEs, both in terms of quality and value. The experiments were performed by using the open data of the Global Energy Forecasting Competition 2014, where the generative models use the conditional information to compute improved weather-based PV power, wind power, and load scenarios. This Chapter demonstrated that NFs are capable of challenging GANs and VAEs as they are, overall, more accurate both in terms of quality and value (see Chapter 15), and can be used effectively by non-expert deep learning practitioners. In addition, NFs have several advantages over more traditional deep learning approaches that should motivate their introduction into power system applications:

1. NFs directly learn the stochastic multivariate distribution of the underlying process by maximizing the likelihood. Therefore, in contrast to VAEs and GANs, NFs provide access to the exact likelihood of the model's parameters, hence offering a sound and direct way to optimize the network parameters [152]. It may open a new range of advanced applications benefiting from this advantage. For instance, to transfer scenarios from one location to another based on the knowledge of the probability density function. A second application is the importance sampling for stochastic optimization based on a scenario approach. Indeed, NFs provide for each generated scenario its likelihood making it possible to filter relevant scenarios to be used in stochastic optimization.
2. In our opinion, NFs are easier to use by non-expert deep learning practitioners, once the libraries are available, as they are more reliable and robust in terms of hyper-parameters selection. GANs and VAEs are particularly sensitive to the latent space dimension, the structure of the neural networks, the learning rate, etc. GANs convergence, by design, is unstable, and for a given set of hyper-parameters, the scenario's quality may differ completely. In contrast, it was easier to retrieve relevant NFs hyper-parameters by testing manually a few sets of values that led to satisfying training convergence and quality results.

Yet, their usage as a base component of the machine learning toolbox is still limited in comparison to GANs or VAEs.

8.7 Appendix: Table 8.1 justifications

Wang et al. [150] use a Wasserstein GAN with gradient penalty to model both the uncertainties and the variations of the load. Specifically, point forecasting is first conducted and the corresponding residuals are calculated. Then, the GAN generates residual scenarios that are conditional on the day type, temperatures, and historical loads. The GAN model is compared with the same version without gradient penalty, and two quantile regression models: random forest and gradient boosting regression tree. The quality evaluation is conducted on open load datasets from the Independent System Operator-New England³ with five metrics: (1) the continuous rank probability score; (2) the quantile score; (3) the Winkler score; (4) reliability diagrams; (5) Q-Q plots. Note: the forecast value is not assessed.

Qi et al. [126] propose a concentrating solar power (CSP) configuration method to determine the CSP capacity in multi-energy power systems. The configuration model considers the uncertainty by scenario analysis. The scenarios are produced by a β VAE that is an improved version of the original VAE. The weather forecasts are not considered and the VAE is trained only by using historical observations. The quality evaluation is conducted on two wind farms and six PV plants using three metrics: (1) the leave-one-out accuracy of the 1-nearest neighbor classifier; (2) the comparison of the frequency distributions of the real data and the generated scenarios; (3) the comparison of the spatial and temporal correlations of the real data and the scenarios by computing Pearson correlation coefficients. The value is assessed by considering the case study of the CSP configuration model where the β VAE is used to generate scenarios of PV, wind power, and load. However, for both the quality and value evaluations, the VAE is not compared to another generative model. Note: the dataset does not seem to be in open-access. Finally, the value evaluation case study is not trivial due to the mathematical formulation that requires a certain level of knowledge of the system. Thus, the replicability criterion is partially satisfied.

Ge et al. [53] compared NFs to VAEs and GANs for the generation of daily load profiles. The models do not take into account weather forecasts but only historical observations. However, an example is given to illustrate the principle of generating conditional daily load profiles by using three groups which include light load, medium load, and heavy load. The quality evaluation uses five indicators. Four to assess the

³<https://www.iso-ne.com/>

temporal correlation: (1) probability density function; (2) autocorrelation function; (3) load duration curve; (4) a wave rate is defined to evaluate the volatility of the daily load profile. And one additional for the spatial correlation: (5) Pearson correlation coefficient is used to measure the spatial correlation among multiple daily load profiles. The simulations use the open-access London smart meter and Spanish transmission service operator datasets of Kaggle. The forecast value is not assessed.

8.8 Appendix: background

8.8.1 NFs

NF computation

Evaluating the likelihood of a distribution modeled by a normalizing flow requires computing (8.2), *i.e.*, the normalizing direction, as well as its log-determinant. Increasing the number of sub-flows by K of the transformation results in only $\mathcal{O}(K)$ growth in the computational complexity as the log-determinant of J_{f_θ} can be expressed as

$$\log |\det J_{f_\theta}(\mathbf{x})| = \log \left| \prod_{k=1}^K \det J_{f_{k,\theta}}(\mathbf{x}) \right|, \quad (8.16a)$$

$$= \sum_{k=1}^K \log |\det J_{f_{k,\theta}}(\mathbf{x})|. \quad (8.16b)$$

However, with no further assumption on f_θ , the computational complexity of the log-determinant is $\mathcal{O}(K \cdot T^3)$, which can be intractable for large T . Therefore, the efficiency of these operations is particularly important during training where the likelihood is repeatedly computed. There are many possible implementations of NFs detailed by Papamakarios et al. [116], Kobyzev et al. [91] to address this issue.

Autoregressive flow

The Jacobian of the autoregressive transformation f_θ defined by (8.3) is lower triangular, and its log-absolute-determinant is

$$\log |\det J_{f_\theta}(\mathbf{x})| = \log \prod_{i=1}^T \left| \frac{\partial f^i}{\partial x_i}(x_i; h^i) \right|, \quad (8.17a)$$

$$= \sum_{i=1}^T \log \left| \frac{\partial f^i}{\partial x_i}(x_i; h^i) \right|, \quad (8.17b)$$

that is calculated in $\mathcal{O}(T)$ instead of $\mathcal{O}(T^3)$.

Affine autoregressive flow

A simple choice of transformer is the class of affine functions

$$f^i(x_i; h^i) = \alpha_i x_i + \beta_i, \quad (8.18)$$

where $f^i(\cdot; h^i) : \mathbb{R} \rightarrow \mathbb{R}$ is parameterized by $h^i = \{\alpha_i, \beta_i\}$, α_i controls the scale, and β_i controls the location of the transformation. Invertibility is guaranteed if $\alpha_i \neq 0$, and this can be easily achieved by *e.g.* taking $\alpha_i = \exp(\tilde{\alpha}_i)$, where $\tilde{\alpha}_i$ is an unconstrained parameter in which case $h^i = \{\tilde{\alpha}_i, \beta_i\}$. The derivative of the transformer with respect to x_i is equal to α_i . Hence the log-absolute-determinant of the Jacobian becomes

$$\log |\det J_{f_\theta}(\mathbf{x})| = \sum_{i=1}^T \log |\alpha_i| = \sum_{i=1}^T \tilde{\alpha}_i. \quad (8.19)$$

Affine autoregressive flows are simple and computation efficient but are limited in expressiveness requiring many stacked flows to represent complex distributions. It is unknown whether affine autoregressive flows with multiple layers are universal approximators or not [116], in contrast to the UMNN autoregressive transformation implemented in this study.

8.8.2 VAEs

Figure 8.21 illustrates the VAE process with f the encoder and g the decoder.

Gradients computation

By using (8.6) $\mathcal{L}_{\theta, \varphi}$ is decomposed in two parts

$$\mathcal{L}_{\theta, \varphi}(\mathbf{x}, \mathbf{c}) = \mathbb{E}_{q_\varphi(\mathbf{z}|\mathbf{x}, \mathbf{c})} [\log p_\theta(\mathbf{x}|\mathbf{z}, \mathbf{c})] - \text{KL}[q_\varphi(\mathbf{z}|\mathbf{x}, \mathbf{c}) || p(\mathbf{z})]. \quad (8.20)$$

$\nabla_\theta \mathcal{L}_{\theta, \varphi}$ is estimated with the usual Monte Carlo gradient estimator. However, the estimation of $\nabla_\varphi \mathcal{L}_{\theta, \varphi}$ requires the reparameterization trick proposed by Kingma and Welling [88], where the random variable \mathbf{z} is re-expressed as a deterministic variable

$$\mathbf{z} = g_\varphi(\epsilon, \mathbf{x}), \quad (8.21)$$

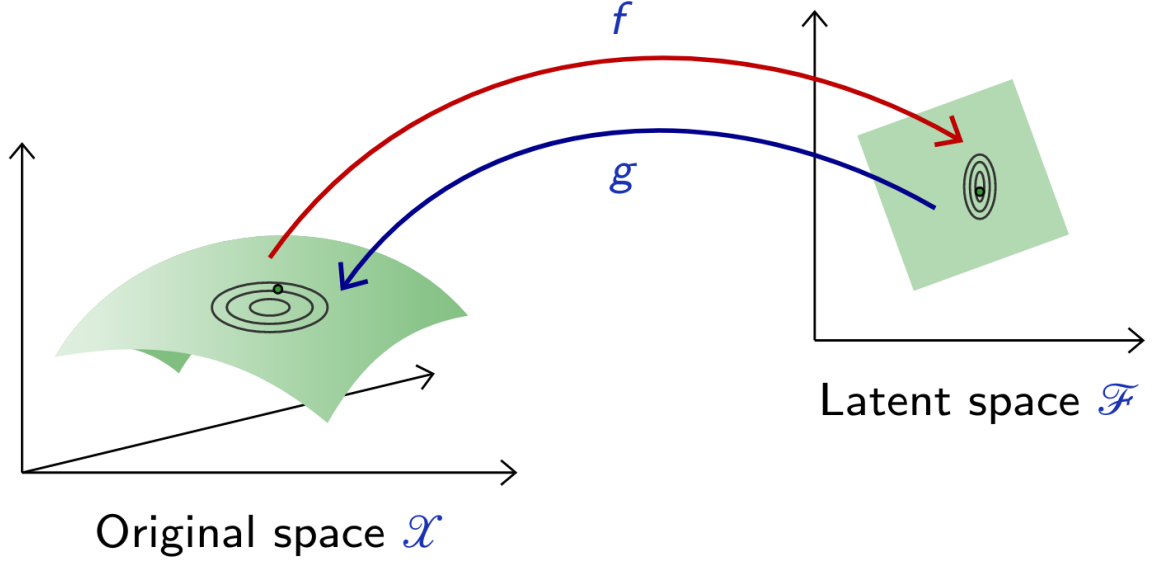


Fig. 8.21 VAE process. Credits: Francois Fleuret, EE559 Deep Learning, EPFL <https://fleuret.org/dlc/>

with ϵ an auxiliary variable with independent marginal p_ϵ , and $g_\varphi(\cdot)$ some vector-valued function parameterized by φ . Then, the first right hand side of (8.20) becomes

$$\mathbb{E}_{q_\varphi(\mathbf{z}|\mathbf{x},\mathbf{c})}[\log p_\theta(\mathbf{x}|\mathbf{z},\mathbf{c})] = \mathbb{E}_{p(\epsilon)}[\log p_\theta(\mathbf{x}|g_\varphi(\epsilon,\mathbf{x}),\mathbf{c})]. \quad (8.22)$$

$\nabla_\varphi \mathcal{L}_{\theta,\varphi}$ is now estimated with Monte Carlo integration.

Conditional VAE implemented

Following Kingma and Welling [88], we implemented Gaussian multi-layer perceptrons (MLPs) for both the encoder NN_φ and decoder NN_θ . In this case, $p(\mathbf{z})$ is a centered isotropic multivariate Gaussian, $p_\theta(\mathbf{x}|\mathbf{z},\mathbf{c})$ and $q_\varphi(\mathbf{x}|\mathbf{z},\mathbf{c})$ are both multivariate Gaussian with a diagonal covariance and parameters $\boldsymbol{\mu}_\theta, \boldsymbol{\sigma}_\theta$ and $\boldsymbol{\mu}_\varphi, \boldsymbol{\sigma}_\varphi$, respectively. Note that there is no restriction on the encoder and decoder architectures, and they could as well be arbitrarily complex convolutional networks. Under these assumptions, the

conditional VAE implemented is

$$p(\mathbf{z}) = \mathcal{N}(\mathbf{z}; \mathbf{0}, \mathbf{I}), \quad (8.23a)$$

$$p_\theta(\mathbf{x}|\mathbf{z}, \mathbf{c}) = \mathcal{N}(\mathbf{x}; \boldsymbol{\mu}_\theta, \boldsymbol{\sigma}_\theta^2 \mathbf{I}), \quad (8.23b)$$

$$q_\varphi(\mathbf{z}|\mathbf{x}, \mathbf{c}) = \mathcal{N}(\mathbf{z}; \boldsymbol{\mu}_\varphi, \boldsymbol{\sigma}_\varphi^2 \mathbf{I}), \quad (8.23c)$$

$$\boldsymbol{\mu}_\theta, \log \boldsymbol{\sigma}_\theta^2 = \text{NN}_\theta(\mathbf{x}, \mathbf{c}), \quad (8.23d)$$

$$\boldsymbol{\mu}_\varphi, \log \boldsymbol{\sigma}_\varphi^2 = \text{NN}_\varphi(\mathbf{z}, \mathbf{c}). \quad (8.23e)$$

Then, by using the valid reparameterization trick proposed by Kingma and Welling [88]

$$\boldsymbol{\epsilon} \sim \mathcal{N}(\mathbf{0}, \mathbf{I}), \quad (8.24a)$$

$$\mathbf{z} := \boldsymbol{\mu}_\varphi + \boldsymbol{\sigma}_\varphi \boldsymbol{\epsilon}, \quad (8.24b)$$

$\mathcal{L}_{\theta, \varphi}$ is computed and differentiated without estimation using the expressions

$$\text{KL}[q_\varphi(\mathbf{z}|\mathbf{x}, \mathbf{c})||p(\mathbf{z})] = -\frac{1}{2} \sum_{j=1}^d (1 + \log \boldsymbol{\sigma}_{\varphi, j}^2 - \boldsymbol{\mu}_{\varphi, j}^2 - \boldsymbol{\sigma}_{\varphi, j}^2), \quad (8.25a)$$

$$\mathbb{E}_{p(\boldsymbol{\epsilon})} [\log p_\theta(\mathbf{x}|\mathbf{z}, \mathbf{c})] \approx -\frac{1}{2} \left\| \frac{\mathbf{x} - \boldsymbol{\mu}_\theta}{\boldsymbol{\sigma}_\theta} \right\|^2, \quad (8.25b)$$

with d the dimensionality of \mathbf{z} .

8.8.3 GANs

GAN

The original GAN value function $V(\phi, \theta)$ proposed by Goodfellow et al. [65] is

$$V(\phi, \theta) = \underbrace{\mathbb{E}_{\mathbf{x}} [\log d_\phi(\mathbf{x}|\mathbf{c})] + \mathbb{E}_{\hat{\mathbf{x}}} [\log(1 - d_\phi(\hat{\mathbf{x}}|\mathbf{c}))]}_{:= -L_d}, \quad (8.26a)$$

$$L_g := -\mathbb{E}_{\hat{\mathbf{x}}} [\log(1 - d_\phi(\hat{\mathbf{x}}|\mathbf{c}))], \quad (8.26b)$$

where L_d is the cross-entropy, and L_g the probability the discriminator wrongly classifies the samples.

WGAN

The divergences which GANs typically minimize are responsible for their training instabilities for reasons investigated theoretically by Arjovsky and Bottou [5]. Arjovsky et al. [6] proposed instead using the *Earth mover* distance, also known as the Wasserstein-1 distance

$$W_1(p, q) = \inf_{\gamma \in \Pi(p, q)} \mathbb{E}_{(x, y) \sim \gamma} [\|x - y\|], \quad (8.27)$$

where $\Pi(p, q)$ denotes the set of all joint distributions $\gamma(x, y)$ whose marginals are respectively p and q , $\gamma(x, y)$ indicates how much mass must be transported from x to y in order to transform the distribution p into q , $\|\cdot\|$ is the L1 norm, and $\|x - y\|$ represents the cost of moving a unit of mass from x to y . However, the infimum in (8.27) is intractable. Therefore, Arjovsky et al. [6] used the Kantorovich-Rubinstein duality [146] to propose the Wasserstein GAN (WGAN) by solving the min-max problem

$$\theta^* = \arg \min_{\theta} \max_{\phi \in \mathcal{W}} \mathbb{E}_{\mathbf{x}} [d_{\phi}(\mathbf{x}|\mathbf{c})] - \mathbb{E}_{\hat{\mathbf{x}}} [d_{\phi}(\hat{\mathbf{x}}|\mathbf{c})], \quad (8.28)$$

where $\mathcal{W} = \{\phi : \|d_{\phi}(\cdot)\|_L \leq 1\}$ is the 1-Lipschitz space, and the classifier $d_{\phi}(\cdot) : \mathbb{R}^T \times \mathbb{R}^{|\mathbf{c}|} \rightarrow [0, 1]$ is replaced by a critic function $d_{\phi}(\cdot) : \mathbb{R}^T \times \mathbb{R}^{|\mathbf{c}|} \rightarrow \mathbb{R}$. However, the weight clipping used to enforce d_{ϕ} 1-Lipschitzness can lead sometimes the WGAN to generate only poor samples or failure to converge [68]. Therefore, we implemented the WGAN-GP to tackle this issue.

Chapter 9

Part [I](#) conclusions

“If you’re lonely when you’re alone, you’re in bad company.”

— **Jean-Paul Sartre**

Part [I](#) presents the forecasting tools and metrics required to produce and evaluate reliable point and probabilistic forecasts to be used as input of decision-making models. These forecasts are introduced in their various forms: point forecasts, quantiles, prediction intervals, confidence intervals, density forecasts, and scenarios. They are evaluated in terms of quality on several case studies.

- The PV and electrical consumption point forecasts using common deep learning models such as recurrent neural networks. It illustrates the forecasting process on a simple case study, and this framework is extended in the following Chapters for probabilistic forecasting.
- PV quantile forecasts are computed by deep learning models such as the encoder-decoder architecture, and recurrent neural networks. These models are trained by quantile regression. The forecast quality is evaluated on a real case study composed of the PV generation of the parking rooftops of the Liège University. The quantile forecasts are used as input of robust optimization planners in Part [II](#) in the form of prediction intervals. The quantile regression models are compared to quantiles derived from deep learning generative models. In terms of forecast quality, the latter models outperform, in this case, the quantile regression models.
- A probabilistic forecasting of imbalance prices with a particular focus on the Belgian case using a confidence interval-based approach. The two-step probabilistic approach consists of the first step to compute the net regulation volume

state transition probabilities. It is used in the second step to infer the imbalance price. A numerical comparison of this approach to common forecasting techniques is performed on the Belgium case. The proposed model outperforms other approaches on probabilistic error metrics but is less accurate at predicting the precise imbalance prices. This probabilistic approach could be improved by deep learning models to avoid making some simplifying assumptions, and by adding input features to better describe the market situation.

- A fair and thorough comparison of NFs with the state-of-the-art deep learning generative models, GANs and VAEs, is conducted both in terms of quality and value. The experiments are performed by using the open data of the Global Energy Forecasting Competition 2014, where the generative models use the conditional information to compute improved weather-based PV power, wind power, and load scenarios. It demonstrated that NFs are capable of challenging GANs and VAEs as they are, overall, more accurate both in terms of quality and value (see Chapter 15), and can be used effectively by non-expert deep learning practitioners.

Part II

Planning and control

Overview

Part II presents the decision-making tools under uncertainty required to address the day-ahead planning of a microgrid. It investigates several approaches: deterministic planning using linear programming based on point forecasts, stochastic programming using scenarios, and robust optimization using quantile forecasts. Several case studies are considered: a grid-connected microgrid using a value function approach to propagate the information from planning to real-time optimization, a grid-connected microgrid in the capacity firming framework, and an energy retailer on the day-ahead market. The case studies use the forecasting techniques studied in Part I.

“*The straight line, a respectable optical
illusion which ruins many a man.*”

— **Victor Hugo**

Figure 9.1 illustrates the organization of the second part. It addresses the energy management of a grid-connected microgrid by using the forecasting techniques studied in Part I. Chapter 10 provides the optimization basics. Chapter 11 proposes a value function-based approach as a way to propagate information from operational planning to real-time optimization. Chapters 12, 13, and 14 propose stochastic, sizing, and robust approaches to address the energy management of a grid-connected renewable generation plant coupled with a battery energy storage device in the capacity firming market, respectively. The capacity firming framework is mainly designed for isolated markets, such as the Overseas France islands. Chapter 15 investigates the forecast value assessment of the deep generative models studied in Dumas et al. [48], by considering an energy retailer portfolio on the day-ahead market, and is the extension of Chapter 8. Finally, Chapter 16 draws the conclusions of Part II.

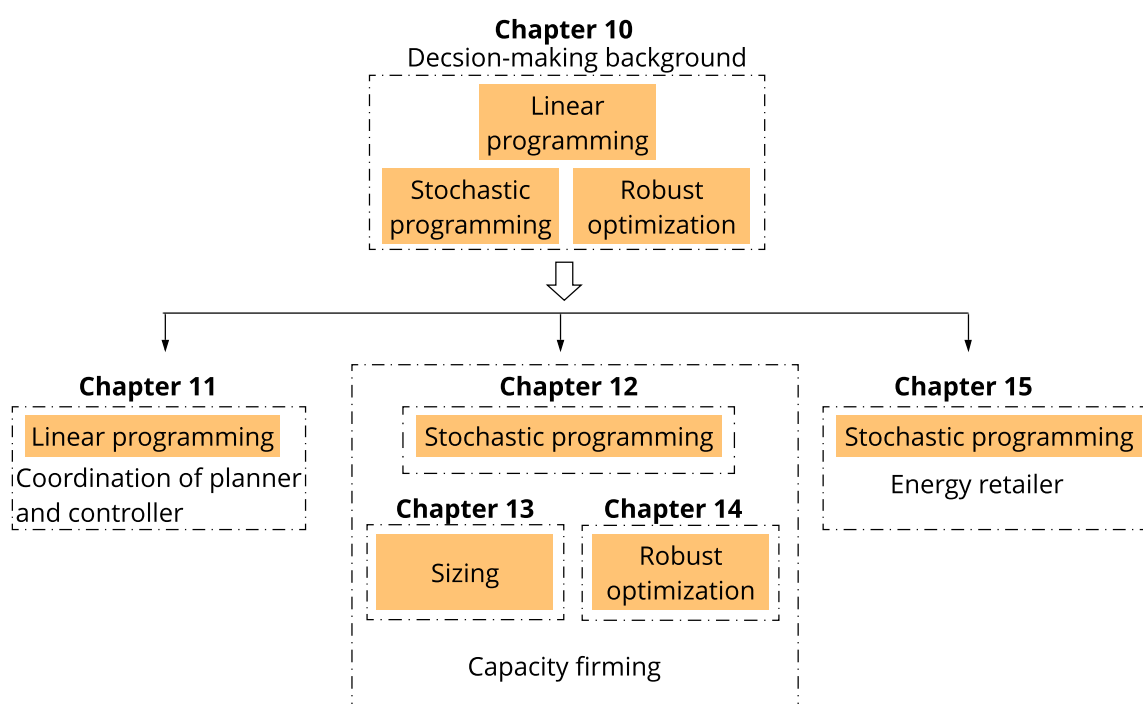


Fig. 9.1 Part II skeleton.

Chapter 10

Decision-making background

Overview

This Chapter introduces some basics of linear programming and optimization methodologies to address uncertainty in decision-making that will be used to formulate the problems considered in Part II.

The interested reader is referred to more general textbooks for further information [105, 13, 19] and the lectures of the courses "Renewables in Electricity Markets"^a and "Advanced Optimization and Game Theory for Energy Systems"^b given by Pierre Pinson, professor at the Technical University of Denmark, and Jalal Kazempour, associate professor at the Technical University of Denmark.

^a<http://pierrepinson.com/index.php/teaching/>

^b<https://www.jalalkazempour.com/teaching>

“ Nothing is more difficult, and therefore more precious, than to be able to decide.”

— **Napoleon Bonaparte**

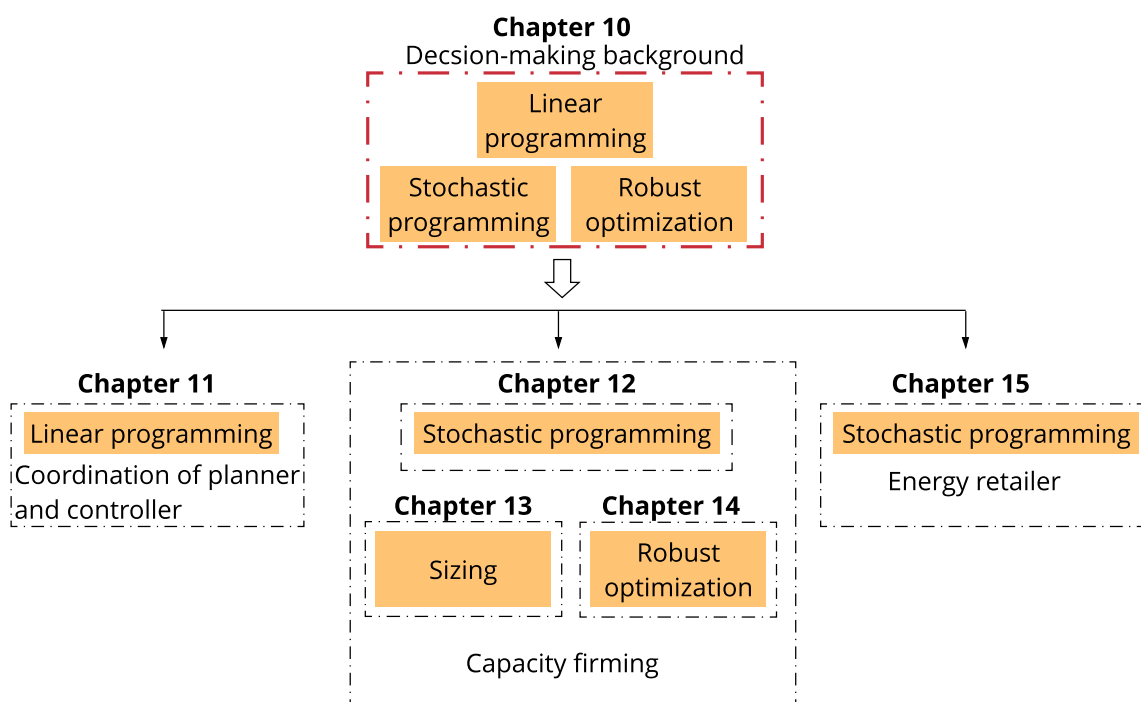


Fig. 10.1 Chapter 10 position in Part II.

Section 10.1 introduces the mathematical formulation of a linear optimization problem. Sections 10.2 and 10.3 present the mathematical formulations of a linear optimization problem when considering uncertainty in the parameters of the problem. First, by considering a stochastic programming approach. Second, by using a robust methodology.

10.1 Linear programming

Formulation of a linear programming problem

The simplest instance of an optimization problem is a linear programming problem.

Definition 10.1.1 (Linear programming). Linear programming (LP) is the problem of minimizing a linear cost function subject to linear equality and inequality constraints.

In a LP problem, we are given a cost vector $\mathbf{c} \in \mathbb{R}^n$ and we seek to minimize a linear cost function $\mathbf{c}^\top \mathbf{x}$ over all n -dimensional vectors $\mathbf{x} \in \mathbb{R}^n$ subject to a set of linear equality and inequality constraints. Suppose that there is a total of m such constraints and let $\mathbf{b} \in \mathbb{R}^m$ and \mathbf{A} be the $m \times n$ matrix. The constraints can be expressed compactly in the form $\mathbf{Ax} \geq \mathbf{b}$.

Definition 10.1.2 (LP in standard form). [13, Chapter 1] A linear programming problem of the form

$$\begin{aligned} \min_{\mathbf{x}} \quad & \mathbf{c}^\top \mathbf{x} \\ \text{s.t.} \quad & \mathbf{Ax} = \mathbf{b}, \\ & \mathbf{x} \geq \mathbf{0}, \end{aligned} \tag{10.1}$$

is said to be in the *standard form*.

LP problems model a wide variety of real-world problems such as day-ahead planning of a microgrid.

Duality in linear programming

Duality theory deals with the relation between a LP problem, called the *primal*, and another LP problem, called the *dual*.

'This theory uncovers the deeper structure of LP, and it is a powerful tool that has numerous applications. Duality theory is motivated as an outgrowth of the Lagrange multiplier method, where a price variable is associated with each constraint. It starts searching for prices under which the presence or absence of the constraints does not affect the optimal cost. It turns out the right prices can be found by solving a new LP problem, called the dual of the original.' [13, Chapter 4]

Definition 10.1.3 (Dual of a LP problem). [13, Chapter 4] Given a primal problem in the standard form (10.1), its dual is defined as

$$\begin{aligned} \max_{\mathbf{p}} \quad & \mathbf{p}^\top \mathbf{b} \\ \text{s.t.} \quad & \mathbf{p}^\top \mathbf{A} \leq \mathbf{c}^\top, \\ & \mathbf{x} \geq \mathbf{0}, \end{aligned} \tag{10.2}$$

with \mathbf{p} the price vector of the same dimension as \mathbf{b}

Note that the dual of the dual problem is the primal problem. The *strong duality* theorem is the central result on linear programming duality.

'If a linear programming problem has an optimal solution so does its dual, and the respective optimal costs are equal.' [13, Chapter 4, Theorem 4.4]

10.2 Stochastic optimization

'Most decision-making problems are subject to uncertainty, due to the inherent randomness of natural phenomena conditioning our choices, *e.g.*, the weather or, more generally, to the inaccurate knowledge of input information. Decision makers are, therefore, eager for methods and tools that lead them to solutions less sensitive to environmental influences or imprecise data, while simultaneously reducing cost, increasing profit, or improving reliability.' [105, Appendix C]

Let consider a LP in the standard form (10.1). If parameters \mathbf{A} , \mathbf{b} , and \mathbf{c} are perfectly known, solution algorithms for linear optimization problems, *e.g.*, the simplex method, can be used to find the best value of the decision variable vector \mathbf{x} .

However, if some of these parameters are contingent on the realization $\xi(\omega)$ of a certain random vector ξ , determining the optimal solution to problem (10.1) may

becomes more challenging. First, the issue of how to guarantee the feasibility of decision vector \mathbf{x} becomes remarkably more involved when optimizing under uncertainty because \mathbf{A} and \mathbf{b} are not completely known in advance. Second, the issue of how to guarantee the optimality of decision vector \mathbf{x} is at stake because \mathbf{c} is not completely known in advance. Finally, the LP problem (10.1) needs to be recast so that solution algorithms for linear programming problems can be used to obtain the optimal value of decision vector \mathbf{x} taking into account the uncertainty of the parameters.

Stochastic programming provides the concepts and tools required to deal with the implications of having uncertain data in an optimization problem for decision making to address the three issues previously stated. It assumes that an accurate probabilistic description of the random variable is assumed available, under the form of the probability distributions or densities. In the following, we consider stochastic programming with *recourse* where the set of decisions is divided into two groups: (1) decisions have to be taken before the realization of uncertain parameters. These decisions are known as *first-stage*, \mathbf{x} , or here-and-now decisions and do not depend on the realization of the random parameters; (2) decisions can be taken after the realization of uncertain parameters. These decisions are called *second-stage*, $\mathbf{y}(\mathbf{x}, \omega)$, or recourse decisions and are dependent on each plausible value of the random parameters. Note, the term recourse points to the fact that second-stage decisions enable the decision-maker to adapt to the actual outcomes of the random events.

Definition 10.2.1 (Two-stage program with fixed recourse). [19, Chapter 2] A classical two-stage stochastic linear program with fixed recourse is

$$\begin{aligned} \min_{\mathbf{x}} \quad & \mathbf{c}^T \mathbf{x} + \mathbb{E}_{\xi}[Q(\mathbf{x}, \xi(\omega))] \\ \text{s.t.} \quad & \mathbf{Ax} = \mathbf{b}, \\ & \mathbf{x} \geq \mathbf{0}, \end{aligned} \tag{10.3}$$

with

$$\begin{aligned} Q(\mathbf{x}, \xi(\omega)) = \min_{\mathbf{y}} \quad & \mathbf{q}(\omega)^T \mathbf{y} \\ \text{s.t.} \quad & \mathbf{Wy} = \mathbf{h}(\omega) - T(\omega)\mathbf{x}, \quad \forall \omega \in \Omega \\ & \mathbf{y} \geq \mathbf{0}, \quad \forall \omega \in \Omega \end{aligned} \tag{10.4}$$

the second-stage value function.

Note, the uncertainty involved in problem (10.3) and (10.4) is assumed to be properly represented by means of a finite set Ω of scenarios ω , with a probability α_ω such that $\sum_{\omega \in \Omega} \alpha_\omega = 1$.

Definition 10.2.2 (Deterministic equivalent problem). [19, Chapter 2] The *deterministic equivalent* problem of the stochastic programming problem (10.3)-(10.4) is

$$\begin{aligned} \min_{\mathbf{x}, \mathbf{y}} \quad & \mathbf{c}^\top \mathbf{x} + \sum_{\omega \in \Omega} \alpha_\omega \mathbf{q}(\omega)^\top \mathbf{y} \\ \text{s.t.} \quad & \mathbf{Ax} = \mathbf{b}, \\ & \mathbf{Wy} = \mathbf{h}(\omega) - \mathbf{T}(\omega)\mathbf{x}, \quad \forall \omega \in \Omega \\ & \mathbf{x} \geq \mathbf{0}, \\ & \mathbf{y} \geq \mathbf{0}, \quad \forall \omega \in \Omega \end{aligned} \tag{10.5}$$

and can be directly processed by off-the-shelf optimization software for linear programs.

10.3 Robust optimization

'Robust optimization addresses optimization problems with uncertain parameters that are not described using probability distributions but *uncertainty sets*. A robust optimization problem seeks to determine a solution to an optimization problem that is feasible for any realization of the uncertain parameters within the uncertainty set, and optimal for the worst-case realization of these uncertain parameters.' [105, Appendix D]

Definition 10.3.1 (Two-stage robust optimization with fixed recourse). The general form of two-stage robust optimization formulation is

$$\begin{aligned} \min_{\mathbf{x}} \quad & \mathbf{c}^\top \mathbf{x} + \max_{\mathbf{u} \in \mathcal{U}} \min_{\mathbf{y} \in \Omega(\mathbf{x}, \mathbf{u})} \mathbf{q}^\top \mathbf{y} \\ \text{s.t.} \quad & \mathbf{Ax} = \mathbf{b}, \\ & \mathbf{x} \geq \mathbf{0}, \end{aligned} \tag{10.6}$$

with \mathcal{U} the uncertainty set and

$$\Omega(\mathbf{x}, \mathbf{u}) = \{\mathbf{y} \geq \mathbf{0} : \mathbf{Wy} = \mathbf{h} - \mathbf{T}\mathbf{x} - \mathbf{Mu}\}. \tag{10.7}$$

The objective of the problem (10.6) is to make the best decisions represented by variable vector \mathbf{x} for the worst realization of parameters in vector \mathbf{u} and consid-

ering the recourse decisions described by variable vector \mathbf{y} . If the right-hand-side problem, the \mathbf{y} -problem, is convex, it can be replaced by its dual and merged with the middle \mathbf{u} -problem rendering it a conventional single-level maximization problem. Overall, the resulting problem is a min-max problem that in some cases can be solved using decomposition such as the Benders-dual cutting plane method [15] or column-and-constraint generation algorithm [157]. Both the Benders-dual method and the column-and-constraint generation procedure are implemented in a master sub-problem framework.

10.3.1 Benders-dual cutting plane algorithm

The key idea of the Benders-dual cutting plane (BD) algorithm is to gradually construct the value function of the first-stage decisions using dual solutions of the second-stage decision problems.

Consider the case where the second-stage decision problem is a linear programming (LP) problem in \mathbf{x} . We first take the *relatively complete recourse* assumption that this LP is feasible for any given \mathbf{x} and \mathbf{u} . Let \mathbf{p} be its dual variables. Then, we obtain its dual problem, which is a maximization problem and can be merged with the maximization over \mathbf{u} . As a result, we have the following dispatch problem, which yields the sub-problem (SP) in the BD algorithm.

Definition 10.3.2 (BD sub-problem).

$$\begin{aligned} R(\mathbf{x}) = \max_{\mathbf{u}, \mathbf{p}} & (\mathbf{h} - \mathbf{T}\mathbf{x} - \mathbf{M}\mathbf{u})^\top \mathbf{p} \\ \text{s.t. } & \mathbf{W}^\top \mathbf{p} \geq \mathbf{q}, \\ & \mathbf{u} \in \mathcal{U}. \end{aligned} \tag{10.8}$$

Note: that the resulting problem in (10.8) is a bilinear optimization problem. Several approaches have been developed to address this issue and depend on the case study.

Suppose, we have an oracle that can solve (10.8) for a given first stage variable \mathbf{x} . Then, the optimal solution is $(\mathbf{p}^*, \mathbf{u}^*)$, and a cutting plane in the form of

$$\theta \geq (\mathbf{h} - \mathbf{T}\mathbf{x} - \mathbf{M}\mathbf{u}^*)^\top \mathbf{p}^* \tag{10.9}$$

can be generated, and included in the master problem (MP).

Definition 10.3.3 (BD master problem). At iteration k of the BD master problem is

$$\min_{\mathbf{x}, \theta} \mathbf{c}^\top \mathbf{x} + \theta \quad (10.10)$$

$$\text{s.t. } \mathbf{Ax} = \mathbf{b},$$

$$\theta \geq (\mathbf{h} - \mathbf{T}\mathbf{x} - \mathbf{Mu}_l^\star)^\top \mathbf{p}_l^\star \quad \forall l \leq k \quad (10.11)$$

$$\mathbf{x} \geq \mathbf{0}, \quad \theta \in \mathbb{R},$$

which can compute an optimal first stage solution \mathbf{x}_k^\star .

The MP and SP provide the lower and upper bounds with $\mathbf{c}^\top \mathbf{x}_k^\star + \theta_k^\star$ and $R(\mathbf{x}_{k-1}^\star)$, respectively, at iteration k . When considering the relatively complete recourse assumption, [157, 15, 12] demonstrated the BD algorithm converges to the optimal solution of the two-stage robust optimization problem. The lower and upper bounds converge in a finite number of steps by iteratively introducing cutting planes (10.9) and computing the MP (10.10). Note: if the SP is a MILP this result is not straightforward. It is the case in the capacity firming problem studied in Chapter 14 where this issue is addressed.

10.3.2 Column and constraints generation algorithm

The column and constraints generation (CCG) algorithm does not create constraints using dual solutions of the second-stage decision problem. It dynamically generates constraints with recourse decision variables in the primal space for an identified scenario. Let assume the uncertainty set \mathcal{U} is a finite discrete set with $\mathcal{U} = \{\mathbf{u}_1, \dots, \mathbf{u}_N\}$ and $\{\mathbf{y}_1, \dots, \mathbf{y}_N\}$ are the corresponding recourse decision variables. Then, the 2-stage RO (10.6) can be reformulated as follows

$$\min_{\mathbf{x}, \theta} \mathbf{c}^\top \mathbf{x} + \theta \quad (10.12)$$

$$\text{s.t. } \mathbf{Ax} = \mathbf{b}, \quad (10.13)$$

$$\theta \geq \mathbf{q}^\top \mathbf{y}^l \quad \forall l \leq N \quad (10.14)$$

$$\mathbf{W}\mathbf{y}^l = \mathbf{h} - \mathbf{T}\mathbf{x} - \mathbf{Mu}^l \quad \forall l \leq N \quad (10.15)$$

$$\mathbf{x} \geq \mathbf{0}, \quad \mathbf{y}^l \geq \mathbf{0} \quad \forall l \leq N, \quad \theta \in \mathbb{R}, \quad (10.16)$$

Thus, it reduces to solve an equivalent, probably large-scale, MILP, which is very close to a 2-stage stochastic programming model if the probability distribution over \mathcal{U} is known. When the uncertainty set is large or is a polyhedron, enumerating all the

possible uncertain scenarios in \mathcal{U} is not feasible. Constraints (10.14) indicate that not all scenarios, and their corresponding variables and constraints, are necessary for defining the optimal value \mathbf{x}^* of the 2-stage RO. It is likely a few relevant scenarios, a small subset of the uncertainty set, play a significant role in the formulation. Therefore, the key idea of the CCG procedure is to generate recourse decision variables for the significant scenarios.

Definition 10.3.4 (CCG sub-problem). Similar to the BD method, the CCG algorithm uses a master sub-problem framework. Let assume an oracle can solve the dispatch problem for a given first-stage \mathbf{x}

$$Q(\mathbf{x}) = \max_{\mathbf{u} \in \mathcal{U}} \min_{\mathbf{y} \in \Omega(\mathbf{x}, \mathbf{u})} \mathbf{q}^\top \mathbf{y}. \quad (10.17)$$

Then, the optimal solution \mathbf{u}^* can be derived to build constraints and variables in the master problem.

Definition 10.3.5 (CCG master problem). At iteration k of the CCG master problem is

$$\min_{\mathbf{x}, \theta} \mathbf{c}^\top \mathbf{x} + \theta \quad (10.18)$$

$$\text{s.t. } \mathbf{Ax} = \mathbf{b}, \quad (10.19)$$

$$\theta \geq \mathbf{q}^\top \mathbf{y}^l \quad \forall l \leq k \quad (10.20)$$

$$\mathbf{Wy}^l = \mathbf{h} - \mathbf{T}\mathbf{x} - \mathbf{Mu}^{*,l} \quad \forall l \leq k \quad (10.21)$$

$$\mathbf{x} \geq \mathbf{0}, \quad \mathbf{y}^l \geq \mathbf{0} \quad \forall l \leq k, \quad \theta \in \mathbb{R}, \quad (10.22)$$

which can compute an optimal first stage solution \mathbf{x}_k^* .

Similar to BD, the MP and SP provide the lower and upper bounds with $\mathbf{c}^\top \mathbf{x}_k^* + \theta_k^*$ and $Q(\mathbf{x}_{k-1}^*)$, respectively, at iteration k .

10.4 Conclusions

This Chapter introduces the basics of linear programming and approaches to handle uncertainty in the parameters with the stochastic programming and robust approach. Depending on the application, each approach has its pros and cons. When considering stochastic programming, the number of scenarios needed to describe the most plausible outcomes of the uncertain parameters may be very large, leading to large-scale optimization problems that may become difficult to solve or intractable. In this case, a robust

approach provides an alternative and compact manner to describe uncertain parameters. However, the robust counterpart optimization problem may be difficult to solve and requires a decomposition technique such as a Benders-dual cutting plane or column and constraints generation algorithm that is not trivial to implement numerically.

Chapter 11

Coordination of the planner and controller

Overview

This Chapter presents a two-layer approach with a value function to propagate information from operational planning to real-time optimization. The value function-based approach shares some similarities with the coordination scheme proposed in Kumar et al. [93], which is based on stochastic dual dynamic programming. This study brings new contributions:

1. The approach is tested by accounting for forecasting errors and high-resolution data monitored on-site corresponding to a "real-life" case.
2. The value function approach allows to deal with indeterminacy issues. When there are several optimal solutions to the upper-level problem, this is accounted for in the lower level part, and a bias term can be added to favor one type of behavior over another, *e.g.*, charge early.
3. This methodology is fully compatible with the energy markets as it can deal with imbalance, reserve, and dynamic selling/purchasing prices.

This study reports results on an industrial microgrid capable of on/off-grid operation. Generation and consumption forecasts are based on weather forecasts obtained with the MAR model [50].

References: This chapter is an adapted version of the following publication:

Jonathan Dumas, Selmane Dakir, Clément Liu, and Bertrand Cornélusse. Coordination of operational planning and real-time optimization in microgrids. *Electric Power Systems Research*, 190:106634, 2021. URL <https://arxiv.org/abs/2106.02374>.

Terminology and notations have been slightly adjusted for the sake of consistency with the rest of this manuscript. The text has also been processed to minimize overlap with respect to the next chapters.

“When making a decision of minor importance, I have always found it advantageous to consider all the pros and cons. In vital matters, however, such as the choice of a mate or a profession, the decision should come from the unconscious, from somewhere within ourselves. In the important decisions of personal life, we should be governed, I think, by the deep inner needs of our nature.”

— Sigmund Freud

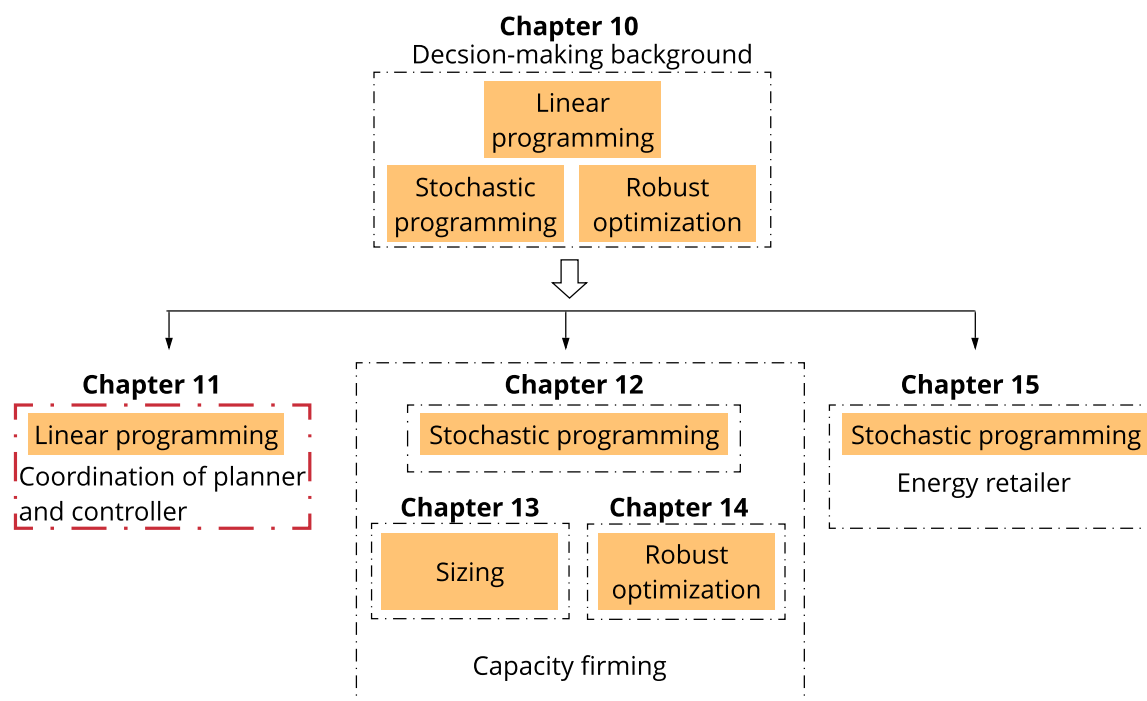


Fig. 11.1 Chapter 11 position in Part II.

The hierarchical microgrid control levels divide a global microgrid control problem in time and space [113]. Control levels range from distributed device level controllers that run at a high frequency to centralized controllers optimizing market integration that run much less frequently. For computation time reasons, centralized controllers are often subdivided into operational planning controllers that optimize decisions over a time horizon of one or several days but with a market period resolution, *e.g.*, 15 minutes, and real-time optimization controllers that deal with actions within the current market period. The coordination of these two levels is of paramount importance to achieve the safest and most profitable operational management of microgrids. Microgrid control and management can be achieved in several ways. Control techniques and the principles of energy-storage systems are summarized in Palizban et al. [113]. A classification of microgrid control strategies into primary, secondary, and tertiary levels is done in Olivares et al. [110]. The two-level approach has been intensively studied. A double-layer coordinated control approach, consisting of the scheduling layer and the dispatch layer is adopted in Jiang et al. [80]. The schedule layer provides an economical operation scheme including state and power of controllable units based on the look-ahead multi-step optimization, while the dispatch layer follows the scheduling layer by considering power flow and voltage limits. A two-stage dispatch strategy for grid-connected systems is discussed in Wu et al. [153], where the first stage deals with the day-ahead schedule, optimizing capital and operational cost, while the lower level handles the rescheduling of the units for few hours ahead with a time resolution of 15 min. A two-stage control strategy for a PV BESS-ICE (Internal Combustion Engine) microgrid is implemented in Sachs and Sawodny [131]. Discrete Dynamic Programming is used in the first layer, while the second layer problem is posed as a Boundary Value Problem. An approach with a high-level deterministic optimizer running at a slow timescale, 15 min, coupled to a low-level stochastic controller running at a higher frequency, 1 min, is studied in Cominesi et al. [31]. A two-layer predictive energy management system for microgrids with hybrid energy storage systems consisting of batteries and supercapacitors is considered in Ju et al. [82]. This approach incorporates the degradation costs of the hybrid energy storage systems. A practical Energy Management System for isolated microgrid which considers the operational constraints of Distributed Energy Resources, active-reactive power balance, unbalanced system configuration and loading, and voltage-dependent loads is studied in Solanki et al. [138]. A two-layer mixed-integer linear programming predictive control strategy was implemented and tested in simulation and experimentally in Polimeni et al. [125], and Moretti et al. [106] implemented a two-layer predictive management strategy for an

off-grid hybrid microgrid featuring controllable and non-controllable generation units and a storage system.

It is organized as follows. Section 11.1 summarizes the notation. Section 11.2 formulates the problem in an abstract manner. Section 11.3 introduces the novel two-level value function-based approach and the assumptions made. Section 11.4 describes the numerical tests. Section 11.5 reports the results. Conclusions are drawn in Section 11.6. The methodology used for forecasting is reported in Chapter 5.

11.1 Notation

Sets and indices

Name	Description
d	Device index.
t, t'	RTO and OP time periods indexes.
$\tau(t)$	Beginning of the next market period at time t .
$\mathcal{T}_i(t)$	Set of RTO time periods $= \{t, t + \Delta t, \dots, t + T_i\}$.
$\mathcal{T}_a^m(t)$	Set of OP time periods $= \{\tau(t), \tau(t) + \Delta \tau, \dots, \tau(t + T_a)\}$.
T_a, T_l	Time durations, with $T_a \ll T_l$
\mathcal{D}^k	Set of non-flexible loads ($k = \text{nfl}$), sheddable loads ($k = \text{she}$), steerable generators ($k = \text{ste}$), non-steerable generators ($k = \text{nst}$), storage devices ($k = \text{sto}$).

Parameters

Name	Description	Unit
Δt	Time delta between t and the market period.	minutes
$\Delta \tau$	Market period.	minutes
$\eta^{\text{cha}}, \eta^{\text{dis}}$	Charge and discharge efficiencies.	%
\bar{P}, \underline{P}	Maximum charging and discharging powers.	kW
$C_{d,t}^{\text{nfl}}$	Non-flexible power consumption.	kW
$C_{d,t}^{\text{she}}$	Flexible power consumption.	kW
$S_{d,t}^{\text{init}}$	Initial state of charge of battery d .	kWh
p_h	Maximum peak over the last twelve months.	kW
π^{P}	Yearly peak power cost.	€/kW
π_{OP}^{s}	Unitary revenue for providing reserve.	€/kW

π_{RTO}^s	Unitary RTO symmetric reserve penalty.	€/kW
$\pi_{d,t}^k$	Cost of load shedding ($k = she$), generating energy ($k = ste$), curtailing generation ($k = nst$).	€/kWh
$\gamma_{d,t}^{sto}$	Fee to use the battery d .	€/kWh
π_t^e, π_t^i	Energy prices of export and import.	€/kWh
π_d^i, π_n^i	Energy prices of day and night imports.	€/kWh
I^{cap}, E^{cap}	Maximum import and export limits.	kW
PV_p, C_p	PV and consumption capacities.	kW
S_p	Storage capacity.	kWh
\bar{S}, \underline{S}	Maximum and minimum battery capacities.	kWh

Forecasted or computed variables

Name	Description	Unit
a_t	Action at t .	-
a_t^m	Purely market related actions.	-
a_t^d	Set-points to the devices of the microgrid	-
$a_{d,t}^k$	Fraction of load shed ($k = she$), generation activated ($k = ste$), generation curtailed ($k = nst$) ($[0, 1]$).	-
$a_{d,t}^{cha}, a_{d,t}^{dis}$	Fraction of the maximum charging and discharging powers used for battery d ($[0, 1]$).	-
e_t^{gri}, i_t^{gri}	Energy export and import.	kWh
$\delta p_{t'}$	OP peak difference between peak at t' and p_h .	kW
$\delta p_{\tau(t-\Delta\tau), \tau(t)}$	RTO peak difference between peak at $\tau(t)$ and p_h .	kW
s_t^{TSO}	TSO symmetric reserve signal (0; 1).	-
r^{sym}	Symmetric reserve.	kW
Δr^{sym}	Reserve difference between OP and RTO.	kW
$r_{d,t'}^{s+}, r_{d,t'}^{s-}$	Upward and downward reserves of power available and provided by storage device d .	kW
$s_{d,t}$	State of charge of battery d .	kWh
s_t	Microgrid state at time t .	-
s_t^m	Information related to the current market position.	-
s_t^d	State of the devices.	-
v_t	The cost-to-go function.	k€
$\hat{\omega}$	Forecast of a random vector ω .	-

\bar{X}	Average of a variable X .	kW
X_{max}, X_{min}	Maximum and minimum of X .	kW
X_{std}	Standard deviation of X .	kW
c_E, c_p, c_t	Energy, peak and total costs.	k€
Δ_p	Peak increment.	kW
I_{tot}, E_{tot}	Total import and export.	MWh

11.2 Problem statement

A global microgrid control problem can be defined, for a given microgrid design and configuration, as operating a microgrid safely and in an economically efficient manner, by harvesting as much renewable energy as possible, operating the grid efficiently, optimizing the service to the demand side, and optimizing other side goals. We refine this definition below and start by making a few assumptions.

11.2.1 Assumptions

In this study, the control optimizes economical criteria, which are only related to active power. All devices are supposed to be connected to the same electrical bus, which can be connected or disconnected from a public grid permanently or dynamically. Device-level controllers offer an interface to communicate their operating point and constraints, *e.g.*, maximum charge power as a function of the current state, and implement control decisions to reach power set-points. Fast load-frequency control, islanding management, as well as reactive power control, are not in scope. The microgrid is a price taker in energy and reserve markets.

11.2.2 Formulation

Abstractly, a microgrid optimization problem can be formulated as follows

$$\min_{\mathbf{a}} \sum_{t \in \mathcal{T}_l} c(a_t, s_t, \omega_t) \quad (11.1a)$$

$$\text{s.t. } \forall t \in \mathcal{T}_l, s_{t+\Delta t} = f(a_t, s_t, \omega_t, \Delta t), \quad (11.1b)$$

$$s_t \in \mathcal{S}_t. \quad (11.1c)$$

A controller has to return a set of actions $a_t = (a_t^m, a_t^d)$ at any time t over the life of the microgrid (\mathcal{T}_l). Actions should be taken as frequently as possible to cope with the economic impact of the variability of the demand and generation sides, but not too

often to let transients vanish, *e.g.*, every few seconds. The time delta between action a_t and the next action taken is denoted by Δt , and is not necessarily constant. Some of these actions are purely market-related a_t^m , while other actions are communicated as set-points to the devices of the microgrid a_t^d . The state $s_t = (s_t^m, s_t^d)$ of the microgrid at time t is thus also made of two parts: s_t^d represents the state of the devices, such as the state of charge of a storage system or the state of a flexible load, while s_t^m gathers information related to the current market position, such as the nominated net position of the microgrid over the next market periods. The cost function c gathers all the economical criteria considered. The transition function f describes the physical and net position evolution of the system. At time instants $t \in \{\Delta\tau, 2\Delta\tau, \dots\}$, with $\Delta\tau$ the market period, some costs are incurred based on the value of some state variables, which are then reset for the next market period. This problem is very difficult to solve since the evolution of the system is uncertain, actions have long-term consequences, and are both discrete and continuous. Furthermore, although functions f and c are assumed time-invariant, they are generally non-convex and parameterized with stochastic variables ω_t .

11.3 Proposed method

In practice, solving the microgrid optimization problem above amounts, at every time t , to forecasting the stochastic variables $\omega_{\mathcal{T}_l(t)}$, then solving the problem¹

$$\mathbf{a}_{\mathcal{T}_l(t)}^* = \arg \min \sum_{t' \in \mathcal{T}_l(t)} c(a_{t'}, s_{t'}, \hat{\omega}_{t'}) \quad (11.2a)$$

$$\text{s.t. } \forall t' \in \mathcal{T}_l(t), s_{t'+\Delta t'} = f(a_{t'}, s_{t'}, \hat{\omega}_{t'}, \Delta t'), \quad (11.2b)$$

$$s_{t'} \in S'_{t'}, \quad (11.2c)$$

and applying a_t^* (potentially changing $a_t^{m,*}$ at some specific moments only). As forecasts are valid only for a relatively near future and optimizing over a long time horizon would anyway be incompatible with real-time operation, this problem is approximated by cropping the lookahead horizon to $\mathcal{T}_a(t) \subset \mathcal{T}_l(t)$. However, market decisions must be refreshed much less frequently than set-points. We thus propose to further decompose the problem in an operational planning problem (OPP) for $\mathcal{T}_a^m(t)$ that computes

¹Which is here expressed as a deterministic problem for simplicity, but should be treated as a stochastic problem in practice.

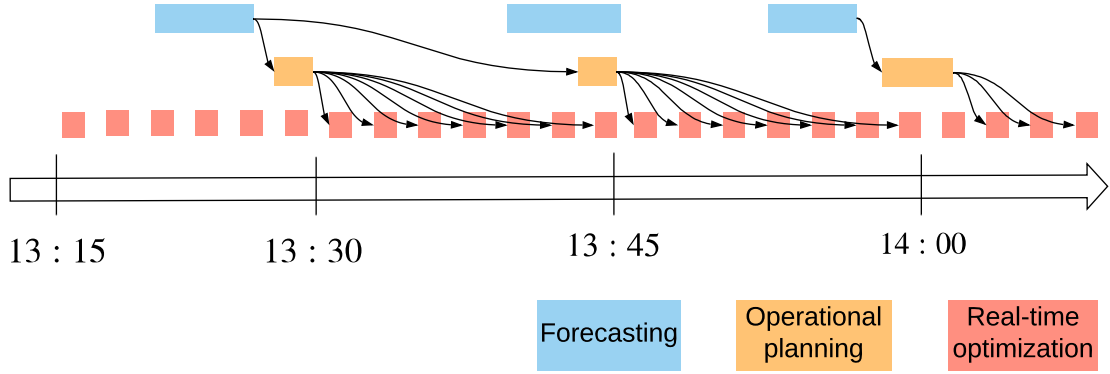


Fig. 11.2 Hierarchical control procedure illustration.

market decisions

$$\mathbf{a}_{\mathcal{T}_a^m(t)}^{m,*} = \arg \min \sum_{t' \in \mathcal{T}_a^m(t)} c^m(a_{t'}^m, s_{t'}, \hat{\omega}_{t'}) \quad (11.3a)$$

$$\text{s.t. } \forall t' \in \mathcal{T}_a^m(t), s_{t'+\Delta\tau} = f^m(a_{t'}^m, s_{t'}, \hat{\omega}_{t'}, \Delta\tau) \quad (11.3b)$$

$$s_{t'} \in S_{t'}, \quad (11.3c)$$

and a real-time problem (RTP) that computes set-points for time t

$$a_t^{d,*} = \arg \min c^d(a_t^d, s_t, \hat{\omega}_t) + v_{\tau(t)}(s_{\tau(t)}) \quad (11.4a)$$

$$\text{s.t. } s_{\tau(t)} = f^d(a_t^d, s_t, \hat{\omega}_t, \tau(t) - t) \quad (11.4b)$$

$$s_{\tau(t)} \in S_{\tau(t)}, \quad (11.4c)$$

with $c(a_t, s_t, w_t) = c^m(a_t^m, s_t, w_t) + c^d(a_t^d, s_t, \omega_t)$. The function v_t is the cost-to-go as a function of the state of the system at the end of the ongoing market period, it regularizes decisions of RTP to account for the longer-term evolution of the system. We detail hereunder how we obtain v_t . An overview of the approach is depicted in Figure 11.2.

11.3.1 Computing the cost-to-go function

The function v_t represents the optimal value of (11.3) as a function of the initial state $s_{\tau(t)}$ of this problem. If we make the assumption that (11.3) is modeled as a linear program, the function $v_{\tau(t)}$ is thus convex and piecewise linear. Every evaluation of

(11.3) with the additional constraint²

$$s_{\tau(t)} = s' \perp \mu \quad (11.5)$$

yields the value $v_{\tau(t)}(s')$ and a supporting inequality (a cut)

$$v_{\tau(t)}(s) \geq v_{\tau(t)}(s') + \mu^T s. \quad (11.6)$$

The algorithm to approximate $v_{\tau(t)}(s')$ works as follows:

1. estimate the domain of $v_{\tau(t)}$, *i.e.*, the range of states reachable at time $\tau(t)$ and the most probable state that will be reached $s_{\tau(t)}^*$;
2. evaluate $v_{\tau(t)}(s_{\tau(t)}^*)$ and the associated μ^* ;
3. repeat step 2 for other state values until all regions of $v_{\tau(t)}$ are explored.

Note that if the state is of dimension one and (11.3) is a linear program, simplex basis validity information can be used to determine for which part of the domain of $v_{\tau(t)}$ the current cut is tight, else a methodology such as proposed in Bemporad et al. [8] can be used.

11.3.2 OPP formulation

The OPP objective function implemented for the case study is

$$J_{\mathcal{T}_a^m(t)}^{OP} = \sum_{t' \in \mathcal{T}_a^m(t)} \left(C_{t'}^{OP} + D_{t'}^{OP} \right) \quad (11.7)$$

with Operational Planner (OP) the name of this planer. $\mathcal{T}_a^m(t)$ is composed of 96 values with $\Delta\tau = 15$ minutes and $T_a = 24$ hours. $C_{t'}^{OP}$ models the immediate costs and $D_{t'}^{OP}$ the delayed costs at t' . $C_{t'}^{OP}$ takes into account different revenues and costs related to energy flows: the costs of shed demand, steered and non steered generation, the revenues from selling energy to the grid, the costs of purchasing energy from the

²The $\perp \mu$ notation means that μ is the dual variable of the constraint.

grid and the costs for using storage

$$C_{t'}^{OP} = \sum_{t' \in \mathcal{T}_a^m(t)} \left(\sum_{d \in \mathcal{D}^{\text{she}}} \Delta\tau \pi_{d,t'}^{\text{she}} C_{d,t'}^{\text{she}} a_{d,t'}^{\text{she}} + \sum_{d \in \mathcal{D}^{\text{ste}}} \Delta\tau \pi_{d,t'}^{\text{ste}} P_{d,t'}^{\text{ste}} a_{d,t'}^{\text{ste}} + \sum_{d \in \mathcal{D}^{\text{nst}}} \Delta\tau \pi_{d,t'}^{\text{nst}} P_{d,t'}^{\text{nst}} a_{d,t'}^{\text{nst}} \right. \\ \left. + \sum_{d \in \mathcal{D}^{\text{sto}}} \Delta\tau \gamma_d^{\text{sto}} [\bar{P}_d \eta_d^{\text{cha}} a_{d,t'}^{\text{cha}} + \frac{P_d}{\eta_d^{\text{dis}}} a_{d,t'}^{\text{dis}}] - \pi_{t'}^e e_{t'}^{\text{gri}} + \pi_{t'}^i i_{t'}^{\text{gri}} \right). \quad (11.8)$$

$D_{t'}^{OP}$ is composed of the peak cost and symmetric reserve revenue

$$D_{t'}^{OP} = \pi^p \delta p_{t'} - \pi_{OP}^s r_{t'}^{\text{sym}}, \quad (11.9)$$

$\delta p_{t'}$ is the peak difference between the previous maximum historic peak p_h and the current peak within the market period t' . $r_{t'}^{\text{sym}}$ is the symmetric reserve provided to the grid within the current market period t' .

11.3.3 OP constraints

The first set of constraints defines bounds on state and action variables, $\forall t' \in \mathcal{T}_a^m(t)$

$$a_{d,t'}^k \leq 1 \quad \forall d \in \mathcal{D}^k, \forall k \in \{\text{ste}, \text{she}, \text{nst}\} \quad (11.10a)$$

$$a_{d,t'}^{\text{cha}} \leq 1 \quad \forall d \in \mathcal{D}^{\text{sto}} \quad (11.10b)$$

$$a_{d,t'}^{\text{dis}} \leq 1 \quad \forall d \in \mathcal{D}^{\text{sto}} \quad (11.10c)$$

$$\underline{S}_d \leq s_{d,t'} \leq \bar{S}_d \quad \forall d \in \mathcal{D}^{\text{sto}}. \quad (11.10d)$$

The energy flows are constrained, $\forall t' \in \mathcal{T}_a^m(t)$, by

$$(e_{t'}^{\text{gri}} - i_{t'}^{\text{gri}})/\Delta\tau - \sum_{d \in \mathcal{D}^{\text{nst}}} (1 - a_{d,t'}^{\text{nst}}) P_{d,t'}^{\text{nst}} + \sum_{d \in \mathcal{D}^{\text{ste}}} a_{d,t'}^{\text{ste}} P_{d,t'}^{\text{ste}} \\ + \sum_{d \in \mathcal{D}^{\text{nfl}}} C_{d,t'}^{\text{nfl}} + \sum_{d \in \mathcal{D}^{\text{she}}} (1 - a_{d,t'}^{\text{she}}) C_{d,t'}^{\text{she}} + \sum_{d \in \mathcal{D}^{\text{sto}}} (\bar{P}_d a_{d,t'}^{\text{cha}} - \underline{P}_d a_{d,t'}^{\text{dis}}) = 0 \quad (11.11a)$$

$$(e_{t'}^{\text{gri}} - i_{t'}^{\text{gri}})/\Delta\tau \leq E_{t'}^{\text{cap}} \quad (11.11b)$$

$$(i_{t'}^{\text{gri}} - e_{t'}^{\text{gri}})/\Delta\tau \leq I_{t'}^{\text{cap}}. \quad (11.11c)$$

The dynamics of the state of charge are, $\forall d \in \mathcal{D}^{sto}$

$$s_{d,1} - \Delta\tau(\bar{P}_d \eta_d^{\text{cha}} a_{d,1}^{\text{cha}} - \frac{P_d}{\eta_d^{\text{dis}}} a_{d,1}^{\text{dis}}) = S_d^{\text{init}} \quad (11.12a)$$

$$s_{d,t'} - s_{d,t'-\Delta\tau} - \Delta\tau(\bar{P}_d \eta_d^{\text{cha}} a_{d,t'}^{\text{cha}} - \frac{P_d}{\eta_d^{\text{dis}}} a_{d,t'}^{\text{dis}}) = 0, \quad \forall t' \in \mathcal{T}_a^m(t) \quad (11.12b)$$

$$s_{d,\tau(T_a)} = S_d^{\text{end}}. \quad (11.12c)$$

The set of constraints related to the peak power $\forall t' \in \mathcal{T}_a^m(t)$

$$(i_{t'}^{\text{gri}} - e_{t'}^{\text{gri}})/\Delta\tau \leq p_{t'} \quad (11.13a)$$

$$-\delta p_{t'} \leq 0 \quad (11.13b)$$

$$-\delta p_{t'} \leq -(p_{t'} - p_h). \quad (11.13c)$$

The last constraints define symmetric reserve $\forall t' \in \mathcal{T}_a^m(t)$

$$r_{d,t'}^{s+} \leq \frac{(s_{d,t'} - \underline{S}_d) \eta_d^{\text{dis}}}{\Delta\tau} \quad \forall d \in \mathcal{D}^{sto} \quad (11.14a)$$

$$r_{d,t'}^{s+} \leq \underline{P}_d(1 - a_{d,t'}^{\text{dis}}) \quad \forall d \in \mathcal{D}^{sto} \quad (11.14b)$$

$$r_{d,t'}^{s-} \leq \frac{(\bar{S}_d - s_{d,t'})}{\eta_d^{\text{cha}} \Delta\tau} \quad \forall d \in \mathcal{D}^{sto} \quad (11.14c)$$

$$r_{d,t'}^{s-} \leq \bar{P}_d(1 - a_{d,t'}^{\text{cha}}) \quad \forall d \in \mathcal{D}^{sto} \quad (11.14d)$$

$$r^{\text{sym, OP}} \leq \sum_{d \in \mathcal{D}^{sto}} r_{d,t'}^{s+} + \sum_{d \in \mathcal{D}^{\text{ste}}} P_{d,t'}^{\text{ste}}(1 - a_{d,t'}^{\text{ste}}) + \sum_{d \in \mathcal{D}^{\text{nst}}} P_{d,t'}^{\text{nst}}(1 - a_{d,t'}^{\text{nst}}) \\ + \sum_{d \in \mathcal{D}^{\text{she}}} C_{d,t'}^{\text{she}}(1 - a_{d,t'}^{\text{she}}) \quad (11.14e)$$

$$r^{\text{sym, OP}} \leq \sum_{d \in \mathcal{D}^{sto}} r_{d,t'}^{s-} + \sum_{d \in \mathcal{D}^{\text{ste}}} P_{d,t'}^{\text{ste}} a_{d,t'}^{\text{ste}} + \sum_{d \in \mathcal{D}^{\text{nst}}} P_{d,t'}^{\text{nst}} a_{d,t'}^{\text{nst}} + \sum_{d \in \mathcal{D}^{\text{she}}} C_{d,t'}^{\text{she}} a_{d,t'}^{\text{she}}. \quad (11.14f)$$

11.3.4 RTP formulation

The RTP objective function implemented for the case study is

$$J_t^{\text{RTO}} = C_t^{\text{RTO}} + D_t^{\text{RTO}} + v_{\tau(t)}(s_{\tau(t)}) \quad (11.15)$$

with Real-Time Optimizer (RTO) the name of this controller. C_t^{RTO} models the immediate costs, D_t^{RTO} the delayed costs and $v_{\tau(t)}(s_{\tau(t)})$ the cost-to-go function of the state of the system at time t within a current market period. C_t^{RTO} is the same as $C_{t'}^{\text{OP}}$ by replacing t' by t , $\Delta\tau$ by Δt and considering only one period of time t . D_t^{RTO}

is composed of the peak cost and symmetric reserve penalty costs

$$D_t^{RTO} = \pi^p \delta p_{\tau(t-\Delta\tau),\tau(t)} + s_t^{TSO} \pi_{RTO}^s \Delta r^{\text{sym}}, \quad (11.16)$$

$\delta p_{\tau(t-\Delta\tau),\tau(t)}$ is the peak difference between the previous maximum historic peak p_h and the current peak within the market period computed by RTO. The difference with OP relies on its computation as at t the market period is not finished. Thus the peak within this market period is computed by adding the peak from the beginning of the market period to t and the one resulting from the actions taken from t to the end of the market period. Δr^{sym} is the difference between the symmetric reserve computed by OP and the current reserve within the market period computed by RTO. s_t^{TSO} is the reserve activation signal to activate the tertiary symmetric reserve. It is set by the TSO, 0 if activated, else 1. The activation occurs at the beginning of the next market period.

11.3.5 RTO constraints

The set of constraints that defines the bounds on state and action variables and the energy flows are the same as the OP (11.10) and (11.11) by replacing t' by t , $\Delta\tau$ by Δt and considering only one period of time t . The next constraint describes the dynamics of the state of charge $\forall d \in \mathcal{D}^{sto}$ and $\forall t \in \mathcal{T}_i(t)$

$$s_{d,\tau(t)} - \Delta t (\bar{P}_d \eta_d^{\text{cha}} a_{d,t}^{\text{cha}} - \frac{P_d}{\eta_d^{\text{dis}}} a_{d,t}^{\text{dis}}) = S_{d,t}^{\text{init}}. \quad (11.17)$$

The set of constraints related to the peak power $\forall t \in \mathcal{T}_i(t)$

$$(i_t^{\text{gri}} - e_t^{\text{gri}})/\Delta t \leq p_{t,\tau(t)} \quad (11.18a)$$

$$-\delta p_{\tau(t)} \leq 0 \quad (11.18b)$$

$$-\delta p_{\tau(t)} \leq -(p_{\tau(t-\Delta\tau),\tau(t)} - p_h) \quad (11.18c)$$

$$p_{\tau(t-\Delta\tau),\tau(t)} = \beta p_{\tau(t-\Delta\tau),t} + (1 - \beta) p_{t,\tau(t)} \quad (11.18d)$$

with $\beta = 1 - \Delta t/\Delta\tau$. The last set of constraints defining the symmetric reserve are the same as the OP (11.14) by replacing t' by t , $r^{\text{sym, OP}}$ by $r^{\text{sym, RTO}}$ and adding $\forall t \in \mathcal{T}_i(t)$

$$-\Delta r^{\text{sym}} \leq 0 \quad (11.19a)$$

$$-\Delta r^{\text{sym}} \leq -(r^{\text{sym, OP}} - r^{\text{sym, RTO}}). \quad (11.19b)$$

11.4 Test description

Our case study is based on the MiRIS microgrid located at the John Cockerill Group's international headquarters in Seraing, Belgium³. It is composed of PV, several energy storage devices, and a non-sheddable load. The load and PV data we use come from on-site monitoring. All data, including the weather forecasts, are available on the Kaggle platform⁴. The case study consists of comparing RTO-OP to a Rule-Based Controller (RBC) for three configurations of the installed PV capacity, cf. Table 11.1. The RBC prioritizes the use of PV production for the supply of electrical demand. If the microgrid is facing a long position, it charges the battery. And if this one is fully charged it exports to the main grid. If the microgrid is facing a short position it prioritizes the use of the battery to supply the demand. And if this one is fully discharged it imports from the main grid. This controller does not take into account any future information, *e.g.*, PV, consumption forecasts, energy prices, or market information such as the peak of the symmetric reserve. Case 3 is the result of a sizing study that defined the optimal device sizes given the PV and consumption data. The sizing methodology used is described in Dakir and Cornélusse [33].

Figure 11.3 shows the PV & consumption data over the simulation period: from May 20, 2019 to June 16, 2019. The selling price π^e is constant, the purchasing price is composed of a day π_d^i and night prices π_n^i . Day prices apply from 5 a.m. to 8 p.m. (UTC) during the weekdays and night prices apply from 8 p.m. to 5 a.m. during weekdays and the entire weekend. The peak mechanism is taken into account with a constant peak price π^p and an initial maximum historic peak p_h . Storage systems are initially fully charged. The PV and consumption data have a 1-second resolution, meaning the RTO could compute its optimization problem each five to ten seconds in operational mode. CPLEX 12.9 is used to solve all the optimization problems, on an Intel Core i7-8700 3.20 GHz based computer with 12 threads and 32 GB of RAM. The average computation time per optimization problem composed of the OP and RTO is a few seconds. However, to maintain a reasonable simulation time RTO is called every

³<https://johncockerill.com/fr/energy/stockage-denergie/>

⁴<https://www.kaggle.com/jonathandumas/liege-microgrid-open-data>

Case	PV_p	\overline{PV}	PV_{max}	PV_{min}	PV_{std}
1	400	61	256	0	72
2	875	133	561	0	157
3	1750	267	1122	0	314
Case	C_p	\overline{C}	C_{max}	C_{min}	C_{std}
1 - 3	1000	153	390	68	72
Case	S_p	$\overline{S}, \underline{S}$	$\underline{P}, \overline{P}$	η^{cha}, η^{dis}	S^{init}
1 - 3	1350	1350, 0	1350, 1350	0.95, 0.95	100
Case	p_h, π^p	I^{cap}	E^{cap}	π_d^i, π_n^i	π^e
1 - 3	150, 40	1500	1500	0.2, 0.12	0.035

Table 11.1 Case studies parameters and data statistics.

minute. The dataset is composed of 28 days with an average computation time of two hours to solve 1440 optimization problems per day, with a one-minute resolution, leading to a total of two days for the entire dataset. The OP computes a planning quarterly corresponding to the Belgian market period. The computation time of the RTO on a regular computer is around a few seconds and the OP around twenty seconds. In total, the simulation computation time is up to a few hours. The OP computes quarterly planning based on PV and consumption twenty-four ahead forecasts. The weather-based forecast methodology is described in detail in Chapter 5. Two "classic" deterministic techniques are implemented, a Recurrent Neural Network (RNN) with the Keras Python library [30] and a Gradient Boosting Regression (GBR) with the Scikit-learn Python library [119]. These models use as input the weather forecasts provided by the Laboratory of Climatology of the Liège University, based on the MAR regional climate model [50]. It is an atmosphere model designed for meteorological and climatic research, used for a wide range of applications, from km-scale process studies to continental-scale multi-decade simulations. To estimate the impact of the PV and consumption forecast errors on the controllers, the simulation is performed with the OP having access to the PV and consumption future values (RTO-OP^{*}). Then, the simulation is performed with the symmetric reserve mechanisms to cope with the forecast errors. A constant symmetric reserve price π_{OP}^s for the OP and a penalty reserve π_{RTO}^s for the RTO are set to 20 (€/ kW).

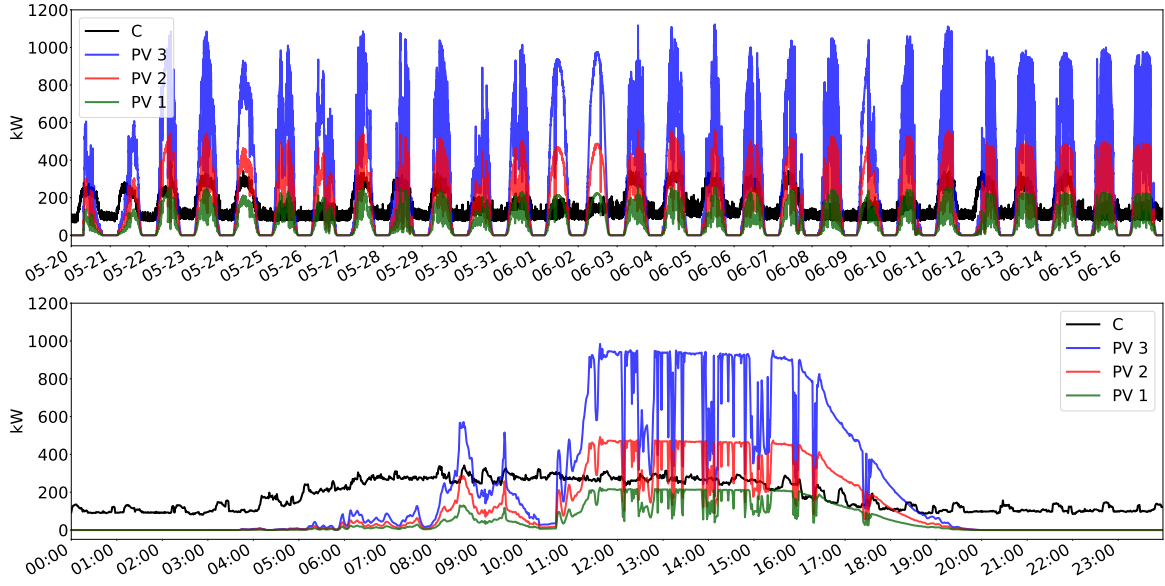


Fig. 11.3 Top: PV & consumption simulation data. Bottom: zoom on *June 12*, 2019.

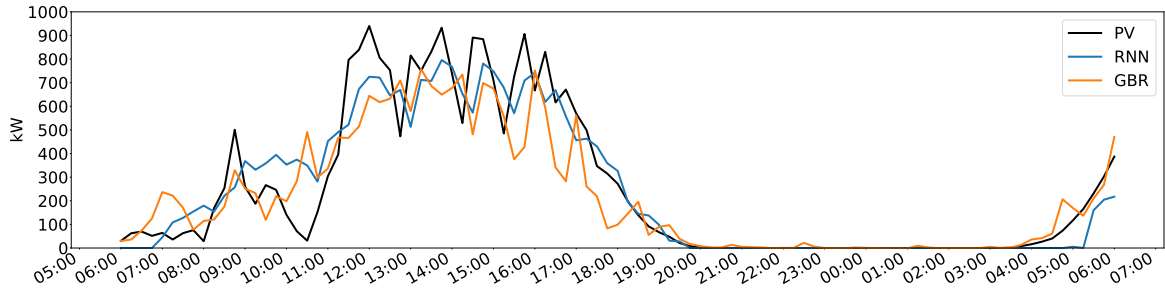


Fig. 11.4 Case 3 PV forecast on *June 12*, 2019, 06h00 UTC.

11.5 Numerical results

11.5.1 No symmetric reserve

Table 11.2 provides the simulation results without taking into account the symmetric reserve. The smaller the PV installed capacity the higher the peak and energy costs. The RTO-OP* provides the minimal peak cost whereas the RBC provides the minimal energy cost on all cases. However, RTO-OP* achieves the minimal total cost, composed of the energy and peak costs. This simulation illustrates the impact of the forecasts on the RTO-OP behavior. The RNN forecaster provides the best results but the RTO-OP^{RNN} is still a long way to manage the peak as RTO-OP* due to the forecasting errors. The peak cost strongly penalizes the benefits as it applies to the entire year ahead once it has been reached.

Case 1	c_E	c_p	c_t	Δ_p	I_{tot}	E_{tot}
RBC	10.13	6.68	16.81	167	61	0
RTO-OP ^{RNN}	10.37	3.62	13.99	91	64	1
RTO-OP ^{GBR}	10.25	5.27	15.53	132	63	1
RTO-OP*	10.24	0.99	11.23	25	64	1
Case 2	c_E	c_p	c_t	Δ_p	I_{tot}	E_{tot}
RBC	3.19	4.85	8.04	121	22	7
RTO-OP ^{RNN}	4.78	2.87	7.65	72	31	15
RTO-OP ^{GBR}	4.30	4.90	9.2	123	28	13
RTO-OP*	4.06	0	4.06	0	26	10
Case 3	c_E	c_p	c_t	Δ_p	I_{tot}	E_{tot}
RBC	-2.13	4.12	1.99	105	3	77
RTO-OP ^{RNN}	-1.66	4.12	2.46	105	7	80
RTO-OP ^{GBR}	-1.67	4.23	2.56	106	7	81
RTO-OP*	-1.90	0	0	0	5	79

Table 11.2 Results without symmetric reserve.

In case 3, all the controllers except RTO-OP* reached the maximum peak on *June* 12, 2019 around 10:30 a.m. as shown on Figure 11.5. Figure 11.3 shows a sudden drop in the PV production around 10 a.m. that is not accurately forecasted by the RNN and GBR forecasters as shown in Figure 11.4. This prediction leads to the non-accurate planning of OP. Thus, the RTO cannot anticipate this drop and has to import at the last minute energy to balance the microgrid. Figure 11.6 shows the controllers behavior on *June* 12, 2019 where the peak is reached. In case 2 all controllers reached the same peak as in case 3 except RTO-OP^{RNN} that reached a smaller one on *June* 5, 2019. The forecast's accuracy explains this behavior as in case 3. Finally, in case 1, each controller reached a different peak. The smallest one is achieved by the RTO-OP*, followed by the RTO-OP^{RNN}. These cases show that the RTO-OP controller optimizes PV-storage usage, and thus requires less installed PV capacity for a given demand level. This result was expected as the peak management is not achieved by the RBC and becomes critical when the PV production is smaller than the consumption. This simulation also demonstrates the forecast accuracy impact on the RTO-OP behavior.

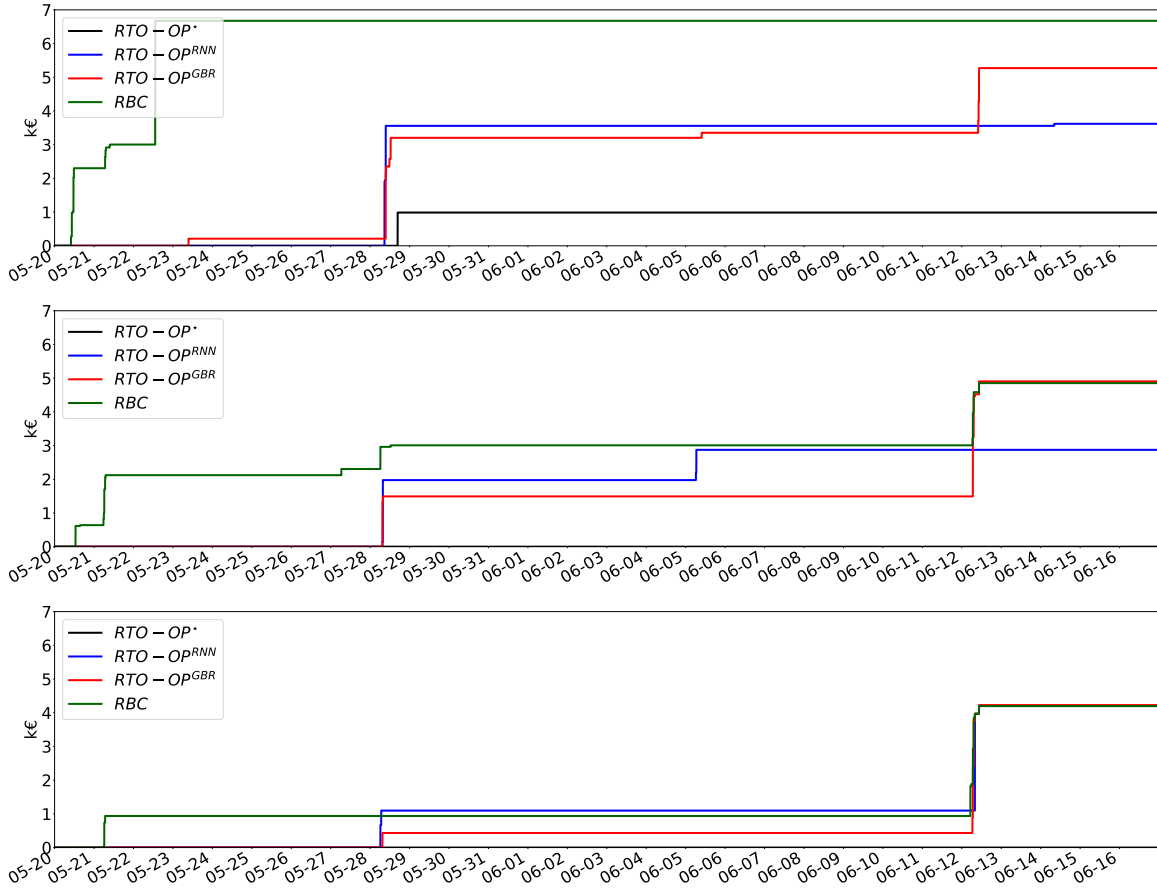


Fig. 11.5 Case 1 (top), 2 (middle), 3 (bottom) cumulative peak costs.

11.5.2 Results with symmetric reserve

Table 11.3 provides the simulation results by taking into account the symmetric reserve. Figure 11.7 depicts on case 3 the behavior differences between RTO-OP^{RNN} without and with symmetric reserve. Figures 11.8 and 11.9 show the SOC and peaks costs evolution of case 2 & 1. The controller tends to maintain a storage level that allows RTO-OP^{RNN} to better cope with forecast error. Indeed for case 3, there is no more peak reached by RTO-OP^{RNN} , only 1 kW for case 2 and it has been almost divided by two for case 1. However, this behavior tends to increase the energy cost if the PV production is important in comparison with the consumption, such as in case 3. Indeed, the controller will tend to store more energy in the battery instead of exporting it. RTO-OP^* did not perform better with the symmetric reserve. The symmetric reserve competes with the peak management and the RTO-OP^* tends to not discharge completely the battery even if it is required to avoid a peak. In case 2, the peak is reached on June 12, 2019 around 08:00. The controller could have avoided it by

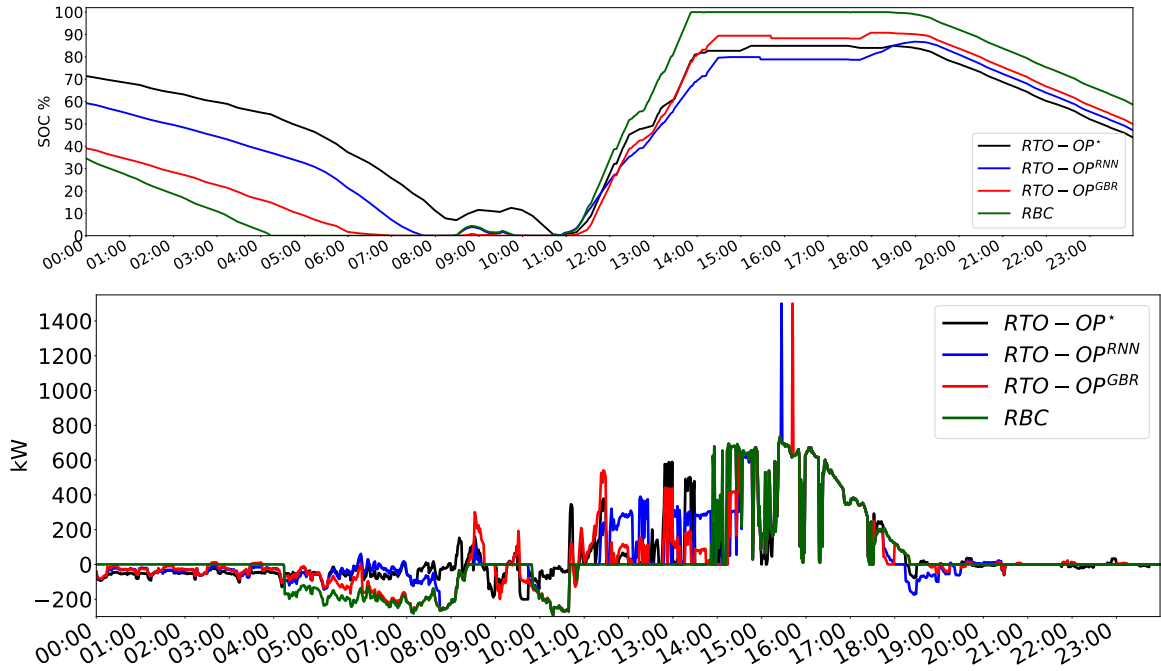


Fig. 11.6 Case 3 SOC (top) and net export power (bottom) on *June 12, 2019*.

totally discharging the battery but did not maintain the reserve level. This is the same behavior in case 1 where the peak could have been limited if all the battery was discharged. There is an economic trade-off to reach to manage the peak and the reserve simultaneously depending on the valorization or not on the market of the symmetric reserve. The reserve can also be valorized internally to cope with non or difficult forecastable events such as a sudden drop of the export or import limits due to loss of equipment or grid congestion.

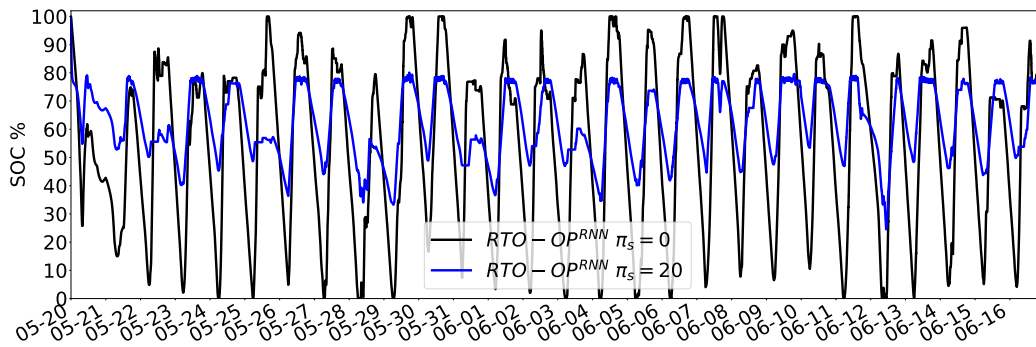


Fig. 11.7 Case 3 SOC comparison for $RTO-OP^{RNN}$ with and without symmetric reserve.

Case 1	c_E	c_p	c_t	Δ_p	I_{tot}	E_{tot}
RTO-OP ^{RNN}	10.50	2.12	12.62	53	65	3
RTO-OP*	10.47	2.75	13.22	69	65	2
Case 2	c_E	c_p	c_t	Δ_p	I_{tot}	E_{tot}
RTO-OP ^{RNN}	5.33	0.04	5.37	1	41	27
RTO-OP*	4.78	0.99	5.77	25	35	20
Case 3	c_E	c_p	c_t	Δ_p	I_{tot}	E_{tot}
RTO-OP ^{RNN}	-0.04	0	-0.04	0	24	99
RTO-OP*	-0.15	0	-0.15	0	23.2	98

Table 11.3 Results with symmetric reserve.

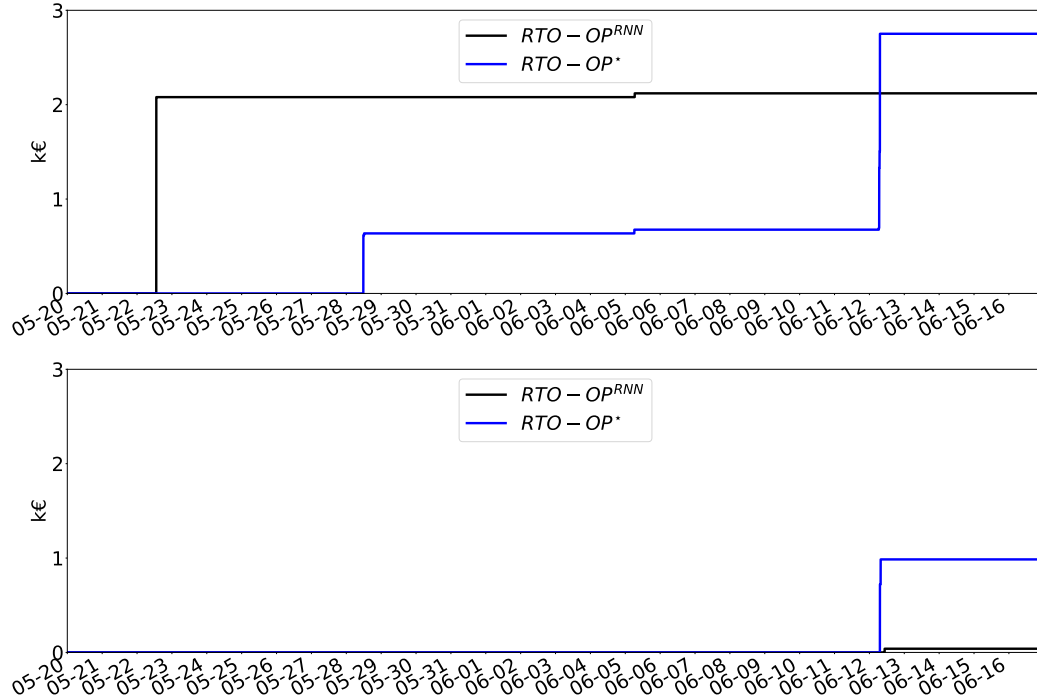


Fig. 11.8 Case 1 (top) and 2 (bottom) cumulative peak costs.

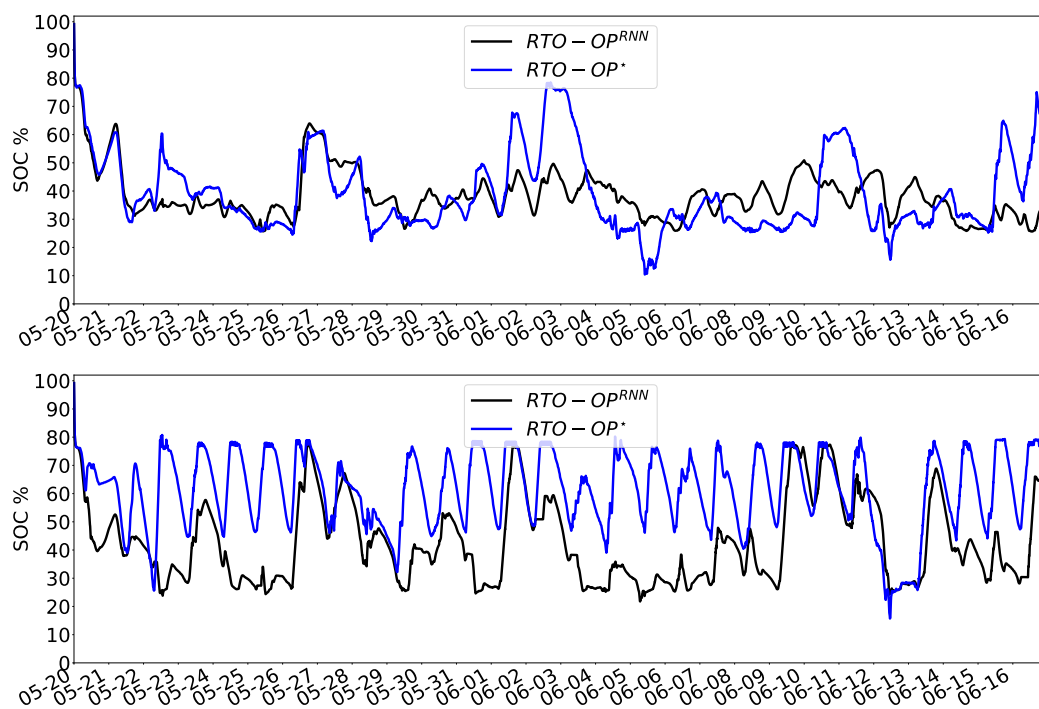


Fig. 11.9 Case 1 (top) and 2 (bottom) SOC.

11.6 Conclusions

A two-level value function-based approach was introduced as a solution method for a multi-resolution microgrid optimization problem. The value function computed by the operational planner based on PV and consumption forecasts allows coping with the forecasting uncertainties. The real-time controller solves an entire optimization problem including the future information propagated by the value function. This approach has been tested on the MiRIS microgrid case study with PV and consumption data monitored on-site. The results demonstrate the efficiency of this method to manage the peak in comparison with a Rule-Based Controller. This test case is completely reproducible as all the data used are open, PV, consumption monitored and forecasted including the weather forecasts. The proposed approach can be extended in several ways. The deterministic formulation of the operational planning problem could be extended to a stochastic formulation, to cope with probabilistic forecasts. Balancing market mechanisms could be introduced. Finally, the approach could be extended to a community by considering several entities inside the microgrid.

Chapter 12

Capacity firming using a stochastic approach

Overview

This Chapter proposes a stochastic approach to address the energy management of a grid-connected renewable generation plant coupled with a battery energy storage device in the capacity firming market. Both deterministic and stochastic approaches result in optimization problems formulated as quadratic problems with linear constraints. The considered case study is a real microgrid with PV production monitored on-site.

References: This chapter is an adapted version of the following publication:

Jonathan Dumas, Bertrand Cornélusse, Antonello Giannitrapani, Simone Paoletti, and Antonio Vicino. Stochastic and deterministic formulations for capacity firming nominations. In *2020 International Conference on Probabilistic Methods Applied to Power Systems (PMAPS)*, pages 1–7. IEEE, 2020. URL <https://arxiv.org/abs/2106.02425>.

Terminology and notations have been slightly adjusted for the sake of consistency with the rest of this manuscript. The text has also been processed to minimize overlap with respect to the other chapters.

“*We are our choices.*”

— **Jean-Paul Sartre**

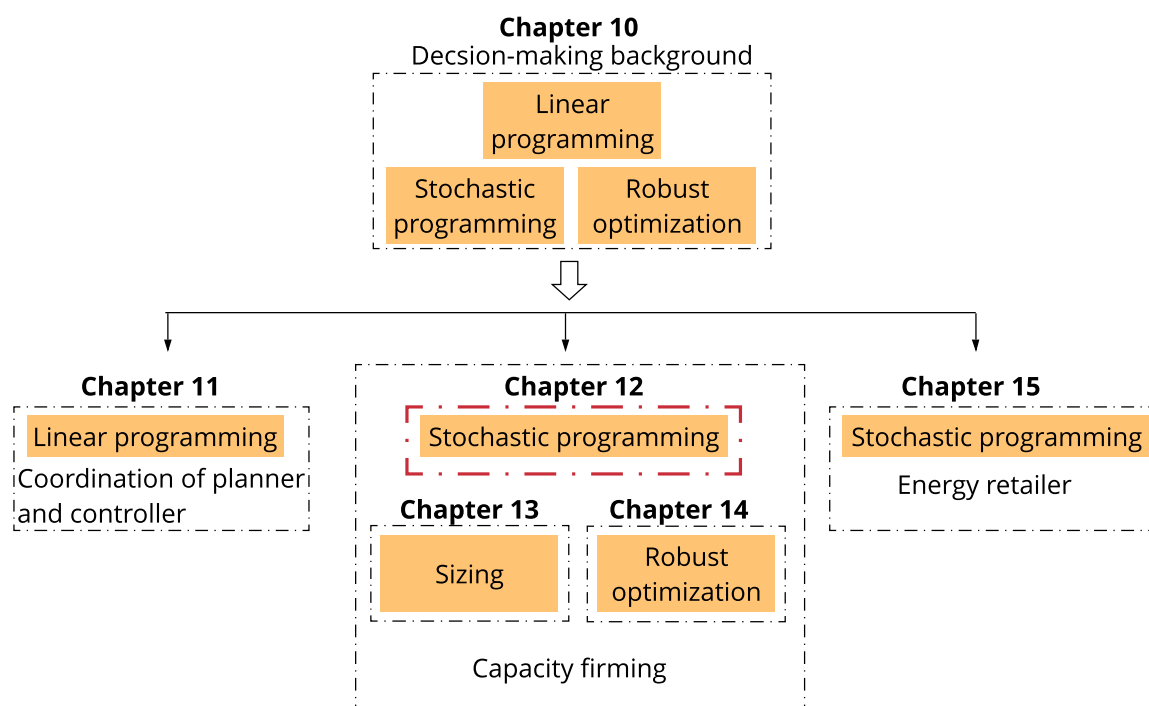


Fig. 12.1 Chapter 12 position in Part II.

The capacity firming framework is mainly designed for isolated markets, such as the Overseas France islands. For instance, the French Energy Regulatory Commission (CRE) publishes capacity firming tenders and specifications. The system considered is a grid-connected renewable energy power plant, *e.g.*, photovoltaic or wind-based, with a battery energy storage system (BESS) for firming the renewable generation. At the tendering stage, offers are selected on the electricity selling price. Then, the successful tenderer builds its plant and sells the electricity exported to the grid at the contracted selling price, but according to a well-defined daily engagement and penalization scheme, specified in the tender specifications. The electricity to be injected in or withdrawn from the grid must be nominated the day-ahead, and engagements must satisfy ramping power constraints. The remuneration is calculated a posteriori by multiplying the realized exports by the contracted selling price minus a penalty. The deviations of the realized exports from the engagements are penalized through a function specified in the tender. A peak option can be activated in the contract for a significant selling price increase during a short period defined a priori. Therefore, the BESS is required to shift the renewable generation during peak hours to maximize revenue and to manage renewable energy uncertainty.

The problem of modeling a two-phase engagement/control with an approach dealing with uncertainty in the context of the CRE capacity framework is still an open issue. This framework has received less attention in the literature than more traditional energy markets such as day-ahead and intraday markets of European countries.

The optimal day-ahead bidding strategies of a plant composed of only a production device have been addressed in, *e.g.*, Pinson et al. [122], Bitar et al. [20], Giannitrapani et al. [55, 56]. The optimal offer turns out to be a suitable percentile of the PV/wind power cumulative distribution function. Under the assumption of time-invariant statistics of power generation, the cumulative distribution functions can be estimated from historical data of the power generated by the plant. This assumption is not always justified especially for PV power generation. In Giannitrapani et al. [56], the authors investigate two approaches to properly take into account the effects of seasonal variation and non-stationary nature of PV power generation in the estimation of PV power statistics. However, incorporating energy storage in the framework is still an open problem, and the literature provides several approaches and methodologies to this end. An optimal power management mechanism for a grid-connected PV system with storage is implemented in [129] using Dynamic Programming (DP) and is compared with simple ruled-based management. The sizing and control of an energy storage system to mitigate wind power uncertainty is addressed by Haessig [69], Haessig et al.

[70, 71] using stochastic dynamic programming (SDP). The framework is similar to the CRE PV capacity firming tender with a wind farm operator that is committed on a day-ahead basis to a production engagement. Finally, three distinct optimization strategies, mixed-integer quadratic programming, simulation-based genetic algorithm, and expert-based heuristic are empirically compared by N’Goran et al. [108] in the CRE framework.

This study addresses the energy management of a grid-connected PV plant and BESS. This topic is studied within the capacity firming specifications of the CRE, in line with the tender AO-CRE-ZNI 2019 published on *July 12, 2019*, using the MiRIS microgrid case study. The capacity firming problem can be decomposed in two steps. The first step consists of computing the day-ahead nominations. The second step consists of computing the renominations and the set-points in real-time to minimize the energy and ramp power deviations from nominations. This study focuses on the first step and proposes both a stochastic and a deterministic formulation. The main goal of this study is to validate the stochastic approach by using an ideal predictor providing unbiased PV scenarios. Thus, the BESS efficiencies are perfect and the degradation is not taken into account for the sake of simplicity. Different levels of prediction accuracy are evaluated. Then, the results are compared with those of the deterministic formulation, assuming perfect forecasts returned by an oracle. Both deterministic and stochastic approaches result in optimization problems formulated as quadratic problems with linear constraints. The considered case study is a real microgrid with PV production monitored on-site.

The study is organized as follows. Section 12.1 provides the notation that is also used for Chapters 13 and 14. Section 12.2 describes the capacity firming framework. Section 12.3 proposes the deterministic and stochastic formulations of the nomination process. Section 12.4 introduces the MiRIS microgrid case study and presents the results. Conclusions are drawn in Section 12.5. Appendix 12.6 describes the methodology to generate the set of unbiased PV scenarios.

12.1 Notation

12.1.1 Sets and indices

Name	Description
------	-------------

t	Time period index.
ω	PV scenario index.
q	PV quantile index.
T	Number of time periods per day.
\mathcal{T}	Set of time periods, $\mathcal{T} = \{1, 2, \dots, T\}$.
\mathcal{D}	$\cup_{i=1}^{i=D} \mathcal{T}_i$ set of D days of market periods.
Ω	PV scenarios set, $\Omega = \{1, 2, \dots, \#\Omega\}$.
$\#\Omega$	Number of PV scenarios in Ω .
\mathcal{U}	PV uncertainty set for robust optimization.

12.1.2 Parameters

Name	Description	Unit
P_c	PV installed capacity.	kWp
\bar{S}	BESS installed capacity.	kWh
y_t^m	Measured power at the grid connection point.	kW
$y_t^{\text{pv,m}}$	Measured PV generation.	kW
\hat{y}_t^{pv}	PV point forecast.	kW
$\hat{y}_{t,\omega}^{\text{pv}}$	PV scenario ω .	kW
$\hat{y}_t^{\text{pv},(q)}$	PV quantile forecast q .	kW
α_ω	Probability of PV scenario ω	-
$y_{\max}^{\text{dis}}, y_{\max}^{\text{cha}}$	BESS maximum (dis)charging power.	kW
$\eta^{\text{dis}}, \eta^{\text{cha}}$	BESS (dis)charging efficiency.	-
s^{\min}, s^{\max}	BESS minimum/maximum capacity with $s^{\max} \leq \bar{S}$.	kWh
$s^{\text{ini}}, s^{\text{end}}$	BESS initial/final state of charge.	kWh
x_t^{\min}, x_t^{\max}	Minimum/maximum engagement.	kW
pP_c	Engagement tolerance, $0 \leq p \leq 1$, kW.	
ΔX	Ramping-up and down limits for the engagement.	kW
y_t^{\min}, y_t^{\max}	Minimum/maximum power at the grid connection point.	kW
π_t	Contracted selling price.	€/kWh
π^e	Slack price.	$\frac{\text{€}}{\text{kWh}^2}$
$\pi_{\bar{S}}$	BESS CAPEX price.	€/kWh
Δt	Time period duration.	minutes
c	Penalty function.	€
u_t^{\min}, u_t^{\max}	Minimum/maximum of the PV uncertainty interval.	kW
Γ	Uncertainty budget for robust optimization.	-

d_q, d_Γ	Uncertainty and budget depths for robust optimization.	%
M_t^-, M_t^+	Big-M's values for robust optimization.	-

12.1.3 Variables

For the sake of clarity the subscript ω is omitted.

Name	Range	Description	Unit
x_t	$[x_t^{\min}, x_t^{\max}]$	Engagement.	kW
y_t	$[y_t^{\min}, y_t^{\max}]$	Net power at the grid connection point.	kW
y_t^{pv}	$[0, \hat{y}_t^{\text{pv}}]$	PV generation.	kW
y_t^{cha}	$[0, y_{\max}^{\text{cha}}]$	BESS charging power.	kW
y_t^{dis}	$[0, y_{\max}^{\text{dis}}]$	BESS discharging power.	kW
y_t^s	$[s^{\min}, s^{\max}]$	BESS state of charge.	kWh
d_t^-, d_t^+	\mathbb{R}_+	Short/long deviation.	kW
y_t^b	$\{0, 1\}$	BESS binary variable.	-
z_t	$\{0, 1\}$	PV uncertainty set binary variable for robust optimization.	-
α_t	$[M_t^-, M_t^+]$	Variables to linearize $z_t \phi_t^{y^{\text{pv}}}$ for robust optimization.	-

Dual variables, and corresponding constraints

Dual variables of constraints are indicated with brackets $[\cdot]$.

Name	Range	Description
$\phi_t^{\text{cha}}, \phi_t^{\text{dis}}$	\mathbb{R}^-	Maximum storage (dis)charging.
$\phi_t^{s^{\min}}, \phi_t^{s^{\max}}$	\mathbb{R}^-	Minimum/maximum storage capacity.
ϕ_t^y	\mathbb{R}	Net power balance.
$\phi_t^{y^{\min}}, \phi_t^{y^{\max}}$	\mathbb{R}^-	Minimum/maximum net power.
$\phi_t^{s^{\text{ini}}}, \phi_t^{s^{\text{end}}}$	\mathbb{R}^-	Initial/final state of charge.
ϕ_t^s	\mathbb{R}^-	BESS dynamics.
$\phi_t^{d^-}, \phi_t^{d^+}$	\mathbb{R}^-	Under/overproduction.
$\phi_t^{y^{\text{pv}}}$	\mathbb{R}^-	Renewable generation.

12.2 The Capacity Firming Framework

The capacity firming framework can be decomposed into a day-ahead engagement process, Section 12.2.1, and a real-time control process, Section 12.2.2. Each day is discretized in T periods of duration Δt . In the sequel the time period duration is the same for day-ahead engagement and the real-time control, t is used as a time period index, and \mathcal{T} is the set of time periods in a day.

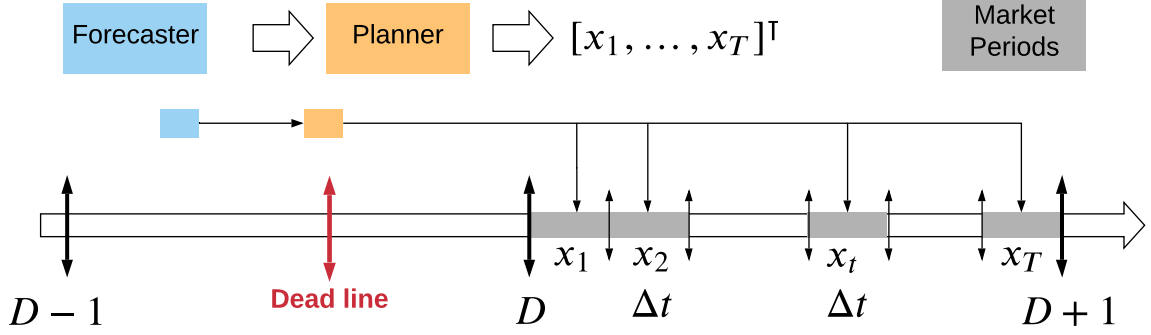


Fig. 12.2 Day-ahead nomination process.

12.2.1 Day-ahead engagement

Each day, the operator of the renewable generation plant is asked to provide the generation profile to be followed the next day to the grid operator, based on renewable generation forecasts. More formally, a planner computes on a day-ahead basis, before a deadline, a vector of engagements composed of T values $[x_1, \dots, x_T]^T$. Figure 12.2 illustrates the day-ahead nomination process. The engagements are accepted by the grid operator if they satisfy the constraints

$$|x_t - x_{t-1}| \leq \Delta X, \forall t \in \mathcal{T} \setminus \{1\} \quad (12.1a)$$

$$-x_t \leq -x_t^{\min}, \forall t \in \mathcal{T} \quad (12.1b)$$

$$x_t \leq x_t^{\max}, \forall t \in \mathcal{T}, \quad (12.1c)$$

with ΔX a power ramping constraint, that is a fraction of the total installed capacity P_c determined at the tendering stage and imposed by the grid operator.

12.2.2 Real-time control

Then, in real-time, a receding-horizon controller computes at each period the generation level and the charge or discharge set-points from t to T , based on forecasts of renewable generation and the engagements. Only the set-points of the first period are applied to the system. The remuneration is calculated ex-post based on the realized power y_t^m at the grid coupling point. For a given control period, the net remuneration r_t of the plant is the gross revenue $\Delta t \pi_t y_t^m$ minus a penalty $c(x_t, y_t^m)$, with π_t the contracted selling price set at the tendering stage

$$r_t = \Delta t \pi_t y_t^m - c(x_t, y_t^m), \forall t \in \mathcal{T}. \quad (12.2)$$

The penalty function c depends on the specifications of the tender. For the sake of simplicity the rest of this Chapter, c is assumed to be symmetric, convex, and quadratic piecewise-linear

$$c(x_t, y_t^m) = \pi^e(\Delta t)^2 \left(\max \left(0, |x_t - y_t^m| - pP_c \right) \right)^2 \quad (12.3)$$

with $0 \leq p \leq 1$, and π^e is a slack price (€/kWh²).

12.3 Problem formulation

The problem statement follows the abstract formulation defined in Chapter 11 where a global microgrid control problem can be defined as operating a microgrid safely and in an economically efficient manner. In the capacity firming context, a two-stage approach is considered with a planner and a controller. The CRE non-convex penalty that leads to a non-linear problem is modeled by a quadratic formulation with linear constraints. In this study, the planner and controller optimize economic criteria, which are only related to active power. The ancillary or grid services are not in the scope of the capacity firming specifications. The BESS degradation is not taken into account. The planner and controller horizons are cropped to twenty-four hours.

Deterministic (D) and stochastic (S) formulations of the day-ahead nomination problem are compared. The deterministic formulation is used as a reference to validate the stochastic approach by considering perfect knowledge of the future (D^{*}). In this Chapter, both approaches consider only exports to the grid¹. The optimization variables and the parameters are defined in Section 12.1.

Deterministic approach

The objective function J_D to minimize is the opposite of the net revenue

$$J_D(x_t, y_t) = \sum_{t \in T} -\pi_t \Delta t y_t + \pi^e(\Delta t)^2 [(d_t^-)^2 + (d_t^+)^2]. \quad (12.4)$$

¹The imports from the grid are allowed only under specific conditions into the contract.

The deterministic formulation is the following Mixed-Integer Quadratic Program (MIQP)

$$\begin{aligned} \min_{x_t \in \mathcal{X}, y_t \in \Omega(x_t, \hat{y}_t^{\text{pv}})} J_D(x_t, y_t) \\ \mathcal{X} = \{x_t : (12.6)\} \\ \Omega(x_t, \hat{y}_t^{\text{pv}}) = \{y_t : (12.7) - (12.11)\}, \end{aligned} \quad (12.5)$$

where \mathcal{X} and $\Omega(x_t, \hat{y}_t^{\text{pv}})$ are the sets of feasible engagements x_t and dispatch solutions y_t for a fixed engagement x_t and renewable generation point forecast \hat{y}_t^{pv} . The optimization variables of (12.5) are the engagement variables x_t , the dispatch variables y_t (the net power at the grid connection point), y_t^{dis} (BESS discharging power), y_t^{cha} (BESS charging power), s_t (BESS state of charge), y_t^b (BESS binary variables), y_t^{pv} (renewable generation), and d_t^-, d_t^+ (deviation variables) (cf. the notation Section 12.1). From (12.1), the engagement constraints are

$$x_t - x_{t-1} \leq \Delta X, \quad \forall t \in \mathcal{T} \setminus \{1\} \quad (12.6a)$$

$$x_{t-1} - x_t \leq \Delta X, \quad \forall t \in \mathcal{T} \setminus \{1\} \quad (12.6b)$$

$$-x_t \leq -x_t^{\min}, \quad \forall t \in \mathcal{T} \quad (12.6c)$$

$$x_t \leq x_t^{\max}, \quad \forall t \in \mathcal{T}. \quad (12.6d)$$

The ramping constraint on x_1 is deactivated to decouple consecutive days of simulation. In reality, the updated value of the last engagement of the previous day would be taken to satisfy the constraint. The set of constraints that bound y_t^{cha} , y_t^{dis} , and y_t^s variables are $\forall t \in \mathcal{T}$

$$y_t^{\text{cha}} \leq y_t^b y_{\max}^{\text{cha}} \quad [\phi_t^{\text{cha}}] \quad (12.7a)$$

$$y_t^{\text{dis}} \leq (1 - y_t^b) y_{\max}^{\text{dis}} \quad [\phi_t^{\text{dis}}] \quad (12.7b)$$

$$-s_t \leq -s^{\min} \quad [\phi_t^{s^{\min}}] \quad (12.7c)$$

$$s_t \leq s^{\max}, \quad [\phi_t^{s^{\max}}] \quad (12.7d)$$

where y_t^b are binary variables that prevent the simultaneous charge and discharge of the BESS. The power balance equation and the constraints on the net power at the

grid connection point are $\forall t \in \mathcal{T}$

$$y_t = y_t^{\text{pv}} + (y_t^{\text{dis}} - y_t^{\text{cha}}) \quad [\phi_t^y] \quad (12.8a)$$

$$-y_t \leq -y^{\text{min}} \quad [\phi_t^{y^{\text{min}}}] \quad (12.8b)$$

$$y_t \leq y^{\text{max}}. \quad [\phi_t^{y^{\text{max}}}] \quad (12.8c)$$

The dynamics of the BESS state of charge are

$$s_1 - s^{\text{ini}} = \Delta t (\eta^{\text{cha}} y_1^{\text{cha}} - \frac{y_1^{\text{dis}}}{\eta^{\text{dis}}}) \quad [\phi^{s^{\text{ini}}}] \quad (12.9a)$$

$$s_t - s_{t-1} = \Delta t (\eta^{\text{cha}} y_t^{\text{cha}} - \frac{y_t^{\text{dis}}}{\eta^{\text{dis}}}), \quad \forall t \in \mathcal{T} \setminus \{1\} \quad [\phi_t^s] \quad (12.9b)$$

$$s_T = s^{\text{end}} = s^{\text{ini}}, \quad [\phi^{s^{\text{end}}}] \quad (12.9c)$$

where the parameters s^{end} and s^{ini} are introduced to decouple consecutive days of simulation. In reality, s^{ini} would be the updated value of the last measured state of charge of the previous day. The variables d_t^-, d_t^+ are defined $\forall t \in \mathcal{T}$ to model the penalty

$$-d_t^- \leq (y_t - (x_t - pP_c)) \quad [\phi_t^{d^-}] \quad (12.10a)$$

$$-d_t^+ \leq ((x_t + pP_c) - y_t), \quad [\phi_t^{d^+}] \quad (12.10b)$$

with $0 \leq p \leq 1$. Finally, the PV generation is bounded $\forall t \in \mathcal{T}$ by the point forecast \hat{y}_t^{pv}

$$y_t^{\text{pv}} \leq \hat{y}_t^{\text{pv}}. \quad [\phi_t^{y^{\text{pv}}}] \quad (12.11)$$

Deterministic approach with perfect forecasts

With perfect forecasts, (12.5) becomes

$$\min_{x_t \in \mathcal{X}, y_t \in \Omega(x_t, \hat{y}_t^{\text{pv}} = y_t^{\text{pv}, \text{m}})} J_{D^*}(x_t, y_t), \quad (12.12)$$

with $\hat{y}_t^{\text{pv}} = y_t^{\text{pv}, \text{m}} \forall t \in \mathcal{T}$ in (12.11).

Stochastic approach

In the stochastic formulation, the objective is given by

$$J_S = \mathbb{E} \left[\sum_{t \in \mathcal{T}} -\pi_t \Delta t y_t + c(x_t, y_t) \right] \quad (12.13)$$

where the expectation is taken with respect to \hat{y}_t^{pv} . Using a scenario-based approach, (12.13) is approximated by

$$J_S \approx \sum_{\omega \in \Omega} \alpha_\omega \sum_{t \in \mathcal{T}} \left[-\pi_t \Delta t y_{t,\omega} + \pi^e (\Delta t)^2 \left((d_{t,\omega}^-)^2 + (d_{t,\omega}^+)^2 \right) \right], \quad (12.14)$$

with α_ω the probability of scenario $\omega \in \Omega$, and $\sum_{\omega \in \Omega} \alpha_\omega = 1$. Then, the problem to solve becomes

$$\min_{x_t \in \mathcal{X}, y_{t,\omega} \in \Omega(x_t, \hat{y}_{t,\omega}^{\text{pv}})} J_S(x_t, y_{t,\omega}). \quad (12.15)$$

All the optimization variables but x_t are now defined $\forall \omega \in \Omega$.

12.3.1 Evaluation methodology

The second step of capacity firming, *i.e.*, computing the set-points in real-time, is required to assess the quality of the nomination process. However, since this study focuses on the computation of day-ahead engagements, we simulate the second step with an ideal real-time controller² once the engagements are fixed. The methodology to assess the engagements consists of solving

$$J^{\text{eval}} = \sum_{t \in \mathcal{T}} -\pi_t x_t + c(x_t, y_t) \quad (12.16)$$

s.t (12.7)-(12.11) with $\hat{y}_t^{\text{pv}} = y_t^{\text{pv,m}}$ in (12.11) and given engagements x_t previously computed by the planner S. The optimization variables of (12.16) are y_t , d_t^- , d_t^+ , y_t^{pv} , y_t^{cha} , y_t^{dis} , and s_t . The optimal value of J_S^{eval} is compared with the optimal value of J_{D^*} in (12.12).

²Using a real-time controller with intraday forecasts is required to assess the planner-controller. However, this study focus only on the nomination step.

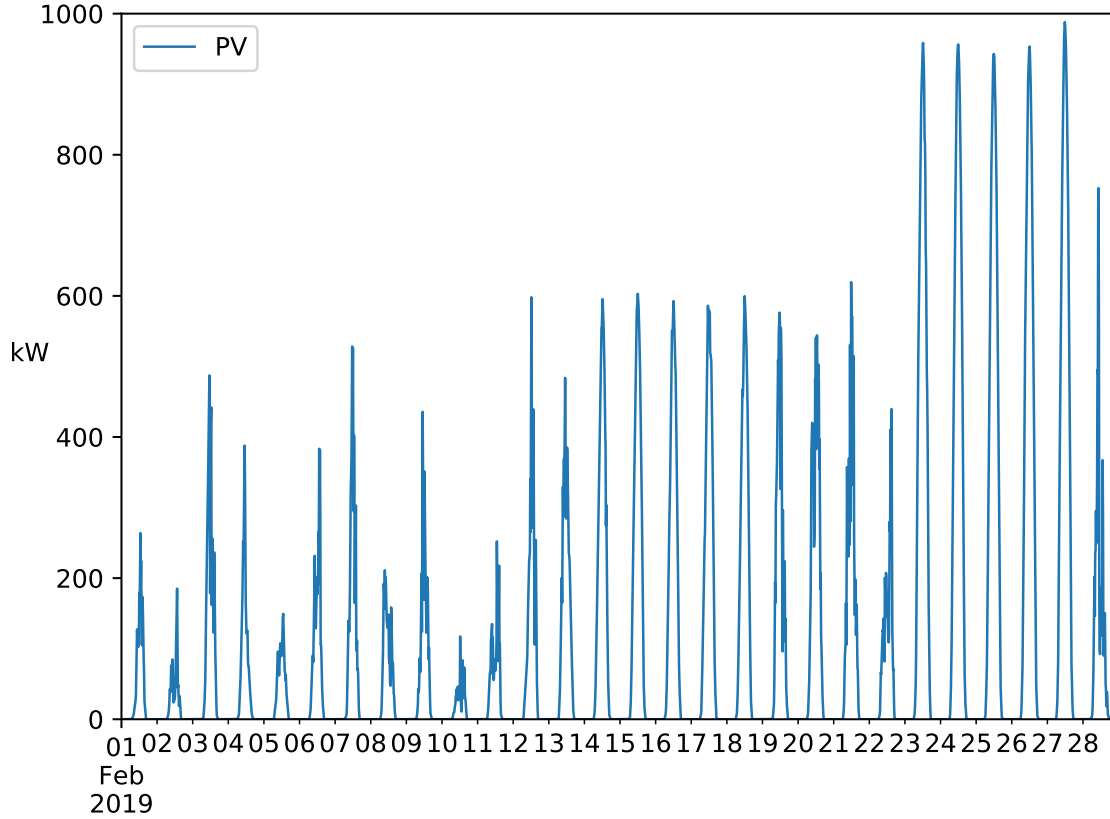


Fig. 12.3 MiRIS February 2019 PV production.

12.4 MiRIS microgrid case study

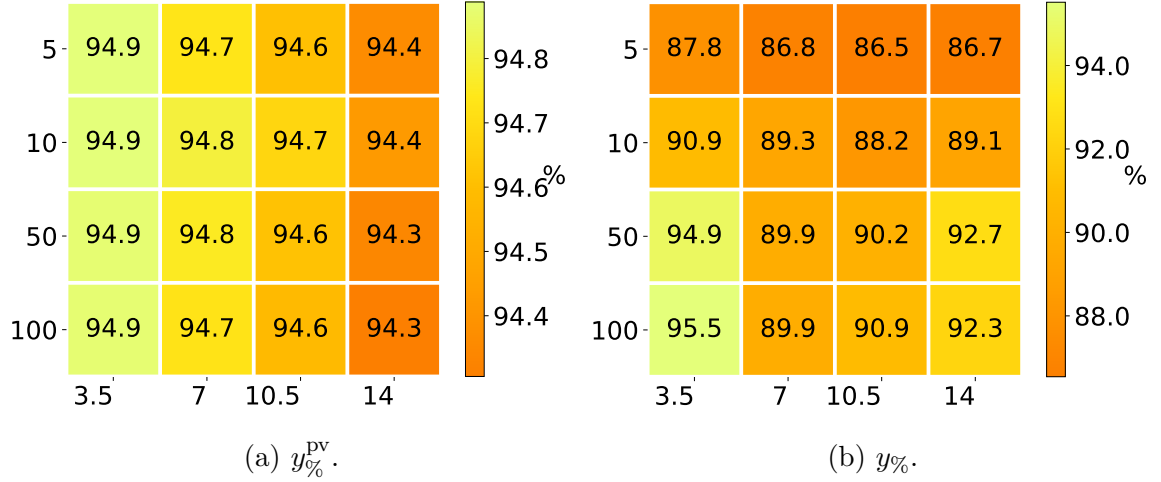
The MiRIS³ microgrid case study, located at the John Cockerill Group's international headquarters in Seraing, Belgium, is composed of a PV production plant, a BESS, and a load. For the need of this study, only historical data of PV generation are required. The BESS capacity \bar{S} is 1000 kWh, $s^{\max} = \bar{S}$, and the total PV installed capacity P_c is 2000 kWp. The market period duration Δt is 15 minutes. The simulation dataset \mathcal{D} is the month of February 2019. Figure 12.3 illustrates the MiRIS PV production and Table 12.1 provides some key statistics. Table 12.2 defines the indicators used in this section. It is of paramount importance to notice that the results of this case study are only valid for this dataset and cannot be extrapolated over an entire year without caution. CPLEX⁴ 12.9 is used to solve all the optimization problems, on an Intel Core

³<https://johncockerill.com/fr/energy/stockage-denergie/>

⁴<https://www.ibm.com/products/ilog-cplex-optimization-studio>

P_c	$\overline{y^{\text{pv},\text{m}}}$	$y_{\text{std}}^{\text{pv},\text{m}}$	$y_{\text{max}}^{\text{pv},\text{m}}$	$y_{\%,\text{max}}^{\text{pv},\text{m}}$	$y_{\text{tot}}^{\text{pv},\text{m}}$
2000	104.6	202.4	988.1	49.4	70.3

Table 12.1 MiRIS February 2019 dataset statistics.

Fig. 12.4 Planner S ratio indicator with $\# \Omega = 5, 10, 50, 100$, $\sigma = 3.5, 7, 10.5, 14\%$.

i7-8700 3.20 GHz based computer with 12 threads and 32 GB of RAM. Tables 12.3 and 12.4 provide the case study and BESS parameters.

12.4.1 Results for unbiased PV scenarios with fixed variance

A set of unbiased PV scenarios is generated for several values of the standard deviation σ of the prediction error. Table 12.5 shows the considered values of σ , expressed as a fraction of the actual PV generation. Moreover, Table 12.5 reports the cardinality of the generated scenario sets. Table 12.6 compares the average computation time per optimization problem between planners S and D*. Note, The optimization problem of planner S with $\# \Omega = 1$ has the same number of variables and constraints as the planner D*. The computation time is compatible with a day-ahead process even with 100 scenarios as it takes on average 7 seconds to compute the nominations for the day-ahead. Table 12.7 and Figure 12.4 provide the results of the ratio indicators, respectively, for the planners D* and S.

For all indicators, the results of both planners are almost equal with the smaller value of σ and the highest value of $\# \Omega$, as expected. On average the curtailment of PV generation equals 5%. The maximum $y_{\%}$ value is achieved with $\sigma = 3.5\%$ because the nominations are more conservative when the variance increases, leading to a smaller

Name	Description	Unit
$\overline{y^{\text{pv},\text{m}}}$	Averaged PV generation.	kW
$y_{\text{std}}^{\text{pv},\text{m}}$	PV generation standard deviation.	kW
$y_{\text{max}}^{\text{pv},\text{m}}$	Maximum PV generation.	kW
$y_{\text{tot}}^{\text{pv},\text{m}}$	Total PV energy produced.	MWh
$y_{\%,\text{max}}^{\text{pv},\text{m}}$	$y_{\text{max}}^{\text{pv},\text{m}}$ divided by the total installed PV capacity P_c .	%
\bar{t}_{CPU}	Averaged computation time per optimization problem.	s
$[X]^D$	Total of a variable X_t : $\sum_{t \in \mathcal{D}} X_t$.	X unit
$[y^{\text{pv}}]^D$	Total PV generation.	MWh
$y_{\%}^{\text{pv}}$	PV generation ratio: $\frac{[y^{\text{pv}}]^D}{[y^{\text{pv},\text{m}}]^D}$.	%
$y_{\%}^{\text{cha}}$	BESS charge ratio: $\frac{[y^{\text{cha}}]^D}{[y^{\text{pv}}]^D}$.	%
$y_{\text{max}\%}^{\text{cha}}$	Percentage of days of the dataset where the BESS achieved its maximum storage capacity.	%
$y_{\%}$	Export ratio: $\frac{[y]^D}{[x]^D}$.	%
R_{max}	Maximum achievable revenue: $\pi[y^{\text{pv},\text{m}}]^D$.	k€
R^e	Gross revenue: $\pi[y]^D$.	k€
r^e	Maximum achievable revenue ratio: $\frac{R^e}{R_{\text{max}}}$.	%
C^e	Quadratic penalty: $[c]^D$.	k€
$R^{n,e}$	Net revenue with quadratic penalty: $R^e - C^e$.	k€

Table 12.2 Comparison indicators.

π	π^e	Δt	ΔX	x^{\max}	y^{\max}	p
0.045	0.0045	15	10	2000	2000	5%

Table 12.3 Case study parameters.

s^{\max}	s^{\min}	y_{\max}^{cha}	y_{\max}^{dis}	η^{cha}	η^{dis}	s^{ini}	s^{end}
1000	0	1000	1000	1	1	0	0

Table 12.4 BESS parameters.

ratio. On average 30% (27%) of the production, for planner D^{*} (S), is stored in the BESS over the entire dataset. $\bar{S}_{\%}$ is equal to 17.9% (17.9%⁵) for the planner D^{*} (S) meaning the BESS reached its maximum storage level 5 days out of the 28 days of the dataset. In fact, during sunny days, the BESS is fully charged. A larger BESS capacity should decrease the curtailment and improve the gross revenue. It should be noted that this is a winter month where the maximum generated PV power reached only half of the installed PV capacity. During a summer month, the maximum production should reach at least 80% of the total installed capacity on sunny days. Thus, with a storage capacity of 1 MWh, the curtailment is expected to be much more important during summer sunny days.

Table 12.8 and Figure 12.5 provide the results of the revenue indicators for the planners D^{*} and S, respectively. It should be noted that in this case, $R^{n,e} = -J_S^{\text{eval}}$. The smallest value of the objective function is achieved by the planner D^{*} and is followed closely by the planner S, even for the highest value of σ . This result demonstrates the validity of the approach when exploiting an unbiased stochastic predictor.

In terms of net revenue, both planners achieved 93.7% of $R_{\max} \approx 3.16$ k€, which results in a loss of 6.3%. Most of this loss is due to the curtailment of PV generation. For both planners, the net revenue increases with the generation.

For sunny days, the difference between the nominations and the exports is higher than the deadband just before the production occurs, between 5 and 8 am, and smaller

⁵The value is the same for the $\#\Omega$ and σ values considered.

σ	3.5%	7%	10.5%	14%
$\#\Omega$	5	10	50	100

Table 12.5 Scenario generation parameters.

$\#\Omega$	1	5	10	50	100
# variables	769	3 457	6 817	33 697	67 297
# constraints	1 248	5 092	9 897	48 337	96 387
$\bar{t}_{\text{CPU S}}$	-	0.3	0.8	3	7
$\bar{t}_{\text{CPU D}^*}$	0.1	-	-	-	-

Table 12.6 Averaged computation times.

$[y^{\text{pv}}]^D$	$y_{\%}^{\text{pv}}$	$y_{\%}^{\text{cha}}$	$y_{\text{max}\%}^{\text{cha}}$	$y_{\%}$
66.7	94.9	29.6	17.9	76.2

Table 12.7 Planner D^{*} ratio indicators.

during the main hours of production, between 10 am and 3 pm. Indeed, the planner tends to maximize the revenue by maximizing the exports. However, the ramping power constraints (12.6) impose a maximum difference between two consecutive nominations. To maximize the net revenue over the entire day, the planner computes nominations that are not achievable at the beginning of the day to maximize the exports during the day. This results in a penalty, between 5 and 8 am.

12.4.2 BESS capacity sensitivity analysis

The goal is to conduct a sensitivity analysis on the BESS capacity \bar{S} to determine its marginal value and the optimal BESS size \bar{S}^* for a given CAPEX $\pi_{\bar{S}}$. The efficiencies are still assumed to be unitary. s^{ini} and s^{end} are set to 0 kWh. Table 12.9 provides the other BESS parameters for the five cases. The scenarios are generated using $\#\Omega = 100$, and $\sigma = 3.5, 7, 10.5, 14\%$. A new indicator, expressed in k€, is defined to quantify the gain provided by the BESS over fifteen years

$$\Delta R_i^{n,e} = 15 \times 12 \times (R_i^{n,e} - R_5^{n,e}) \quad \forall i \in \{1, 2, 3, 4\}. \quad (12.17)$$

R^e	r^e	C^e	$R^{n,e}$	$J_{D^*}^{\text{eval}}$
3.0	94.9	0.04	2.96	-2.96

Table 12.8 Planner D^{*} revenue indicators.

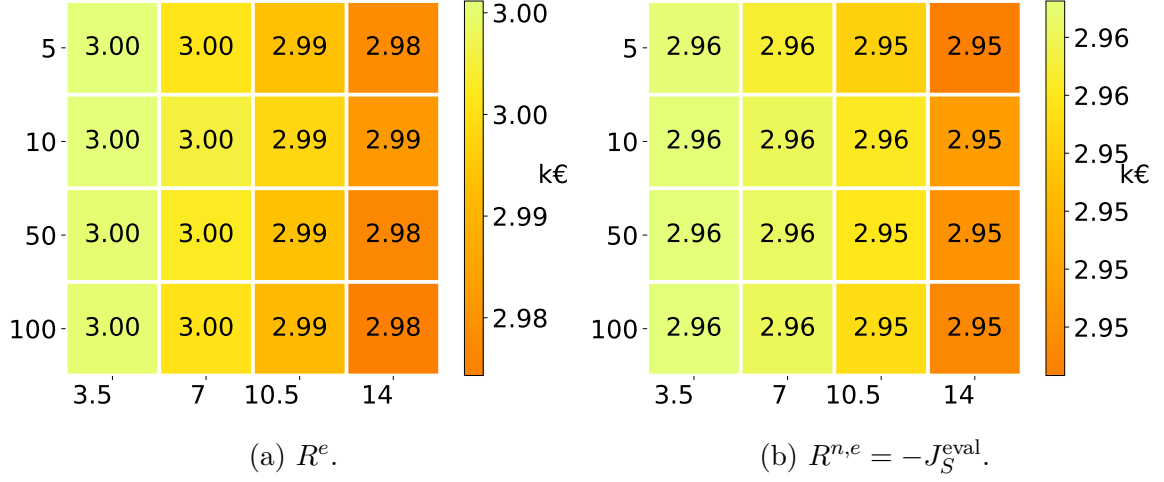


Fig. 12.5 Planner S revenue indicators with $\# \Omega = 5, 10, 50, 100$, $\sigma = 3.5, 7, 10.5, 14\%$.

Case	\bar{S} [kWh]	s^{\min} [kWh]	y_{\max}^{cha} [kW]	y_{\max}^{dis} [kW]
1	2000	0	2000	2000
2	1000	0	1000	1000
3	500	0	500	500
4	250	0	250	250
5	0	0	0	0

Table 12.9 BESS parameters.

It is a lower bound of the total gain as it relies on the results of a winter month. A summer month should provide higher revenue. Table 12.10 provide the planner D* indicators. The results demonstrate the interest in using a BESS to optimize the bidding. The larger the BESS is, the lower the curtailment is. Thus, the net revenue increases with the BESS capacity. The maximum achievable revenue is reached with a storage capacity of 2 MWh. However, the larger the BESS is, the smaller $\Delta R^{n,e}$ increases. It means the marginal benefit decreases with the increase of BESS capacity. A trade-off should be found between the BESS capacity and its CAPEX. Figure 12.6a provides $\Delta R^{n,e}$ and its quadratic interpolation in comparison with two BESS prices $\pi_{\bar{S}} = 0.1$ and 0.228 k€/kWh. The value of the derivative $[\frac{d\Delta R^{n,e}}{d\bar{S}}]_{\bar{S}=0}$ provides the maximum CAPEX that provides a profitable BESS. Then, the optimal storage capacity \bar{S}^* for a given CAPEX is provided solving $[\frac{d\Delta R^{n,e}}{d\bar{S}}]_{\bar{S}} = \pi_{\bar{S}}$. For instance, with a CAPEX of 0.1 k€/kWh, \bar{S}^* is approximately 350 kWh. Figure 12.6b provides the values of $\Delta R^{n,e} - \pi_{\bar{S}}\bar{S}$ with a quadratic interpolation.

Case	$[y^{\text{pv}}]^D$	$y_{\%}^{\text{pv}}$	$y_{\%}^{\text{cha}}$	$y_{\text{max}\%}^{\text{cha}}$	$y_{\%}$
1	70.3	100	45.6	17.9	77.7
2	66.7	94.9	29.6	17.9	76.2
3	63.6	90.5	17.3	39.3	76.4
4	61.7	87.7	11.1	46.4	75.2
5	56.0	79.6	-	-	70.4
Case	R^e	C^e	$R^{n,e}$	$J_{D^*}^{\text{eval}}$	$\Delta R^{n,e}$
1	3.16	0.01	3.15	-3.15	128
2	3.0	0.04	2.96	-2.96	94
3	2.86	0.04	2.84	-2.84	72
4	2.77	0.06	2.71	-2.71	49
5	2.52	0.08	2.44	-2.44	0

Table 12.10 Planner D* ratio and revenue indicators BESS capacity sensitivity analysis.

Figure 12.7 provides the planner S revenue indicators. The results are still almost identical for all indicators for the smallest value of σ and very close with the highest one, as is expected.

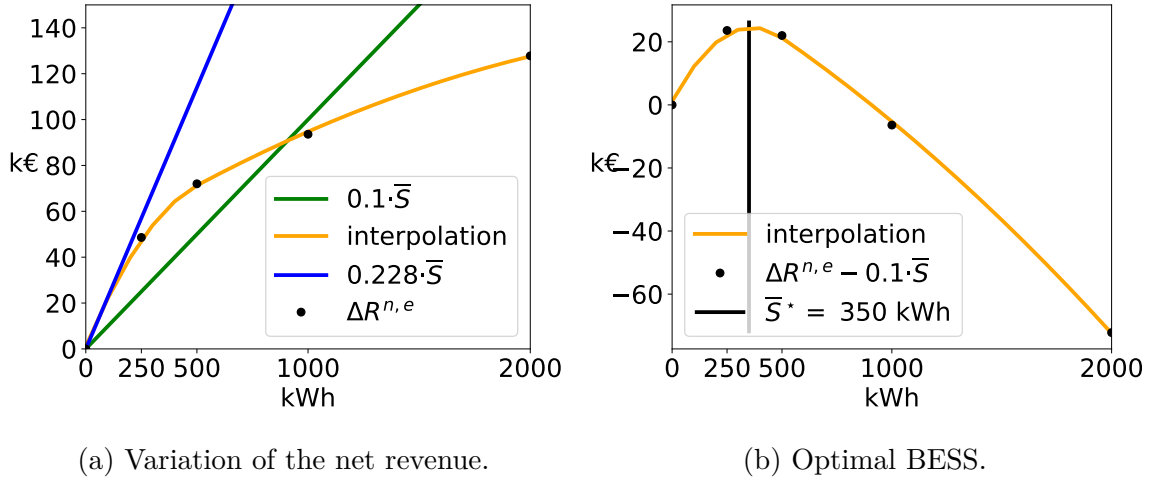


Fig. 12.6 Optimal BESS for a given CAPEX price.

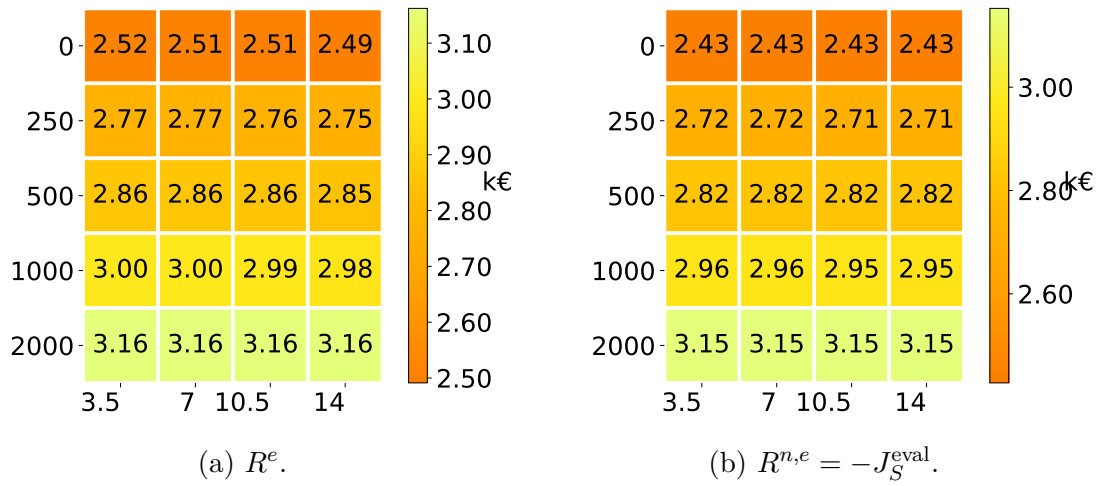


Fig. 12.7 Planner S revenue indicators BESS capacity sensitivity analysis with $\#\Omega = 100$, $\sigma = 3.5, 7, 10.5, 14\%$.

12.5 Conclusions and perspectives

This Chapter addresses the energy management of a grid-connected PV plant coupled with a BESS within the capacity firming framework, which is decomposed in two steps: computing the day-ahead nominations, then computing the renominations and the set-points in real-time to minimize the energy and ramp power deviations from nominations. This Chapter investigates the first step by comparing a stochastic and a deterministic formulation. The main goal is to validate the stochastic approach by using an ideal predictor providing unbiased PV scenarios.

The results of the stochastic planner are comparable with those of the deterministic planner, even when the prediction error variance is non-negligible. Finally, the results of the BESS capacity sensitivity analysis demonstrate the advantage of using a BESS to optimize the bidding day-ahead strategy. However, a trade-off must be found between the marginal gain provided by the BESS and its investment and operational costs.

Several extensions of this work are under investigation. The first is to better assess the planner's behavior using a full year of data. Then, the next challenge is to use a more realistic methodology to generate PV generation scenarios. Several scenario generation approaches could be investigated, based on a point forecast model such as the PVUSA model [39, 16, 17], combined with Gaussian copula [114, 121, 61]. Or using the deep generative models introduced in Chapter 8. Another challenge is to consider the non-convex penalty function specified by the CRE into the objective. Finally, the last challenge is to investigate the second step of the capacity firming problem, for instance by adapting the approach implemented in Dumas et al. [47].

12.6 Appendix: PV scenario generation

This Annex describes the methodology to generate the set of unbiased PV scenarios. The goal is to define an ideal unbiased predictor with a fixed variance over all lead times. In this section, let t be the current time index, k be the lead time of the prediction, K be the maximum lead time of the prediction, y_{t+k} be the true value of the signal y at time $t + k$, and $\hat{y}_{t+k|t}$ be the value of y_{t+k} predicted at time t . The forecasts are computed at 4 pm (nominations deadline) for the day-ahead. With a market period duration of fifteen minutes, K is equal to 128. The PV forecasts are needed for lead times from $k = 33$ (00:00 to 00:15 am) to $k = K = 128$ (11:45 to 12:00 pm). Then,

$\hat{y}_{t+k|t}$ and y_{t+k} are assumed to be related by

$$\hat{y}_{t+k|t} = y_{t+k}(1 + \epsilon_k). \quad (12.18)$$

The error term ϵ_k is generated by the moving-average model [25, Chapter 3]

$$\epsilon_1 = \eta_1 \quad (12.19a)$$

$$\epsilon_k = \eta_k + \sum_{i=1}^{k-1} \alpha_i \eta_{k-i} \quad \forall k \in \{2, \dots, K\} \quad (12.19b)$$

with $\{\alpha_i\}_{i=1}^{K-1}$ scalar coefficients, $\{\eta_k\}_{k=1}^K$ independent and identically distributed sequences of random variables from a normal distribution $\mathcal{N}(0, \sigma)$. Thus, the variance of the error term is

$$\text{Var}(\epsilon_1) = \sigma^2 \quad (12.20a)$$

$$\text{Var}(\epsilon_k) = \left(1 + \sum_{i=1}^{k-1} \alpha_i^2\right) \sigma^2 \quad \forall k \in \{2, \dots, K\}. \quad (12.20b)$$

It is possible to simulate with this model an increase of the prediction error variance with the lead time k by choosing

$$\alpha_i = p^i \quad \forall i \in \{1, \dots, K-1\}. \quad (12.21)$$

(12.20a) becomes, $\forall k \in \{1, \dots, K\}$

$$\text{Var}(\epsilon_k) = \sigma^2 A_{\epsilon_k} \quad (12.22)$$

with A_{ϵ_k} defined $\forall k \in \{1, \dots, K\}$ by

$$A_{\epsilon_k} = \sum_{i=0}^{k-1} (p^2)^i = \frac{1 - (p^2)^k}{1 - p^2}. \quad (12.23)$$

Then, with $0 \leq p < 1$, it is possible to make the prediction error variance independent of the lead time as it increases. Indeed:

$$\lim_{k \rightarrow \infty} A_{\epsilon_k} = A_{\infty} = \frac{1}{1 - p^2}. \quad (12.24)$$

For instance, with $p = 0.9$ and $K = 128$, for $k \geq 33$, $A_{\epsilon_k} \approx A_\infty$ that is approximately 5.26. Thus, $\forall k \in \{33, \dots, K\}$

$$\text{Var}(\epsilon_k) \approx 5.26\sigma^2. \quad (12.25)$$

Finally, the σ value to set a maximum ϵ_{\max} with a high probability of 0.997, corresponding to a three standard deviation confidence interval from a normal distribution, is found by imposing $\epsilon_{\max} = 3\sqrt{\text{Var}(\epsilon_K)}$:

$$\sigma \approx \frac{\epsilon_{\max}}{3\sqrt{A_\infty}}, \quad (12.26)$$

with $\epsilon_{\max} = 0.25, 0.50, 0.75, 1.0$, $\sigma = 3.5, 7, 10.5, 14\%$.

Chapter 13

Capacity firming sizing

Overview

This Chapter proposes an approach to size a grid-connected renewable generation plant coupled with a battery energy storage device in the capacity firming market. The main novelties, in the CRE capacity framework context, are three-fold.

1. First, a MIQP formulation is proposed to address the planning stage of the two-phase engagement control, that is compatible with a scenario approach, to approximate the Mixed-Integer Non-Linear Programming problem generated by the CRE non-convex penalty function. It is compared to the deterministic formulation using perfect knowledge of the future and PV point forecasts on empirical data from the PV production monitored on-site at the Liège University (ULiège), Belgium.
2. Second, a transparent and easily reproducible Gaussian copula methodology is implemented to generate PV scenarios based on the parametric PVUSA model using a regional climate model.
3. Finally, the sizing of the system is addressed by a grid search to approximate the optimal sizing for a given selling price using both the deterministic and stochastic approaches.

References: This chapter is an adapted version of the following publication:

Jonathan Dumas, Bertrand Cornélusse, Xavier Fettweis, Antonello Giannitrapani, Simone Paoletti, and Antonio Vicino. Probabilistic forecasting for sizing in the capacity firming framework. In *2021 IEEE Madrid PowerTech*, pages 1–6, 2021. doi: 10.1109/PowerTech46648.2021.9494947. URL <https://arxiv.org/abs/2106.02323>.

Terminology and notations have been slightly adjusted for the sake of consistency with the rest of this manuscript. The text has also been processed to minimize overlap with respect to the other chapters.

“Each player must accept the cards life deals him or her: but once they are in hand, he or she alone must decide how to play the cards in order to win the game.”

— Voltaire

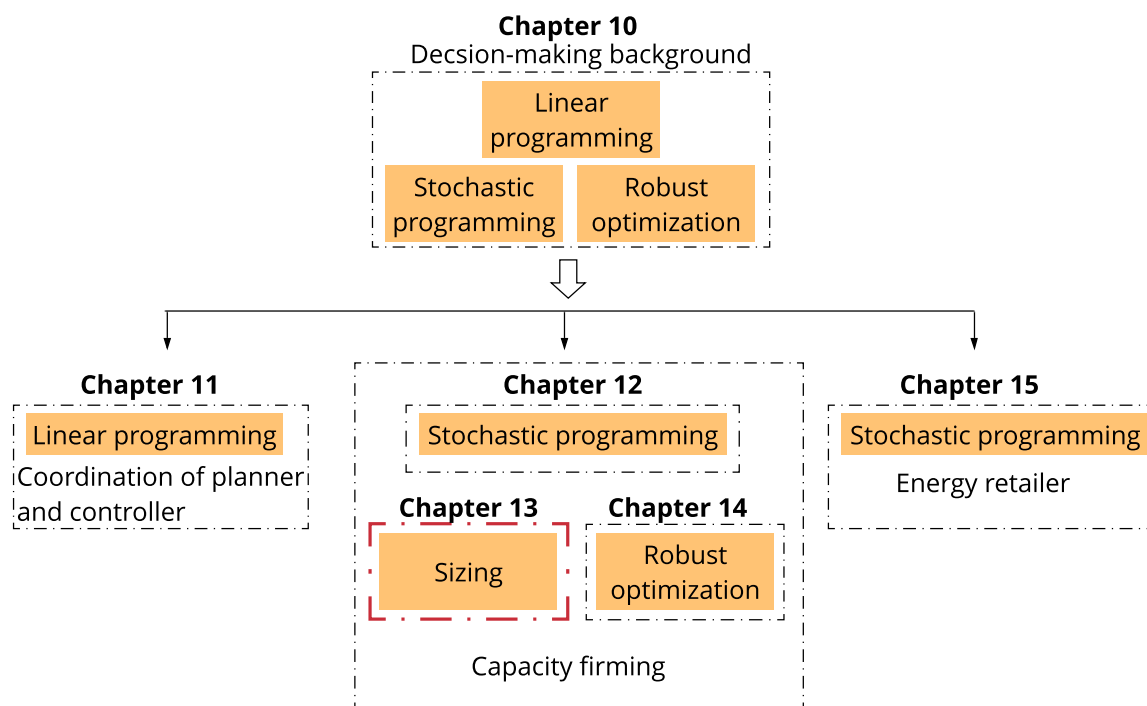


Fig. 13.1 Chapter 13 position in Part II.

The sizing has only been investigated by Haessig [69] in a similar context but with a wind farm. The main thread motivating the contribution of this Chapter is to extend Chapter 12 to address the sizing of a grid-connected PV plant and a BESS subject to grid constraints in this context. However, the sizing problem is difficult due to this two-phase engagement control with a day-ahead nomination and an intraday control to minimize deviations from the planning. A single sizing optimization problem would result in a non-linear bilevel optimization problem with an upper level, the sizing part, and a lower level, the two-phase engagement control. Thus, a grid search is conducted to approximate the optimal sizing for a given selling price using both the deterministic and stochastic approaches. In the two-phase engagement control, the PV uncertainty is taken into account at the planning stage by considering a stochastic approach that uses PV scenarios generated by a Gaussian copula methodology. The planner determines the engagement profile on a day-ahead basis given a selling price profile, the PV scenarios, and the current state of the system, including the battery state of charge. Then, the engagement plan is sent to the grid operator and to the controller that computes every 15 minutes the production, *i.e.*, injection or withdrawal, and set-points, *e.g.*, BESS charge or discharge, until the end of the day. The optimization problems are formulated as Mixed-Integer Quadratic Problems (MIQP) with linear constraints.

The remainder of this Chapter is organized as follows. Section 13.1 defines the problem statement. Section 13.2 provides the PVUSA parametric point forecast model, and the Gaussian Copula approach to generate PV scenarios. Section 13.3 investigates the system sizing using both the deterministic and stochastic MIQP approaches. Finally, Section 13.4 summarizes the main findings and highlights ideas for further work. Note, the capacity firming process is described in Section 12.2 of Chapter 12.

13.1 Problem statement

In this Chapter, the problem formulation is almost strictly identical to Chapter 12. The only difference lies in the definition (12.2) of the penalty c . To conduct the sizing, the penalty defined in the CRE specifications of the tender AO-CRE-ZNI 2019 published on July 12, 2019 is adopted. The optimization variables and the parameters are defined in Section 12.1.

Stochastic approach

A stochastic planner with a MIQP formulation and linear constraints is implemented using a scenario-based approach. The planner computes on a day-ahead basis the engagement plan x_t , $\forall t \in \mathcal{T}$ to be sent to the grid. The problem formulation is given by (12.15) where only short deviations are considered with the penalty defined in the CRE specifications of the tender AO-CRE-ZNI 2019 published on *July* 12, 2019. In compact form, the optimization problem is

$$\min \sum_{\omega \in \Omega} \alpha_{\omega} \sum_{t \in \mathcal{T}} \left[-\Delta t \pi_t y_{t,\omega} + \frac{\Delta t \pi_t}{P_c} d_{t,\omega}^- (d_{t,\omega}^- + 4pP_c) \right] \quad \text{s.t.:} \quad (13.1a)$$

$$x_t - x_{t-1} \leq \Delta X_t, \forall t \in \mathcal{T} \setminus \{1\} \quad (13.1b)$$

$$x_{t-1} - x_t \leq \Delta X_t, \forall t \in \mathcal{T} \setminus \{1\} \quad (13.1c)$$

$$x_t \leq x_t^{\max}, \forall t \in \mathcal{T} \quad (13.1d)$$

$$-x_t \leq -x_t^{\min}, \forall t \in \mathcal{T} \quad (13.1e)$$

$$-d_{t,\omega}^- \leq y_{t,\omega} - (x_t - pP_c), \forall t \in \mathcal{T} \quad (13.1f)$$

$$y_{t,\omega} \leq (x_t + pP_c), \forall t \in \mathcal{T} \quad (13.1g)$$

$$y_{t,\omega}^{\text{pv}} \leq \hat{y}_{t,\omega}^{\text{pv}}, \forall t \in \mathcal{T} \quad (13.1h)$$

$$y_{t,\omega}^{\text{cha}} \leq y_{t,\omega}^b y_{\max}^{\text{cha}}, \forall t \in \mathcal{T} \quad (13.1i)$$

$$y_{t,\omega}^{\text{dis}} \leq (1 - y_{t,\omega}^b) y_{\max}^{\text{dis}}, \forall t \in \mathcal{T} \quad (13.1j)$$

$$-s_{t,\omega} \leq -s^{\min}, \forall t \in \mathcal{T} \quad (13.1k)$$

$$s_{t,\omega} \leq s^{\max}, \forall t \in \mathcal{T} \quad (13.1l)$$

$$y_{t,\omega} = y_{t,\omega}^{\text{pv}} + y_{t,\omega}^{\text{dis}} - y_{t,\omega}^{\text{cha}}, \forall t \in \mathcal{T} \quad (13.1m)$$

$$y_{t,\omega} \leq y_t^{\max}, \forall t \in \mathcal{T} \quad (13.1n)$$

$$-y_{t,\omega} \leq -y_t^{\min}, \forall t \in \mathcal{T} \quad (13.1o)$$

$$s_{1,\omega} - s^{\text{ini}} = \Delta t (\eta^{\text{cha}} y_{1,\omega}^{\text{cha}} - \frac{y_{1,\omega}^{\text{dis}}}{\eta^{\text{dis}}}) \quad (13.1p)$$

$$s_{t,\omega} - s_{t-1,\omega} = \Delta t (\eta^{\text{cha}} y_{t,\omega}^{\text{cha}} - \frac{y_{t,\omega}^{\text{dis}}}{\eta^{\text{dis}}}), \forall t \in \mathcal{T} \setminus \{1\} \quad (13.1q)$$

$$s_{T,\omega} = s^{\text{end}} = s^{\text{ini}}. \quad (13.1r)$$

The optimization variables are x_t (engagement at the coupling point), $y_{t,\omega}$ (net power at the coupling point), $\forall \omega \in \Omega$, $d_{t,\omega}^-$ (underproduction), $y_{t,\omega}^{\text{pv}}$ (PV generation), $y_{t,\omega}^b$ (BESS binary variable), $y_{t,\omega}^{\text{cha}}$ (BESS charging power), $y_{t,\omega}^{\text{dis}}$ (BESS discharging power), and $s_{t,\omega}$ (BESS state of charge) (cf. the notation Section 12.1). The engagement

constraints are (13.1b)-(13.1e), where the ramping constraint on x_1 is deactivated to decouple consecutive days of simulation. The CRE non-convex piecewise quadratic penalty function is modeled by the constraints (13.1f) $\forall \omega \in \Omega$, that defines the variables $d_{t,\omega}^- \in \mathbb{R}_+$ to model the quadratic penalty for underproduction, and (13.1g) $\forall \omega \in \Omega$ forbidding overproduction that is non-optimal as curtailment is allowed [108]. The set of constraints that bound $y_{t,\omega}^{\text{pv}}$, $y_{t,\omega}^{\text{cha}}$, $y_{t,\omega}^{\text{dis}}$, and $s_{t,\omega}$ variables are (13.1h)-(13.1l) $\forall \omega \in \Omega$ where $\hat{y}_{t,\omega}^{\text{pv}}$ are PV scenarios, and $y_{t,\omega}^b$ are binary variables that prevent the BESS from charging and discharging simultaneously. The power balance equation and the production constraints are (13.1m) and (13.1n)-(13.1o) $\forall \omega \in \Omega$. The dynamics of the BESS state of charge is provided by constraints (13.1p)-(13.1r) $\forall \omega \in \Omega$. Note, the parameters s^{end} and s^{ini} are introduced to decouple consecutive days of simulation.

Deterministic approach

The deterministic (D) formulation of the planner is a specific case of the stochastic formulation by considering only one scenario where $y_{t,\omega}^{\text{pv}}$ become \hat{y}_t^{pv} , PV point forecasts. The deterministic formulation with perfect forecasts (D^*) is D with $\hat{y}_t^{\text{pv}} = y_t^{\text{pv,m}} \forall t \in \mathcal{T}$. For both the deterministic planners D and D^* , the optimization variables are x_t , y_t , d_t^- , y_t^{pv} , b_t , y_t^{cha} , y_t^{dis} , and s_t .

Oracle controller

The oracle controller is an ideal real-time controller that assumes perfect knowledge of the future by using as inputs the engagement profile to compute the set-points, maximize the revenues and minimize the deviations from the engagements. The oracle controller is D^* where the engagements are parameters.

13.2 Forecasting methodology

The Gaussian copula approach has been widely used to generate wind and PV scenarios in power systems [124, 61]. However, to the best of our knowledge, there is almost no guidance available on which copula family can describe correlated variations in PV generation [61], hence the Gaussian copula family is selected instead of copulas like Archimedean or Elliptical.

13.2.1 Gaussian copula-based PV scenarios

In this section, let t be the current time index, k be the lead time of the prediction, $Z = \{Z_1, \dots, Z_T\}$ a multivariate random variable, $F_{Z_k}(\cdot)$, $k = 1, \dots, T$ the marginal cumulative distribution functions, and R_Z the correlation matrix. The goal is to generate samples of Z . The Gaussian copula methodology consists of generating a trajectory $u = [u_1, \dots, u_T]$ from the multivariate Normal distribution $\mathcal{N}(0, R_Z)$. Then, to transform each entry u_k through the standard normal cumulative distribution function $\phi(\cdot)$: $\tilde{u}_k = \phi(u_k)$, $k = 1, \dots, T$, and finally, to apply to each entry \tilde{u}_k the inverse marginal cumulative distribution function of Z_k : $z_k = F_{Z_k}^{-1}(\tilde{u}_k)$, $k = 1, \dots, T$. In our case, Z is defined as the error between the PV measurement x and the PV point forecast \hat{y}^{PV}

$$Z_k = y_{t+k}^{\text{PV,m}} - \hat{y}_{t+k|t}^{\text{PV}} \quad k = 1, \dots, T. \quad (13.2)$$

$\hat{F}_{Z_k}(\cdot)$ and \hat{R}_Z are estimated from the data, and following the methodology described above, a PV scenario i at time t is generated for time $t + k$

$$\hat{y}_{t+k|t}^{\text{PV},(i)} = \hat{y}_{t+k|t}^{\text{PV}} + z_k^i \quad k = 1, \dots, T. \quad (13.3)$$

The PV point forecasts $\hat{y}_{t+k|t}^{\text{PV}}$ are computed by using the PVUSA model presented in the following Section.

13.2.2 PV point forecast parametric model

A PV plant can be modeled using the well-known PVUSA parametric model [39], which expresses the instantaneous generated power as a function of irradiance and air temperature

$$y_t^{\text{PV,m}} = aI_t + bI_t^2 + cI_tT_t, \quad (13.4)$$

where $y_t^{\text{PV,m}}$, I_t and T_t are the generated power, irradiance and air temperature at time t , respectively, and $a > 0$, $b < 0$, $c < 0$ are the PVUSA model parameters. These parameters are estimated following the algorithm of Bianchini et al. [16] that efficiently exploits only the power generation measurements and the theoretical clear-sky irradiance, and is characterized by very low computational effort. The same implementation of the algorithm is used with a sliding window of 12 hours. The parameters reached the steady-state values in 50 days on the Uliège case study,

described in the following Section, with

$$[\tilde{a}, \tilde{b}, \tilde{c}]^\top = [0.573, -7.68 \cdot 10^{-5}, -1.86 \cdot 10^{-3}]^\top. \quad (13.5)$$

The weather hindcasts from the MAR regional climate model [50], provided by the Laboratory of Climatology of the Liège University, are used as inputs of the parametric PVUSA model. The MAR regional climate is forced by the ERA5 reanalysis database, the fifth-generation European Centre for Medium-Range Weather Forecasts atmospheric reanalysis of the global climate, to produce weather hindcasts. Finally, the PV point forecasts are computed

$$\hat{y}_{t+k|t}^{\text{PV}} = \tilde{a}\hat{I}_{t+k|t} + \tilde{b}\hat{I}_{t+k|t}^2 + \tilde{c}\hat{I}_{t+k|t}\hat{T}_{t+k|t}, \quad \forall k = k_1, \dots, k_T, \quad (13.6)$$

and use as inputs to generate PV scenarios following the Gaussian copula approach.

13.2.3 PV scenarios

The Uliège case study is composed of a PV generation plant with an installed capacity of 466.4 kWp. The simulation dataset is composed of the period of August 2019 to December 2019, 151 days in total, with a total production of 141.3 MWh. The Uliège PV generation is monitored on a minute basis and is resampled to 15 minutes. The set of PV scenarios is generated using the Gaussian copula approach based on the PVUSA point forecasts. Figure 13.2 illustrates a set of 5 PV scenarios on four days of the dataset. The PV scenarios are used as input of a stochastic optimization problem.

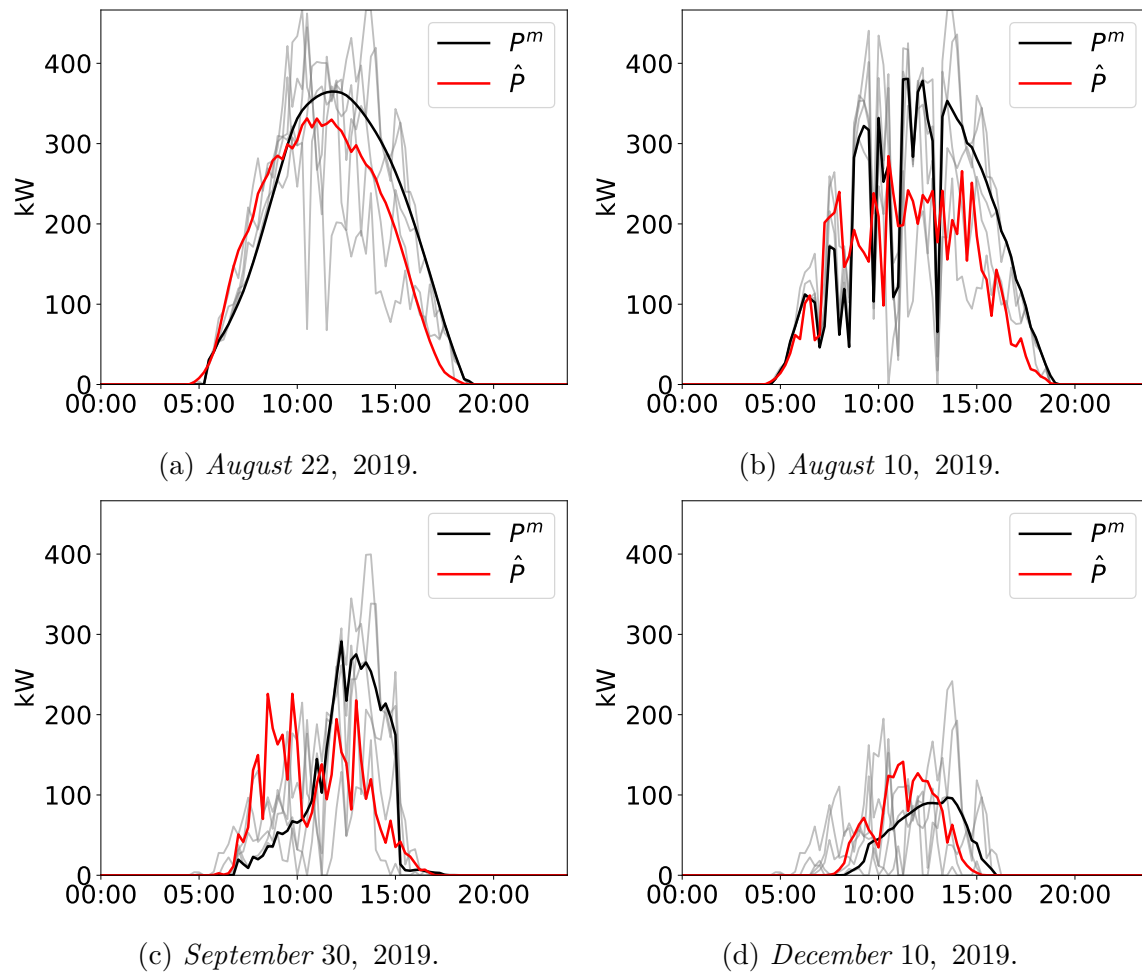


Fig. 13.2 5 PV scenarios (gray), PVUSA point forecasts (red), and PV measurements (black).

13.3 Sizing study

The goal is to determine the optimal sizing of the BESS and PV for a given selling price and its related net revenue over the lifetime project to optimally bid at the tendering stage.

13.3.1 Problem statement and assumptions

The ratio $r_{\bar{S}} = \frac{\bar{S}}{P_c}$, BESS maximum capacity over the PV installed capacity, is introduced to model several BESS and PV system configurations. The total exports, imports, deviation costs, number of charging and discharging cycles for several $r_{\bar{S}}$ and selling prices are computed. Based on the BESS and PV CapEx (Capital Expenditure) I and OpEx (Operational Expenditure) O&M, the LCOE (Levelized Cost Of Energy) is calculated

$$\text{LCOE} = \frac{\text{CRF} \cdot \text{I} + \text{O\&M} + \text{W} + \text{C}}{\text{E}}, \quad (13.7)$$

with CRF the Capital Recovery Factor (or Annuity Factor), and E, W, C, the annual export, withdrawal, and deviation costs, respectively. Then, the net revenue over the lifetime project is defined as the annual gross revenue R divided by the annual export to the grid minus the LCOE

$$\text{net}(\pi, r_{\bar{S}}) := \frac{R}{E} - \text{LCOE}. \quad (13.8)$$

The higher the net revenue, the more profitable the system. Section 13.3.2 details the LCOE definition and the assumptions to establish (13.7) and (13.8). Finally, the optimal sizing for a given selling price is provided by

$$r_{\bar{S}}^*(\pi) = \arg \max_{r_{\bar{S}} \in \mathcal{R}_{\bar{S}}} \text{net}(\pi, r_{\bar{S}}), \quad (13.9)$$

with $\mathcal{R}_{\bar{S}}$ the sizing space, and the sizing approach is depicted in Figure (13.3).

13.3.2 Levelized cost of energy (LCOE)

The LCOE (€/ MWh) is "the unique break-even cost price where discounted revenues, price times quantities, are equal to the discounted net expenses"¹. It means the LCOE is the lower bound of the selling price to be profitable over the lifetime of the project

¹Annex II Metrics & Methodology of the AR5 IPCC report.

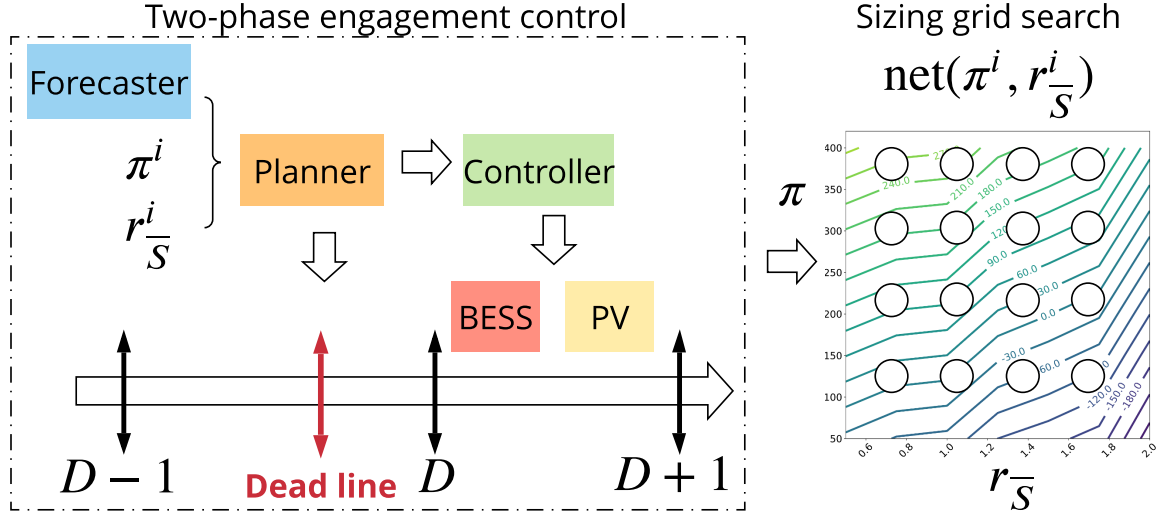


Fig. 13.3 Sizing approach.

and is defined as

$$\sum_{t=0}^n \frac{E_t \cdot \text{LCOE}}{(1+i)^t} = \sum_{t=0}^n \frac{\text{Expenses}_t}{(1+i)^t}, \quad (13.10)$$

with i (%) the discount rate, n (years) the lifetime of the project, and E_t (MWh) the annual energy at year t . Considering energy conversion technologies, the lifetime expenses comprise investment costs I that are the upfront investment (or CapEx) (€/kW for PV and €/kWh for BESS), operation and maintenance cost (or OpEx) O&M (€/kW for PV and €/kWh for BESS), the annual cost of the energy withdrawn from the grid W (€), and the annual deviation cost penalty C (€)

$$\text{LCOE} = \frac{\sum_{t=0}^n \frac{I_t + \text{O\&M}_t + W_t + C_t}{(1+i)^t}}{\sum_{t=0}^n \frac{E_t}{(1+i)^t}}. \quad (13.11)$$

We assume the annual cost of the energy E_t (W_t) exported (withdrawn), the annual OpEx O\&M_t , and the annual deviation cost C_t are constant during the lifetime of the project: E , W , C and $\text{O\&M} \forall t > 0$. The investment costs I are the sum of all capital expenditures needed to make the investment fully operational discounted to $t = 0$. Thus, $I_t = 0 \forall t > 0$ and $I_0 = I$. Finally, the system is operational at year $t = 1$: $E_0 = 0$, $\text{O\&M}_0 = 0$, $W_0 = 0$, and $C_0 = 0$. (13.11) becomes

$$\text{LCOE} = \frac{I + (\text{O\&M} + W + C) \sum_{t=1}^n \frac{1}{(1+i)^t}}{E \sum_{t=1}^n \frac{1}{(1+i)^t}}, \quad (13.12)$$

that is re-written

$$\text{LCOE} = \frac{\text{CRF} \cdot I + \text{O\&M} + W + C}{E}, \quad (13.13)$$

with $\text{CRF} = (\sum_{t=1}^n \frac{1}{(1+i)^t})^{-1} = \frac{i}{1-(1+i)^{-n}}$. The gross revenue is the energy exported to the grid that is remunerated at the selling price. The annual gross revenue R is assumed to be constant over the project lifetime. Then, the LCOE can be compared to R divided by the annual export E to assess the financial viability of the project by calculating (13.8).

13.3.3 Case study description

The ULiège case study is composed of a PV generation plant with an installed capacity P_c of 466.4 kW. The simulation dataset is composed of the period from August 2019 to December 2019, 151 days in total. The ULiège PV generation is monitored on a minute basis and is resampled to 15 minutes.

The simulation parameters of the planners and the oracle controller are identical. The planning and controlling periods are $\Delta t = 15$ minutes. The peak hours are between 7 pm and 9 pm (UTC+0). The specifications of the tender AO-CRE-ZNI 2019 published on *July* 12, 2019 define the ramping power constraint on the engagements $\Delta X = 7.5\%P_c$ ($15\%P_c$) during off-peak (peak) hours. The lower bound on the engagement is $x_t^{\min} = -5\%P_c$ ($x_t^{\min} = 20\%P_c$) during off-peak (peak) hours. The lower bound on the production is $y_t^{\min} = -5\%P_c$ ($y_t^{\min} = 15\%P_c$) during off-peak (peak) hours. The upper bounds on the engagement and production are $x_t^{\max} = y_t^{\max} = P_c$. Finally, the engagement deadband is 5% of P_c .

The Python Pyomo² 5.6.7 library is used to implement the algorithms in Python 3.7. IBM ILOG CPLEX Optimization Studio³ 12.9 is used to solve all the mixed-integer quadratic optimization problems. Numerical experiments are performed on an Intel Core i7-8700 3.20 GHz based computer with 12 threads and 32 GB of RAM running on Ubuntu⁴ 18.04 LTS. The average computation time per optimization problem of the S planner with $\#\Omega = 20$ scenarios is 3 (s) for an optimization problem with 15 000 variables and 22 000 constraints.

²[www.http://www.pyomo.org/](http://www.pyomo.org/)

³<https://www.ibm.com/products/ilog-cplex-optimization-studio>

⁴<https://ubuntu.com>

13.3.4 Sizing parameters

The BESS and PV CAPEX are 300 €/kWh and 700 €/kW, the BESS and PV OPEX are 1% of the CAPEX, the project lifetime is 20 years, and the weighted average cost of capital is 5%. The BESS lifetime in terms of full charging and discharging cycles is 3 000. The BESS is assumed to be capable of fully charging or discharging in one hour $y_{\max}^{\text{cha}} = y_{\max}^{\text{dis}} = s^{\max}/1$, with charging and discharging efficiencies $\eta^{\text{cha}} = \eta^{\text{dis}} = 0.95$. Each simulation day is independent with a discharged battery at the first and last period to its minimum capacity $s^{\text{ini}} = s^{\text{end}} = 10\%s^{\max}$. The BESS minimum (s^{\min}) and maximum (s^{\max}) capacities are 10% and 90% of the total BESS storage capacity \bar{S} . The sizing space is a grid composed of 56 values with $\mathcal{R}_{\bar{S}} = \{0.5, 0.75, 1, 1.25, 1.5, 1.75, 2\}$ and $\mathcal{P} = \{50, 100, 150, 200, 250, 300, 350, 400\}$.

13.3.5 Sizing results

The D^* , D , and $S^{\Omega=20}$ planners are used with the oracle controller over the simulation dataset. E, W, C, and the number of full charging and discharging cycles are calculated by extrapolating the results from 151 days to one year. Figure 13.4 provides the grid search sizing results for the three planners. For a given selling price, the net is maximal when $r_{\bar{S}} = 0.5$. When $r_{\bar{S}}$ increases, the BESS is more and more used to withdraw and export during peak hours. It leads to an increase in the number of charging/discharging cycles that implies an increase of the number of BESS required during the project lifetime, and consequently an increase of the BESS CAPEX. As the LCOE is mainly driven by the BESS CAPEX, $\frac{R}{E}$ is not capable of compensating the LCOE increase resulting in a net decrease. The number of charging and discharging cycles is approximately the same for both the D and S planners, independently of the selling price, and rises from 4 700 with $r_{\bar{S}} = 0.5$ to 13 000 with $r_{\bar{S}} = 2$.

The differences between D^* , D , and S planners are small. D^* tends to overestimate the net by underestimating the LCOE (underestimating the deviation, BESS CAPEX, and withdrawal costs) and overestimating $\frac{R}{E}$. However, the minimal selling price to be profitable with $r_{\bar{S}} = 0.5$, is approximately 80 €/ MWh for all planners as shown by Figure 13.4. Then, the higher the selling price, the higher the net. In the CRE specifications, the best tender is mainly selected based on the selling price criterion. A trade-off should be reached between the net and the selling price to be selected.

This sizing study seems to indicate that it is not very sensitive to the control policy, *i.e.*, deterministic with perfect knowledge, deterministic with point forecasts, and stochastic with scenarios. However, it may be dangerous not considering the uncertainty

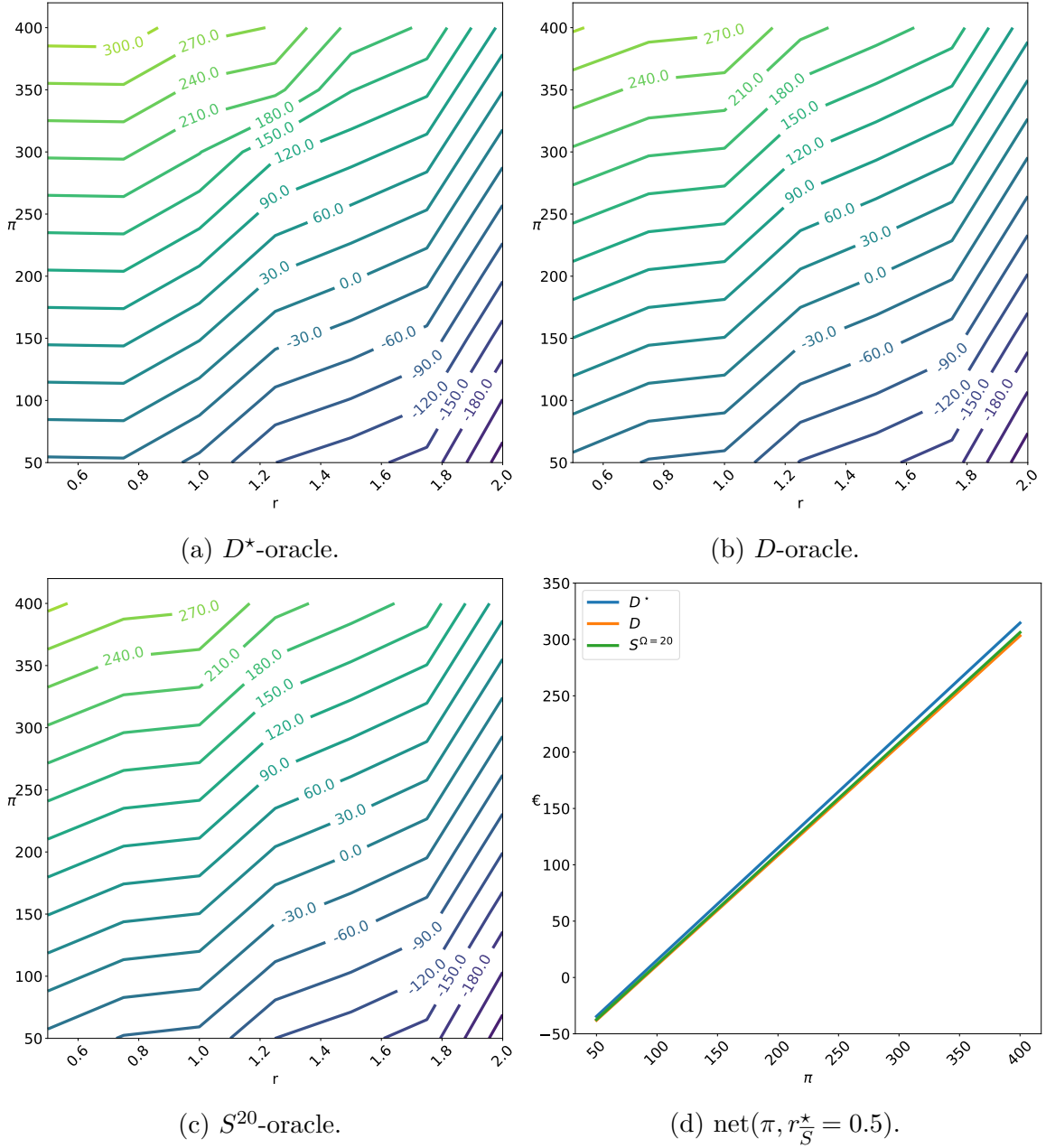


Fig. 13.4 Sizing results: $\text{net}(\pi, r_S^*)$ (€/ MWh).

at the sizing stage and could lead to an overestimation of the system performance and an underestimation of the sizing. Indeed, the net revenues of the two-phase engagement control are similar between planners explaining the small differences in terms of sizing. Two main limitations could explain this result. First, large deviations (15-20%) from the engagement plan at the control step occur rarely. Indeed, the oracle controller may compensate for inadequate planning and limits the deviations. A more realistic

controller with point forecasts should be considered. Second, when such deviations occur, most of the time they are within the tolerance deadband where there is no penalty. And when the deviations are outside, the penalty is rather small in comparison with the gross revenue. A sensitivity analysis of the numerical settings of the CRE specifications should be performed.

13.4 Conclusions and perspectives

The key idea of this Chapter is to propose a methodology to size the PV and BESS in the context of the capacity firming framework. Indeed, the two-phase engagement control cannot easily be modeled as a single sizing optimization problem. Such an approach would result in a non-linear bilevel optimization problem difficult to solve with an upper level, the sizing part, and a lower level, the two-phase engagement control. The two-phase engagement control is decomposed in two steps: computing the day-ahead engagements, then recomputing the set-points in real-time to minimize the deviations from the engagements. The CRE non-convex penalty function is modeled by a threshold-quadratic penalty that is compatible with a scenario approach. The stochastic formulation using a scenario approach is compared to the deterministic formulation. The PV scenarios are generated using a Gaussian copula methodology and PV point forecasts computed with the PVUSA model. The minimal selling price to be profitable, on this dataset, in the context of the capacity firming framework is approximately 80 €/ MWh with a BESS having a maximal capacity, fully charged or discharged in one hour, of half the total PV installed power. The sizing study indicates that it is not very sensitive to the control policy, deterministic with perfect knowledge, deterministic with point forecasts, and stochastic with scenarios. However, further investigations are required to implement a more realistic controller that uses intraday point forecasts, and to conduct a sensitivity analysis on the simulation parameters.

Several extensions are under investigation.

- A PV generation methodology that is less dependent on the PV point forecasts and takes into account the error dependency of the PV power should be implemented.
- PV scenarios clustering and reduction techniques could be considered to select relevant PV scenarios and improve the stochastic planner results.
- A sizing formulation as a single optimization problem with the PV and BESS capacities as variables to directly compute the optimum and avoid making a grid

search. Such a formulation is not trivial due to the specific two-phase engagement control of the capacity firming framework.

- Finally, the BESS aging process could be modeled in the sizing study and a dataset with at least a full year of data should be considered to fully take into account the PV seasonality.

Chapter 14

Capacity firming using a robust approach

Overview

This Chapter proposes a robust approach to address the energy management of a grid-connected renewable generation plant coupled with a battery energy storage device in the capacity firming market. It is an extension of Chapter 12 by considering another optimization formulation to handle the PV uncertainty. The main contributions are two-fold:

1. The core contribution is the application of the robust optimization framework to the capacity firming market in a tractable manner thanks to a Benders decomposition of the optimization problem and a warm start of the algorithm. In addition, a dynamic risk-averse parameters selection taking advantage of the quantile forecast distribution is proposed.
2. The secondary contribution is the use of the Normalizing Flows, which is a new advanced forecasting technique, to provide the uncertainty estimation in the form of PV quantiles for the robust planner. To the best of our knowledge, it is the first study to use NFs in a power system application.

References: This chapter is an adapted version of the following publication:

Jonathan Dumas, Colin Cointe, Antoine Wehenkel, Antonio Sutera, Xavier Fetsweis, and Bertrand Cornélusse. A probabilistic forecast-driven strategy for a risk-aware participation in the capacity firming market. Manuscript submitted for publication to IEEE Transactions on Sustainable Energy, 2021. URL <https://arxiv.org/abs/2105.13801>.

Terminology and notations have been slightly adjusted for the sake of consistency with the rest of this manuscript. The text has also been processed to minimize overlap with respect to the other chapters.

“You have to start with the truth. The truth is the only way that we can get anywhere. Because any decision-making that is based upon lies or ignorance can’t lead to a good conclusion.”

— Julian Assange

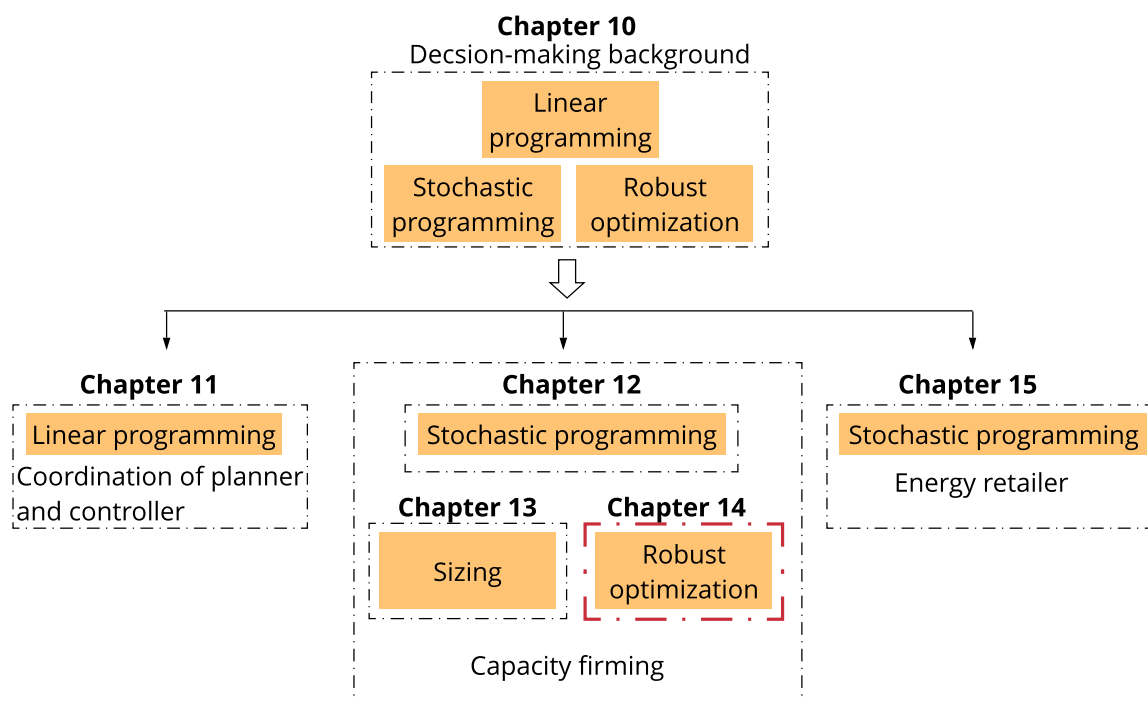


Fig. 14.1 Chapter 14 position in Part II.

There are several approaches to deal with renewable energy uncertainty. One way is to consider a two-stage stochastic programming approach [19]. It has already been applied to the capacity firming framework [46, 107, 69, 117]. The generation uncertainty is captured by a set of scenarios modeling possible realizations of the power output. However, this approach has three drawbacks. First, the problem size and computational requirement increase with the number of scenarios, and a large number of scenarios are often required to ensure the good quality of the solution. Second, the accuracy of the algorithm is sensitive to the scenario generation technique. Finally, it may be challenging to identify an accurate probability distribution of the uncertainty. Another option is to consider robust optimization (RO) [9, 14], applied to unit commitment by [15, 81], and in the capacity firming setting [107]. RO accounts for the worst generation trajectory to hedge the power output uncertainty, where the uncertainty model is deterministic and set-based. Indeed, the RO approach puts the random problem parameters in a predetermined uncertainty set containing the worst-case scenario. It has two main advantages [15]: (1) it only requires moderate information about the underlying uncertainty, such as the mean and the range of the uncertain data; (2) it constructs an optimal solution that immunizes against all realizations of the uncertain data within a deterministic uncertainty set. Therefore, RO is consistent with the risk-averse fashion way to operate power systems. However, the RO version of a tractable optimization problem may not itself be tractable, and some care must be taken in the choice of the uncertainty set to ensure that tractability is preserved.

Traditionally, a two-stage RO model is implemented for the unit commitment problem in the presence of uncertainty. However, it is challenging to compute and often NP-hard. Two classes of cutting plane strategies have been developed to overcome the computational burden. The Benders-dual cutting plane (BD) algorithms are the most used and seek to derive exact solutions in the line of Benders' decomposition [10] method. They decompose the overall problem into a master problem involving the first-stage commitment decisions at the outer level and a sub-problem associated with the second-stage dispatch actions at the inner level. Then, they gradually construct the value function of the first-stage decisions using dual solutions of the second-stage decision problems [15, 81]. In contrast, the column-and-constraint generation (CCG) procedure, introduced by [164, 157] does not create constraints using dual solutions of the second-stage decision problem. Instead, it dynamically generates constraints with recourse decision variables in the primal space for an identified scenario. In the CCG procedure, the generated variables and constraints are similar to those in the

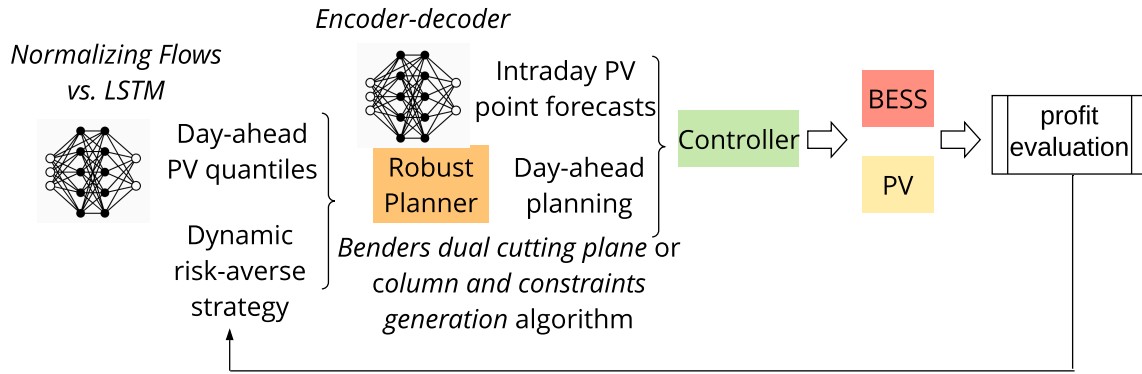


Fig. 14.2 Forecast-driven robust optimization strategy.

deterministic equivalent of a two-stage stochastic programming model. To the best of our knowledge, the BD and CCG algorithms have not been compared in the capacity firming framework.

This Chapter proposes a reliable and computationally tractable probabilistic forecast-driven robust optimization strategy, that can use either a BD or CCG algorithm, in the capacity firming framework, depicted in Figure 14.2. Our work goes several steps further than [107]. The main contributions of this Chapter are three-fold:

1. The core contribution is the application of the robust optimization framework to the capacity firming market in a tractable manner by using a Benders decomposition. The non-linear robust optimization problem is solved both using the Benders-dual cutting plane and the column-and-constraint generation algorithms. It is the first time, to the best of our knowledge, that a comparison of these algorithms is performed in the capacity firming framework. In addition, the convergence of the BD algorithm is improved with a warm-start procedure. It consists of building an initial set of cuts based on renewable generation trajectories assumed to be close to the worst case scenario. The results of both the CCG and BD two-stage RO planners are compared to the deterministic planner using perfect knowledge of the future, the nominal point forecasts, *i.e.*, the baseline to outperform, and the quantiles (a conservative approach). The case study is the photovoltaic (PV) generation monitored on-site at the University of Liège (ULiège), Belgium.
2. Second, a dynamic risk-averse parameters selection taking advantage of the quantile forecast distribution is investigated and compared to a strategy with fixed risk-averse parameters.

3. Finally, the *normalizing flows* (NFs), a new class of probabilistic generative models that has gained increasing interest from the deep learning community in recent years, is implemented. NFs are used to compute day-ahead quantiles of renewable generation for the robust planner. Then, an encoder-decoder architecture forecasting model [24] computes the intraday point forecasts for the controller. To the best of our knowledge, it is the first study to use NFs in a power system application.

In addition to these contributions, this study also provides open-access to the Python code¹ to help the community to reproduce the experiments. The rest of this Chapter is organized as follows. Section 14.1 provides the mathematical formulations of the robust and deterministic planners. Section 14.2 develops the Benders-dual cutting plane algorithm. The case study and computational results are presented in Section 14.3. Finally, Section 14.4 concludes this study and draws some perspectives of future works. Note, the capacity firming process is described in Section 12.2 of Chapter 12, and Section 6.5 in Chapter 6 introduces the forecasting techniques and proposes a quality evaluation.

14.1 Problem formulation

For the sake of simplicity in this Chapter, the penalty c defined in (12.2) is assumed to be symmetric, convex, and piecewise-linear

$$c(x_t, y_t^m) = \pi \Delta t \beta \left(\max \left(0, |x_t - y_t^m| - pP_c \right) \right), \quad (14.1)$$

with β a penalty factor. Note, in this Chapter, both the import and export are considered in contrast to Chapter 12. A two-stage robust optimization formulation is built to deal with the engagement for the uncertain renewable generation that is modeled with an uncertainty set. The deterministic and robust formulations of the planner are presented in Sections 14.1.1 and 14.1.2. The robust optimization problem with recourse has the general form of a min-max-min optimization problem. The uncertainty set is defined by quantiles forecasts and a budget of uncertainty Γ . Section 14.1.3 uses the dual of the inner problem to formulate a min-max optimization problem. Finally, Section 14.1.4 presents the formulation of the controller. The optimization variables and the parameters are defined in Section 12.1.

¹<https://github.com/jonathandumas/capacity-firming-ro>

14.1.1 Deterministic planner formulation

The deterministic formulation of the planner is provided in Section 12.3 of Chapter 12. The only difference lies in the definition of the penalty c that is assumed to be symmetric, convex, and piecewise-linear instead of a quadratic penalty in (12.5). Therefore, in this Chapter, the objective function J of the deterministic planner to minimize is

$$J(x_t, y_t) = \sum_{t \in \mathcal{T}} \pi_t \Delta t [-y_t + \beta(d_t^- + d_t^+)]. \quad (14.2)$$

The deterministic formulation is the following Mixed-Integer Linear Program (MILP)

$$\begin{aligned} \min_{x_t \in \mathcal{X}, y_t \in \Omega(x_t, \hat{y}_t^{\text{pv}})} \quad & J(x_t, y_t) \\ \mathcal{X} = \quad & \{x_t : (12.6)\} \\ \Omega(x_t, \hat{y}_t^{\text{pv}}) = \quad & \{y_t : (12.7) - (12.11)\} \end{aligned} \quad (14.3)$$

where \mathcal{X} and $\Omega(x_t, \hat{y}_t^{\text{pv}})$ are the sets of feasible engagements x_t and dispatch solutions y_t , respectively. The optimization variables of (14.3) are the engagement variables x_t , the dispatch variables y_t (the net power at the grid connection point), y_t^{dis} (BESS discharging power), y_t^{cha} (BESS charging power), s_t (BESS state of charge), y_t^b (BESS binary variables), y_t^{pv} (renewable generation), and d_t^-, d_t^+ (deviation variables) (cf. the notation Section 12.1).

14.1.2 Robust planner formulation

The uncertain renewable generation \hat{y}_t^{pv} of (12.11) is assumed to be within an interval $\mathcal{U} = [u_t^{\min}, u_t^{\max}]$ that can be obtained based on the historical data or an interval forecast composed of quantiles. In the following \hat{y}_t^{pv} is replaced by u_t in (12.11). The proposed two-stage robust formulation of the capacity firming problem consists of minimizing the objective function over the worst renewable generation trajectory

$$\max_{u_t \in \mathcal{U}} \left[\min_{x_t \in \mathcal{X}, y_t \in \Omega(x_t, u_t)} J(x_t, y_t) \right], \quad (14.4)$$

that is equivalent to

$$\min_{x_t \in \mathcal{X}} \left[\max_{u_t \in \mathcal{U}} \min_{y_t \in \Omega(x_t, u_t)} J(x_t, y_t) \right]. \quad (14.5)$$

The worst-case dispatch cost has a max-min form, where

$$\min_{y_t \in \Omega(x_t, u_t)} J(x_t, y_t)$$

determines the economic dispatch cost for a fixed engagement and a renewable generation trajectory, which is then maximized over the uncertainty set \mathcal{U} .

In the capacity firming framework, where curtailment is allowed, the uncertainty interval consists only in downward deviations $[u^{\min}, \hat{y}_t^{\text{pv},(0.5)}]$, with $\hat{y}_t^{\text{pv},(0.5)}$ the PV 50% quantile forecast.

Demonstration 1. *Let consider $\mathcal{U}_1 = [u_t^{\min}, \hat{y}_t^{\text{pv},(0.5)}]$, $\mathcal{U}_2 = [\hat{y}_t^{\text{pv},(0.5)}, u^{\max}]$, $u_t^1 \in \mathcal{U}_1$, $u_t^2 \in \mathcal{U}_2$, $y_t^1 \in \Omega_1 = \Omega(x_t, u_t^1 \in \mathcal{U}_1)$, and $y_t^2 \in \Omega_2 = \Omega(x_t, u_t^2 \in \mathcal{U}_2)$. Then, for a given engagement x_t*

$$\max_{u_t \in \mathcal{U}} \min_{y_t \in \Omega(x_t, u_t)} J(x_t, y_t) = \max \left[\max_{u_t^1 \in \mathcal{U}_1} \min_{y_t^1 \in \Omega_1} J(x_t, y_t^1), \max_{u_t^2 \in \mathcal{U}_2} \min_{y_t^2 \in \Omega_2} J(x_t, y_t^2) \right]. \quad (14.6)$$

The only difference between Ω_1 and Ω_2 is provided by (12.11) where $y_{t,1}^{\text{pv}} \leq u_t^1$ and $y_{t,2}^{\text{pv}} \leq u_t^2$. By definition of the uncertainty sets $u_t^1 \leq u_t^2 \forall t \in \mathcal{T}$, and it is straightforward that $y_{t,1}^{\text{pv}} \leq u_t^1$. In addition, the variables y_t^1 satisfy all the other constraints of $\Omega_2 \forall t \in \mathcal{T}$. Therefore, $y_t^1 \in \Omega_2 \forall t \in \mathcal{T}$, and $\Omega_1 \subseteq \Omega_2$. Thus, for a given engagement x_t , $\forall u_1 \in \mathcal{U}_1$, and $\forall u_2 \in \mathcal{U}_2$

$$\min_{y_t^2 \in \Omega_2} J(x_t, y_t^2) = J_2^* \leq \min_{y_t^1 \in \Omega_1} J(x_t, y_t^1) = J_1^*. \quad (14.7)$$

Finally, $\max[J_2^*, J_1^*] = J_1^*$. It means the worst case is in Ω_1 that corresponds to \mathcal{U}_1 .

In addition, the worst generation trajectories, in robust unit commitment problems, are achieved when the uncertain renewable generation u_t reaches the lower or upper bounds of the uncertainty set [164, Proposition 2]. Thus, the uncertainty set at t is composed of two values and $u_t \in \{u^{\min}, \hat{p}_t^{(0.5)}\}$.

Following [15, 81], to adjust the degree of conservatism, a budget of uncertainty Γ taking integer values between 0 and 95 is employed to restrict the number of time periods that allow u_t to be far away from its nominal value, *i.e.*, deviations are very large. Therefore, the uncertainty set of renewable generation \mathcal{U} is defined as follows

$$\mathcal{U} = \left\{ u_t \in \mathbb{R}^T : \sum_{t \in \mathcal{T}} z_t \leq \Gamma, z_t \in \{0; 1\}, u_t = \hat{y}_t^{\text{pv},(0.5)} - z_t u_t^{\min} \forall t \in \mathcal{T} \right\}, \quad (14.8)$$

where $u_t^{\min} = \hat{y}_t^{\text{pv},(0.5)} - \hat{y}_t^{\text{pv},(q)}$, with $0 \leq q \leq 0.5$. When $\Gamma = 0$, the uncertainty set $\mathcal{U} = \{\hat{y}_t^{\text{pv},(0.5)}\}$ is a singleton, corresponding to the nominal deterministic case. As Γ increases the size of \mathcal{U} enlarges. This means that a larger total deviation from the expected renewable generation is considered, so that the resulting robust solutions are more conservative and the system is protected against a higher degree of uncertainty. When $\Gamma = T$, \mathcal{U} spans the entire hypercube defined by the intervals for each u_t .

14.1.3 Second-stage planner transformation

The robust formulation (14.5) consists of solving a min-max-min problem, which cannot be solved directly by a commercial software such as CPLEX or GUROBI. A scenario-based approach, *e.g.*, enumerating all possible outcomes of u_t that could lead to the worst-case scenario for the problem, results in at least 2^Γ possible trajectories². Thus, to deal with the huge size of the problem a Benders type decomposition algorithm is implemented.

Constraints (12.7a)-(12.7b) make the dispatch problem a MILP, for which a dual formulation cannot be derived. In view of this, following [81], the constraints (12.7a)-(12.7b) are relaxed (the convergence of the relaxed dispatch problem is discussed in Section 14.2.2). Then, by applying standard tools of duality theory in linear programming, the constraints and the objective function of the dual of the dispatch problem are derived. The dual of the feasible set $\Omega(x_t, u_t)$, with (12.7a)-(12.7b) relaxed, provides the dual variables ϕ_t and the following objective

$$G(x_t, u_t, \phi_t) = \sum_{t \in \mathcal{T}} \left[\phi_t^{\text{cha}} y_{\max}^{\text{cha}} + \phi_t^{\text{dis}} y_{\max}^{\text{dis}} - \phi_t^{s^{\min}} s^{\min} + \phi_t^{s^{\max}} s^{\max} - \phi_t^{y^{\min}} y^{\min} + \phi_t^{y^{\max}} y^{\max} \right. \\ \left. + \phi^{s^{\text{ini}}} s^{\text{ini}} + \phi^{s^{\text{end}}} s^{\text{end}} - \phi_t^{d^-} (x_t - pP_c) + \phi_t^{d^+} (x_t + pP_c) + \phi_t^{y^{\text{pv}}} u_t \right]. \quad (14.9)$$

Then, the dual of the dispatch problem $\min_{y_t \in \Omega(x_t, u_t)} J(x_t, y_t)$ is

$$\max_{\phi_t \in \Phi} G(x_t, u_t, \phi_t) \quad (14.10)$$

$$\Phi = \left\{ (14.11a) - (14.11k) \right\},$$

²There are $n = \sum_{k=0}^{\Gamma} \binom{96}{k}$ possible trajectories where n is within the interval $[2^\Gamma, 2^{96}]$ as $(1+1)^\Gamma = \sum_{k=0}^{\Gamma} \binom{\Gamma}{k}$ and $(1+1)^{96} = \sum_{k=0}^{96} \binom{96}{k}$ by using the binomial formula.

with the set of constraints Φ defined by

$$\phi_t^y - \phi_t^{y^{\min}} + \phi_t^{y^{\max}} - \phi_t^{d^-} + \phi_t^{d^+} = -\pi_t \Delta t, \quad \forall t \in \mathcal{T} \quad [y_t] \quad (14.11a)$$

$$-\phi_t^{d^-} \leq \beta \pi_t \Delta t, \quad \forall t \in \mathcal{T} \quad [d_t^-] \quad (14.11b)$$

$$-\phi_t^{d^+} \leq \beta \pi_t \Delta t, \quad \forall t \in \mathcal{T} \quad [d_t^+] \quad (14.11c)$$

$$\phi_1^{\text{dis}} - \phi_1^y + \phi^{s^{\text{ini}}} \frac{\Delta t}{\eta^{\text{dis}}} \leq 0 \quad [y_1^{\text{dis}}] \quad (14.11d)$$

$$\phi_t^{\text{dis}} - \phi_t^y + \phi_t^s \frac{\Delta t}{\eta^{\text{dis}}} \leq 0, \quad \forall t \in \mathcal{T} \setminus \{1\} \quad [y_t^{\text{dis}}] \quad (14.11e)$$

$$\phi_1^{\text{cha}} + \phi_1^y - \phi^{s^{\text{ini}}} \eta^{\text{cha}} \Delta t \leq 0 \quad [y_1^{\text{cha}}] \quad (14.11f)$$

$$\phi_t^{\text{cha}} + \phi_t^y - \phi_t^s \eta^{\text{cha}} \Delta t \leq 0, \quad \forall t \in \mathcal{T} \setminus \{1\} \quad [y_t^{\text{cha}}] \quad (14.11g)$$

$$-\phi_1^{s^{\min}} + \phi_1^{s^{\max}} + \phi^{s^{\text{ini}}} - \phi_2^s \leq 0 \quad [s_1] \quad (14.11h)$$

$$-\phi_t^{s^{\min}} + \phi_t^{s^{\max}} + \phi_{t-1}^s - \phi_t^s \leq 0, \quad \forall t \in \mathcal{T} \setminus \{1, 2, T\} \quad [s_t] \quad (14.11i)$$

$$-\phi_T^{s^{\min}} + \phi_T^{s^{\max}} + \phi^{s^{\text{end}}} + \phi_T^s \leq 0 \quad [s_T] \quad (14.11j)$$

$$-\phi_t^y + \phi_t^{y^{\text{pv}}} \leq 0, \quad \forall t \in \mathcal{T} \quad [y_t^{\text{pv}}]. \quad (14.11k)$$

Definition 14.1.1 (Sub-Problem). As a result, the worst-case dispatch problem $\max_{u_t \in \mathcal{U}} \left[\min_{y_t \in \Omega(x_t, u_t)} J(x_t, y_t) \right]$ is equivalent to the following problem, which yields the sub-problem (SP) in the Benders-dual cutting plane and column-and-constraint generation algorithms

$$\mathbf{SP} : R(x_t) = \max_{u_t \in \mathcal{U}, \phi_t \in \Phi} G(x_t, u_t, \phi_t). \quad (14.12)$$

Overall, (14.5) becomes a min-max problem

$$\min_{x_t \in \mathcal{X}} \left[\max_{u_t \in \mathcal{U}, \phi_t \in \Phi} G(x_t, u_t, \phi_t) \right], \quad (14.13)$$

that can be solved using a Benders decomposition technique such as BD or CCG, between a master problem, that is linear, and a sub-problem, that is bilinear, since Indeed, G has the following bilinear terms $\phi_t^{y^{\text{pv}}} u_t = \phi_t^{y^{\text{pv}}} \hat{p}_t^{(0.5)} - \phi_t^{y^{\text{pv}}} z_t u_t^{\min}$. It is possible to linearize the products of the binary and continuous variables $z_t \phi_t^{y^{\text{pv}}}$ of G by using a standard integer algebra trick [134] with the following constraints $\forall t \in \mathcal{T}$

$$-M_t^- z_t \leq \alpha_t \leq M_t^+ z_t \quad (14.14a)$$

$$-M_t^-(1 - z_t) \leq \phi_t^{y^{\text{pv}}} - \alpha_t \leq M_t^+(1 - z_t), \quad (14.14b)$$

where M_t^\pm are the big-M's values of $\phi_t^{y^{pv}}$ and α_t is an auxiliary continuous variable. The definition of the uncertainty set (14.8) with binary variables, based on the Proposition 2 of [164], is essential to linearize G .

14.1.4 Controller formulation

The controller uses as parameters the engagements x_t , the system last measured values, and renewable generation intraday point forecasts. It computes at each time period t the set-points from t to the last period T of the day. The formulation is the following MILP

$$\min_{y_t \in \Omega(x_t, \hat{y}_t^{pv})} J(x_t, y_t). \quad (14.15)$$

14.2 Solution methodology

Following the methodology described by Bertsimas et al. [15], Jiang et al. [81], a two-level algorithm can be used to solve the min-max (14.5) problem with a Benders-dual cutting plane algorithm.

Definition 14.2.1 (Master Problem). The following master problem (MP) is solved iteratively by adding new constraints to cut off the infeasible or non-optimal solutions, and is defined at iteration j by

$$\text{MP : } \min_{x_t \in \mathcal{X}, \theta} \theta \quad (14.16a)$$

$$\theta \geq G(x_t, \alpha_{t,l}, \phi_{t,l}), \quad \forall l \leq j \quad \text{optimality cuts} \quad (14.16b)$$

$$G(x_t, \tilde{\alpha}_{t,k}, \tilde{\phi}_{t,k}) \leq 0, \quad \forall k \leq j, \quad \text{feasibility cuts} \quad (14.16c)$$

where constraints (14.16b) represent the optimality cuts, generated by retrieving the optimal values $\alpha_{t,l}, \phi_{t,l}$ of the SP (14.12), while constraints (14.16c) represent the feasibility cuts, generated by retrieving the extreme rays $\tilde{\alpha}_{t,k}, \tilde{\phi}_{t,k}$ of (14.12), and θ is the optimal value of the second-stage problem.

The MP can compute an optimal solution at iteration j ($x_{t,j}, \theta_j$). Note, that $R(x_{t,j})$ provides an upper bound and θ_{j+1} provides a lower bound to the optimal value of (14.5). Therefore, by iteratively introducing cutting planes (14.16b and (14.16c) from the SP and computing MP (14.16), lower and upper bounds will converge and an optimal solution of (14.5) can be obtained.

14.2.1 Convergence warm start

A four-dimension taxonomy of algorithmic enhancements and acceleration strategies is proposed by [127]: solution generation, solution procedure, decomposition strategy, cut generation. The solution generation is the method used to set trial values for the SP. The quality of these solutions has an impact on the number of iterations, as they are used by the SP to generate cuts and bounds. The common strategy is to solve the MP without modification. However, heuristics can be used as a warm-start strategy to generate an initial set of tight cuts to strengthen the MP. A simple heuristic is proposed by [98] to generate feasible solutions and a set of good initial cuts. Computational evidence demonstrated the efficiency of this approach in terms of solution quality and time. Therefore, we designed the following warm-start method to improve the Benders convergence by building an initial set of cuts $\{\theta_i\}_{1 \leq i \leq I}$ for the master problem (14.16). It consists of sampling renewable generation trajectories that are assumed to be close to the worst trajectory of \mathcal{U} . Let t_1 and t_f be the time periods corresponding to the first and last non null PV 50% quantile forecast values. If $m = t_f - (t_1 + \Gamma - 1) > 0$, m trajectories are sampled. The m^{th} sampled trajectory is built by setting the Γ values of the PV 50% quantile forecast to the u_t^{\min} lower bound for time periods $t_1 + (m - 1) \leq t \leq t_1 + \Gamma - 1 + (m - 1)$. An additional trajectory is built by setting the Γ maximum values of the PV 50% quantile forecast to u_t^{\min} lower bound. Then, for each sampled trajectory $u_{t,i}$, the MILP formulation (14.3) is used to compute the related engagement plan $x_{t,i}$. Finally, the cut θ_i is built by solving (14.12) where the uncertainty set is a singleton $\mathcal{U} = \{u_{t,i}\}$, and the engagement plan is $x_{t,i}$ to retrieve the optimal values with (14.16b)

$$\theta_i = G(x_{t,i}, \alpha_{t,i}, \phi_{t,i}), \quad i = 1 \dots I.$$

14.2.2 Algorithm convergence

First³, we make the *relatively complete recourse* assumption that the SP is feasible for any engagement plan x_t and generation trajectory u_t . This assumption is true in the capacity firming framework where curtailment is allowed. If the system faces underproduction where x_t is large, the generation is 0, and the BESS discharged, penalties are applied. If it encounters overproduction where x_t is close to 0, the generation is large, and the BESS is charged, the excess of generation is curtailed. In

³The comments of this subsection apply to the BD and CCG algorithms.

both cases, there is always a feasible dispatch. Notice, when the relatively complete recourse assumption does not hold, [12] propose an extension of the CCG algorithm.

Second, the convergence of the relaxed SP is checked at each iteration of the algorithm by ensuring there is no simultaneous charge and discharge. However, such a situation should not occur, because in case of overproduction, the excess of generation can be curtailed. It is true that simultaneous charging and discharging could be an equivalent solution to dissipate the excess energy. That solution can be avoided in practice by adding a tiny penalty for using the storage system, but we never observed simultaneous charge and discharge over the hundreds of simulations carried out. Thus, it is not required to implement an extension of the BD or CCG algorithm that handles a linear two-stage robust optimization model with a mixed-integer recourse problem such as proposed by [163].

Finally, the overall convergence of the algorithm toward the optimal solution is checked. Indeed, depending on the big-M's values, the algorithm may converge in terms of the gap between the MP and SP but it does not ensure the optimal solution is reached. Therefore, once the convergence between the MP and SP is reached at iteration $j = J$, the objective of the MP at J is compared to the objective of the MILP formulation (14.3) using the generation worst-case trajectory $u_t^{\star,J}$ as parameters. If the absolute gap $|MILP^J - MP^J|$ is higher than a convergence threshold ϵ , the convergence is not reached. Then, larger big-M's values are set, and the algorithm is restarted until convergence or a stopping criterion is reached.

14.2.3 Benders-dual cutting plane algorithm

The Benders-dual cutting plane algorithm consists of solving (14.13) without constraints [(12.7a)-(12.7b)] following the procedure previously described, and to obtain a day-ahead robust schedule $x_{t,J}$ at the last iteration J .

Definition 14.2.2 (Benders-dual cutting plane algorithm). The initialization step consists of setting the initial big-M's values $M_t^- = 1$ and $M_t^+ = 0 \forall t \in \mathcal{T}$, the time limit resolution of the sub-problem (14.12) to 10 s, and the threshold convergence ϵ to 0.5 €. Let MP^j , SP^j , be the MP and SP objective values at iteration j , the lower and upper bounds, respectively, and $MILP^J$ the MILP objective value using the worst renewable generation trajectory $u_t^{\star,J}$ at iteration J .

Initialization.

Warm-start: build the initial set of cuts $\{\theta_i\}_{1 \leq i \leq I}$.

```

while  $|MILP^J - MP_2^J| > \epsilon$  and  $M_t^- < 500$  do
  Initialize  $j = 0$ , solve the MP (14.16) and retrieve  $x_{t,0}$ .
  while the 10 last  $|MP^j - SP^j|$  are not  $< \epsilon$  do
    Solve the SP (14.12) with  $x_{t,j}$  as parameters:
    if the SP is unbounded then
      Retrieve the extreme rays  $\tilde{\alpha}_{t,k}, \tilde{\phi}_{t,k}, 0 \leq k \leq j$ .
      Add the  $k$ -th feasibility cut:  $G(x_{t,j}, \tilde{\alpha}_{t,k}, \tilde{\phi}_{t,k}) \leq 0$ .
    else
      Retrieve the optimal values  $\alpha_{t,l}, \phi_{t,l}, 0 \leq l \leq j$ .
      Add the  $l$ -th optimality cut:  $\theta \geq G(x_{t,j}, \alpha_{t,l}, \phi_{t,l})$ .
      Update the upper bound  $SP^j = R(x_{t,j})$ .
      SP check: no simultaneous charge and discharge.
    end if
    Solve the MP (14.16): get the optimal values  $\theta_j, x_{t,j}$ .
    Update the lower bound  $MP^j = \theta_j$  and  $j = j + 1$ .
  end while
   $j = J$ : convergence between the SP and MP is reached. Check convergence with
  MILP: get  $u_t^{*,J}$  from  $SP^J$  and compute  $MILP^J$  (14.3).
  if  $|MILP^J - MP^J| > \epsilon$  then
    if  $M_t^- \leq 50$  then
      Update big-M's values  $M_t^- = 10 + M_t^- \forall t \in \mathcal{T}$ .
    else
      Update big-M's values  $M_t^- = 100 + M_t^- \forall t \in \mathcal{T}$ .
    end if
    Reset  $j$  to 0 and restart algorithm with a new  $MP$ .
  end if
end while
Retrieve the final  $x_{t,J}$  engagement.

```


14.2.4 Column and constraints generation algorithm

We implemented the the column and constraints generation procedure proposed by [164, 157]. The following master problem (MP_2) is solved at iteration j

$$\min_{x_t \in \mathcal{X}, \theta, \{y_t^s\}_{0 \leq s \leq j}} \theta \quad (14.17a)$$

$$\theta \geq J(x_t, y_t^s), \quad s = 0 \dots j \quad (14.17b)$$

$$y_t^s \in \Omega(x_t, u_t^{*,s}), \quad s = 0 \dots j, \quad (14.17c)$$

where constraints (14.17b) and (14.17c) serve as optimality and feasibility, respectively. $\{y_t^s\}_{0 \leq s \leq j}$ are the new variables added to the MP_2 , and $u_t^{*,s}$ represent the worst PV trajectory computed by the SP at iteration $0 \leq s \leq j$. Note: in our CCG implementation we solve the SP with the same approach as the SP of the BD algorithm.

Definition 14.2.3 (Column and constraints generation algorithm). The initialization step is identical to BD, and the CCG algorithm implemented is similar to BD. Note: there is a maximum of 50 iterations between the SP and the MP_2 before checking the convergence with the MILP. If the criterion is not reached the big-M's values are increased. Indeed, at each iteration j the y_t^j variables are added to the MP_2 . In our case, it represents approximately 1 000 new variables at each iteration. With 50 iterations, the MP_2 is a MILP with approximately 50 000 variables which begins to be hard to solve within a reasonable amount of time.

Initialization.

while $|MILP^J - MP_2^J| > \epsilon$ and $M_t^- < 500$ **do**

Initialize $j = 0$, solve the MP_2 (14.17) and retrieve $x_{t,0}$.

while the two last $|MP_2^j - SP^j|$ are not $< \epsilon$ and $j < 50$ **do**

Solve the SP (14.12) with $x_{t,j}$ as parameters:

Create variables y_t^j in MP_2 .

Retrieve $u_t^{*,j}$ from the SP.

Add the feasibility cut to the MP_2 : $y_t^j \in \Omega(x_t, u_t^{*,j})$.

if the SP is bounded **then**

Add the optimality cut: $\theta \geq J(x_t, y_t^j)$.

Update the upper bound: $SP^j = R(x_{t,j})$.

SP check: no simultaneous charge and discharge.

end if

Solve the MP_2 (14.17): get the optimal values $\theta_j, x_{t,j}$.

Update the lower bound: $MP_2^j = \theta_j$ and $j = j + 1$.

```

end while
 $j = J$ : convergence between the SP and MP is reached. Check convergence with
MILP: get  $u_t^{*,J}$  from  $SP^J$  and compute  $MILP^J$  (14.3).
if  $|MILP^J - MP_2^J| > \epsilon$  then
    if  $M_t^- \leq 50$  then
        Update big-M's values  $M_t^- = 10 + M_t^- \forall t \in \mathcal{T}$ .
    else
        Update big-M's values  $M_t^- = 100 + M_t^- \forall t \in \mathcal{T}$ .
    end if
    Reset  $j$  to 0 and restart algorithm with a new  $MP_2$ .
end if
end while
Retrieve the final  $x_{t,J}$  engagement.

```

14.3 Case Study

The BD and CCG algorithms are compared on the ULiège case study. The ULiège case study is composed of a PV generation plant with an installed capacity $P_c = 466.4$ kWp. The PV generation is monitored on a minute basis and the data are resampled to 15 minutes. The dataset is composed of 350 days from August 2019 to November 2020, missing data during March 2020. The NFs approach is compared to a widely used neural architecture, referred to as Long Short-Term Memory (LSTM). In total eight versions of the planner are considered. Four RO versions: BD-LSTM, BD-NF, CCG-LSTM, and CCG-LSTM. Four deterministic versions: the oracle that uses perfect knowledge of the future, a benchmark that uses PV nominal point forecasts, and two versions using NFs and LSTM PV quantiles. The set of PV quantiles is $\mathcal{Q} = \{q = 10\%, \dots, 50\%\}$. The controller uses PV intraday point forecasts and the day-ahead engagements computed by the planners to compute the set-points and the profits. They are normalized by the profit obtained with the oracle planner and expressed in %.

Section 14.3.1 presents the numerical settings. Section 14.3.2 provides the results of the sensitivity analysis for several risk-averse pairs $[u_t^{min} = \hat{y}_t^{pv,(q)}, \Gamma]$, with $q = 10, \dots, 40\%$, and $\Gamma = 12, 24, 36, 48$. Section 14.3.3 investigates a dynamic risk-averse parameter selection. Section 14.3.4 presents the improvement in terms of computation time provided by the initial set of cuts. Finally, Section 14.3.5 compares the BD and CCG algorithms.

14.3.1 Numerical settings

30 random days are randomly selected from the dataset to compose the testing set. The simulation parameters of the planners and the controller are identical. The planning and controlling time periods duration are $\Delta t = 15$ minutes. The peak hours are set between 7 pm and 9 pm (UTC+0). The ramping power constraint on the engagements are $\Delta X_t = 7.5\%P_c$ ($15\%P_c$) during off-peak (peak) hours. The lower bounds on the engagement x^{\min} and the net power y^{\min} are set to 0 kW. The upper bound on the engagement x^{\max} and the net power y^{\max} are set to P_c . Finally, the engagement tolerance is $pP_c = 1\%P_c$, and the penalty factor $\beta = 5$. The BESS minimum s^{\min} and maximum s^{\max} capacity are 0 kWh and 466.4 kWh, respectively. It is assumed to be capable of fully charging or discharging in one hour $y_{\max}^{\text{dis}} = y_{\max}^{\text{cha}} = s^{\max}/1$ with charging and discharging efficiencies $\eta^{\text{cha}} = \eta^{\text{dis}} = 95\%$. Each simulation day is independent with a fully discharged battery at the first and last period $s^{\text{ini}} = s^{\text{end}} = 0$ kWh. The Python Gurobi library is used to implement the algorithms in Python 3.7, and Gurobi⁴ 9.0.2 to solve all the optimization problems. Numerical experiments are performed on an Intel Core i7-8700 3.20 GHz based computer with 12 threads and 32 GB of RAM running on Ubuntu 18.04 LTS.

Figures 14.3a and 14.3b illustrate the LSTM and NFs PV quantile forecasts, observation, and nominal point forecasts on *September 14, 2019*. Figures 14.3c and 14.3d provide the engagement plan (x) and the BESS state of charge (s) computed with the RO planner, the deterministic planner with the nominal point forecasts, and the perfect knowledge of the future.

⁴<https://www.gurobi.com/>

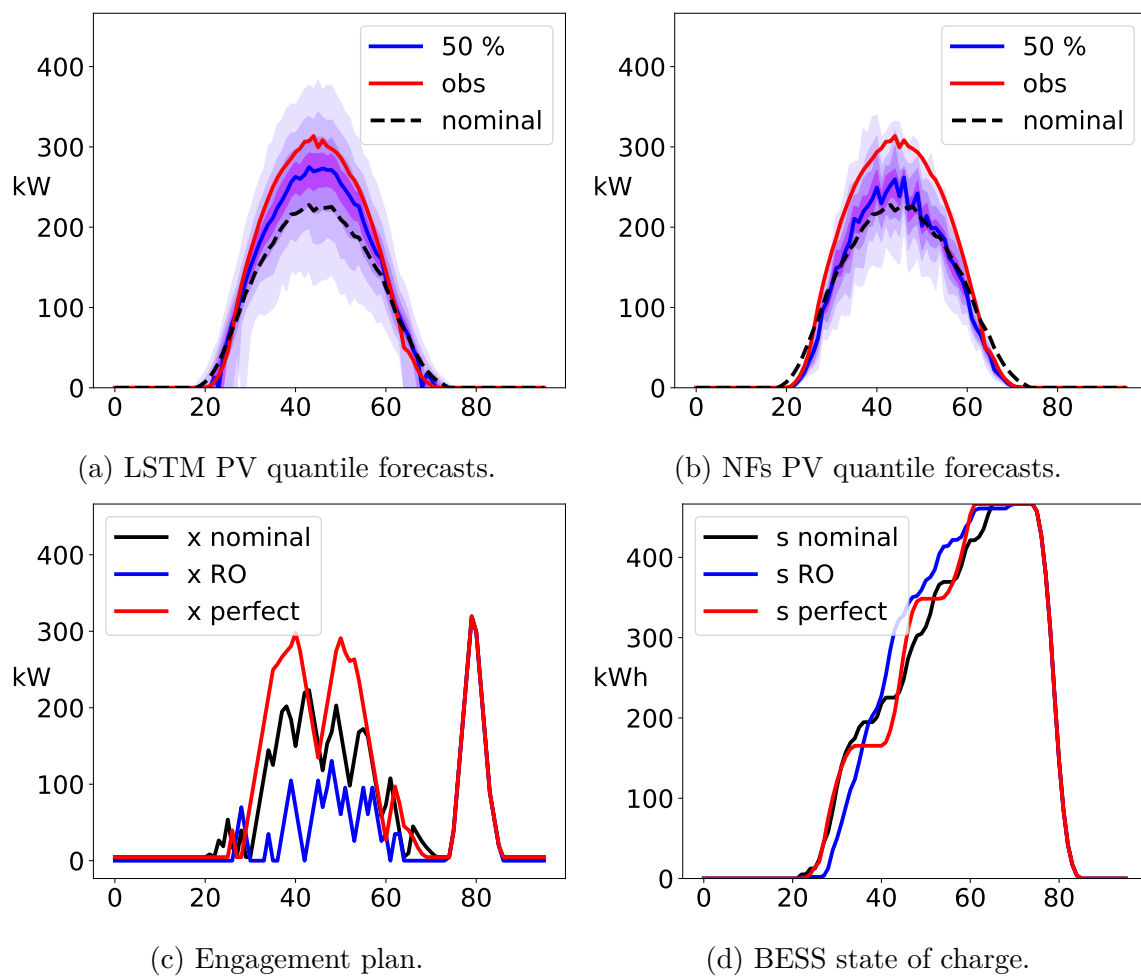


Fig. 14.3 Results illustration on *September 14, 2019*.

14.3.2 Constant risk-averse parameters strategy

The risk-averse parameters of the RO approach $[\hat{y}_t^{\text{pv},(q)}, \Gamma]$ are constant over the dataset. One way to identify the optimal pair is to perform a sensitivity analysis [149]. Figure 14.4 provides the normalized profits of the BD-RO, CCG-RO and deterministic planners using PV quantiles, left with LSTM and right with NFs, and nominal point forecasts. Both using the LSTM and NFs quantiles, the RO and deterministic planners outperform by a large margin the deterministic planner with nominal point forecasts that cannot deal with PV uncertainty and achieved only 53.3 %. Then, the planners using NFs quantiles significantly outperform the planners with LSTM quantiles. Overall, the CCG algorithm achieved better results for almost all pairs of risk-averse parameters. The highest profits achieved by the CCG-NF, BD-NF and NF-deterministic planners are 73.8 %, 72.6 % and 74.1 %, respectively, with the risk-averse parameters $[q = 20\%, \Gamma = 24]$, $[q = 20\%, \Gamma = 48]$, and the quantile 30 %. It should be possible to improve the RO results by tuning the risk-averse parameters $[\hat{y}_t^{\text{pv},(q)}, \Gamma]$. However, these results emphasize the interest to consider a deterministic planner with the relevant PV quantile as point forecasts, that is easy to implement, fast to compute (a few seconds), and less prone to convergence issues than the RO approach.

14.3.3 Dynamic risk-averse parameters strategy

In this section, the risk-averse parameters $[u_t^{\text{min}}, \Gamma]$ of the RO approach are dynamically set based on the day-ahead quantile forecasts distribution, and u_t^{min} is not necessarily equal to the same quantile $\hat{y}_t^{\text{pv},(q)} \forall t \in \mathcal{T}$. The motivation of this strategy is to assume that the sharper the quantile forecast distribution around the median is, the more risk-averse the RO approach should be.

Two parameters are designed to this end: (1) the PV uncertainty set max depth d_q to control u_t^{min} ; (2) the budget depth d_Γ to control Γ . d_q is a percentage of the distance between the median and the 10% quantile d_{50-10} , and d_Γ is a percentage of the total installed capacity P_c . Then, two rules are designed to dynamically set the risk-averse parameters $[u_t^{\text{min}}, \Gamma]$ for each day of the dataset. For a given day, and the set of time periods where the PV median is non null, the distances between the PV median and the PV quantiles 20, 30, and 40% are computed: d_{50-20} , d_{50-30} , d_{50-40} .

$\{\theta_i\}_{1 \leq i \leq I}$	t^{av}	$t^{50\%}$	t^{min}	t^{max}	t^{tot}
False	3.5	2.0	< 0.1	34.1	105.4
True	2.0	0.7	< 0.1	30.4	61.3

Table 14.1 Computation times (min) statistics.

u_t^{min} is dynamically set at each time period t as follows

$$u_t^{min} = \begin{cases} \hat{y}_t^{pv,(0.1)} & \text{if } d_t^{50-20/30/40} > d_q d_t^{50-10} \\ \hat{y}_t^{pv,(0.2)} & \text{if } d_t^{50-20/30} > d_q d_t^{50-10} \\ \hat{y}_t^{pv,(0.3)} & \text{if } d_t^{50-20} > d_q d_t^{50-10} \\ \hat{y}_t^{pv,(0.4)} & \text{otherwise} \end{cases}. \quad (14.18)$$

For a given day, the budget of uncertainty Γ is dynamically set based on the following rule

$$\Gamma = \#\{t : d_t^{50-10} > d_\Gamma P_c\}. \quad (14.19)$$

Figure 14.5 provides the normalized profits of the CCG-RO, BD-RO, and deterministic planners for several pairs $[d_\Gamma, d_q]$ using both the LSTM and NF quantiles. The planners achieved better results when using the NF quantiles. Overall, for both the LSTM and NF quantiles, the results are improved in comparison with fixed risk-averse parameters for all the planners. The highest profits achieved by the CCG-NF, BD-NF and NF-deterministic planners are 75.0 %, 72.6 % and 75.0 %, respectively, with $[d_\Gamma, d_q] = [10, 30]$, $[d_\Gamma, d_q] = [10, 5]$, and $d_q = 50\%$.

14.3.4 BD convergence warm start improvement

The initial set of cuts impact on the convergence is assessed by considering the dynamic risk-averse parameters strategy with $[d_\Gamma, d_q] = [10, 10]$. Figure 14.6 illustrates the reduction of the total number of iteration J required to converge below the threshold ϵ , on a specific day of the dataset, that is divided by 3.6 from 159 to 44. The computation time is divided by 4.1 from 7.4 min to 1.8 min. Table 14.1 provides the computation times (min) statistics over the entire dataset with and without warm start. The averaged t^{av} and total t^{tot} computation times are reduced significantly when using the initial set of cuts.

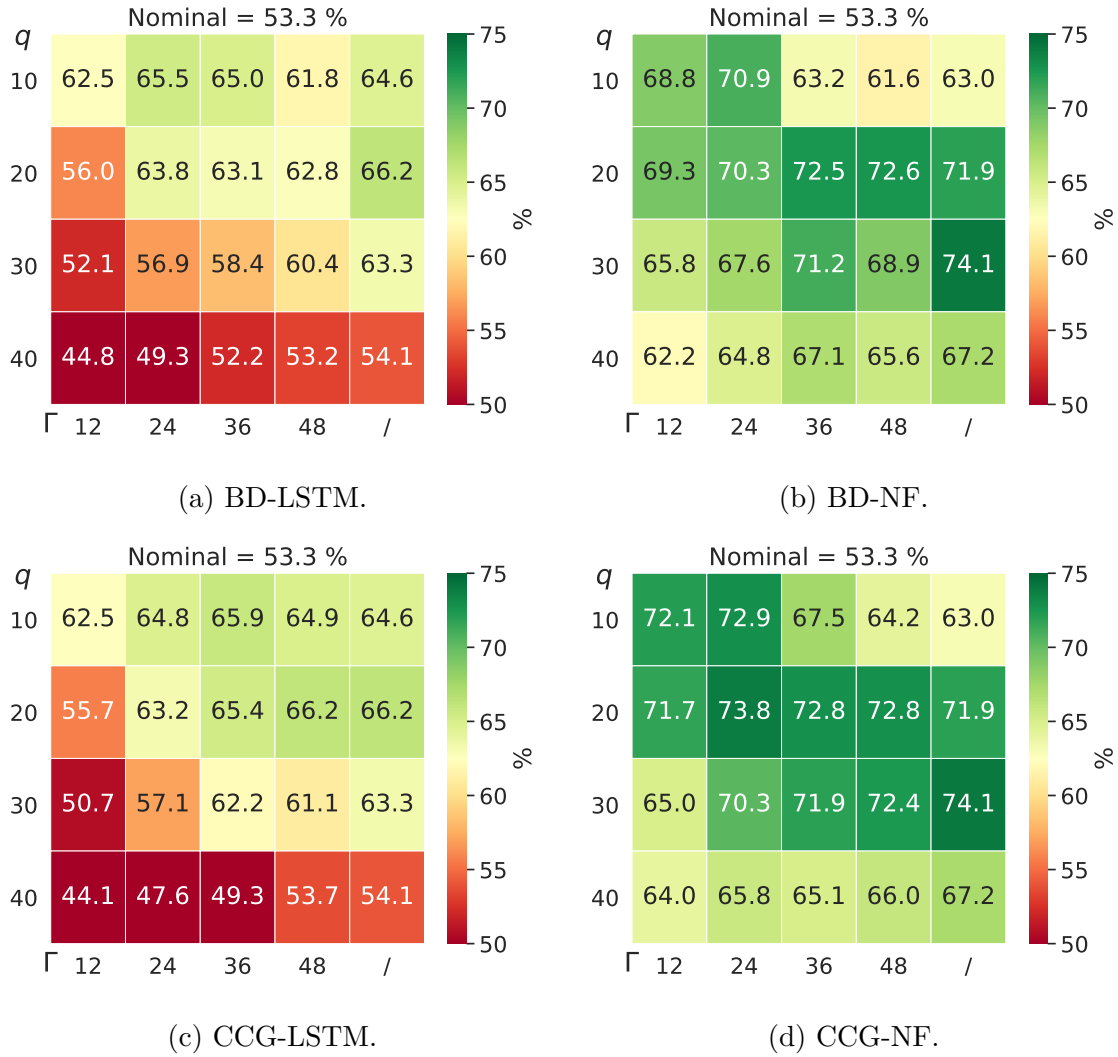


Fig. 14.4 Results with constant risk-averse parameters. Normalized profit (%) of the BD and CCG RO planners ($[\Gamma, q]$), deterministic ($[/, q]$) planner, and the reference that is the deterministic planner with point-forecasts (Nominal). Left part: LSTM quantiles, right part: NF quantiles.

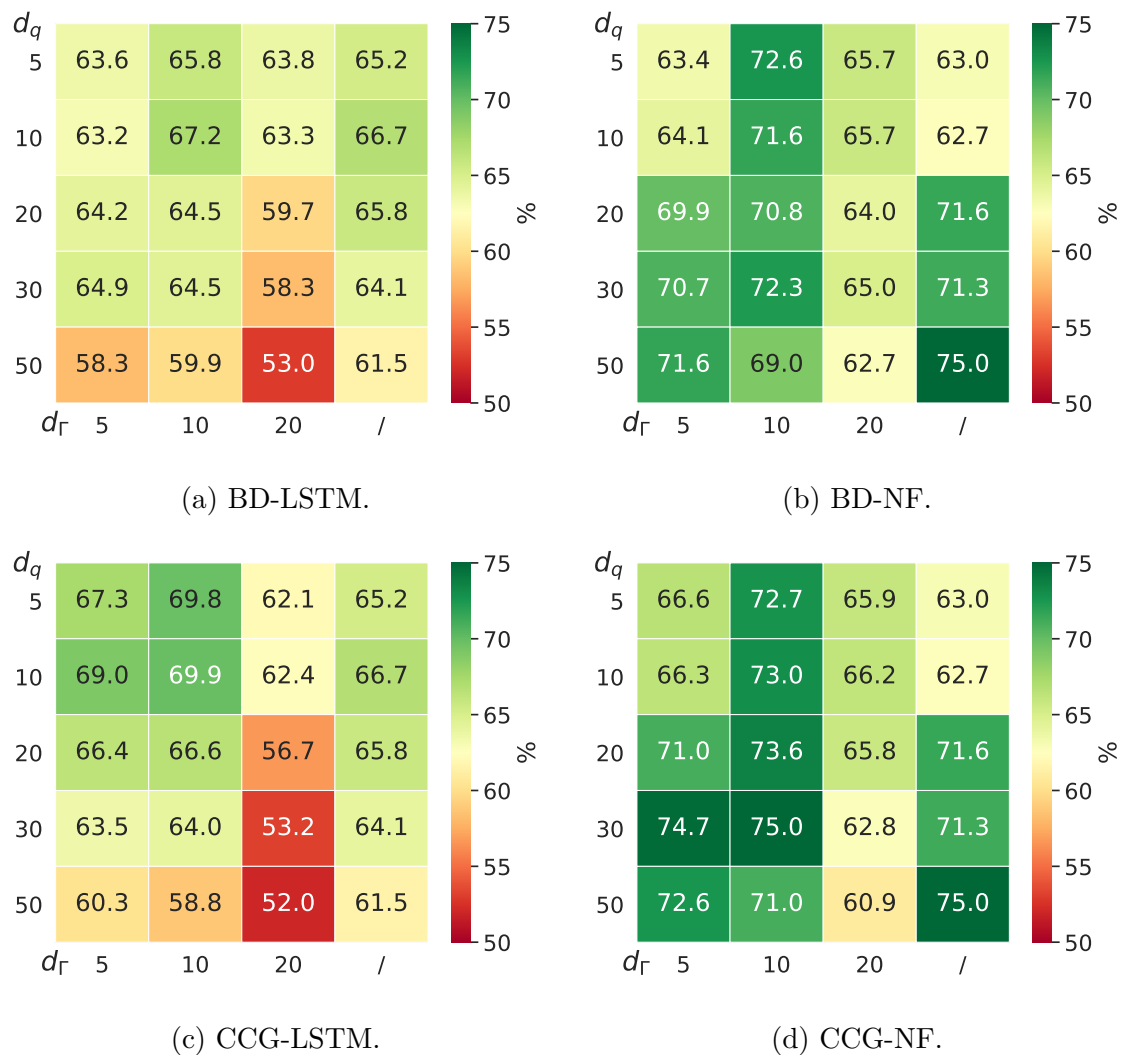


Fig. 14.5 Results with dynamic risk-averse parameters. Normalized profit (%) of the BD and CCG RO planners ($[d_r, d_q]$), and deterministic ($[/, d_q]$) planner. Left part: LSTM quantiles, right part: NF quantiles.

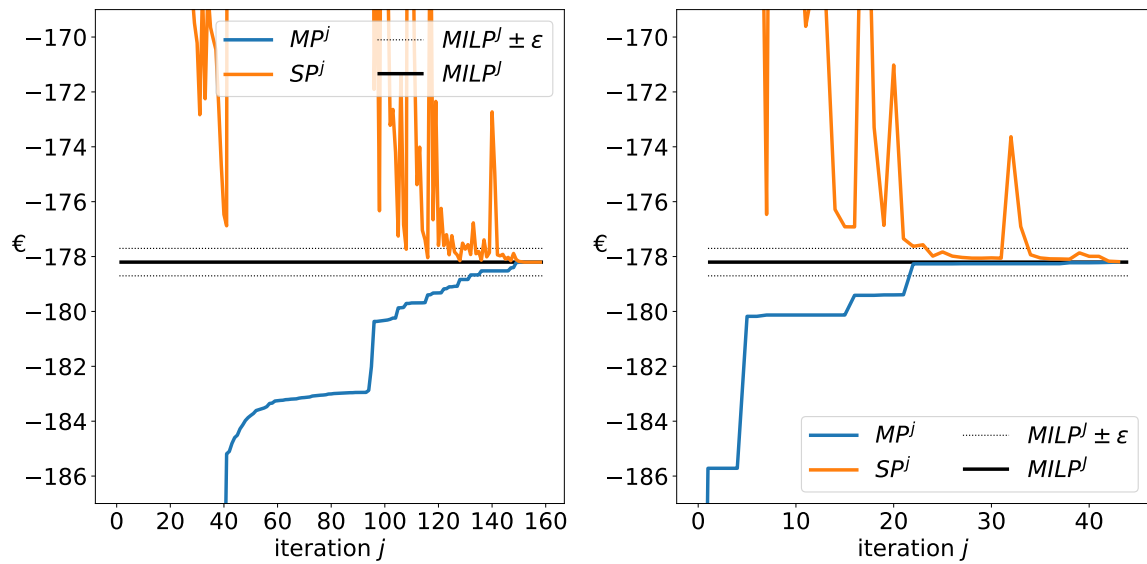


Fig. 14.6 Benders convergence without (left) and with (right) an initial set of cuts on September 14, 2019.

Algorithm	RO-type	\bar{t}	1%	J^{max}
BD-NF	static	85.2 (151.9)	0.0	72.6
CCG-NF	static	7.5 (6.0)	1.9	73.8
BD-NF	dynamic	102.3 (107.3)	0.0	72.6
CCG-NF	dynamic	9.2 (5.5)	4.2	75.0

Table 14.2 BD vs CCG statistics.

\bar{t} (s) is the averaged computation time per day with the standard deviation in bracket. 1% (%) is the % of instances that did not terminate with optimality. \bar{t} and 1% are computed over all days of the testing set and for all pair of constant (dynamic) risk-averse parameters $[u_t^{min}, \Gamma]$ ($[d_\Gamma, d_q]$). J^{max} (%) is the best normalized profit achieved using the NF quantiles over all risk-averse parameters.

14.3.5 BD and CCG comparison

Table 14.2 provides a comparison of the BD and CCG algorithms when using NF quantiles for both the static and dynamic robust optimization strategies. Overall, the CCG algorithm converges in 5-10 iterations instead of 50-100 for BD. Therefore, the CCG computes the day-ahead planning in approximately 10 seconds, ten times faster than BD. This observation is consistent with [157] that demonstrated the CCG algorithm converges faster than BD. Let n be the number of extreme points of the uncertainty set \mathcal{P} and m of the space Φ defined by constraint (14.11). The BD algorithm computes an optimal solution in $O(nm)$ iterations, and the CCG procedure in $O(n)$ iterations [157]. Note: the BD algorithm is still competitive in an operational framework as it takes on average 1-2 minutes to compute the day-ahead planning. However, we observed the CCG does not always converge to an optimal solution (see Section 14.2.2), which never happened with the BD algorithm. Fortunately, these cases amount to only a few % of the total instances. Overall, the CCG algorithm achieved better results than the BD for almost all the risk-averse parameters. Finally, in our opinion, both algorithms require the same amount of knowledge to be implemented. Indeed, the only difference is the MP as the SP are solved identically.

14.4 Conclusion

The core contribution of this study is to address the two-phase engagement/control problem in the context of capacity firming. A secondary contribution is to use a recent deep learning technique, Normalizing Flows, to compute PV quantiles. It is compared to a common neural architecture, referred to as Long Short-Term Memory. We developed an integrated forecast-driven strategy modeled as a min-max-min robust optimization problem with recourse that is solved using a Benders decomposition procedure. A comparison of the two main cutting plane algorithms used to address the two-stage RO unit commitment problems is conducted: the Benders-dual cutting plane and the column-and-constraint generation algorithms. The convergence is checked by ensuring a gap below a threshold between the final objective and the corresponding deterministic objective value. A risk-averse parameter assessment is conducted to select the optimal robust parameters and the optimal conservative quantile for the deterministic planner. Both the NF-based and LSTM-based planners outperformed the deterministic planner with nominal point PV forecasts. The NF model outperforms the LSTM in terms of forecast value as the planner using the NF quantiles achieved higher profit than the planner with LSTM quantiles. Finally, a dynamic risk-averse parameter selection strategy is built by taking advantage of the PV quantile forecast distribution and provides further improvements. In this case study, the CCG procedure converges ten times faster than the BD algorithm and achieves better results. However, it does not always converge to an optimal solution.

Overall, the RO approach for both the BD and CCG algorithms allows finding a trade-off between conservative and risk-seeking policies by selecting the optimal robust optimization parameters, leading to improved economic benefits in comparison with the baseline. Therefore, offering a probabilistic guarantee for the robust solution. However, the deterministic planner with the relevant PV quantile achieved interesting results. It emphasizes the interest to consider a well-calibrated deterministic approach, easy to implement, computationally tractable for large scale problem, and less prone to convergence issues, that is not considered in [107]. Note: this approach can be used in any other case study. It only requires a few months of data, renewable generation and weather forecasts, to train the forecasting models to compute reliable forecasts for the planner.

Several extensions are under investigation: (1) a stochastic formulation of the planner with improved PV scenarios based on Gaussian copula methodology or generated by a state-of-the-art deep learning technique such as Normalizing Flows, Generative Adversarial Networks or Variational AutoEncoders; (2) an improved dynamic risk-averse

parameter selection strategy based on a machine learning tool capable of better-taking advantage of the PV quantiles distribution.

Chapter 15

Energy retailer

Overview

This Chapter investigates the forecast value assessment of the deep generative models studied in Chapter 8. The reader is referred to 8 for the context, main contributions, the NFs, GANs, and VAEs background, and the description of the Global Energy Forecasting Competition 2014 (GEFcom 2014) case study.

References: This chapter is an adapted version of the following publication:

Jonathan Dumas, Antoine Wehenkel, Damien Lanaspeze, Bertrand Cornélusse, and Antonio Sutera. Deep generative modeling for probabilistic forecasting in power systems. Manuscript submitted for publication to Applied Energy, 2021. URL <https://arxiv.org/abs/2106.09370>.

Terminology and notations have been slightly adjusted for the sake of consistency with the rest of this manuscript. The text has also been processed to minimize overlap with respect to the other chapters.

“Be willing to make decisions. That’s the most important quality in a good leader.”

— **George S. Patton**

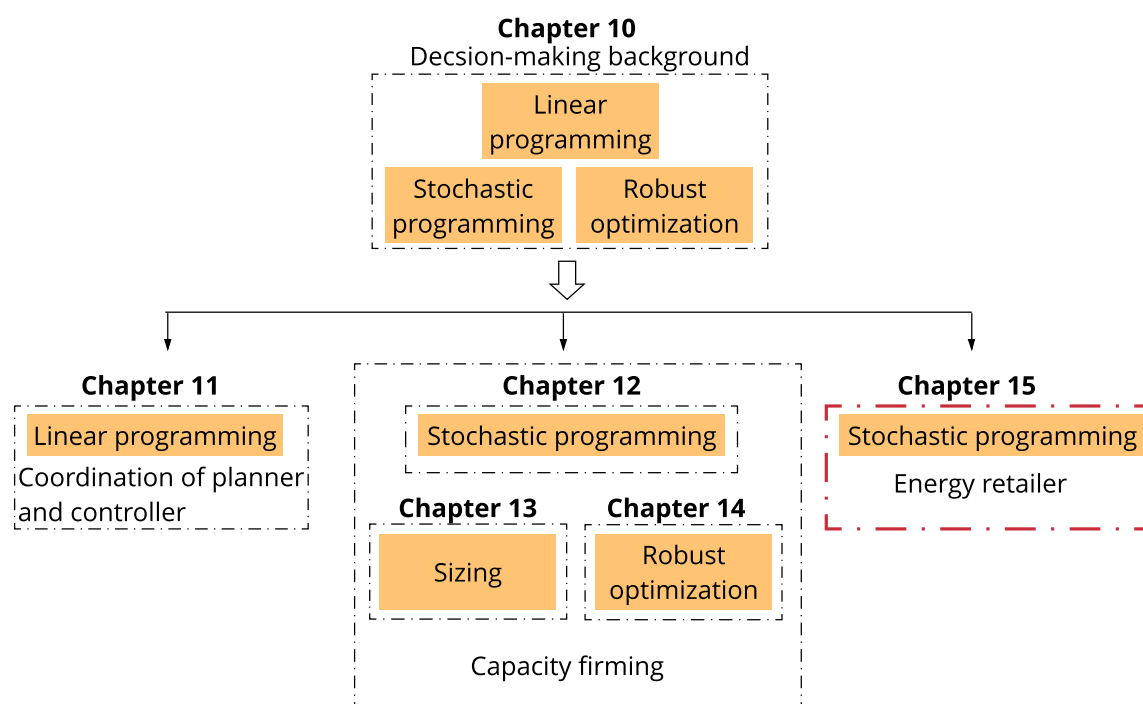


Fig. 15.1 Chapter 15 position in Part II.

A model that yields lower errors in terms of forecast quality may not always point to a more effective model for forecast practitioners [76]. To this end, similarly to Toubeau et al. [143], the forecast value is assessed by considering the day-ahead market scheduling of electricity aggregators, such as energy retailers or generation companies. The energy retailer aims to balance its portfolio on an hourly basis, to avoid financial penalties in case of imbalance, by exchanging the surplus or deficit of energy in the day-ahead electricity market. The energy retailer may have a battery energy storage system (BESS) to manage its portfolio and to minimize imports from the main grid when day-ahead prices are prohibitive.

Section 15.2 introduces the notations used in this Chapter. Section 15.2 presents the formulation of the energy retailer case study. Section 15.3 details empirical value results on the GEFcom 2014 dataset, and Section 15.4 summarizes the main findings and highlights ideas for further work.

15.1 Notation

Sets and indices

Name	Description
t	Time period index.
ω	Scenario index.
T	Number of time periods per day.
$\#\Omega$	Number of scenarios.
\mathcal{T}	Set of time periods, $\mathcal{T} = \{1, 2, \dots, T\}$.
Ω	Set of scenarios, $\Omega = \{1, 2, \dots, \#\Omega\}$.

Parameters

Name	Description	Unit
e_t^{min}, e_t^{max}	Minimum/maximum day-ahead bid.	MWh
y_t^{min}, y_t^{max}	Minimum/maximum retailer net position.	MWh
$y_{max}^{dis}, y_{max}^{cha}$	BESS maximum (dis)charging power.	MW
η^{dis}, η^{cha}	BESS (dis)charging efficiency.	-
s^{min}, s^{max}	BESS minimum/maximum capacity.	MWh
s^{ini}, s^{end}	BESS initial/final state of charge.	MWh
π_t	Day-ahead price.	€/MWh

$\bar{q}_t, \bar{\lambda}_t$	Negative/positive imbalance price.	€/MWh
Δt	Duration of a time period.	hour

Variables

For the sake of clarity the subscript ω is omitted.

Name	Range	Description	Unit
e_t	$[e_t^{\min}, e_t^{\max}]$	Day-ahead bid.	MWh
y_t	$[y_t^{\min}, y_t^{\max}]$	Retailer net position.	MWh
y_t^{pv}	$[0, 1]$	PV generation.	MW
y_t^{w}	$[0, 1]$	Wind generation.	MW
y_t^{l}	$[0, 1]$	Load.	MW
y_t^{cha}	$[0, y_{\max}^{\text{cha}}]$	Charging power.	MW
y_t^{dis}	$[0, y_{\max}^{\text{dis}}]$	Discharging power.	MW
s_t	$[s^{\min}, s^{\max}]$	BESS state of charge.	MWh
d_t^-, d_t^+	\mathbb{R}_+	Short/long deviation.	MWh
y_t^b	$\{0, 1\}$	BESS binary variable.	-

15.2 Problem formulation

Let e_t [MWh] be the net energy retailer position on the day-ahead market during the t -th hour of the day, which is modeled as a first stage variable. Let y_t [MWh] be the realized net energy retailer position during the t -th hour of the day, which is modeled as a second stage variable due to the stochastic processes of the PV generation, wind generation, and load. Let π_t [€/ MWh] the clearing price in the spot day-ahead market for the t -th hour of the day, q_t ex-post settlement price for negative imbalance $y_t < e_t$, and λ_t ex-post settlement price for positive imbalance $y_t > e_t$. The energy retailer is assumed to be a price taker in the day-ahead market. This is motivated by the fact that the individual energy retailer capacity is negligible relative to the whole market. The forward settlement price π_t is assumed to be fixed and known. As imbalance prices tend to exhibit volatility and are difficult to forecast, they are modeled as random variables, with expectations denoted by $\bar{q}_t = \mathbb{E}[q_t]$ and $\bar{\lambda}_t = \mathbb{E}[\lambda_t]$. They are assumed to be independent random variables from the energy retailer portfolio.

Stochastic planner

A stochastic planner with a linear programming formulation and linear constraints is implemented using a scenario-based approach. The planner computes the day-

ahead bids e_t that cannot be modified in the future when the uncertainty is resolved. The second stage corresponds to the dispatch decisions $y_{t,\omega}$ in scenario ω that aims at avoiding portfolio imbalances modeled by a cost function f^c . The second-stage decisions are therefore scenario-dependent and can be adjusted according to the realization of the stochastic parameters. The stochastic planner objective to maximize is

$$J_S = \mathbb{E} \left[\sum_{t \in \mathcal{T}} \pi_t e_t + f^c(e_t, y_{t,\omega}) \right], \quad (15.1)$$

where the expectation is taken with respect to the random variables that are the PV generation, wind generation, and load. Using a scenario-based approach, (15.1) is approximated by

$$J_S \approx \sum_{\omega \in \Omega} \alpha_\omega \sum_{t \in \mathcal{T}} \left[\pi_t e_t + f^c(e_t, y_{t,\omega}) \right], \quad (15.2)$$

with α_ω the probability of scenario $\omega \in \Omega$, and $\sum_{\omega \in \Omega} \alpha_\omega = 1$. The mixed-integer linear programming (MILP) optimization problem to solve is

$$\max_{e_t \in \mathcal{X}, y_{t,\omega} \in \mathcal{Y}(e_t)} \sum_{\omega \in \Omega} \alpha_\omega \sum_{t \in \mathcal{T}} \left[\pi_t e_t - \bar{q}_t d_{t,\omega}^- - \bar{\lambda}_t d_{t,\omega}^+ \right], \quad (15.3a)$$

$$\mathcal{X} = \left\{ e_t : e_t \in [e_t^{\min}, e_t^{\max}] \right\}, \quad (15.3b)$$

$$\mathcal{Y}(e_t) = \left\{ y_{t,\omega} : (15.4a) - (15.4m) \right\}. \quad (15.3c)$$

The optimization variables are e_t , day-ahead bid of the net position, $\forall \omega \in \Omega$, $y_{t,\omega}$, retailer net position in scenario ω , $d_{t,\omega}^-$, short deviation, $d_{t,\omega}^+$, long deviation, $y_{t,\omega}^{\text{PV}}$, PV generation, $y_{t,\omega}^{\text{w}}$, wind generation, $y_{t,\omega}^{\text{cha}}$, battery energy storage system (BESS) charging power, $y_{t,\omega}^{\text{dis}}$, BESS discharging power, $s_{t,\omega}$, BESS state of charge, and $y_{t,\omega}^b$ a binary variable to prevent from charging and discharging simultaneously. The imbalance penalty is modeled by the constraints (15.4a)-(15.4b) $\forall \omega \in \Omega$, that define the short and long deviations variables $d_{t,\omega}^-, d_{t,\omega}^+ \in \mathbb{R}_+$. The energy balance is provided by (15.4c) $\forall \omega \in \Omega$. The set of constraints that bound $y_{t,\omega}^{\text{PV}}$ and $y_{t,\omega}^{\text{w}}$ variables are (15.4d)-(15.4e) $\forall \omega \in \Omega$ where $\hat{y}_{t,\omega}^{\text{PV}}$ and $\hat{y}_{t,\omega}^{\text{w}}$ are PV and wind generation scenarios. The load is assumed to be non-flexible and is a parameter (15.4f) $\forall \omega \in \Omega$ where $\hat{y}_{t,\omega}^{\text{l}}$ are load scenarios. The BESS constraints are provided by (15.4g)-(15.4j), and the BESS dynamics by

(15.4k)-(15.4m) $\forall \omega \in \Omega$.

$$-d_{t,\omega}^- \leq -(e_t - y_{t,\omega}), \forall t \in \mathcal{T} \quad (15.4a)$$

$$-d_{t,\omega}^+ \leq -(y_{t,\omega} - e_t), \forall t \in \mathcal{T} \quad (15.4b)$$

$$\frac{y_{t,\omega}}{\Delta t} = y_{t,\omega}^{\text{pv}} + y_{t,\omega}^{\text{w}} - y_{t,\omega}^{\text{l}} + y_{t,\omega}^{\text{dis}} - y_{t,\omega}^{\text{cha}}, \forall t \in \mathcal{T} \quad (15.4c)$$

$$y_{t,\omega}^{\text{pv}} \leq \hat{y}_{t,\omega}^{\text{pv}}, \forall t \in \mathcal{T} \quad (15.4d)$$

$$y_{t,\omega}^{\text{w}} \leq \hat{y}_{t,\omega}^{\text{w}}, \forall t \in \mathcal{T} \quad (15.4e)$$

$$y_{t,\omega}^{\text{l}} = \hat{y}_{t,\omega}^{\text{l}}, \forall t \in \mathcal{T} \quad (15.4f)$$

$$y_{t,\omega}^{\text{cha}} \leq y_{t,\omega}^{\text{b}} y_{\text{max}}^{\text{cha}}, \forall t \in \mathcal{T} \quad (15.4g)$$

$$y_{t,\omega}^{\text{dis}} \leq (1 - y_{t,\omega}^{\text{b}}) y_{\text{max}}^{\text{dis}}, \forall t \in \mathcal{T} \quad (15.4h)$$

$$-s_{t,\omega} \leq -s^{\text{min}}, \forall t \in \mathcal{T} \quad (15.4i)$$

$$s_{t,\omega} \leq s^{\text{max}}, \forall t \in \mathcal{T} \quad (15.4j)$$

$$\frac{s_{1,\omega} - s^{\text{ini}}}{\Delta t} = \eta^{\text{cha}} y_{1,\omega}^{\text{cha}} - \frac{y_{1,\omega}^{\text{dis}}}{\eta^{\text{dis}}}, \quad (15.4k)$$

$$\frac{s_{t,\omega} - s_{t-1,\omega}}{\Delta t} = \eta^{\text{cha}} y_{t,\omega}^{\text{cha}} - \frac{y_{t,\omega}^{\text{dis}}}{\eta^{\text{dis}}}, \forall t \in \mathcal{T} \setminus \{1\} \quad (15.4l)$$

$$s_{T,\omega} = s^{\text{end}} = s^{\text{ini}}. \quad (15.4m)$$

Notice that, if $\bar{\lambda}_t < 0$, the surplus quantity is remunerated with a non-negative price. In practice, such a scenario could be avoided provided that the energy retailer has curtailment capabilities, and $(\bar{q}_t, \bar{\lambda}_t)$ are strictly positive in our case study. The deterministic formulation with perfect forecasts, the oracle (O), is a specific case of the stochastic formulation by considering only one scenario where $y_{t,\omega}^{\text{pv}}$, $y_{t,\omega}^{\text{w}}$, and $y_{t,\omega}^{\text{l}}$ become the actual values of PV, wind, and load $\forall t \in \mathcal{T}$. The optimization variables are e_t , y_t , d_t^- , d_t^+ , y_t^{pv} , and y_t^{w} , y_t^{cha} , y_t^{dis} , s_t , and y_t^{b} .

Dispatching

Once the bids e_t have been computed by the planner, the dispatching consists of computing the second stage variables given observations of the PV, wind power, and load. The dispatch formulation is a specific case of the stochastic formulation with e_t as parameter and by considering only one scenario where $y_{t,\omega}^{\text{pv}}$, $y_{t,\omega}^{\text{w}}$, and $y_{t,\omega}^{\text{l}}$ become the actual values of PV, wind, and load $\forall t \in \mathcal{T}$. The optimization variables are y_t , d_t^- , d_t^+ , y_t^{pv} , and y_t^{w} , y_t^{cha} , y_t^{dis} , s_t , and y_t^{b} .

15.3 Value results

The energy retailer portfolio is composed of wind power, PV generation, load, and a battery energy storage device. The 50 days of the testing set are used and combined with the 30 possible PV and wind generation zones (3 PV zones and 10 wind farms), resulting in 1 500 independent simulated days. A two-step approach is employed to evaluate the forecast value:

- First, for each generative model and the 1 500 days simulated, the two-stage stochastic planner computes the day-ahead bids of the energy retailer portfolio using the PV, wind power, and load scenarios. After solving the optimization, the day-ahead decisions are recorded.
- Then, a real-time dispatch is carried out using the observations of the PV, wind power, and load, with the day-ahead decisions as parameters.

This two-step methodology is applied to evaluate the three generative models, namely the NF, GAN, and VAE. Figure 15.2 illustrates an arbitrary random day of the testing set with the first zone for both the PV and wind. π_t [€/ MWh] is the day-ahead prices on *February* 6, 2020 of the Belgian day-ahead market used for the 1 500 days simulated. The negative \bar{q}_t and positive $\bar{\lambda}_t$ imbalance prices are set to $2 \times \pi_t$, $\forall t \in \mathcal{T}$. The retailer aims to balance the net power, the red curve in Figure 15.2, by importing/exporting from/to the main grid. Usually, the net is positive (negative) at noon (evening) when the PV generation is maximal (minimal) and the load is minimal (maximal). As the day-ahead spot price is often maximal during the evening load peak, the retailer seeks to save power during the day by charging the battery to decrease the import during the evening. Therefore, the more accurate the PV, wind generation, and load scenarios are, the better is the day-ahead planning.

The battery minimum s^{\min} and maximum s^{\max} capacities are 0 and 1, respectively. It is assumed to be capable of fully (dis)charging in two hours with $y_{\max}^{\text{dis}} = y_{\max}^{\text{cha}} = s^{\max}/2$, and the (dis)charging efficiencies are $\eta^{\text{dis}} = \eta^{\text{cha}} = 95\%$. Each simulation day is independent with a fully discharged battery at the first and last period of each day $s^{\text{ini}} = s^{\text{end}} = 0$. The 1 500 stochastic optimization problems are solved with 50 PV, wind generation, and load scenarios. The python Gurobi library is used to implement the algorithms in Python 3.7, and Gurobi¹ 9.0.2 is used to solve the optimization problems. Numerical experiments are performed on an Intel Core i7-8700 3.20 GHz based computer with 12 threads and 32 GB of RAM running on Ubuntu 18.04 LTS.

¹<https://www.gurobi.com/>

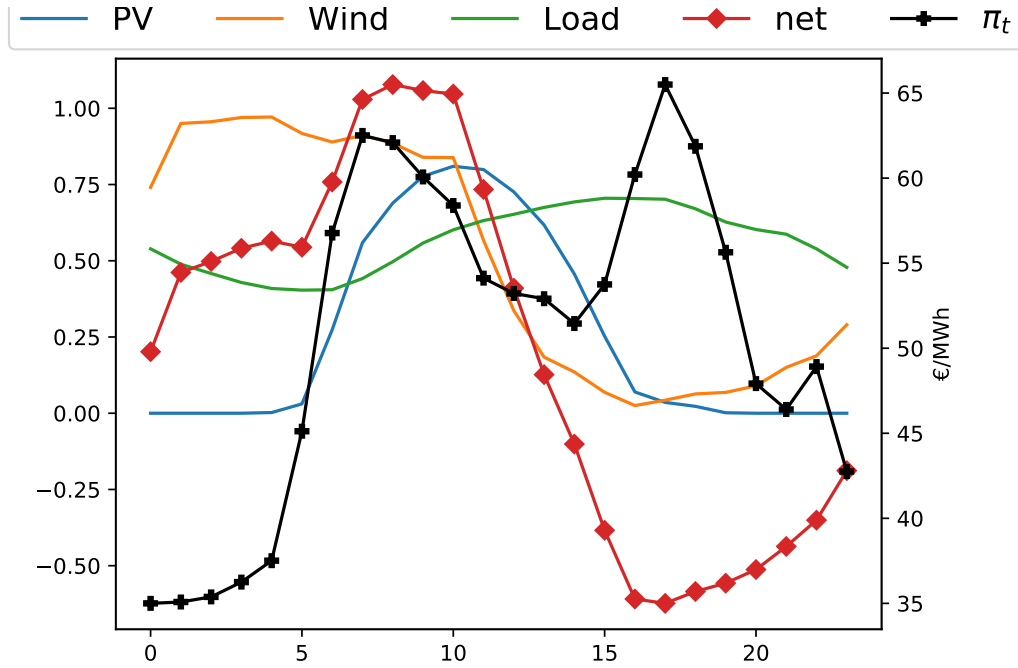


Fig. 15.2 Energy retailer case study: illustration of the observations on a random day of the testing set.

The energy retailer portfolio is composed of PV generation, wind power, load, and a storage device. The PV, wind power, and load scenarios from the testing set are used as inputs of the stochastic day-ahead planner to compute the optimal bids. The net is the power balance of the energy retailer portfolio. The day-ahead prices π_t are obtained from the Belgian day-ahead market on *February 6, 2020*.

The net profit, that is the profit minus penalty, is computed for the 1 500 days of the simulation and aggregated in the first row of Table 15.1. The ranking of each model is computed for the 1 500 days, and the cumulative ranking is expressed in terms of percentage in Table 15.1. NF outperformed both the GAN and VAE with a total net profit of 107 k€. There is still room for improvement as the oracle, which has perfect knowledge of the future, achieved 300 k€. NF, ranked first 39.0% during the 1 500 simulation days and achieved the first and second ranks 69.6%. Overall, in terms of forecast value, the NF outperforms the VAE and GAN. However, this case study is "simple" and stochastic optimization relies mainly on the quality of the average of the scenarios. Therefore, one may consider taking advantage of the particularities of a specific method by considering more advanced case studies. In particular, the specificity of the NFs to provide direct access to the probability density function may be of great interest in specific applications. This is left for future investigations as such more advanced case studies would prevent a fair comparison between models.

	NF	VAE	GAN
Net profit (k€)	107	97	93
1 (%)	39.0	31.8	29.2
1 & 2 (%)	69.6	68.3	62.1
1 & 2 & 3 (%)	100	100	100

Table 15.1 Total net profit (k€) and cumulative ranking (%).

The stochastic planner using the NF PV, wind power, and load scenarios achieved the highest net profit with 107 k€, ranked first 39.0 %, second 30.6 %, and third 30.4 % over 1 500 days of simulation. In comparison, the second-best model, the VAE, achieved a net profit of 97 k€, ranked first 31.8 %, second 36,5 %, and third 31.7 %.

15.3.1 Results summary

Table 15.2 summarizes the main results of this study by comparing the VAE, GAN, and NF implemented through easily comparable star ratings. The rating for each criterion is determined using the following rules - 1 star: third rank, 2 stars: second rank, and 3 stars: first rank. Specifically, training speed is assessed based on reported total training times for each dataset: PV generation, wind power, and load; sample speed is based on reported total generating times for each dataset; quality is evaluated with the metrics considered; value is based on the case study of the day-ahead bidding of the energy retailer; the hyper-parameters search is assessed by the number of configurations tested before reaching satisfactory and stable results over the validation set; the hyper-parameters sensitivity is evaluated by the impact on the quality metric of deviations from the optimal the hyper-parameter values found during the hyper-parameter search; the implementation-friendly criterion is appraised regarding the complexity of the technique and the amount of knowledge required to implement it.

Criteria	VAE	GAN	NF
Train speed	★★★	★★★	★★★
Sample speed	★★★	★★★	★★★
Quality	★★★	★★★	★★★
Value	★★★	★★★	★★★
Hp search	★★★	★★★	★★★
Hp sensibility	★★★	★★★	★★★
Implementation	★★★	★★★	★★★

Table 15.2 Comparison between the deep generative models.

The rating for each criterion is determined using the following rules - 1 star: third rank, 2 stars: second rank, and 3 stars: first rank. Train speed: training computation time; Sample speed: scenario generation computation time; Quality: forecast quality based on the eight complementary metrics considered; Value: forecast value based on the day-ahead energy retailer case study; Hp search: assess the difficulty to identify relevant hyper-parameters; Hp sensibility: assess the sensitivity of the model to a given set of hyper-parameters (the more stars, the more robust to hyper-parameter modifications); Implementation: assess the difficulty to implement the model (the more stars, the more implementation-friendly). Note: the justifications are provided in Appendix 15.5.

15.4 Conclusions

This Chapter proposed a fair and thorough comparison of NFs with the state-of-the-art deep learning generative models, GANs and VAEs, in terms of value. The experiments were performed by using the open data of the Global Energy Forecasting Competition 2014, where the generative models use the conditional information to compute improved weather-based PV power, wind power, and load scenarios. This study demonstrated that NFs are capable of challenging GANs and VAEs as they are, overall, more accurate both in terms of quality (see Chapter 8) and value, and can be used effectively by non-expert deep learning practitioners. Note, Section 8.6 in Chapter 8 presents the NFs advantages over more traditional deep learning approaches that should motivate their introduction into power system applications.

15.5 Appendix: Table 15.2 justifications

The VAE is the fastest to train with a recorded computation time of 7 seconds on average per dataset. The training time of the GAN is approximately three times longer with an average computation time of 20 seconds per dataset. Finally, the NF is the slowest with an average training time of 4 minutes. Concerning the sample speed, this ranking is preserved with the VAE the fastest followed by the GAN and NF models. The VAE and the GAN generate the samples over the testing sets, 5 000 in total, in less than a second. However, the NF considered takes a few minutes. In contrast, the affine autoregressive version of the NF is much faster to train and generate samples. Note: even a training time of a few hours is compatible with day-ahead planning applications. In addition, once the model is trained it is not necessarily required to retrain it every day.

The quality and value assessments have already been discussed in Sections 8.5 and 15.3. Overall, the NF outperforms both the VAE and GAN models.

Concerning the hyper-parameters search and sensibility, the NF tends to be the easiest model to calibrate. In comparison with the VAE and GAN, we found relevant hyper-parameter values by testing only a few combinations. In addition, the NF is robust to hyper-parameter modifications. In contrast, the GAN is the most sensitive. Variations of the hyper-parameters may result in very poor scenarios both in terms of quality and shape. Even for a fixed set of hyper-parameters values, two separate training may not converge towards the same results illustrating the GAN training instabilities.

The VAE is easier to train than the GAN but is also sensitive to hyper-parameters values. However, it is less obvious than the GAN.

Finally, we discuss the implementation-friendly criterion of the models. Note: this discussion is only valid for the models implemented in this study. There exist various architectures of GANs, VAEs, and NFs with simple and complex versions. In our opinion, the VAE is the effortless model to implement as the encoder and decoder are both simple feed-forward neural networks. The only difficulty lies in the reparameterization trick that should be carefully addressed. The GAN is a little bit more difficult to deploy due to the gradient penalty to handle but is similar to the VAE with both the discriminator and the generator that are feed-forward neural networks. The NF is the most difficult model to implement from scratch because the UMNN-MAF approach requires an additional integrand network. An affine autoregressive NF is easier to implement. But it may be less capable of modeling the stochasticity of the variable of interest. However, forecasting practitioners do not necessarily have to implement generative models from scratch and can use numerous existing Python libraries.

Chapter 16

Part II conclusions

“Everything has been figured out, except how to live.”

— **Jean-Paul Sartre**

Part II presents several approaches to address the energy management of a grid-connected microgrid. It proposes to handle the renewable generation uncertainty by considering deterministic, stochastic, and robust approaches that rely on point forecasts, scenarios, and quantiles forecasts, respectively. These approaches are evaluated on several case studies.

- A value function-based approach as a way to propagate information from operational planning to real-time optimization is implemented on MiRIS microgrid located at the John Cockerill Group’s international headquarters in Seraing, Belgium. It uses a deterministic approach relying on point forecasts. The results demonstrate the efficiency of this method to manage the peak in comparison with a Rule-Based Controller.
- A stochastic approach to address the energy management of a grid-connected renewable generation plant coupled with a battery energy storage device in the capacity firming market is implemented on the MiRIS microgrid case study. The results of the stochastic planner are comparable with those of the deterministic planner, even when the prediction error variance is non-negligible. However, further investigations are required to use a more realistic methodology to generate PV scenario, and a realistic controller.
- A sizing and an energy management using a robust approach of this system are proposed on the ULiège case study, respectively. The sizing study indicates that

it is not very sensitive to the control policy, deterministic with perfect knowledge, deterministic with point forecasts, and stochastic with scenarios. However, further investigations are required to implement a more realistic controller that uses intraday point forecasts, and to conduct a sensitivity analysis on the simulation parameters. Overall, the robust approach allows finding a trade-off between conservative and risk-seeking policies by selecting the optimal robust optimization parameters, leading to improved economic benefits in comparison with the baseline.

- Finally, a stochastic approach is used to deal with the optimal bidding of an energy retailer portfolio on the day-ahead market. This study demonstrated that NFs are capable of challenging GANs and VAEs as they are, overall, more accurate both in terms of quality (see Chapter 8) and value, and can be used effectively by non-expert deep learning practitioners.

Chapter 17

General conclusions and perspectives

Overview

This chapter concludes the thesis and identifies some possible directions of future researches in both forecasting and planning for microgrids. In particular, by using deep learning techniques that could take advantage of the underlying processes.

“*Words are loaded pistols.*”

— **Jean-Paul Sartre**

17.1 Summary

This thesis considers a microgrid system on a day-ahead basis. The two main research questions are:

- How to produce reliable probabilistic forecasts of renewable generation, consumption, and electricity prices?
- How to make decisions with uncertainty using probabilistic forecasts?

Part [I](#) proposes some research directions to the first question by providing some forecasting techniques and quality metrics required to produce and evaluate point and probabilistic forecasts to be used as input of decision-making models in Part [II](#). Chapters [2](#) and [3](#) provide the basics by introducing the different types of forecasts to characterize the behavior of stochastic variables, such as renewable generation,

and the tools to assess the different types of forecasts. The point forecasts, quantile forecasts, scenarios, and confidence intervals are studied in the next Chapters of Part I. Chapter 5 uses common deep-learning models such as recurrent neural networks to compute PV and electrical consumption point forecasts. Chapter 6 proposes to implement deep-learning models such as the encoder-decoder architecture to produce PV quantile forecasts. Chapter 7 presents a confidence interval-based approach to compute probabilistic forecasting of imbalance prices with a particular focus on the Belgian case. Chapter 8 studies the scenarios of renewable generation and electrical consumption. In particular, it compares extensively the normalizing flows, variational autoencoders, and generative adversarial networks deep generative models. Chapter 4 introduces a classification in two dimensions of load forecasting studies to decide which forecasting tools to use in which case. For the sake of clarity, this study is not detailed in this thesis, and only a summary of the main ideas is proposed.

Part II presents several approaches and methodologies, based on optimization, for decision-making under uncertainty to study the second research question. Chapter 10 introduces the different types of decision making under uncertainty using optimization strategies. Chapter 11 presents a value function-based approach as a way to propagate information from operational planning to real-time optimization, in a deterministic framework. Chapters 12, 13, and 14 consider a grid-connected renewable generation plant coupled with a battery energy storage device in the capacity firming market, designed to promote renewable power generation facilities in small non-interconnected grids. First, a stochastic approach is proposed. Second, a sizing of the system is investigated. Finally, a robust approach is studied. Chapter 15, is the extension of Chapter 8, and presents the forecast value of the deep learning generative models by considering the day-ahead market scheduling of an energy retailer.

17.2 Future directions

Graphical deep learning models

Nowadays, the renewable energy forecasting field is extremely active and dynamic. It is hence expected that new forecasting methods will be proposed and used in operational problems related to power system applications in the coming years. The type of forecasts to be used as input to operational problems will depend upon the nature of the problem itself, and how the corresponding optimization problem is formulated. For instance, techniques that take advantage of the power system characteristics such as graphical

neural networks [152, 38] that are capable of learning the power network structure, and could be applied to hierarchical forecasting. Indeed, probabilistic graphical models reduce to Bayesian networks with a pre-defined topology and a learnable density at each node [152]. From this new perspective, the graphical normalizing flow provides a promising way to inject domain knowledge into normalizing flows while preserving both the interpretability of Bayesian networks and the representation capacity of normalizing flows.

Machine learning for optimization

There is a broad consensus in the power system community that the uncertain nature of renewable energy sources like wind and solar is likely to induce significant changes in the paradigms of power systems management [105]. The actual electricity market is the result of integrating traditional practices, such as unit commitment or economic dispatch, designed given a generation mix mostly formed by dispatchable plants. Therefore, they are now to be reexamined so that stochastic producers can compete on equal terms. For instance, the capacity firming market is a new design conceived to promote renewable generation on isolated markets. The type of decision-making tools to be used to deal with these new market designs and systems such as microgrids depend upon the nature of the problem itself, as investigated in this second part. These tools have been studied intensively and it is hence expected that new methods will be proposed and used in power system applications. In particular, machine learning for optimization by learning partially or totally the sizing space to provide a fast and efficient sizing tool, or simplifying optimization planning problems by learning a sub-optimal space is a hot topic. For instance:

- Misyris et al. [103] propose a framework for physics-informed neural networks in power system applications. In this line, Fioretto et al. [51] present a deep learning approach to the optimal power flows. The learning model exploits the information available in the similar states of the system, as well as a dual Lagrangian method to satisfy the physical and engineering constraints present in the optimal power flows.
- Donon et al. [38] propose a neural network architecture that emulates the behavior of a physics solver that solves electricity differential equations to compute electricity flow in power grids. It uses proxies based on graph neural networks.

- Tsaousoglou et al. [144] consider an economic dispatch problem for a community of distributed energy resources, where energy management decisions are made online and under uncertainty. The economic dispatch problem is formulated as a multi-agent Markov Decision Process where the difficulties lie in the curse of dimensionality and in guaranteeing the satisfaction of constraints under uncertainty. A novel method, that combines duality and deep learning, is proposed to tackle these challenges.

References

- [1] Martín Abadi, Ashish Agarwal, Paul Barham, Eugene Brevdo, Zhifeng Chen, Craig Citro, Greg S Corrado, Andy Davis, Jeffrey Dean, Matthieu Devin, et al. Tensorflow: Large-scale machine learning on heterogeneous systems, 2015. URL <https://www.tensorflow.org/>.
- [2] International Energy Agency. Net zero by 2050: A roadmap for the global energy system. Technical report, International Energy Agency, 2021.
- [3] Michael S Albergo, Denis Boyda, Daniel C Hackett, Gurtej Kanwar, Kyle Cranmer, Sébastien Racanière, Danilo Jimenez Rezende, and Phiala E Shanahan. Introduction to normalizing flows for lattice field theory. *arXiv preprint arXiv:2101.08176*, 2021.
- [4] Myles Allen, Mustafa Babiker, Yang Chen, and Heleen C. de Coninck. *IPCC SR15: Summary for Policymakers*. Intergovernmental Panel on Climate Change, October 2018. Drafting Authors: Myles Allen (UK), Mustafa Babiker (Sudan), Yang Chen (China), Heleen de Coninck (Netherlands/EU), Sarah Connors (UK), Renée van Diemen (Netherlands), Opha Pauline Dube (Botswana), Kristie L. Ebi (USA), Francois Engelbrecht (South Africa), Marion Ferrat (UK/France), James Ford (UK/Canada), Piers Forster (UK), Sabine Fuss (Germany), Tania Guillén Bolaños (Germany/Nicaragua), Jordan Harold (UK), Ove Hoegh-Guldberg (Australia), Jean-Charles Hourcade (France), Daniel Huppmann (Austria), Daniela Jacob (Germany), Kejun Jiang (China), Tom Gabriel Johansen (Norway), Mikiko Kainuma (Japan), Kiane de Kleijne (Netherlands/EU), Elmar Kriegler (Germany), Debora Ley (Guatemala/Mexico), Diana Liverman (USA), Natalie Mahowald (USA), Valérie Masson-Delmotte (France), J. B. Robin Matthews (UK), Richard Millar (UK), Katja Mintenbeck (Germany), Angela Morelli (Norway/Italy), Wilfran Moufouma-Okia (France/Congo), Luis Mundaca (Sweden/Chile), Maike Nicolai (Germany), Chukwumerije Okereke (UK/Nigeria), Minal Pathak (India), Antony Payne (UK), Roz Pidcock (UK), Anna Pirani (Italy), Elvira Poloczanska (UK/Australia), HansOtto Pörtner (Germany), Aromar Revi (India), Keywan Riahi (Austria), Debra C. Roberts (South Africa), Joeri Rogelj (Austria/Belgium), Joyashree Roy (India), Sonia I. Seneviratne (Switzerland), Priyadarshi R. Shukla (India), James Skea (UK), Raphael Slade (UK), Drew Shindell (USA), Chandni Singh (India), William Solecki (USA), Linda Steg (Netherlands), Michael Taylor (Jamaica), Petra Tschakert (Australia/Austria), Henri Waisman (France), Rachel Warren (UK), Panmao Zhai (China), Kirsten Zickfeld (Canada).

- [5] Martin Arjovsky and Léon Bottou. Towards principled methods for training generative adversarial networks. *arXiv preprint arXiv:1701.04862*, 2017.
- [6] Martin Arjovsky, Soumith Chintala, and Léon Bottou. Wasserstein generative adversarial networks. In *International conference on machine learning*, pages 214–223. PMLR, 2017.
- [7] Mikhail Belkin, Daniel Hsu, Siyuan Ma, and Soumik Mandal. Reconciling modern machine learning practice and the bias-variance trade-off. *arXiv preprint arXiv:1812.11118*, 2018.
- [8] Alberto Bemporad, Andrea Garulli, Simone Paoletti, and Antonio Vicino. A greedy approach to identification of piecewise affine models. In *International Workshop on Hybrid Systems: Computation and Control*, pages 97–112. Springer, 2003.
- [9] Aharon Ben-Tal, Laurent El Ghaoui, and Arkadi Nemirovski. *Robust optimization*, volume 28. Princeton University Press, 2009.
- [10] Jacques F Benders. Partitioning procedures for solving mixed-variables programming problems. *Numerische mathematik*, 4(1):238–252, 1962.
- [11] Yoshua Bengio and Yves Grandvalet. No unbiased estimator of the variance of k-fold cross-validation. *Journal of machine learning research*, 5(Sep):1089–1105, 2004.
- [12] Dimitris Bertsimas and Shimrit Shtern. A scalable algorithm for two-stage adaptive linear optimization. *arXiv preprint arXiv:1807.02812*, 2018.
- [13] Dimitris Bertsimas and John N Tsitsiklis. *Introduction to linear optimization*, volume 6. Athena Scientific Belmont, MA, 1997.
- [14] Dimitris Bertsimas, David B Brown, and Constantine Caramanis. Theory and applications of robust optimization. *SIAM review*, 53(3):464–501, 2011.
- [15] Dimitris Bertsimas, Eugene Litvinov, Xu Andy Sun, Jinye Zhao, and Tongxin Zheng. Adaptive robust optimization for the security constrained unit commitment problem. *IEEE transactions on power systems*, 28(1):52–63, 2012.
- [16] Gianni Bianchini, Simone Paoletti, Antonio Vicino, Franco Corti, and Federico Nebiacolombo. Model estimation of photovoltaic power generation using partial information. In *IEEE PES ISGT Europe 2013*, pages 1–5. IEEE, 2013.
- [17] Gianni Bianchini, Daniele Pepe, and Antonio Vicino. Estimation of photovoltaic generation forecasting models using limited information. *Automatica*, 113:108688, 2020.
- [18] Lukas Biewald. Experiment tracking with weights and biases, 2020. URL <https://www.wandb.com/>. Software available from wandb.com.
- [19] John R Birge and Francois Louveaux. *Introduction to stochastic programming*. Springer Science & Business Media, 2011.

- [20] Eilyan Y Bitar, Ram Rajagopal, Pramod P Khargonekar, Kameshwar Poolla, and Pravin Varaiya. Bringing wind energy to market. *IEEE Transactions on Power Systems*, 27(3):1225–1235, 2012.
- [21] Sam Bond-Taylor, Adam Leach, Yang Long, and Chris G Willcocks. Deep generative modelling: A comparative review of vaes, gans, normalizing flows, energy-based and autoregressive models. *arXiv preprint arXiv:2103.04922*, 2021.
- [22] Trine Krogh Boomsma, Nina Juul, and Stein-Erik Fleten. Bidding in sequential electricity markets: The nordic case. *European Journal of Operational Research*, 238(3):797–809, 2014.
- [23] Ali Borji. Pros and cons of gan evaluation measures. *Computer Vision and Image Understanding*, 179:41–65, 2019.
- [24] Jérémie Bottieau, Louis Hubert, Zacharie De Grève, François Vallée, and Jean-François Toubéau. Very-short-term probabilistic forecasting for a risk-aware participation in the single price imbalance settlement. *IEEE Transactions on Power Systems*, 35(2):1218–1230, 2019.
- [25] George EP Box, Gwilym M Jenkins, Gregory C Reinsel, and Greta M Ljung. *Time series analysis: forecasting and control*. John Wiley & Sons, 2015.
- [26] Simon Camal, Fei Teng, Andrea Michiorri, Georges Kariniotakis, and L Badesa. Scenario generation of aggregated wind, photovoltaics and small hydro production for power systems applications. *Applied Energy*, 242:1396–1406, 2019.
- [27] Yize Chen, Pan Li, and Baosen Zhang. Bayesian renewables scenario generation via deep generative networks. In *2018 52nd Annual Conference on Information Sciences and Systems (CISS)*, pages 1–6. IEEE, 2018.
- [28] Yize Chen, Yishen Wang, Daniel Kirschen, and Baosen Zhang. Model-free renewable scenario generation using generative adversarial networks. *IEEE Transactions on Power Systems*, 33(3):3265–3275, 2018.
- [29] Zhenghua Chen and Chaoyang Jiang. Building occupancy modeling using generative adversarial network. *Energy and Buildings*, 174:372–379, 2018.
- [30] François Chollet et al. Keras. <https://keras.io>, 2015.
- [31] Stefano Raimondi Cominesi, Marcello Farina, Luca Giulioni, Bruno Picasso, and Riccardo Scattolini. A two-layer stochastic model predictive control scheme for microgrids. *IEEE Transactions on Control Systems Technology*, 26(1):1–13, 2017.
- [32] Abdelkader Dairi, Fouzi Harrou, Ying Sun, and Sofiane Khadraoui. Short-term forecasting of photovoltaic solar power production using variational auto-encoder driven deep learning approach. *Applied Sciences*, 10(23):8400, 2020.
- [33] Selmane Dakir and Bertrand Cornélusse. Combining optimization and simulation for microgrid sizing. 2019.

- [34] Jan G De Gooijer and Rob J Hyndman. 25 years of time series forecasting. *International journal of forecasting*, 22(3):443–473, 2006.
- [35] Kristof De Vos. Negative wholesale electricity prices in the german, french and belgian day-ahead, intra-day and real-time markets. *The Electricity Journal*, 28(4):36–50, 2015.
- [36] Masson Delmotte, P. Zhai V., A. Pirani, S. L. Connors, C. Péan, S. Berger, N. Caud, Y. Chen, L. Goldfarb, M. I. Gomis, M. Huang, K. Leitzell, E. Lonnoy, J. B. R. Matthews, T. K. Maycock, T. Waterfield, O. Yelekçi, R. Yu, and B. Zhou (eds.). *IPCC, 2021: Summary for Policymakers. In: Climate Change 2021: The Physical Science Basis. Contribution of Working Group I to the Sixth Assessment Report of the Intergovernmental Panel on Climate Change*. Cambridge University Press, 2021.
- [37] Francis X Diebold and Robert S Mariano. Comparing predictive accuracy. *Journal of Business & economic statistics*, 20(1):134–144, 2002.
- [38] Balthazar Donon, Benjamin Donnot, Isabelle Guyon, and Antoine Marot. Graph neural solver for power systems. In *2019 International Joint Conference on Neural Networks (IJCNN)*, pages 1–8. IEEE, 2019.
- [39] RN Dows and EJ Gough. Pvusa procurement, acceptance, and rating practices for photovoltaic power plants. Technical report, Pacific Gas and Electric Co., San Ramon, CA (United States). Dept. of Research and Development, 1995.
- [40] Laurine Duchesne. *Machine Learning of Proxies for Power Systems Reliability Management in Operation Planning*. PhD thesis, Université de Liège, Liège, Belgique, 2021.
- [41] Jonathan Dumas and Bertrand Cornélusse. Classification of load forecasting studies by forecasting problem to select load forecasting techniques and methodologies. *arXiv preprint arXiv:1901.05052*, 2018. URL <https://arxiv.org/abs/1901.05052>.
- [42] Jonathan Dumas, Ioannis Boukas, Miguel Manuel de Villena, Sébastien Mathieu, and Bertrand Cornélusse. Probabilistic forecasting of imbalance prices in the belgian context. In *2019 16th International Conference on the European Energy Market (EEM)*, pages 1–7. IEEE, 2019. URL <https://arxiv.org/abs/2106.07361>.
- [43] Jonathan Dumas, Bertrand Cornélusse, Antonello Giannitrapani, Simone Paoletti, and Antonio Vicino. Stochastic and deterministic formulations for capacity firming nominations. In *2020 International Conference on Probabilistic Methods Applied to Power Systems (PMAPS)*, pages 1–7. IEEE, 2020. URL <https://arxiv.org/abs/2106.02425>.
- [44] Jonathan Dumas, Colin Cointe, Xavier Fettweis, and Bertrand Cornélusse. Deep learning-based multi-output quantile forecasting of pv generation. In *2021 IEEE Madrid PowerTech*, pages 1–6, 2021. doi: 10.1109/PowerTech46648.2021.9494976. URL <https://arxiv.org/abs/2106.01271>.

- [45] Jonathan Dumas, Colin Cointe, Antoine Wehenkel, Antonio Sutera, Xavier Fettweis, and Bertrand Cornélusse. A probabilistic forecast-driven strategy for a risk-aware participation in the capacity firming market. Manuscript submitted for publication to *IEEE Transactions on Sustainable Energy*, 2021. URL <https://arxiv.org/abs/2105.13801>.
- [46] Jonathan Dumas, Bertrand Cornélusse, Xavier Fettweis, Antonello Giannitrapani, Simone Paoletti, and Antonio Vicino. Probabilistic forecasting for sizing in the capacity firming framework. In *2021 IEEE Madrid PowerTech*, pages 1–6, 2021. doi: 10.1109/PowerTech46648.2021.9494947. URL <https://arxiv.org/abs/2106.02323>.
- [47] Jonathan Dumas, Selmane Dakir, Clément Liu, and Bertrand Cornélusse. Coordination of operational planning and real-time optimization in microgrids. *Electric Power Systems Research*, 190:106634, 2021. URL <https://arxiv.org/abs/2106.02374>.
- [48] Jonathan Dumas, Antoine Wehenkel, Damien Lanaspéze, Bertrand Cornélusse, and Antonio Sutera. Deep generative modeling for probabilistic forecasting in power systems. Manuscript submitted for publication to *Applied Energy*, 2021. URL <https://arxiv.org/abs/2106.09370>.
- [49] Tom Fawcett. Roc graphs: Notes and practical considerations for researchers. *Machine learning*, 31(1):1–38, 2004.
- [50] Xavier Fettweis, Jason Box, Cécile Agosta, Charles Amory, Christoph Kittel, Charlotte Lang, Dirk van As, Horst Machguth, and Hubert Gallée. Reconstructions of the 1900–2015 greenland ice sheet surface mass balance using the regional climate MAR model. *Cryosphere (The)*, 11:1015–1033, 2017.
- [51] Ferdinando Fioretto, Terrence WK Mak, and Pascal Van Hentenryck. Predicting ac optimal power flows: Combining deep learning and lagrangian dual methods. In *Proceedings of the AAAI Conference on Artificial Intelligence*, volume 34, pages 630–637, 2020.
- [52] Maria P Garcia and Daniel S Kirschen. Forecasting system imbalance volumes in competitive electricity markets. *IEEE Transactions on Power Systems*, 21(1): 240–248, 2006.
- [53] Leijiao Ge, Wenlong Liao, Shouxiang Wang, Birgitte Bak-Jensen, and Jayakrishnan Radhakrishna Pillai. Modeling daily load profiles of distribution network for scenario generation using flow-based generative network. *IEEE Access*, 8: 77587–77597, 2020.
- [54] Stuart Geman, Elie Bienenstock, and René Doursat. Neural networks and the bias/variance dilemma. *Neural computation*, 4(1):1–58, 1992.
- [55] Antonio Giannitrapani, Simone Paoletti, Antonio Vicino, and Donato Zarrilli. Bidding strategies for renewable energy generation with non stationary statistics. *IFAC Proceedings Volumes*, 47(3):10784–10789, 2014.

- [56] Antonio Giannitrapani, Simone Paoletti, Antonio Vicino, and Donato Zarrilli. Bidding wind energy exploiting wind speed forecasts. *IEEE Transactions on Power Systems*, 31(4):2647–2656, 2015.
- [57] Antonio Giannitrapani, Simone Paoletti, Antonio Vicino, and Donato Zarrilli. Bidding wind energy exploiting wind speed forecasts. *IEEE Transactions on Power Systems*, 31(4):2647–2656, 2016.
- [58] Tilmann Gneiting and Matthias Katzfuss. Probabilistic forecasting. *Annual Review of Statistics and Its Application*, 1:125–151, 2014.
- [59] Tilmann Gneiting and Adrian E Raftery. Strictly proper scoring rules, prediction, and estimation. *Journal of the American statistical Association*, 102(477):359–378, 2007.
- [60] Tilmann Gneiting, Larissa I Stanberry, Eric P Gritmit, Leonhard Held, and Nicholas A Johnson. Assessing probabilistic forecasts of multivariate quantities, with an application to ensemble predictions of surface winds. *Test*, 17(2):211–235, 2008.
- [61] Faranak Golestaneh, Hoay Beng Gooi, and Pierre Pinson. Generation and evaluation of space–time trajectories of photovoltaic power. *Applied Energy*, 176: 80–91, 2016.
- [62] Faranak Golestaneh, Pierre Pinson, and Hoay Beng Gooi. Very short-term nonparametric probabilistic forecasting of renewable energy generation—with application to solar energy. *IEEE Transactions on Power Systems*, 31(5):3850–3863, 2016.
- [63] Ian Goodfellow, Yoshua Bengio, and Aaron Courville. *Deep Learning*. MIT Press, 2016. <http://www.deeplearningbook.org>.
- [64] Ian Goodfellow, Yoshua Bengio, Aaron Courville, and Yoshua Bengio. *Deep learning*, volume 1. MIT press Cambridge, 2016.
- [65] Ian J Goodfellow, Jean Pouget-Abadie, Mehdi Mirza, Bing Xu, David Warde-Farley, Sherjil Ozair, Aaron Courville, and Yoshua Bengio. Generative adversarial networks. *arXiv preprint arXiv:1406.2661*, 2014.
- [66] Richard Green and Nicholas Vasilakos. Market behaviour with large amounts of intermittent generation. *Energy Policy*, 38(7):3211–3220, 2010.
- [67] Stephen R Green and Jonathan Gair. Complete parameter inference for gw150914 using deep learning. *Machine Learning: Science and Technology*, 2(3):03LT01, 2021.
- [68] Ishaan Gulrajani, Faruk Ahmed, Martin Arjovsky, Vincent Dumoulin, and Aaron Courville. Improved training of wasserstein gans. *arXiv preprint arXiv:1704.00028*, 2017.

- [69] Pierre Haessig. *Dimensionnement et gestion d'un stockage d'énergie pour l'atténuation des incertitudes de production éolienne*. PhD thesis, Cachan, Ecole normale supérieure, 2014.
- [70] Pierre Haessig, Bernard Multon, Hamid Ben Ahmed, Stéphane Lascaud, and Lionel Jamy. Aging-aware nas battery model in a stochastic wind-storage simulation framework. In *2013 IEEE Grenoble Conference*, pages 1–6. IEEE, 2013.
- [71] Pierre Haessig, Bernard Multon, Hamid Ben Ahmed, Stéphane Lascaud, and Pascal Bondon. Energy storage sizing for wind power: impact of the autocorrelation of day-ahead forecast errors. *Wind Energy*, 18(1):43–57, 2015.
- [72] Trevor Hastie, Robert Tibshirani, and Jerome Friedman. *The elements of statistical learning: data mining, inference, and prediction*. Springer Science & Business Media, 2009.
- [73] Hansika Hewamalage, Christoph Bergmeir, and Kasun Bandara. Recurrent neural networks for time series forecasting: Current status and future directions. *International Journal of Forecasting*, 37(1):388–427, 2020.
- [74] Tao Hong and Shu Fan. Probabilistic electric load forecasting: A tutorial review. *International Journal of Forecasting*, 32(3):914–938, 2016.
- [75] Tao Hong, Pierre Pinson, Shu Fan, Hamidreza Zareipour, Alberto Troccoli, and Rob J Hyndman. Probabilistic energy forecasting: Global energy forecasting competition 2014 and beyond, 2016.
- [76] Tao Hong, Pierre Pinson, Yi Wang, Rafal Weron, Dazhi Yang, Hamidreza Zareipour, et al. Energy forecasting: A review and outlook. Technical report, Department of Operations Research and Business Intelligence, Wroclaw . . . , 2020.
- [77] Chin-Wei Huang, David Krueger, Alexandre Lacoste, and Aaron Courville. Neural autoregressive flows. In *International Conference on Machine Learning*, pages 2078–2087. PMLR, 2018.
- [78] Semich Impram, Secil Varbak Nese, and Bülent Oral. Challenges of renewable energy penetration on power system flexibility: A survey. *Energy Strategy Reviews*, 31:100539, 2020.
- [79] Congmei Jiang, Yongfang Mao, Yi Chai, and Mingbiao Yu. Day-ahead renewable scenario forecasts based on generative adversarial networks. *International Journal of Energy Research*, 45(5):7572–7587, 2021.
- [80] Quanyuan Jiang, Meidong Xue, and Guangchao Geng. Energy management of microgrid in grid-connected and stand-alone modes. *IEEE transactions on power systems*, 28(3):3380–3389, 2013.
- [81] Ruiwei Jiang, Jianhui Wang, and Yongpei Guan. Robust unit commitment with wind power and pumped storage hydro. *IEEE Transactions on Power Systems*, 27(2):800–810, 2011.

- [82] Chengquan Ju, Peng Wang, Lalit Goel, and Yan Xu. A two-layer energy management system for microgrids with hybrid energy storage considering degradation costs. *IEEE Transactions on Smart Grid*, 9(6):6047–6057, 2017.
- [83] Sami H Karaki, Bassel A Salim, and Riad B Chedid. Probabilistic model of a two-site wind energy conversion system. *IEEE Transactions on Energy Conversion*, 17(4):530–536, 2002.
- [84] SH Karaki, RB Chedid, and R Ramadan. Probabilistic performance assessment of autonomous solar-wind energy conversion systems. *IEEE Transactions on energy conversion*, 14(3):766–772, 1999.
- [85] Janina C Ketterer. The impact of wind power generation on the electricity price in germany. *Energy Economics*, 44:270–280, 2014.
- [86] Abdolrahman Khoshrou and Eric J Pauwels. Short-term scenario-based probabilistic load forecasting: A data-driven approach. *Applied Energy*, 238:1258–1268, 2019.
- [87] Diederik P Kingma and Jimmy Ba. Adam: A method for stochastic optimization. *arXiv preprint arXiv:1412.6980*, 2014.
- [88] Diederik P Kingma and Max Welling. Auto-encoding variational bayes. *arXiv preprint arXiv:1312.6114*, 2013.
- [89] Diederik P Kingma, Tim Salimans, Rafal Jozefowicz, Xi Chen, Ilya Sutskever, and Max Welling. Improving variational inference with inverse autoregressive flow. *arXiv preprint arXiv:1606.04934*, 2016.
- [90] Gro Klæboe, Anders Lund Eriksrud, and Stein-Erik Fleten. Benchmarking time series based forecasting models for electricity balancing market prices. *Energy Systems*, 6(1):43–61, 2015.
- [91] Ivan Kobyzev, Simon Prince, and Marcus Brubaker. Normalizing flows: An introduction and review of current methods. *IEEE Transactions on Pattern Analysis and Machine Intelligence*, 2020.
- [92] Roger Koenker and Gilbert Bassett Jr. Regression quantiles. *Econometrica: journal of the Econometric Society*, pages 33–50, 1978.
- [93] Ranjeet Kumar, Michael J Wenzel, Matthew J Ellis, Mohammad N ElBsat, Kirk H Drees, and Victor M Zavala. A stochastic dual dynamic programming framework for multiscale mpc. *IFAC-PapersOnLine*, 51(20):493–498, 2018.
- [94] Jian Lan, Qinglai Guo, and Hongbin Sun. Demand side data generating based on conditional generative adversarial networks. *Energy Procedia*, 152:1188–1193, 2018.
- [95] Mark Landry, Thomas P Erlinger, David Patschke, and Craig Varrichio. Probabilistic gradient boosting machines for gefcom2014 wind forecasting. *International Journal of Forecasting*, 32(3):1061–1066, 2016.

- [96] Philippe Lauret, Mathieu David, and Pierre Pinson. Verification of solar irradiance probabilistic forecasts. *Solar Energy*, 194:254–271, 2019.
- [97] Erich L Lehmann and Joseph P Romano. *Testing statistical hypotheses*. Springer Science & Business Media, 2006.
- [98] Hui Lin and Halit Üster. Exact and heuristic algorithms for data-gathering cluster-based wireless sensor network design problem. *IEEE/ACM transactions on networking*, 22(3):903–916, 2013.
- [99] Haitao Liu, Jianfei Cai, and Yew-Soon Ong. Remarks on multi-output gaussian process regression. *Knowledge-Based Systems*, 144:102–121, 2018.
- [100] B Looney. Statistical review of world energy, 2020, 2020.
- [101] Gilles Louppe. Understanding random forests: From theory to practice. *arXiv preprint arXiv:1407.7502*, 2014.
- [102] Aleksei Mashlakov, Toni Kuronen, Lasse Lensu, Arto Kaarna, and Samuli Honkapuro. Assessing the performance of deep learning models for multivariate probabilistic energy forecasting. *Applied Energy*, 285:116405, 2021.
- [103] George S Misyris, Andreas Venzke, and Spyros Chatzivasileiadis. Physics-informed neural networks for power systems. In *2020 IEEE Power & Energy Society General Meeting (PESGM)*, pages 1–5. IEEE, 2020.
- [104] Juan M Morales, Roberto Minguez, and Antonio J Conejo. A methodology to generate statistically dependent wind speed scenarios. *Applied Energy*, 87(3): 843–855, 2010.
- [105] Juan M Morales, Antonio J Conejo, Henrik Madsen, Pierre Pinson, and Marco Zugno. *Integrating renewables in electricity markets: operational problems*, volume 205. Springer Science & Business Media, 2013.
- [106] L Moretti, S Polimeni, L Meraldi, P Raboni, S Leva, and G Manzolini. Assessing the impact of a two-layer predictive dispatch algorithm on design and operation of off-grid hybrid microgrids. *Renewable Energy*, 143:1439–1453, 2019.
- [107] Arnold N’Goran. *Contrôle optimal et gestion énergétique d’une station d’énergie autonome par optimisation robuste*. PhD thesis, Université Paris sciences et lettres, 2020.
- [108] Arnold N’Goran, Bruno Daugrois, Marc Lotteau, and Sophie Demassey. Optimal engagement and operation of a grid-connected pv/battery system. In *2019 IEEE PES Innovative Smart Grid Technologies Europe (ISGT-Europe)*, pages 1–5. IEEE, 2019.
- [109] Anne Olhoff and John M Christensen. Emissions gap report 2020. 2020. URL <https://www.unep.org/emissions-gap-report-2020>.

- [110] Daniel E Olivares, Ali Mehrizi-Sani, Amir H Etemadi, Claudio A Cañizares, Reza Iravani, Mehrdad Kazerani, Amir H Hajimiragha, Oriol Gomis-Bellmunt, Maryam Saeedifard, Rodrigo Palma-Behnke, et al. Trends in microgrid control. *IEEE Transactions on smart grid*, 5(4):1905–1919, 2014.
- [111] Aaron Oord, Yazhe Li, Igor Babuschkin, Karen Simonyan, Oriol Vinyals, Koray Kavukcuoglu, George Driessche, Edward Lockhart, Luis Cobo, Florian Stimberg, et al. Parallel wavenet: Fast high-fidelity speech synthesis. In *International conference on machine learning*, pages 3918–3926. PMLR, 2018.
- [112] Jorge Ángel González Ordiano, Lutz Gröll, Ralf Mikut, and Veit Hagenmeyer. Probabilistic energy forecasting using the nearest neighbors quantile filter and quantile regression. *International Journal of Forecasting*, 36(2):310–323, 2020.
- [113] Omid Palizban, Kimmo Kauhaniemi, and Josep M Guerrero. Microgrids in active network management part i: Hierarchical control, energy storage, virtual power plants, and market participation. *Renewable and Sustainable Energy Reviews*, 36:428–439, 2014.
- [114] George Papaefthymiou and Dorota Kurowicka. Using copulas for modeling stochastic dependence in power system uncertainty analysis. *IEEE Transactions on Power Systems*, 24(1):40–49, 2008.
- [115] George Papamakarios, Theo Pavlakou, and Iain Murray. Masked autoregressive flow for density estimation. In *Advances in Neural Information Processing Systems*, pages 2338–2347, 2017.
- [116] George Papamakarios, Eric Nalisnick, Danilo Jimenez Rezende, Shakir Mohamed, and Balaji Lakshminarayanan. Normalizing flows for probabilistic modeling and inference. *arXiv preprint arXiv:1912.02762*, 2019.
- [117] Alessandra Parisio, Evangelos Rikos, and Luigi Glielmo. Stochastic model predictive control for economic/environmental operation management of microgrids: An experimental case study. *Journal of Process Control*, 43:24–37, 2016.
- [118] Adam Paszke, Sam Gross, Soumith Chintala, Gregory Chanan, Edward Yang, Zachary DeVito, Zeming Lin, Alban Desmaison, Luca Antiga, and Adam Lerer. Automatic differentiation in pytorch. In *NIPS-W*, 2017.
- [119] Fabian Pedregosa, Gaël Varoquaux, Alexandre Gramfort, Vincent Michel, Bertrand Thirion, Olivier Grisel, Mathieu Blondel, Peter Prettenhofer, Ron Weiss, Vincent Dubourg, et al. Scikit-learn: Machine learning in python. *the Journal of machine Learning research*, 12:2825–2830, 2011.
- [120] Fernando Pérez-Cruz. Kullback-leibler divergence estimation of continuous distributions. In *2008 IEEE international symposium on information theory*, pages 1666–1670. IEEE, 2008.
- [121] Pierre Pinson and Robin Girard. Evaluating the quality of scenarios of short-term wind power generation. *Applied Energy*, 96:12–20, 2012.

- [122] Pierre Pinson, Christophe Chevallier, and George N Kariniotakis. Trading wind generation from short-term probabilistic forecasts of wind power. *IEEE Transactions on Power Systems*, 22(3):1148–1156, 2007.
- [123] Pierre Pinson, Henrik Aa Nielsen, Jan K Møller, Henrik Madsen, and George N Kariniotakis. Non-parametric probabilistic forecasts of wind power: required properties and evaluation. *Wind Energy: An International Journal for Progress and Applications in Wind Power Conversion Technology*, 10(6):497–516, 2007.
- [124] Pierre Pinson, Henrik Madsen, Henrik Aa Nielsen, George Papaefthymiou, and Bernd Klöckl. From probabilistic forecasts to statistical scenarios of short-term wind power production. *Wind Energy: An International Journal for Progress and Applications in Wind Power Conversion Technology*, 12(1):51–62, 2009.
- [125] Simone Polimeni, Luca Moretti, Giampaolo Manzolini, Sonia Leva, Lorenzo Meraldi, and Pietro Raboni. Numerical and experimental testing of predictive EMS algorithms for PV-BESS residential microgrid. *IEEE-PES Powertech (accepted)*, page 6, 2019.
- [126] Yuchen Qi, Wei Hu, Yu Dong, Yue Fan, Ling Dong, and Ming Xiao. Optimal configuration of concentrating solar power in multienergy power systems with an improved variational autoencoder. *Applied Energy*, 274:115124, 2020.
- [127] Ragheb Rahmaniani, Teodor Gabriel Crainic, Michel Gendreau, and Walter Rei. The benders decomposition algorithm: A literature review. *European Journal of Operational Research*, 259(3):801–817, 2017.
- [128] Danilo Rezende and Shakir Mohamed. Variational inference with normalizing flows. In *International Conference on Machine Learning*, pages 1530–1538. PMLR, 2015.
- [129] Yann Riffonneau, Seddik Bacha, Franck Barruel, and Stephane Ploix. Optimal power flow management for grid connected pv systems with batteries. *IEEE Transactions on sustainable energy*, 2(3):309–320, 2011.
- [130] Lars Ruthotto and Eldad Haber. An introduction to deep generative modeling. *GAMM-Mitteilungen*, page e202100008, 2021.
- [131] Julia Sachs and Oliver Sawodny. A two-stage model predictive control strategy for economic diesel-pv-battery island microgrid operation in rural areas. *IEEE Transactions on Sustainable Energy*, 7(3):903–913, 2016.
- [132] Yves-Marie Saint-Drenan. Wind power predictions analysis. part 1. tennet imbalance price system. development of a model for tennet imbalance price. Technical report, Energy research Centre of the Netherlands ECN, 2002.
- [133] David Salinas, Valentin Flunkert, Jan Gasthaus, and Tim Januschowski. Deepar: Probabilistic forecasting with autoregressive recurrent networks. *International Journal of Forecasting*, 36(3):1181–1191, 2020.

- [134] Iacopo Savelli, Bertrand Cornélusse, Antonio Giannitrapani, Simone Paoletti, and Antonio Vicino. A new approach to electricity market clearing with uniform purchase price and curtailable block orders. *Applied energy*, 226:618–630, 2018.
- [135] Michael Scheuerer and Thomas M Hamill. Variogram-based proper scoring rules for probabilistic forecasts of multivariate quantities. *Monthly Weather Review*, 143(4):1321–1334, 2015.
- [136] Heng Shi, Minghao Xu, and Ran Li. Deep learning for household load forecasting—a novel pooling deep rnn. *IEEE Transactions on Smart Grid*, 9(5): 5271–5280, 2017.
- [137] Jéssica Alice A Silva, Juan Camilo López, Nataly Bañol Arias, Marcos J Rider, and Luiz CP da Silva. An optimal stochastic energy management system for resilient microgrids. *Applied Energy*, 300:117435, 2021.
- [138] Bharatkumar V Solanki, Claudio A Cañizares, and Kankar Bhattacharya. Practical energy management systems for isolated microgrids. *IEEE Transactions on Smart Grid*, 2018.
- [139] Mucun Sun, Cong Feng, and Jie Zhang. Probabilistic solar power forecasting based on weather scenario generation. *Applied Energy*, 266:114823, 2020.
- [140] Antonio Sutera. *Importance measures derived from random forests: characterisation and extension*. PhD thesis, Université de Liège, Liège, Belgique, 2021.
- [141] Souhaib Ben Taieb, Gianluca Bontempi, Amir F Atiya, and Antti Sorjamaa. A review and comparison of strategies for multi-step ahead time series forecasting based on the nn5 forecasting competition. *Expert systems with applications*, 39(8):7067–7083, 2012.
- [142] Lucas Theis, Aäron van den Oord, and Matthias Bethge. A note on the evaluation of generative models. *arXiv preprint arXiv:1511.01844*, 2015.
- [143] Jean-François Toubreau, Jérémie Bottieau, François Vallée, and Zacharie De Grève. Deep learning-based multivariate probabilistic forecasting for short-term scheduling in power markets. *IEEE Transactions on Power Systems*, 34(2):1203–1215, 2018.
- [144] Georgios Tsaousoglou, Katerina Mitropoulou, Konstantinos Steriotis, Nikolaos G Paterakis, Pierre Pinson, and Emmanouel Varvarigos. Managing distributed flexibility under uncertainty by combining deep learning with duality. *IEEE Transactions on Sustainable Energy*, 2021.
- [145] Vladimir Vapnik. Principles of risk minimization for learning theory. In *Advances in neural information processing systems*, pages 831–838, 1992.
- [146] Cédric Villani. *Optimal transport: old and new*, volume 338. Springer Science & Business Media, 2008.
- [147] Bo Wang and Tao Chen. Gaussian process regression with multiple response variables. *Chemometrics and Intelligent Laboratory Systems*, 142:159–165, 2015.

- [148] Pu Wang, Bidong Liu, and Tao Hong. Electric load forecasting with recency effect: A big data approach. *International Journal of Forecasting*, 32(3):585–597, 2016.
- [149] Ran Wang, Ping Wang, and Gaoxi Xiao. A robust optimization approach for energy generation scheduling in microgrids. *Energy Conversion and Management*, 106:597–607, 2015.
- [150] Yi Wang, Gabriela Hug, Zijie Liu, and Ning Zhang. Modeling load forecast uncertainty using generative adversarial networks. *Electric Power Systems Research*, 189:106732, 2020.
- [151] Antoine Wehenkel and Gilles Louppe. Unconstrained monotonic neural networks. In *Advances in Neural Information Processing Systems*, pages 1545–1555, 2019.
- [152] Antoine Wehenkel and Gilles Louppe. Graphical normalizing flows. *arXiv preprint arXiv:2006.02548*, 2020.
- [153] Xiong Wu, Xiuli Wang, and Chong Qu. A hierarchical framework for generation scheduling of microgrids. *IEEE Transactions on Power Delivery*, 29(6):2448–2457, 2014.
- [154] Qiantong Xu, Gao Huang, Yang Yuan, Chuan Guo, Yu Sun, Felix Wu, and Kilian Weinberger. An empirical study on evaluation metrics of generative adversarial networks. *arXiv preprint arXiv:1806.07755*, 2018.
- [155] Ran Yuan, Bo Wang, Zhixin Mao, and Junzo Watada. Multi-objective wind power scenario forecasting based on pg-gan. *Energy*, page 120379, 2021.
- [156] Michaël Zamo and Philippe Naveau. Estimation of the continuous ranked probability score with limited information and applications to ensemble weather forecasts. *Mathematical Geosciences*, 50(2):209–234, 2018.
- [157] Bo Zeng and Long Zhao. Solving two-stage robust optimization problems using a column-and-constraint generation method. *Operations Research Letters*, 41(5):457–461, 2013.
- [158] Aston Zhang, Zachary C. Lipton, Mu Li, and Alexander J. Smola. *Dive into Deep Learning*. 2020. <https://d2l.ai>.
- [159] Aston Zhang, Zachary C. Lipton, Mu Li, and Alexander J. Smola. Dive into deep learning. *arXiv preprint arXiv:2106.11342*, 2021.
- [160] Hongxuan Zhang, Zongxiang Lu, Wei Hu, Yiting Wang, Ling Dong, and Jietan Zhang. Coordinated optimal operation of hydro–wind–solar integrated systems. *Applied Energy*, 242:883–896, 2019.
- [161] Yufan Zhang, Qian Ai, Fei Xiao, Ran Hao, and Tianguang Lu. Typical wind power scenario generation for multiple wind farms using conditional improved wasserstein generative adversarial network. *International Journal of Electrical Power & Energy Systems*, 114:105388, 2020.

- [162] Hongxuan Zhanga, Wei Hua, Rui Yub, Maolin Tangb, and Lijie Dingc. Optimized operation of cascade reservoirs considering complementary characteristics between wind and photovoltaic based on variational auto-encoder. In *MATEC Web of Conferences*, volume 246, page 01077. EDP Sciences, 2018.
- [163] Long Zhao and Bo Zeng. An exact algorithm for two-stage robust optimization with mixed integer recourse problems. *submitted, available on Optimization-Online.org*, 2012.
- [164] Long Zhao and Bo Zeng. Robust unit commitment problem with demand response and wind energy. In *2012 IEEE power and energy society general meeting*, pages 1–8. IEEE, 2012.
- [165] Shengjia Zhao, Jiaming Song, and Stefano Ermon. Towards deeper understanding of variational autoencoding models. *arXiv preprint arXiv:1702.08658*, 2017.
- [166] Muhammad Fahad Zia, Elhoussin Elbouchikhi, and Mohamed Benbouzid. Microgrids energy management systems: A critical review on methods, solutions, and prospects. *Applied energy*, 222:1033–1055, 2018.
- [167] Florian Ziel and Rafał Weron. Day-ahead electricity price forecasting with high-dimensional structures: Univariate vs. multivariate modeling frameworks. *Energy Economics*, 70:396–420, 2018.